# New Methods for Passive and Active Microrheology

Dissertation zur Erlangung des
Doktorgrades Dr. rer. nat. der Fakultät für
Naturwissenschaften der Universität Ulm
vorgelegt von


## Tobias Paust

aus Günzburg





2012


Institut für Experimentelle Physik
Universität Ulm

Amtierender Dekan: Prof. Dr. Joachim Ankerhold

Gutachter
1. Prof. Dr. sc. nat. ETH Zürich Othmar Marti
2. Prof. Dr. Kay-Eberhard Gottschalk

Tag der Promotion

Datum: 16.04.2013

# Introduction

In the last decades, science has made large steps forward with the invention of the first working laser in 1960 [1], the setup of the optical tweezers [2] in 1986, and in the same year the atomic force microscope (AFM, [3]). These scientific breakthroughs were soon applied to the field of biological substances. Beside the quantitation of protein concentrations [4] and the screening on the nanometer scale ([5], [6]), those novel applications made it possible to investigate the mechanical properties and gather first insights towards the stiffness or forces appearing in biological systems. In this way mechanical properties of cells, which are the basic structure of the human body, can be investigated. Nowadays the need to achieve knowledge about the cell and its functions is large because of the multitude of diseases based on malfunction of the cell. Hence, by understanding the structure, behavior and both the internal and external mechanism of the cell, possibilities to cure diseases or at least to improve the probability to survive, are in the focus of many research groups.
Pancreatic cells which migrate and spread in the pancreas are, in the case of malfunction, one of the most aggressive diseases with a probability of cure at only 3% [7]. This is because of the difficulties to discover the tumor in the body. At a later stadium of cancer development, therapies are less successful. Although several properties of these cells are well described, some still are not completely understood or even revealed ([8],[9]). Basically there are two approaches to determine the features of the cell. The first one is the top-down approach when the cell is taken into pieces and the interesting parts are examined. Vice versa it is possible as a bottom up approach to rebuilt parts of the cell. Pancreatic cancer cells are known to be very soft due to a modified intermediate filament network in the cytoskeleton that enables them to pass through the surrounding tissue. Thus, in research on the elastic properties, the top-down approach is the extraction of the cells intermediate filament network and the bottom-up approach the controlled assembly of an independent network. For gaining new insights into the cell behavior, especially in sense of the mechanics and dynamics of its network, microrheology is the common method and a

suitable tool to describe the network properties. By recording the particles' motion, which are embedded in the observed medium, the information about stiffness and dynamics can be determined. In order to reduce errors at the calculations or get more information about the medium at the measurement, the existing methods have to be improved or new ones developed. In this work the focus of interest on the one hand is the improvement of the passive microrheology method and on the other hand the development of a novel active method.
The first chapter describes the basics about the structure of the cell, its origin in the pancreas and its inner apparatus. In addition, with special regard on the intermediate filaments, the cytoskeletal components are illustrated. Since the intermediate filament proteins K8 and K18 build the monomers and later the filaments of the network in the pancreatic cancer cell, the assembly process is illustrated to explain the network formation.
In the second chapter the theoretical principles of optical tweezers are illustrated. The two common possible approaches for trapping particles are described. This helps to understand why focused light can hold small particles and applies a force on soft materials. This knowledge is important because the novel method described afterwards uses the optical tweezers for the oscillation of particles. Additionally an overview over the position and force calibration methods of optical tweezers is given in this chapter. For the passive microrheology one of these calibration methods was used to gather further network information.
The third chapter is about microrheology and is divided into two main parts. The first part covers the subject of passive microrheology in general including its theoretical principles. Moreover the conventional methods with their assumptions beside the general ones are explained. Since for the determination of the mechanical properties an unilateral Laplace transformation is necessary, which is up to now only possible to perform by approximations, the predominant methods introduce errors at this step. This is the motivation to develop a novel method that uses a function which can be transformed exactly, and therefore is less prone to those errors. The second part of this chapter describes the theory of active microrheology. In active microrheology a trapped particle gets excited by the optical trap and the response is recorded by a photo-diode.
The setup of the optical tweezers is described in the fourth chapter. A light microscope with a high-speed camera on the one hand are the central parts for passive microrheology measurements. The optical trap on the other hand is used for the active measurements in the network. Additional supporting devices of the setup are illustrated because they offer the opportunity to new applications. Some of those

applications are mentioned in the outlook.
The fifth and sixth chapter are concerned with the introduction of the two novel methods. As mentioned above the goal of the first method is to improve the technique to determine the dynamic shear modulus and thus the elastic and diffusive properties of both the cell and the *in vitro* assembled networks. The second method is a completely new concept which deals with several particles that are dependent on each other via the network. This method can be the first step to confirm theoretical works which predict force channeling and the isostaticity in the cell. Both chapters include simulations which confirm the validity of the methods.
Finally, the last chapter shows the application of the developed tools. Test measurements at simple media like water are presented that confirm the general functionality of the method and the devices used for the measurements. The investigation of *in vitro* assembled K8/18 networks and the pancreatic cancer cells on the one hand validates the method and on the other hand offers additional information about the cell and its network. In that chapter further results are presented, which help to understand the assumptions taken at the simulations presented in Chapter 5. Since these assumptions originate from measurements, it is feasible to present the underlying data in this chapter.
The thesis concludes with a summary, an outlook and an appendix, where additional developments are presented which were not in the main focus of the work. These are worth to be shown due to their possible application in future works.
To summarize, the goal of this thesis is to help to develop a continuative understanding of the physics of pancreatic cancer cells, especially in sense of the mechanical properties of both the bottom up and the top down approach.

# Contents

**Introduction** **i**

**1 Theoretical Aspects of Cells and Biopolymers** **1**
1.1 Cells - General and Pancreatic Cancer . . . . . 1
1.2 Biopolymers . . . . . 6

**2 Theoretical Principles of Optical Tweezers** **15**
2.1 Theoretical Principles of Optical Trapping . . . . . 15
2.2 Position Calibration of Optical Tweezers . . . . . 24
2.3 Force Calibration of Optical Tweezers . . . . . 27

**3 Theoretical Aspects of Microrheology** **31**
3.1 Passive Microrheology . . . . . 32
3.1.1 General Assumptions . . . . . 34
3.1.2 Conventional Methods . . . . . 37
3.2 Active Microrheology . . . . . 43

**4 Setup of the Optical Tweezers** **47**
4.1 Light Microscope and Components . . . . . 48
4.2 Optical Tweezers Setup . . . . . 51
4.3 Total Internal Reflection Fluorescence Microscope Setup . . . . . 53

**5 Conversion of the Mean Squared Displacement into the Shear Modulus** **55**
5.1 Introduction to the New Method . . . . . 55
5.2 Simulations . . . . . 60

**6 New Insights for Active Microrheology - the Lock-In Method** **79**
6.1 Deformation of an Isotropic, Elastic Body . . . . . 79
6.2 Lock-In Method and Transfer Tensor . . . . . 86
6.3 Simulations . . . . . 89

**7 Applications of the Developed Tools 97**
7.1 Sample Preparation and General Parameters . . . . . 97
7.2 Passive Microrheology . . . . . 99
7.2.1 Well-known Media . . . . . 100
7.2.2 *In Vitro* Assembled Keratin 8/18 Networks . . . . . 109
7.2.3 Pancreatic Cancer Cells . . . . . 117
7.2.4 Human Granolyzytes . . . . . 128
7.3 Active Microrheology . . . . . 132
7.3.1 Bi-distilled Water . . . . . 132
7.3.2 *In Vitro* Assembled Keratin 8/18 Networks . . . . . 135
7.4 Further Results . . . . . 144
7.4.1 Network Potentials . . . . . 144
7.4.2 Surface of Equal Probability . . . . . 147

**8 Summary 153**

**9 Outlook 159**

**10 Acknowledgements 161**

**A Correlative Microscopy 167**

**B Polymer Brushes 171**

**C Multiple Optical Tweezers 175**

**D MATLAB Programming 177**

**Bibliography 188**

**List of Figures 203**

**List of Tables 207**

**Curriculum Vitae 209**

# 1 Theoretical Aspects of Cells and Biopolymers

The mechanical properties of cells *in vivo* are determined by the composition of their membrane, the cytoskeleton and the organelles. However, the cytoskeleton is mainly responsible for those mechanical properties. In order to gain insight about the function and structure of the cell and its inner networks, it is necessary to know the biological background. Furthermore, if physical models and methods are developed to determine the mechanical properties of the cell, this background helps in understanding the mechanisms which play a major role. In this chapter the whole cell as well as the network of the cell - the cytoskeleton - is described in detail. In a first part the eukaryotic and additionally the pancreatic epithelial cells and their functions are explained. In the second part the main focus is on the intermediate filaments and their assembly to a whole network.

## 1.1 Cells - General and Pancreatic Cancer

Above all, there are two cell types which can form organisms. On the one hand there are prokaryotes which build single cellular organisms, and are less elaborate because of the lack of a nucleus and intracellular organelles. On the other hand there are eukaryotic cells which are big and more elaborate. In contrast to prokaryotic cells they can form multicellular organisms and are the main building blocks of all animals, plants and fungi [10]. Typical eukaryotic cells comprise an internal compartment which is called nucleus. The nucleus is surrounded by a double layer membrane which encloses the deoxyribonucleic acid (DNA), the genetic information of the cell. Furthermore it is embedded in the cytoplasm which contains the scaffold of the cell - the cytoskeleton - and the cell organelles. The cell organelles contain the Golgi apparatus, the endoplasmic reticulum, mitochondria, ribosomes and other

organelles which organize cell processes like saving energy and the modification of proteins [10],[11]. Further organelles can be seen in Figure 1.1 and are not described here.

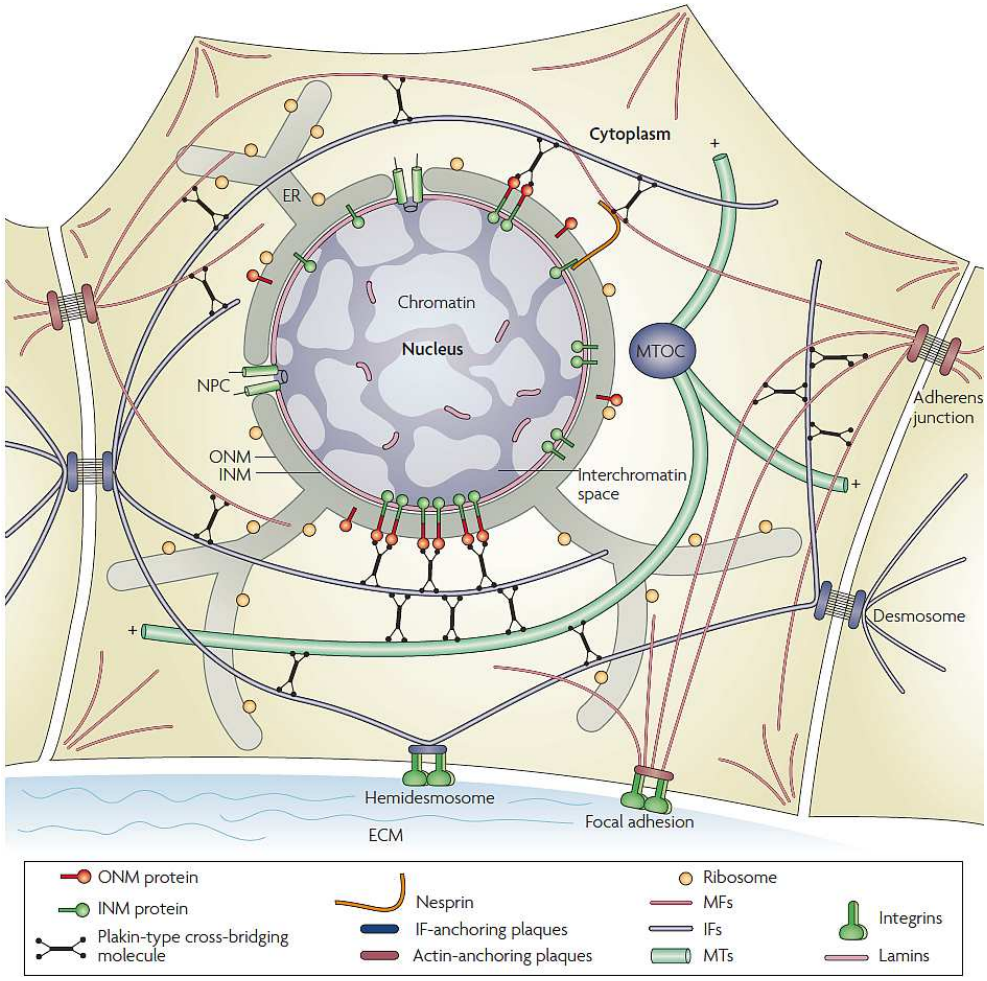



Figure 1.1: Sketch of an epithelial cell with important proteins and molecules. The three filament types (actin or microfilaments, intermediate filaments, microtubules) are shown in the nucleus periphery. The lamins are located in the nucleus and additionally, the anchoring plaques which connect the filaments to the extracellular matrix (ECM) are illustrated [13].

The cytoskeleton can be divided into three kinds of networks which control the cell strength, the internal arrangement, the migration and split the cell during division (actin or microfilaments MFs, intermediate filaments IFs, microtubules MTs). Furthermore, the adaption to changing external circumstances is another major task of

the cytoskeleton. The following description of the major functions of the different groups of filaments are taken from [10].
Actin filament networks build one part of the cytoskeleton and are responsible for the shape of the cell's surface and migration of the cell. The network itself is located at the outer region of the cell close to the plasma membrane. With accessory proteins the network filaments are linked to other cell components and to each other. The migration is performed by reorganization, depolymerization and polymerization of the actin filament network. The structure of single actin filaments and the structure of the subunits is explained in Section 1.2.
Another part of the cytoskeleton is the microtubule network. Microtubules are very rigid because of their hollow cylindrical shape. One end is attached to the microtubule-organizing center (MTOC) and the other points towards the rim of the cell. In that way this network covers large areas of the cell and therefore is responsible for the protein transport inside the cell. The MTOC is located close to the cell nucleus, and during division it builds up the spindle apparatus. The subunits which form microtubules are illustrated in Section 1.2.
The third and major part of this work is the intermediate filament network. Intermediate filaments (IF) which are attached to the cell nucleus and to the focal adhesion points of the cell, build a network with growing density in the nucleus region. The main task of this network is to stabilize and strengthen the cell, shield the cell nucleus from external stress and reorganize during migration and cell division. More details about the structure of intermediate filaments and their networks are given in Section 1.2. The intermediate filament network of cells is typically a cross-linked network. In this case cross-linked signifies that the filaments form chemical bounds and cannot slip along each other. Networks which were assembled *in vitro* are physically connected with entanglements unless there are no chemical linkers within the solvent.
To enclose the organelles the cell has a plasma membrane. This membrane controls the exchange of proteins of the extracellular matrix and the cell. Filopodia and lamellipodia ensure the cell migration which depends on the roughness of the surface and the temperature.
There are many varieties of eukaryotic cells in nature. The cells examined in this work are epithelial cells. All animals and plants of the Eumetazoa group contain epithelial cells. Within the other group called Parazoa, where for example sponges belong to, the cells are differentiated, but not organized into tissues. Hence, the epithelial cells are tissue cells which surround the organs inside and outside the body and line major cavities and organs of the body. Additionally, they form the

skin of the body and are the first type of cell which differentiates in the embryonic stage. Therefore, one of the main functions of epithelial cells is to cover inner and outer linings of body cavities and organs. They also replicate to replace damaged and dead cells. Moreover, they can aid in the transportation of material, adsorb, lubricate and secrete fluids which are necessary for digestion and other processes [12], [14].
Other cell types are located in the muscle tissue, the connective tissue and the nervous tissue. They are interconnected through signaling processes or chemical interactions via proteins or fluids. The epithelial cells of the organs have further properties and functions. For example, the pancreatic epithelial cells cover the pancreas and perform, their main function, the digestion and glucose metabolism [15].

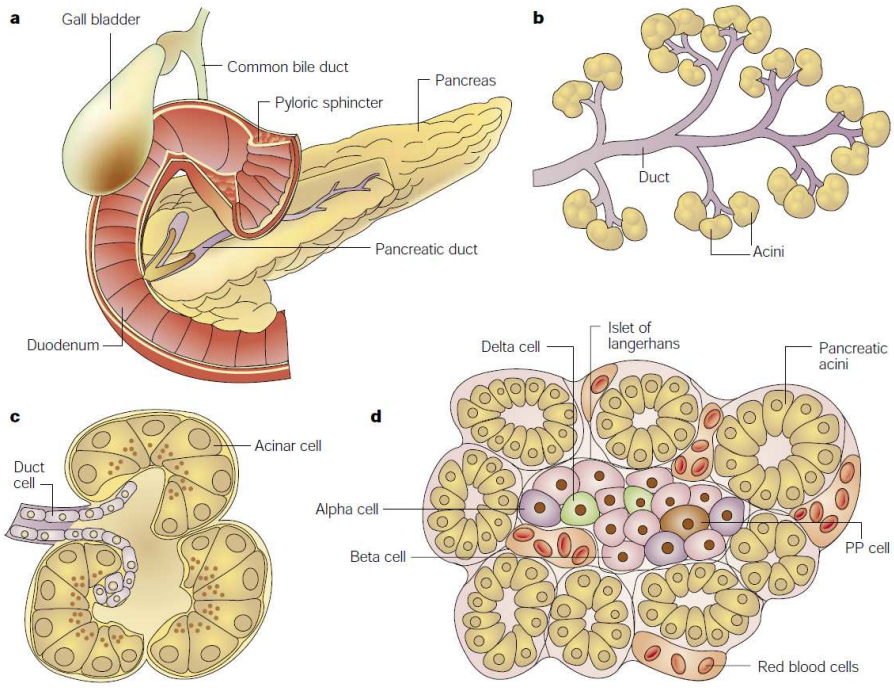



Figure 1.2: Sketch of the pancreas. a) The whole pancreas which in general is divided into the parts head, neck, body and tail (not explicitly shown here). The pancreatic duct inside the nucleus is the location for cancer tumors. b) At a closer view the duct and acini form a tree-like structure. c) The duct is divided into acinar cells and duct cells. d) The exocrine tissue is divided into pancreatic acini, red blood cells and the langerhans islets, which surround alpha, beta, PP and delta cells [18].

The pancreas (presented in Figure 1.2), which is divided into four main regions - head, neck, body and tail - consists of two different types of tissue: The exocrine pancreas that secretes enzymes into the intestine, and the endocrine pancreas that secretes hormones into the bloodstream [16], [17]. The exocrine pancreas consists of acinar and duct cells [18]. The acinar cells are organized into grape-shaped clusters whereas the duct cells form a network of increasing size. Around the duct cells, there are epithelial cells which form the ductal epithelium. In case of malfunction, these epithelial cells can convert to pancreatic cancer cells. Malfunction in this context means a genetical modification of the cells. Thus, pancreatic cancer results from the successive accumulation of gene mutations in the cells [19]. Hence, there are three elements which form a tumor, including the pancreatic-cancer cells, the corresponding stem cells and the so-called tumor stroma. The pancreatic cancer stem cells originate in an asymmetric division of a mature stem cell. The division normally leads to two mature stem cells, but in some cases cancer stem cells are generated. In a next iteration, beside a new cancer stem cell, a cancer cell is built. After that, these cancer cells can form a tissue-like structure and with a dense stroma, this is known as the tumor [20], [19]. Pancreatic cancer exhibits various chromosomal abnormalities such as aneuploidy, translocations, deletions, double minute chromosomes and chromosome duplication, causing unregulated cell proliferation and migration. This makes the cells grow faster and spread over the organ [21]. This change in the properties of the cell can be described as a *journey* when the cell morphs over time from a phenotype into an invasive or metastatic entity. The steps of this journey are marked by a variety of genetic modifications like the amplification or deactivation of some genes, expression of new tumor markers, and alterations in cell and external tissue morphology [22]. Since the cytoskeleton has major control over the dynamics of the cell, a modified cytoskeletal structure might play a role in tumor metastasis. In case of a manipulated cytoskeleton, it has been shown that the changes in the intermediate filament network contribute to the cells stiffness and its growth [23].
In this work the measurements at pancreatic cancer cells of type Panc-1 were performed to gather information about the mechanical properties of the cell as well as of its cytoskeletal network. Since keratin 8 and 18 occur as intermediate filament network in the most simple epithelia, also carcinoma cells express keratin 8/18 networks [24]. Therefore, the network at this cell type consists of a dense arrangement of keratin 8/18 filaments surrounding the cell's nucleus. Another feature of the cell line Panc-1 is that they lack vimentin which is usually not the case in epithelia [25].

## 1.2 Biopolymers

In this section the three filament types of the cytoskeleton are described in detail. The first part briefly shows the structure and function of actin and its networks, whereas in the second the constitution of microtubules is illustrated. In the third part the intermediate filaments are discussed with focus on K8/18 proteins and their assembly into networks.

**Actin Filaments**

Actin filaments are built of the protein actin. The elementary building block of this protein consists of the protein G-actin ('G' for globular) which is formed by a single chain of about 375 amino acids and a molecular mass of 42 kDa. In this chain there are 36 negative and 30 positive charged amino acids, and therefore an actin filament has a negative net charge [11]. If the single string assembles into a longer string of several G-actin proteins, it is called F-actin, the filamentous actin. For this the strings of G-actin monomers are intertwined strands. Therefore the whole filament has a diameter of approximately $7 - 8$ nm with a mass per unit length of 16 kDa/nm [26]. In Figure 1.3 a typical structure of an actin filament is shown and the right-handed helical structure of the G-actin monomers can be seen.

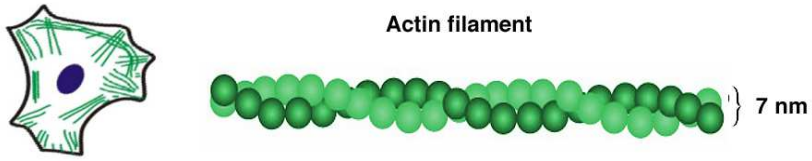



Figure 1.3: Sketch of an actin filament. On the left-hand side, a sketch of a cell is shown with its nucleus and the typical regions inside the cell where the actin filament network is located. On the right-hand side, the structure of an actin filament is depicted. The circles denote the G-actin which polymerizes to F-actin - the filament [10].

The distance between the molecules on the helical axis is 27.6 Å. If G-actin polymerizes to F-actin, the binding protein plays a major role. As an example, if the transition is made by the protein cofilin, the $\alpha$-helical pitch of F-actin will be modified and that will increase the flexibility of the whole filament. When F-actin interacts

with myosin, a basis for the contraction of muscles is built [27]. In this way it is important for the filaments to interact. In case of the cell the actin interacts with itself and builds a network or an array which has the functions shown in Section 1.1. The assembly to an array can be divided into two types of networks - web-like (gel-like) networks and bundles. Both types of arrays consist of proteins which are called gel-forming proteins or bundling proteins. The latter link the filaments parallel to each other. In the cell these bundles can be found in the filopodia which are helpful when the cell explores its environment. Furthermore, the stress fibers inside the cell are bundled actin filaments. In the gel-like network the filaments, which are linked to each other, form a larger angle. Dependent on the mesh size the network is looser or stiffer. Examples for bundling proteins are fimbrin and $\alpha$-actinin while spectrin is a well-studied gel-forming protein [10].

### Microtubules

The second structure contributing to the cell cytoskeleton is the network of microtubules which is frequently found in a star-like array in the cell with the centrosome (microtubule-organizing center) as its center [10]. The key features of the microtubules are the cell transport, cell division and the influence on the cell shape and its motility. A microtubule filament consists of the protein tubulin which, as a heterodimer, binds linearly with its head to the tail of a second tubulin. The protein tubulin has several subunits which are named $\alpha$-tubulin and $\beta$-tubulin monomers [28]. Each of these monomers has a molecular mass of about 50 kDa. The structures the $\alpha$- and $\beta$-tubulin form are hollow cylinders built of 13 protofilaments. Figure 1.4 shows the structure of a mircotubule.

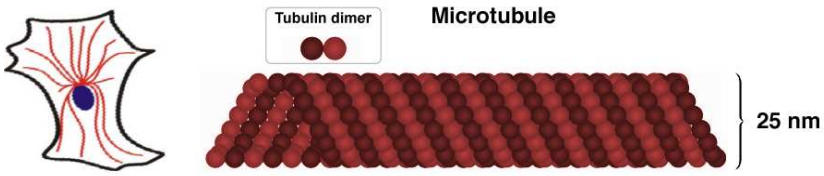



Figure 1.4: The microtubule network is spread all over the cell. One end of a microtubule is located at the microtubule organizing center (MTOC) which is the origin of a star-like network (left). The structure of a microtubule with its cylindrical hollow shape built of the $\alpha$- and $\beta$-tubulin monomers can be seen on the right [10].

The whole microtubule has an overall mass per unit of about 16 kDa/nm [26]. The mass per unit is ten times higher compared to the actin filaments and its diameter with about 25 nm is three times larger than the diameter of actin. The length of a microtubule in cells can reach several micrometers. The flexural rigidity which corresponds to the persistence length is at about 5 mm which can be observed by thermal fluctuation measurements [29]. Drastic changes in the persistence length can be observed when electric forces are applied and it decreases to about 0.08 mm for short filaments [30].

### Intermediate Filaments

In the cytoskeleton a third filament system forming a network around the nucleus can be found, which consists of intermediate filaments. Since the measurements in this work were performed with *in vitro* assembled intermediate filament networks and extracted pancreatic cancer cells, the structure and properties of this filament type are described in more detail. Sketch 1.5 illustrates the structure and the location of intermediate filaments.

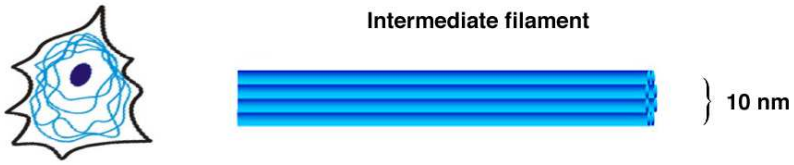



Figure 1.5: The intermediate filament network is located close to the nucleus. In that way one of its functions is the shielding of the nucleus and the damping of mechanical external stresses (left). The structure of an intermediate filament consists of laterally bound dimers which assemble longitudinally as unit length filaments (ULFs, right) [10].

In this sketch the intermediate filament network is shown as one part of the cytoskeleton. In the sketch it is not obvious that there are intermediate filaments inside the nucleus (the lamins) and those that are indirectly connected to the outside of the cell, the extra cellular matrix (ECM). This connection is built via the integrins at the focal adhesions [10].
All intermediate filaments can be grouped into six types. The keratins, which are seen as the most complex intermediate filament proteins (IF), allocate two groups because of their varying chemical properties. Hence, type I keratins are acidic and

include eleven epithelial keratins named K9-K20. Type II keratins are basic with eight different proteins named K1-K8. Additionally, in both groups there are hair keratins (Ha1-Ha4, Hb1-Hb4) [31], [32]. Keratins can only assemble as heteropolymers. While the major pair for squamous epithelia is K5 and K14 [33], in almost all simple epithelia K8 and K18 is expressed.

Type III IF proteins are produced by mesenchymal cell types and by a variety of transformed cell lines. In muscle cells the cytoskeleton IFs are called desmin and beside vimentin, this is one of the most expressed IFs of this group. Vimentin can be found in fibroblasts and blood vessels. Moreover, glial fibrillary acidic protein (GFAP) and peripherin, which is expressed in peripheral neurons, are members of type III IFs. These IFs can exist as homopolymers, but it is also possible to form heteropolymers with type III proteins and with type IV IFs [34].

In this classification, the type IV IFs include neurofilaments and $\alpha$-internexin which occur in axons and dendrites in neurons. In this group $\alpha$-internexin can form homopolymers, whereas the rest are obligate heteropolymers.

The proteins concerning the nuclear lamina are in a separate group. They are called type V IFs. The nuclear lamina can be divided into lamin B which is mainly expressed in vertebrate embryo cells, and lamin A which exists in addition to lamin B in somatic cells [31].

In the last group there are IFs that do not belong to the other groups. One example of type VI IFs is nestin. Nestin is expressed in several fibroblastic but not epithelioid cell lines and is able to coassemble with type III vimentin and type IV $\alpha$ internexin [35].

The structural organization of IFs of different groups are similar. Thus the schematic box presentation in Figure 1.6 A) is valid for almost all IFs. The IF consists of a central $\alpha$-helical rod domain which begins with a non-$\alpha$-helical amino-terminal head (N-terminal) and ends with a carboxyterminal tail domain (C-terminal). Hence, the structure of the rod domain is divided into three parts - coil1A, coil1B and coil2 which are sub helices with a number of amino acids that are similar for each IF (coil2 before 2009 was seen to be divided by linker L2 into two parts. Crystallographic studies showed that this is not the case and coil2 forms a continuous coiled-coil structure and L2 does not exist [36]). Between the helical domains there are linker domains (L1 and L12), whose structure is not completely known up to now. The former linker L2 is a short parallel bundle pb (the two $\alpha$ helices are not intertwined), and the stutter st is hidden in the coiled-coil segment of coil2. The stutter is a part of the $\alpha$-helical domain where a discontinuity appears in the heptad repeat pattern. In the box model the red box represents IF-consensus motifs and the yellow one is

a pre-coil domain that is formed in vimentin proteins [37].

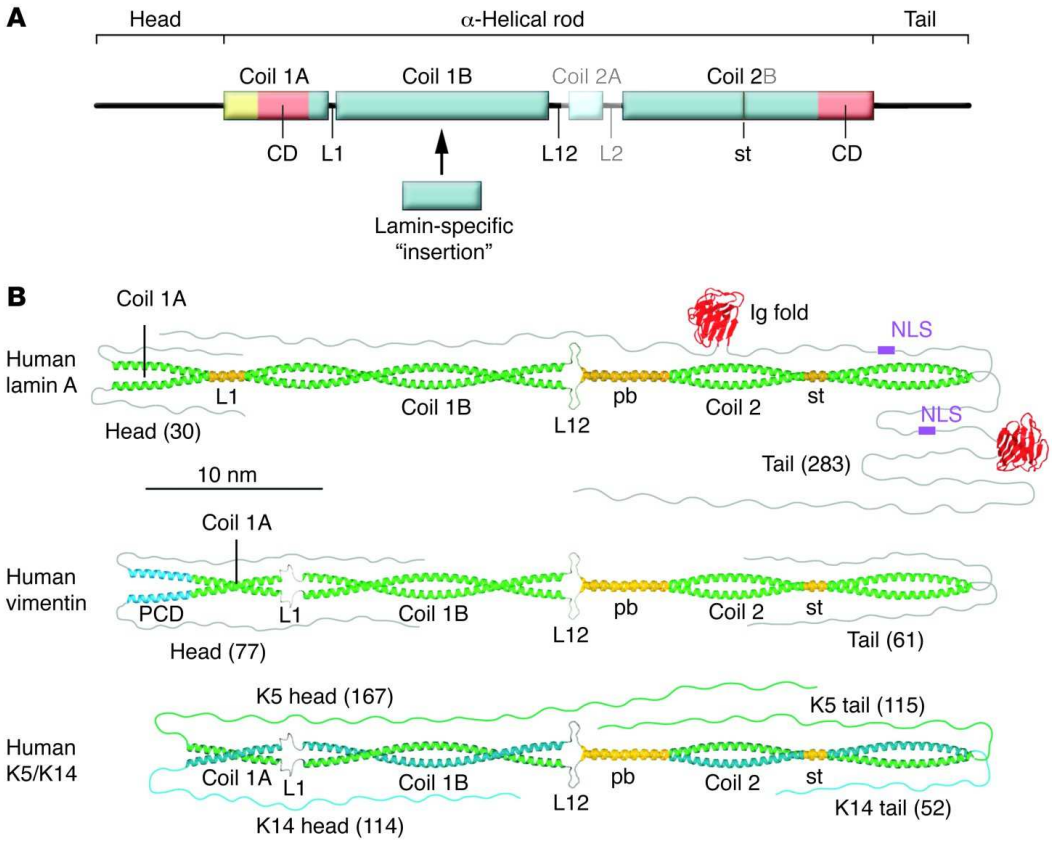



Figure 1.6: A) A schematic box illustration of the general structure of IFs. The $\alpha$-helical rod is separated in coil 1A, coil 1B and coil 2. The former coil 2A and coil 2B have been shown to be only one part - coil 2. Therefore, the coils are divided by linker L1 and L12, and not by linker L2 which was assumed previously. The red box denotes the IF-consensus motifs whereas yellow is a domain only formed by vimentin proteins. In coil 2 stutter st is a discontinuity in the heptad repeat pattern. B) Three examples for structures of intermediate filaments of different types - lamin A (type V), vimentin (type III) and keratin 5/14 (type I, II). Keratin 5/14 is similar to keratin 8/18 which is not presented here. At the beginning of coil 2 a parallel bundle (pb) was observed. The different colors at human keratin 5/14 show that the dimer is heteropolymeric ([37] modified).

Within the $\alpha$-helical rod domain, amino acids are regularly organized in heptad repeats. The amino acids are connected via hydrogen and covalent bonds forming an amino acid chain. Every first and fourth amino acid of the chain is hydrophobic

which allows to form a coiled-coil dimer between two $\alpha$-helical domains with a shielding of the surrounding fluid. The length of the rod is approximately 45 nm and 7 nm longer at lamins. All IFs have a head and a tail domain which are involved in the assembly process [38]. In Figure 1.6 B the differences between the IF structures for lamin A, vimentin and keratin 5/14 can be observed. The parenthesized numbers denote the number of amino acids. Human keratin 8/18 which was investigated in this work has a similar structure to the shown keratin 5/14. The different colors of the $\alpha$-helices indicate that the IF consists of two different protein types - of type I and type II.

The assembly process of the IF monomers to longer IF filaments is divided in three different groups named assembly group 1, assembly group 2 and assembly group 3. The third group contains the assembly of lamin IFs. In a first step the dimer assembles longitudinally to a protofilament where the heads of the dimer bind to the tail, too. In the second step the protofilaments bind laterally to an extended fibril.

In the second assembly group the assembly of desmin or vimentin is explained. In this case it is important that both homopolymers and heteropolymers can be the result of the assembly process.

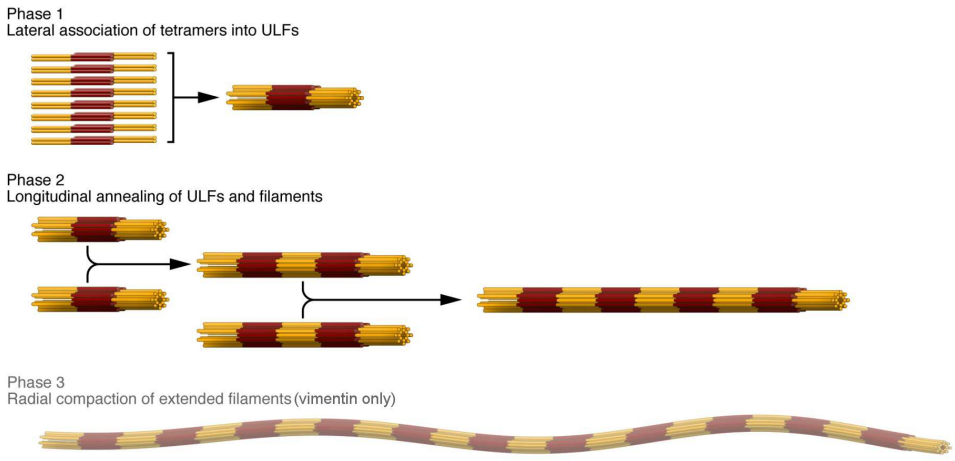



Figure 1.7: The three phases of the intermediate filament assembly. In phase 1 the dimers align laterally to tetramers which form in association into ULFs. In the second phase the longitudinal annealing takes place. After that the whole filament length increases and decreases in diameter ([37], modified). The third phase only occurs at the formation of vimentin filaments, but not during the keratin assembly.

Hence at the beginning the assembly starts from antiparallel homopolymeric dimers which bind laterally to a so-called unit length filament (ULF). After that, the ULFs assemble longitudinally to the resulting homopolymer filament. After longitudinal annealing they show a compaction of the diameter which leads to the final filaments. Keratin filaments are heteropolymers and therefore their assembly formalism is illustrated separately for the assembly group 1. This assembly process can be seen in Figure 1.7 [37]. The dimer of the IF which consists of two monomers out of the protein group type I and II, has a C-terminal and a N-terminal end. In phase 1 the dimer forms a tetramer by lateral binding in a half-staggered way so that always their coils point to the same kind of end (C- or N-terminal) stick together. In the same process hexamers, octamers and up to $1 \times 32$-mers are formed. Via the binding of the associations an unit length filament is built. When several ULFs are available, longitudinal annealing takes place and the filament length increases while the ULF building process simultaneously continues [38], [37].
The dynamics of the assembly depends on several parameters. The result of the assembly, namely the length of the filaments, their persistence length and whether there is a network formation or not, are regulated by these parameters. Parameters like temperature, protein concentration and the time after the assembly is stopped, can be changed to gather insight into the assembly kinetics. A detailed description of this can be found in [40] and measurements and results of the length distribution of single filaments are shown in [39], [41]. The kinetics of the assembly are described by several models which try to predict the length distribution and the assembly probabilities. Further works and results are illustrated for example in [42], [43] and [44].
For long assembly times and high protein concentrations the filaments form networks *in vitro*. This network formation can be observed at intermediate filaments as well as at actin filaments. In the cell the filaments are also formed as a network. The network dynamics and its mechanical properties depend on parameters like the observed protein, its concentration, the temperature and whether there are additional cross-linker. How to determine the mechanical properties is explained in the following chapters. The different kinds of networks, namely entangled or cross-linked, are discussed in the following.
Concerning the binding among the filaments, one can separate networks into two groups. On the one hand, there are networks which are chemically linked at their contact points. This type of network is also known as cross-linked network. If the network gets stressed, the single filaments within the network suffer the external force and elongate, but without any changes at the crossing points.

On the other hand, there is the entangled network or physical network. The filaments of these networks are not chemically fixed at their contact points, but entangled around each other so that they build a node. Depending on the apparent stress applied to the network, the filaments can slip along each other. By adding chemical cross-linker like $MgCl_2$ or plectin the physical networks become chemical ones ([40] and Chapter 7). The description of models for both kinds of networks can be found in [45], [46], [47] and [48].

# 2 Theoretical Principles of Optical Tweezers

This chapter describes the theoretical principles of optical tweezers. Optical tweezers are used to trap small particles like polystyrene beads in liquid environment. In literature, the device often is called optical trap and photonic force microscope (PFM), too. By focusing a laser beam, the optical tweezers apply a force to the sample via the trapped particle. This force reaches from the femto-Newton [49] to the nano-Newton range depending on the intensity of the laser, the numerical aperture of the focusing objective and the material properties of the particle and medium. The force in general is sufficient to manipulate DNA or intracellular structures like filament networks [50], [51].
In the first section the principles of optical trapping in theory is introduced. In this theoretical part the trapping of small particles in two different regimes - the geometrical optics and the Rayleigh approach - is described. Additional a short overview is given about the more general theory that describes stable trapping in the regime, where particle size and laser wavelength are in the same range. The subsequent sections present the practical calibration methods of the optical tweezers. These are divided into the calibration of the position of the trapped particle - the second section - and in the third section the determination of the force constant. Hence, the displacement of the particle can be recorded in the unit of meter and the force of the optical tweezers via the stiffness constant.

## 2.1 Theoretical Principles of Optical Trapping

The first observations of an influence of light at dielectric particles was reported by Ashkin in 1970. At that time he focused a green laser beam and observed that particles were pushed into the propagation direction of the laser beam by the radiation pressure. The trapping, as described in his article, was performed by pushing the

particle against a glass surface or by using two counter-propagating laser beams. For the latter case a stable trap was built because both beams pushed the particle in direction of the propagating light [52]. Several years later, Ashkin published an article about single beam optical trapping. Modern optical tweezers are built on the setup presented in the publication of Ashkin. An objective with high numerical aperture focused a laser beam to gain a high gradient force [2]. The theoretical principles for the optical tweezers in this work is based on Ashkin's work.
There are two forces which play an important role in optical trapping - an attractive force $F_{\text{grad}}$ which pulls the particle into the focus, and a scattering force $F_{\text{scat}}$ which pushes the particle towards the direction of the focused laser beam. In addition to that, there is always a thermal motion of the particle (the Brownian motion). This motion is constraint by the effect of the trapping forces. For the explanation of the trapping forces the Brownian motion is neglected.
The theory behind trapping particles can be approached via the consideration of two different regimes. In the first regime the particle trapped is assumed to be much larger than the wavelength of laser light. At these length scales the geometrical optics are valid and the beam can be considered as many photons which carry a momentum. Hence, the incident light hits the particle at its surface and partially is reflected while the rest is transmitted through the particle. The latter part gets divided into another reflected and transmitted parts when the light leaves the particle. As a result, there is a net momentum transfer to the particle via the photons which, dependent on their angle of incidence, contribute to the scattering or to the gradient force [53]. Further parameters that determine the trap strength are the numerical aperture (NA), the ratio of refractive index of the medium and particle, the coating of the particle and the intensity cross section of the laser beam. Apart from the latter, all parameters can be found in Snell's law and Fresnel's equations which describe the whole theory in geometrical optics. If e.g. the NA is too low, the laser beam will be not focused tightly and the momentum of the photons mostly contribute to the scattering force. For a refractive index of the medium which is higher than the one of the particle, e.g. if air bubbles are in the medium, the momentum of the photons will push the bubbles out of the beam focus. If the Gaussian beam is not expanded before getting focused or its cross section is not a clean Gaussian function, the trapping is influenced in a negative way. Hence, overall the change of momentum leads to an attractive force into the focus of light which, for small displacements, is proportional to the light intensity. In Figure 2.1 exemplary rays which contribute to a stable trapping are shown. In all three cases shown (particle below, beside or above the focus ), the particle gets pulled into the focus. Further

details for particles in the geometrical optics regime are discussed in [54].

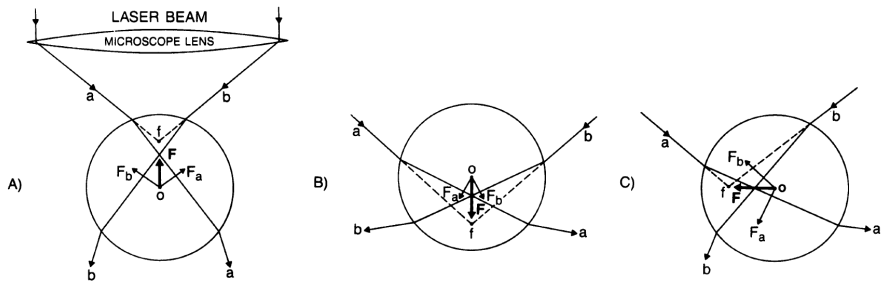



Figure 2.1: Pathway of the outermost rays of the laser beam. A) Scenario when the particle center is located below the laser focus. The rays get deflected so that the resulting momentum of the beam points into the direction of propagation. Because of the conservation of momentum the particle's momentum points towards the laser beam and moves to the focus. B) The particle's center is above the focus. Vice versa to A), the particle gets pushed downwards into the focus. C) Scenario when the particle is laterally displaced out of the focus. The resulting ray momentum leads to a force pulling the particle into the focus [54].

The second regime describes the interaction of the particle's dipoles with the electromagnetic field of the laser. This means that the particle's material is polarized by the field in the focus. The field has a gradient which is dependent on the distance to the focus and induces a change of polarization in the particle. If the diameter of the particle compared to the wavelength of the laser is small, the conditions for Rayleigh scattering are satisfied. This leads to a treatment of the particle as a point dipole. Similar to the upper geometrical optics approach the total force on the particle can be divided into two parts. On the one hand there is the scattering force and on the other hand the gradient force. First one has to take into account that the laser beam is of $TEM_{00}$ mode, also known as Gaussian beam. If a Gaussian beam passes a lens or an objective, the beam will get narrow with a minimum in its waist at the focus. For larger distances the beam diameter gets larger. Figure 2.2 shows this behavior and marks the coordinate system with $x$ and $y$ as the lateral directions and $z$ as the axial component. The waist width can be approximated by calculating the propagation of the Gaussian beam. This leads to a width depending on the NA and the wavelength of the laser $\lambda$ of

$$w_{\text{trap}} \geq \frac{1.22\lambda}{n}\sqrt{\left(\frac{n}{NA}\right)^2 - 1} \tag{2.1}$$

where $n$ denotes the refractive index of the liquid the optical trap is placed in [55].

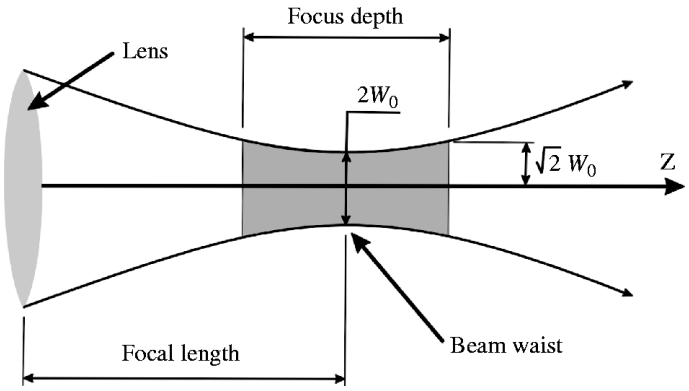



Figure 2.2: A Gaussian beam passing an ideal lens. At the focal length the narrowest point of the laser beam is called beam waist with a width of $2W_0 = 2w_0$. The focus depth is the region where the laser beam diameter is $2\sqrt{2}w_0$. For larger distances to the lens the laser beam diverges [56].

The electric field around the focus can be described in terms of a complex amplitude by the following equation. $\vec{x}$ in this case denotes the unit vector in the direction of the polarization [57]. The electric field is

$$\vec{E}(x,y,z) = \vec{x}E_0\frac{ik_{\text{W}}w_0^2}{ik_{\text{W}}w_0^2 + 2z}e^{-ik_{\text{W}}z}e^{-i\frac{2k_{\text{W}}z(x^2+y^2)}{(k_{\text{W}}w_0^2)^2+4z^2}}e^{-\frac{2k_{\text{W}}z(x^2+y^2)}{(k_{\text{W}}w_0^2)^2+4z^2}} \tag{2.2}$$

with $w_0$ being the beam waist and $E_0$ the electric field at position $x = 0$, $y = 0$ and $z = 0$. $k_{\text{W}} = 2\pi/\lambda$ denotes the wave number of the laser beam. Thus, the electric field of the laser beam for every position around the focus can be determined. Furthermore the Poynting vector of this field is given by $\vec{S}(x,y,z,t) = \vec{E}(x,y,z,t) \times \vec{H}(x,y,z,t)$, which is dependent on time because of the temporal angular frequency of the light. With $\vec{H} = \vec{z} \times \vec{E}(x,y,z)/\sqrt{\mu_2/\epsilon_2}$, the Poynting vector can be developed further and by time-averaging the intensity of the light $I$ can be determined dependent on the position. The dielectric constant of the medium is $\epsilon_2$ and its magnetic permeability is $\mu_2$, whereas the particle of radius $a$ has a dielectric

constant $\epsilon_1$.

$$\vec{I}(\widetilde{x},\widetilde{y},\widetilde{z}) = \vec{z}I(\widetilde{x},\widetilde{y},\widetilde{z}) = \vec{z}\frac{2P}{\pi w_0^2}\frac{1}{1+4\widetilde{z}^2}e^{-\frac{2(\widetilde{x}^2+\widetilde{y}^2)}{1+4\widetilde{z}^2}} \tag{2.3}$$

where $P$ is the beam power and $\widetilde{x}$,$\widetilde{y}$ and $\widetilde{z}$ are normalized coordinates, expressed by $(\widetilde{x},\widetilde{y},\widetilde{z}) = (x/w_0, y/w_0, z/k_{\mathrm{W}}w_0^2)$. The radiation forces in the Rayleigh scattering regime can be determined by knowing the intensity of the laser beam. For the derivation of the gradient force the Lorentz force builds the basis. Furthermore, the dipole moment $\vec{p}$ is used and can be written as follows

$$\begin{aligned} \vec{p} &= \bar{\alpha}\vec{E} \\ \vec{p}(x,y,z,t) &= 4\pi\epsilon_2 a^3\left(\frac{m^2-1}{m^2+2}\right)\vec{E}(x,y,z,t) \end{aligned} \tag{2.4}$$

with $\bar{\alpha}$ the polarizability of the medium. The usage of the Clausius-Mossotti equation leads to a dependency of the dipole moment on $m = n_1/n_2$, the ratio refractive indices of the particle and the medium and the relative permittivity $\epsilon_2$ of the medium [58]. In this case the Lorentz force is

$$\vec{F}_{\mathrm{Lorentz}} = (\vec{p}\cdot\nabla)\vec{E} + \frac{1}{c}\partial\vec{p}\times\vec{B} \tag{2.5}$$

with $\vec{B}$ being the magnetic field [59]. By using $(\vec{E}\cdot\nabla)\vec{E} = \nabla(1/2\vec{E}^2) - \vec{E}\times(\nabla\times\vec{E})$ and the third Maxwell equation $\nabla\times\vec{E} = -\partial\vec{B}/\partial t$, the Lorentz force of Equation (2.5) can be written as

$$\vec{F}_{\mathrm{Lorentz}} = \vec{F}_{\mathrm{grad}} = \frac{1}{2}\alpha\nabla\vec{E}^2 + \frac{\alpha}{c}\partial(\vec{E}\times\vec{B}) \tag{2.6}$$

where $\alpha = 4\pi\epsilon_2 a^3(m^2-1)/(m^2+2)$ and the second term being zero if the assumption holds that the frequency of sampling is much smaller than the frequency of the laser light [60]. In almost every case (when the laser works in cw-mode) this is valid and the resulting time averaged gradient force is given by

$$\vec{F}_{\mathrm{grad}}(x,y,z) = \left\langle \vec{F}_{\mathrm{grad}}(x,y,z,t)\right\rangle_T = \frac{2\pi n_2 a^3}{c}\left(\frac{m^2-1}{m^2+2}\right)\nabla I(x,y,z). \tag{2.7}$$

If the intensity $I$ of Equation (2.3) is inserted into the latter equation, the gradient force can be used for calculations dependent on the position close to the focus. Hence, the gradient force consists of three rectangular components which are restoring forces towards the focus - the center of the beam waist. This is only valid, if the ratio of refractive indexes is larger than one. The maximal values for the force

occur in $x$ and $y$ at $\pm w_0/2$ and for $z$ at $\pm k_\mathrm{W} w_0^2/2\sqrt{3}$.
The scattering force on the other hand can be derived as follows. The induced dipole follows the oscillations of the electric field. Thus, the particle acts as an as oscillating electric dipole and emits waves in all directions. These emitted waves are secondary or scattered waves. This event changes the energy flux of the external electromagnetic wave and the result is a momentum transfer, which is noticeable as the scattering force [57].

$$\vec{F}_\mathrm{scat}(x,y,z) = -\frac{C_\mathrm{sc}\left\langle \vec{S}(x,y,z,t)\right\rangle_T}{c/n_2} = \vec{z}\frac{n_2}{c}C_\mathrm{sc}I(x,y,z) \tag{2.8}$$

with $C_\mathrm{sc}$ as cross section of radiation pressure concerning the particle or equally the scattering cross section. This scattering force acts in the direction of beam propagation and not as the gradient force in the direction of the focus. $C_\mathrm{sc}$ is given by

$$C_\mathrm{sc} = \frac{8}{3}\pi(k_\mathrm{W}a)^4 a^2 \left(\frac{m^2-1}{m^2+2}\right)^2. \tag{2.9}$$

If this equation is inserted in Equation (2.8), the scattering force can be calculated in dependency on the intensity of the beam and on the position. The resulting force is the sum of both the gradient and the scattering force. Hence, one can write (the particle is on the optical axis)

$$\begin{aligned}\vec{F}_\mathrm{total}(0,0,\widetilde{z}) &= \vec{F}_\mathrm{grad}(0,0,\widetilde{z}) + \vec{F}_\mathrm{scat}(0,0,z)\\ &= \frac{2\pi n_2}{c}\left[-\beta\frac{8\widetilde{z}}{k_\mathrm{W}w_0^2(1+4\widetilde{z}^2)} + \frac{4}{3}k_\mathrm{W}^4\beta^2\right] I(0,0,\widetilde{z})\end{aligned} \tag{2.10}$$

with $\beta = a^3(m^2-1)/(m^2+2)$ and $\widetilde{z}$ the normalized coordinate in $z$ direction.
Overall, the total force can be described for three different scenarios. At those scenarios the particle is located on the optical axis and the ratio between gradient and scattering force varies. In Figure 2.3 on the left-hand side the scattering force (red line) is larger than the gradient force (blue line) which makes the total force always be positive. If the particle is displaced towards the negative $z$-direction, the force will point into the positive direction. That means the particle will move into the focus. If the particle is moved to the positive $z$-direction, the total force points into the positive direction again and therefore will push the particle away. In this case the particle cannot be trapped. At the second graph, in the middle, the scattering force is slightly larger than the gradient force leading to the total force becoming zero for displacements in $+z$ direction.

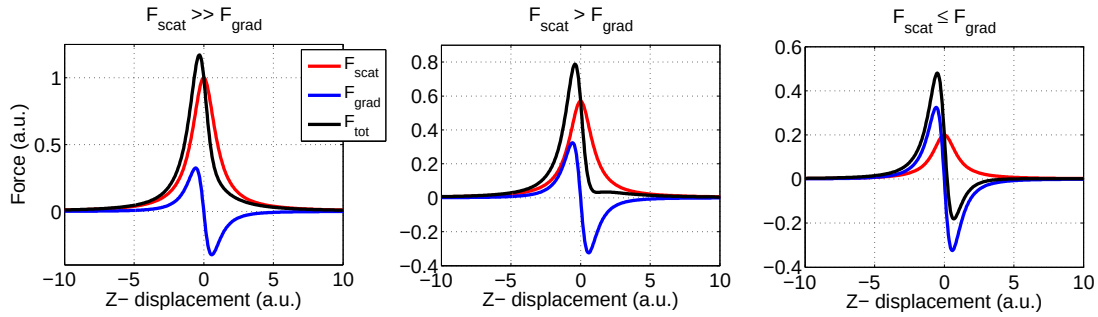



Figure 2.3: Simulations of varying scattering and gradient forces. Left: The scattering force (red line) is much bigger than the gradient force (blue line). Hence, independent on the displacement the total force pushes the particle along the direction of the laser beam. Center: Simulation where the gradient force is slightly smaller than the scattering force. The particle only gets pushed away for a displacement to one side. For a displacement to the other side, the forces are equal to zero and the particle is not influenced by the trap. Right: The gradient force dominates and independent on the displacement, the particle gets pulled into the focus.

For this case the particle is not influenced if it moved in $+z$, but it is not trapped either. The right side shows the case if the gradient and scattering force are of same strength or the gradient force is larger. Here the particle is pulled back if it moves in the $+z$ direction because the force points into the negative direction. In this case a particle is trapped as long as the Brownian motion is not higher than the total force.

Due to the two theoretical models, the theory behind the trapping of particles can be described if the particle size lies in one of these two regimes. The particles used in this work are not in these regimes. For the theory of trapping particles in the intermediate regime a complete electromagnetic theory is required to provide an accurate description. Hence, a numerical estimate for the forces in the general Mie regime has to be evaluated. This regime is valid for all sphere sizes and is more complicated than the Rayleigh approximation. The solution of the general calculations involves an incident wave which gets scattered at the spherical particle and is expanded as an infinite series of vector spherical harmonics. The net force exerted on the particle, or more general on an arbitrary object, is entirely determined by the Maxwell stress tensor [61]. If the size of the object gets small, the gradient and scattering force of the Rayleigh regime are obtained. To derive the Maxwell stress tensor the Maxwell

equations and the general Lorentz force law are the basis, considering the situation in vacuum and a single charge $q$ moving with a velocity $\vec{v}$. By the addition the first and the second of Maxwell's equations and the multiplication with the electric and magnetic field, one obtains tensors for the outer product of the electric and for the magnetic field. With the upper combination of the Maxwell equations and the outer products, the stress tensor $\bar{T}$ can be derived as

$$\bar{T} = \left[\epsilon_0 \vec{E}\vec{E} - \mu_0 \vec{H}\vec{H} - \frac{1}{2}(\epsilon_0 E^2 + \mu_0 H^2)\bar{I}\right] \tag{2.11}$$

where $\bar{I}$ denotes the unit tensor, $\vec{E}$ and $\vec{H}$ the electric and magnetic fields, and $\vec{E}\vec{E}$ (or $\vec{H}\vec{H}$) the outer product. By integration over the arbitrary volume, which includes all charges and currents, one gets the mechanical force on the volume. By averaging the force over one period of oscillation the force becomes

$$\left\langle \vec{F} \right\rangle = \int_{\partial V} \left\langle \bar{T}(\vec{r}, t) \right\rangle \cdot \vec{n}(\vec{r}) da \tag{2.12}$$

with the surface integral over the volume dependent on position $\vec{r}$ and time $t$. $\vec{n}$ is the unit vector perpendicular to the surface and $da$ the infinitesimal surface element. The upper mentioned motion of charge in a vacuum was chosen to simplify the derivation. In general the volume is surrounded by a medium with $\epsilon$ and $\mu$ as material constants, which changes the Maxwell stress tensor to

$$\bar{T} = \left[\epsilon_0 \epsilon \vec{E}\vec{E} - \mu_0 \mu \vec{H}\vec{H} - \frac{1}{2}(\epsilon_0 \epsilon E^2 + \mu_0 \mu H^2)\bar{I}\right] \tag{2.13}$$

An important fact is that the considered electric field is a superposition of the incident and scattered fields. Hence, the force can be determined when the electromagnetic fields are known [61]. Additional information about the theoretical calculations are also presented in [62] and [64].

In addition to the general optical trapping forces, potential aberrations through the optics components can be considered. These have an influence on the stiffness of the optical tweezers when the trap moves along the axial direction and varying distance to the substrate. At about 20 µm distance to the surface only 10% of the optical tweezers strength remains for particle trapping [65].

The laser beam which is responsible for the gradient and scattering force is a Gaussian beam as already mentioned above. When the wavefront of this laser beam gets focused and hits the particle, one part transmits and the other part of the beam bypasses the particle. In the latter case the wavefront stays the same. The light

passing through the particle generates a spherical wavefront which interferes with the unmodified Gaussian beam. The interference pattern created is dependent on the position of the particle as well as in the lateral and in the axial direction. Figure 2.4 depicts the signals of the laser and the particle on the photo-diode to explain this theory.

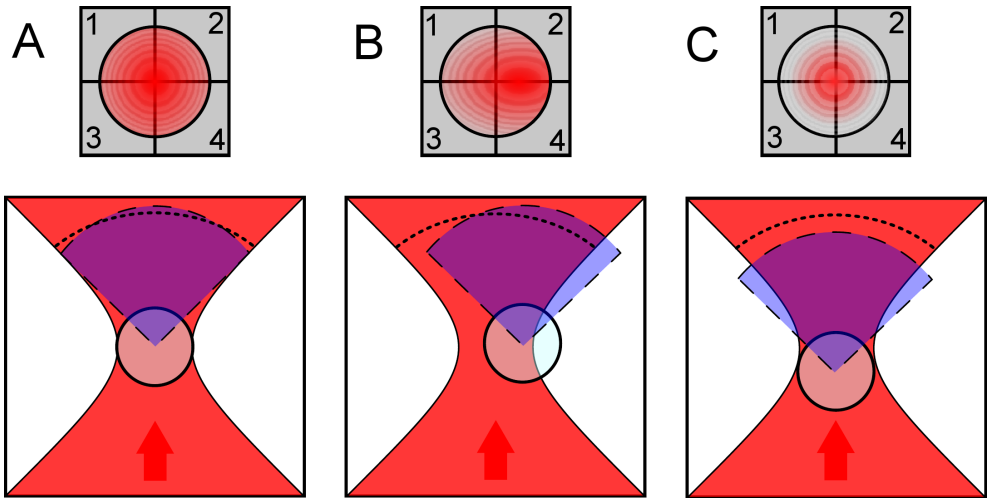



Figure 2.4: A) The particle is located in the focus of the optical tweezers. On the quadrant photo diode a centered interference pattern of both the beam passing the particle and transmitting the particle is detected. B) In case of lateral displacement of the particle in the trap, the interference pattern is laterally shifted on the quadrant photo diode. The difference of the left and right quadrants leads to a value for the displacement of the particle. C) Due to Gouy's phase-shift the interference pattern on the photo-diode changes when the particle in the trap is displaced axially. The change in the sum of the quadrants' signals lead to a value for the particle's axial motion ([97], modified).

A lateral displacement shifts the interference pattern laterally and an axial displacement leads to an increase or decrease of the overall intensity. This can be explained by a varying ratio of maxima and minima of the interference pattern and is called Gouy's phase-shift. In the end the interference pattern is recorded with a four quadrant photo-diode where the subtraction of upper and lower quadrants leads to the y-motion of the particle, and the left minus right side or vice versa results in the x-motion of the particle. The z-motion, the axial motion is recorded via the sum of the four quadrants of the photo-diode [59].

## 2.2 Position Calibration of Optical Tweezers

This and the following section describe several ways to calibrate an optical tweezers. The calibration itself consists of two steps. In the first step a precise determination of the displacement of a trapped object from its equilibrium position has to be performed. This is required for the computation of the force in the next step and permits the direct measurement of nanometer-scale motion of trapped particles.
In principle, three different ways of the position calibration are possible. The first method uses the thermal motion of the particle while being trapped in the optical tweezers. The detector (quadrant photo diode) records the Brownian motion of the particle and the measured signal results in a voltage over time. For long times the equipartition theorem holds with

$$k_V = \frac{k_\mathrm{B}T}{\langle x_\mathrm{V}^2 \rangle}, \tag{2.14}$$

where $x_\mathrm{V}^2$ being the root mean square (RMS) amplitude of the particle's motion and $T$ the temperature of the medium. The thermal energy and RMS are used to determine a conversion value $k_\mathrm{V}$ which in units of $[k_\mathrm{V}]$ =Nm/V$^2$. A theoretical conversion value $k_\mathrm{m}$ with $[k_\mathrm{m}]$ =Nm/m$^2$ leads to the calibration factor $a_\mathrm{RMS} = \sqrt{k_\mathrm{V}/k_\mathrm{m}}$. For the determination of $k_\mathrm{m}$ a round particle in a fluid is considered. Furthermore, a laminar flow around the particle and no-slip boundary is assumed (Stokes model). Hence, $k_\mathrm{m}$ is determined by

$$k_\mathrm{m} = \frac{\gamma}{\tau} \tag{2.15}$$

with $\tau$ being the autocorrelation time and $\gamma = 6\pi\eta a$ the drag coefficient. The particle size is denoted by its radius $a$ and the viscosity of the medium is $\eta$. For short times, before the autocorrelation-function of the particle motion decays under a value of $1/e$, an exponential function fitted to the autocorrelation function leads to the autocorrelation time. Alternatively, the fit of a reciprocal function to the power spectral density (PSD), the Fourier transformation of the particle motion, can be used to determine the needed time value $\tau$. The ratio of $k_\mathrm{V}$ and $k_\mathrm{m}$ results in the conversion factor $a_\mathrm{RMS}$ with $[a_\mathrm{RMS}]$ =V/m.
An alternative way to gain the conversion value via the Brownian motion can be performed by observing the particle's motion during very short times. This can be done when the sampling rate of the detector is much higher than the inverse of the autocorrelation time $1/\tau$ of the particle. The diffusion constant $D_\mathrm{V}$ of the

measured mean squared displacement of the particle leads to a conversion factor of unit $[D_\mathrm{V}]$ =V$^2$/s. Thus,

$$D_\mathrm{V} = \frac{\langle \Delta x(\Delta t)^2_\mathrm{V} \rangle}{2\Delta t} \tag{2.16}$$

where $\langle \Delta x(\Delta t)^2_\mathrm{V} \rangle$ is the mean squared displacement (MSD) for short times and time steps $\Delta t$. Hence, for $D_\mathrm{V}$ the equivalent $D_\mathrm{m}$ can be found by the Stokes-Einstein equation

$$D_m = \frac{k_\mathrm{B}T}{\gamma}. \tag{2.17}$$

In the same way as above the conversion factor $a_\mathrm{MSD}$ relates $D_\mathrm{m}$ and $D_\mathrm{V}$. Using this method, the motion of a trapped particle can be used to calibrate the displacement without the need of a steerable trap or piezoelectric stage [59].
A third method uses the piezoelectric table to calibrate the position. For this a particle, which is fixed on the surface, is moved perpendicular to the laser beam. For small displacements of the particle in the trap, the recorded signal at the photodiode changes linearly with the displacement. In this linear regime one can apply an oscillation to the piezoelectric table of known amplitude while measuring the laser signal. Because of the known amplitude $A_\mathrm{m}$ with $[A_\mathrm{m}]$ =nm, the conversion factor $a_\mathrm{fix}$ can be calculated. If the oscillation is of triangular curvature with frequency $f$, the detected displacement $A_\mathrm{V}$ of the particle has to be a triangle (in the linear regime). Thus, the conversion value is

$$a_\mathrm{fix} = \frac{sl_\mathrm{V}}{sl_\mathrm{m}} = \frac{\frac{T}{4A_\mathrm{V}}}{\frac{T}{4A_\mathrm{m}}} = \frac{A_\mathrm{m}}{A_\mathrm{V}} \quad \text{with} \quad [a_\mathrm{fix}] = \frac{\mathrm{nm}}{\mathrm{V}}, \tag{2.18}$$

where $sl_\mathrm{x}$ denotes the slope of the triangles either in volts or in meters. In this way, the calibration is performed in three directions. Since one measurement averages the slopes over several periods, external error sources like noise decrease. One drawback of this method is the difficulty to determine whether the particle is exactly in the trap focus. A possible solution is to do a raster scan over the particle to determine the center of the trap and for the complete description of the focus [53].
Another possible position calibration method takes advantage of one steerable trap. In this case, a particle is trapped at larger distance to the surface to reduce surface effects. The motion of the trap excites the particle to oscillations. As an alternative, the trap could be hold at rest while the piezoelectric stage oscillates. Thus, the motion of the stage or the movable trap is sinusoidal with $x_\mathrm{drive}(t) = A\sin(2\pi f_\mathrm{drive}t)$ which is dependent on time, and its velocity $v_\mathrm{drive} = \dot{x}_\mathrm{drive}$ [66]. If hydrodynamical and inertial effects are ignored, the resulting Langevin equation of the particle will

be

$$\gamma[\dot{x} - v_{\text{drive}}(t)] + \kappa x(t) = F_{\text{T}}(t). \tag{2.19}$$

Here $x(t)$ is the displacement of the particle in the trap, $\gamma$ the drag and $\kappa$ the stiffness of the trap. On the right side of Equation (2.19), $F_{\text{T}} = \gamma\sqrt{2D}\xi(t)$ ($D$ is the diffusion constant) describes the factor for the Brownian motion of the particle which is seen as white noise. If Equation (2.19) is solved, a general solution is gained which depends on the sum of two terms corresponding to the two forces $F_{\text{T}}$ and $\gamma v_{\text{drive}}$

$$x_{\text{response}}(t) = \frac{x_{\text{drive}}(t - t_{\text{lag}})}{\sqrt{1 + (\frac{f_{\text{c}}}{f_{\text{drive}}})^2}} \tag{2.20}$$

with $f_{\text{c}}$ being the corner frequency $f_{\text{c}} = \kappa/(2\pi\gamma)$ and $t_{\text{lag}}$ with

$$t_{\text{lag}} = \frac{\arctan(\frac{f_{\text{drive}}}{f_{\text{c}}}) - \pi/2}{2\pi f_{\text{drive}}}.$$

Since it is difficult to fit $x_{\text{response}}$ to measured data because of the thermal noise, the power spectral density (PSD) is calculated. Hence, the calibration factor $a_{\text{PSD}} = x(t)/x^{\text{volt}}(t)$ can be expressed in terms of the power spectra ($P_{\text{response}}$, $P^{\text{volt}}_{\text{response}}$). The calibration factor $a_{\text{PSD}}$ in this equation is the only unknown, since $P^{\text{volt}}_{\text{response}}$ is determined in the experiment. Moreover $A$ is the input amplitude and $f_{\text{drive}}$ the oscillation frequency, which both are given values. The corner frequency $f_{\text{c}}$ is evaluated with the power spectral density. For the position calibration one determines additionally the power in the spike of the experimental $W_{\text{ex}}$ and the spike in the theoretical data $W_{\text{th}}$. This means

$$\begin{aligned} a_{\text{PSD}} &= \sqrt{\frac{W_{\text{th}}}{W_{\text{ex}}}} \qquad \text{with} \qquad [a_{\text{PSD}}] = \text{m/V} \\ &\text{where} \\ W_{th} &= \int_0^{f_{\text{Nyq}}} P_{\text{response}}(f)df = \frac{A^2}{2(1 + f_{\text{c}}^2/f_{\text{drive}}^2)} \\ W_{ex} &= [P^{\text{volt}}(f_{\text{drive}}) - P_T^{\text{volt}}(f_{\text{drive}})]\Delta f. \end{aligned} \tag{2.21}$$

Hence, $W_{\text{ex}}$ is dependent on $P^{\text{volt}}(f_{\text{drive}})$ which is the experimentally determined height of the spike at $f_{\text{drive}}$. $P_T^{\text{volt}}(f_{\text{drive}})$ is the PSD of the thermal background at $f_{\text{drive}}$. The frequency resolution is given by $\Delta f$. The Nyquist frequency is denoted by $f_{\text{Nyq}}$ and the half of the sampling frequency. In addition to the position calibration, the force calibration can be performed using this method (Section 2.3). Moreover,

this method can be used to determine the drag coefficient $\gamma$ of the medium [66].
Another way to calibrate the displacement of the particle can be achieved by using a second trap beside the steerable one. In this case a static trap records the motion of the particle which oscillates due to the motion of the dynamic trap. The recorded displacement is linear at a small range around the focus. In the same way as mentioned above, by the oscillation of a fixed particle, the conversion value is determined with a oscillation at small amplitudes. Hence, the conversion factor $a_{\mathrm{Dual}}$ is

$$a_{\mathrm{Dual}} = \frac{sl_{\mathrm{V}}}{sl_{\mathrm{m}}} = \frac{\frac{T}{4A_{\mathrm{V}}}}{\frac{T}{4A_{\mathrm{m}}}} = \frac{A_{\mathrm{m}}}{A_{\mathrm{V}}} \quad \text{with} \quad [a_{\mathrm{Dual}}] = \frac{\mathrm{nm}}{\mathrm{V}} \tag{2.22}$$

with the same notations as used above. A problem of this method is the Brownian motion which adds noise to the measured signal and brings an uncertainty to the estimation of the slope $sl_{\mathrm{V}}$. Furthermore, there is friction during the motion which displaces the particle during its oscillation. The latter one can be reduced by moving the particle at a low oscillation frequencies through the medium, so that the particle is closer to the focus. The first drawback will be eliminated if several periods of oscillations are averaged.
This section shows that there are several methods to do the position calibration for the relative displacement. A determination of the absolute axial position is another part of the calibration and is described in [53]. This is an important, when the distance to the surface has to be known accurately, and for the knowledge of the dependency of the hydrodynamic drag on the height above the surface.

## 2.3 Force Calibration of Optical Tweezers

In the last section of this chapter several methods to calibrate the force of an optical tweezers will be described. Since it is necessary to calibrate the position of the optical trap for a measurement, it is also obligatory to perform the force calibration for each sample, because of setup parameters which always change when a new sample is placed in the device. For example, the distance of the objective and the condenser change, because for each sample the objective has to be re-approached.
The first method presented is the equipartition method. It assumes that the trap has a harmonic potential and the stiffness $k_{\mathrm{trap}}$. The variance $\langle x^2 \rangle$ of the thermal

fluctuations of particle's motion is equal to the thermal energy. Thus,

$$\frac{1}{2}k_{\mathrm{B}}T = \frac{1}{2}k_{\mathrm{trap}}\left\langle x^2\right\rangle \tag{2.23}$$

where $x$ is the displacement of the particle out of its equilibrium position. The major drawback of this method is that there is an additional noise or a drift, which increases the overall variance. Consequently, the stiffness is assumed to be lower than the real value.

Another method takes advantage of the drag the particle is exposed to during the movement through the medium. If a sinusoidal or triangular oscillation is applied to the optical trap or the piezoelectric stage, the particle gets displaced because of the viscosity of the surrounding medium. If the viscosity $\eta$ is known and other parameters like the radius of the particle $a$ are clear, the drag coefficient $\gamma$ can be determined. With the knowledge of this coefficient and a triangular excitation the resulting motion of the particle is

$$x(t) = \frac{\gamma A_0 f}{2k_{\mathrm{trap}}}[1 - e^{-\frac{k_{\mathrm{trap}}}{\gamma}t}] \tag{2.24}$$

with

$$\gamma = \frac{6\pi\eta a}{(1 - \frac{9}{16}\frac{a}{h} + \frac{1}{8}\frac{a}{h}^3 - \frac{45}{256}\frac{a}{h}^4 - \frac{1}{16}\frac{a}{h}^5)}. \tag{2.25}$$

Here Faxén's law is included and $h$ denotes the distance between surface and trapped particle [67]. $A_0$ is the amplitude of triangular oscillation and $f$ its frequency. The underlying assumption for this method is a round particle and a laminar flow around it. One drawback of this method is that it has to be performed slowly because fast oscillations make the particles jump or fall out of the trap. The drag force method can be performed at a motion with constant velocity, too. The particle gets displaced dependent on the velocity. The faster the piezoelectric stage moves the higher is the displacement. Thus, it is possible to vary the velocity and detect the correspondent displacement. These parameters should be related linearly with the slope containing the trap stiffness.

The method introduced by Tolić-Nørrelykke in 2006 has the advantage, that in addition to the calibration of the position, the force constant can be determined simultaneously [66]. This makes the method more attractive than other methods. If a particle moves sinusoidally because of an oscillating optical trap or a piezoelectric stage, the power spectral density can be used for the calibration of the force constant. Hence, the underlying assumption is that the trap's force on the particle is

$k_{\text{trap}}x$. Parameter $x$ is the displacement in meters, because of the foregoing position calibration. Another assumption is that Einstein's relation is valid and therefore, the trap stiffness can be written

$$k_{\text{trap}} = 2\pi f_{\text{c}} \frac{k_{\text{B}}T}{D} \tag{2.26}$$

where $D$ denotes the diffusion coefficient. By fitting the thermal background to the experimental power spectrum, the diffusion coefficient $D^{\text{volt}}$ can be distinguished ($[D^{\text{volt}}] = V^2/s$). To get the diffusion coefficient of Equation (2.26), the previously determined conversion factor $a_{\text{PSD}}$ is used with the relation $D = a_{\text{PSD}}^2 D^{\text{volt}}$. Moreover, the corner frequency has to be found at the power spectral density which allows to determine the trap stiffness or force constant $k_{\text{trap}}$:

$$k_{\text{trap}} = 2\pi f_{\text{c}} \frac{k_{\text{B}}T}{a_{\text{PSD}}^2 D^{\text{volt}}}. \tag{2.27}$$

As could be seen the method makes usage of the power spectral density and the motion of either the dynamical trap or the piezoelectric stage [66].
If the trap is static and cannot be moved, another method can be used for the force calibration. This method is an extension to the equipartition method, and called optical potential analysis. It is assumed that the trapped particle is located in a potential. This means that the probability of the displacement, which is the complete distribution of the thermal motion in the trap, follows the Boltzmann distribution [53]. By calculating a histogram of the particle's motion, the force constant $k_{\text{trap}}$ can be derived. Thus, the distribution is given by

$$p(x)dx = Ce^{-\frac{U(x)}{k_{\text{B}}T}} \tag{2.28}$$

with the probability $p(x)dx$ of the particle in a potential $U(x)$. The constant $C$ is the normalization factor so that the integral over the probability is one. If the Equation (2.28) is solved for the potential, the equation can be written as

$$U(x) = -k_{\text{B}}T \ln p(x) + k_{\text{B}}T \ln C. \tag{2.29}$$

In Equation (2.29) the last term with the normalization factor $C$ is an offset and can be neglected. If the potential is assumed to be harmonic $U(x) = \alpha x^2$, the variable of the squared term $\alpha$ will be equal to the stiffness constant or force constant $k_{\text{trap}}$. Consequently, via the motion of a particle in the harmonic trap the stiffness of the trap can be determined [68]. An important issue of this method is the binning of

the histogram of the particle's motion. If on the one side the number of bins is small compared to the amount of measured positions of the particle, the trap stiffness will be overestimated. However, if the amount of bins is too high, there are empty bins and the distribution is too flat. That means that the trap stiffness is underestimated. The following example [69] shows the differences of varying bin numbers.

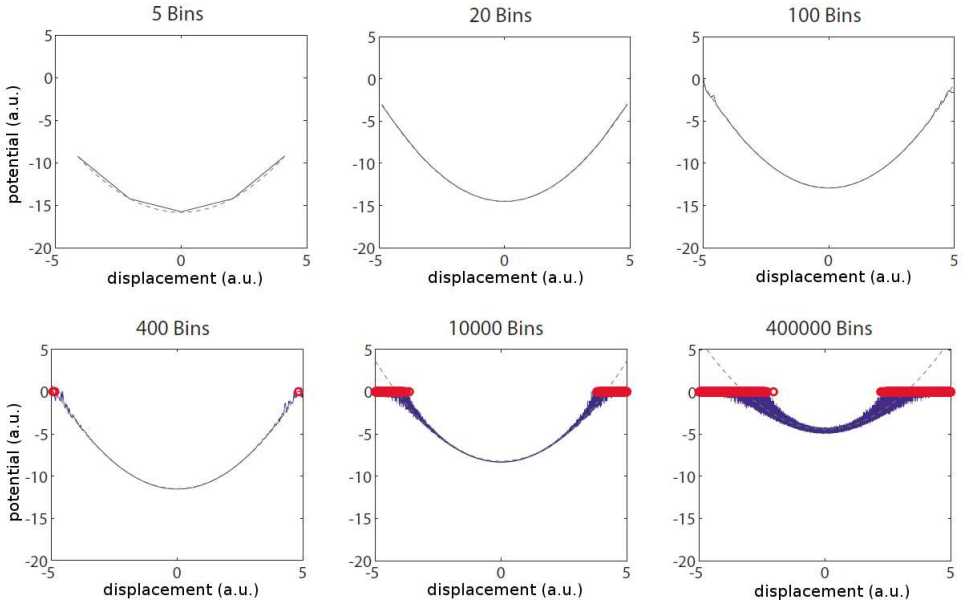



Figure 2.5: Simulations to show the dependency of the potential on the binning of the displacement. The dashed line shows the harmonic fit, the line the simulated data and the red circles are empty bins [69].

Figure 2.5 shows simulations of potentials are shown where the number of bins vary. For a low number of bins the quality (when $R^2$, the factor for the goodness of the fit, is considered) decreases and for a high number of bins the number of empty bins increases (red circles). The optimal value can be found in between when the change of bin number leads to only small or no changes in the trap stiffness.
There are some more methods to gather information about the trap stiffness and position calibrations which are not described in this work. An overview of publications with common calibration methods and optical tweezers setups can be found in [71] or [70].

# 3 Theoretical Aspects of Microrheology

In this chapter the theoretical principles of the technique 'Microrheology' are described. This background is important to understand the ideas behind the development of the new method for the conversion of rheological data into the dynamic shear modulus.
Rheology in general is the observation of flow properties of different kinds of media. On the one hand the observed media can be a viscous fluid like pure water or on the other hand a complete elastic solid like rubber. These are examples for the extremes in this field and are able to either dissipate the mechanical energy completely or store all of the energy of an external stress. The so called complex fluids which consist of structures with a larger length scale inherent in them, are able to both store and dissipate energy. This ability depends on parameters like the applied external shear stress, the temperature and the concentration of the structures in the medium [73], [74]. Examples for complex, or viscoelastic, media are colloidal suspensions, emulsions and polymer networks.
The polymer networks, which are in the main focus in this work, can be divided into two groups - flexible and semi-flexible polymers. Synthetic polymers that show small monomer sizes like polyacrylamide (PAAm) gels are flexible polymers. Their properties and dynamics are described by Doi and Edwards in [45]. Biopolymers are semi-flexible because the persistence length is larger than the diameter, and in the same order of magnitude as the contour length [77]. The biopolymers described in Chapter 1 - actin and intermediate filaments - belong to this group. The latter ones build networks as well as *in vitro* and *in vivo*. The networks are observed inter alia with the microrheology technique [75]. As mentioned in Chapter 1, the polymer networks can be entangled or cross-linked, depending on the concentration of protein and additional salts like $MgCl_2$ or plectin.
In literature there are simple models which are able to describe the general properties of viscoelastic fluids. One of these properties is the creep behavior which means, in case of external stress, that the medium does not instantaneously follow the de-

formation, but slowly changes its structure to get elongated. The model describing this situation is called the Kelvin or Voigt model and is represented by a system of a spring and a dashpot connected with each other in parallel. If the equations of stress and strain are connected for spring and dashpot, a differential equation is generated. The equation can be solved and the result is a exponential curvature for the creep. The second property is the stress relaxation. If the medium is already deformed and the stress releases, then the body does not recover its shape immediately. The Maxwell model describes this behavior with the usage of a parallel series of spring and dashpot. Similar to the Kelvin model the solution of the occurring differential equation is an exponential function which describes the relaxation. The more general model is the standard linear solid model which allows to combine several Kelvin and Maxwell models. Further details are in [78].
The quantitative determination of the mechanical properties of a specific viscoelastic medium can be done by converting rheological data like strains into the so-called dynamic shear modulus. The dynamic shear modulus $G^*$ is of complex nature and can be divided in its real and imaginary part, $G'$ and $G''$. These parameters stand for the elastic and the viscous or dissipative behavior of the medium. Both are dependent on the strain and show the in phase and out of phase part of the strain. For the determination of the dynamic shear modulus the techniques like the conventional rheology or microrheology are used. Microrheology determines the local properties of a complex fluid and is in contrast to conventional rheology where the bulk properties of a medium are measured. The local mechanical properties, namely the ability to store and dissipate energy, can be determined by means of small tracer particles which are embedded in the medium. These particles apply shear to the medium by their motion - passively by Brownian motion (thermal fluctuations) or actively by an external force. Since both methods are used in this work, the first section depicts the theoretical principles of the passive method, whereas in the second section the theory of active microrheology is presented.

## 3.1 Passive Microrheology

As mentioned before microrheology has to be divided into two methods. The passive method takes advantage of the thermal motion of small tracer particles which are embedded in the medium. The analysis of the motion of the particles leads to the

complex shear modulus.
Nowadays there are three main measuring techniques to directly or indirectly determine the motion of the particles. Dynamic wave spectroscopy (DWS) is a special form of dynamic light scattering (DLS) and measures the thermally excited motion of ensembles of particles. The conversion of the motion of the particle to the dynamic shear modulus is done via the power spectral density. One of the advantages of this method is that a larger frequency range can be covered within one measurement. Local disturbances in the medium on the one hand are averaged out, but one the other hand if these local properties are important, they might not be determined [76], [75].
Another technique is the laser deflection particle tracking (LDPT), which uses laser and photo diodes to measure the particles motion. The setup is similar to an optical tweezers setup, but the laser power has to be chosen very low ($\approx 0.6\,\mathrm{mW}$ [75]). In this way there is no influence of the particle's motion by the scattering and gradient forces of the optical tweezers. Compared to DWS it is also possible to measure the local properties of the medium because the motion of only one particle is observed. The frequency range reaches several decades which is comparable to DWS ($\approx 10^{-3} - 10^{4}\,\mathrm{Hz}$). One of the drawbacks of this method is the uncertainty about the influence of the laser, and the nonlinearity in determination of the laser signal when the particle moves too much. The observation of several particles at the same time is only possible by using a time sharing algorithm which decreases the accuracy of the measurement [76], [75].
The video-based technique is the third of the major techniques to gather information about the particles' motion. By the usage of a high-speed camera several particles can be tracked simultaneously. The frequency range for this method is limited to the speed of the camera, but a range of $\approx 10^{-1} - 10^{3}\,\mathrm{Hz}$ is accessible. In that way the measurement has no drawback like nonlinearities or the loss of locality, but a decreased measurement speed. In this work the video-based technique was used because a high-speed camera (Imaging Solutions, Motion Pro X4) for frequencies up to $5000\,\mathrm{Hz}$ at $512 \times 512\,\mathrm{pixel}$ was available while both LDPT and DWS were not realizable at the beginning. By recording the particles motion directly it is possible to calculate the mean squared displacement (MSD) which is related to the complex shear modulus $G^*$. This will be described in the following.

### 3.1.1 General Assumptions

The conversion of the mean squared displacement (MSD) $\langle r^2(t)\rangle$ into the dynamic shear modulus $G^*$ underlies the same assumptions for all the methods described and used in this work. Therefore in a separate section the general assumptions are introduced and the relation between mean squared displacement and complex shear modulus is derived. As mentioned above the motion of the tracer particle is the key to gather information about the mechanics of the medium. When a particle moves in a viscoelastic medium, there are only the forces of the molecules that interact with the particle, unless there are no external forces. These forces of the molecules act randomly with a Gaussian distribution with a mean of zero and a variance dependent on the temperature of the surrounding medium. Due to causality, the stochastic forces are independent of time and decoupled from past distributions [79]. Additionally to the random force, which appears in all kinds of fluids, the viscoelastic media can store energy. This means that there is a memory function which is able to save past events because it is non-local in time. Thus, the energy stored can be returned to the particle at later times, and this can be mathematically expressed with an integral over time. Hence, the equation of motion for a particle is described by a generalization of the classical Langevin equation [80],[81]:

$$m\dot{v}(t) = f_R(t) - m\int_0^t \zeta(t-\tau)v(\tau)d\tau. \tag{3.1}$$

The generalized Langevin equation considers particles of mass $m$ in an unbound state moving with velocity $v$ in an isotropic, incompressible complex fluid with the memory function $\zeta$. The random thermal forces acting on the particle are denoted with $f_R(t)$. By multiplying the velocity $v(0)$ at time $t = 0$ by the latter equation and taking the thermal average [82], the equation changes to

$$\langle \dot{v}(t)v(0)\rangle = -\int_0^t \zeta(t-\tau)\,\langle v(\tau)v(0)\rangle\, d\tau. \tag{3.2}$$

As mentioned above, the stochastic force is independent on time and in this way $\langle v(0)f_R(t)\rangle = 0$. The ensemble averaged velocities $\langle v(\tau)v(0)\rangle$ are known as velocity correlation function and can be substituted with $k_BT/m$ due to the equipartition theorem. The Laplace transform of Equation (3.2) leads to a relation for the velocity

correlation in the frequency regime:

$$\langle \tilde{v}(s)v(0)\rangle = \frac{k_B T}{\tilde{\zeta}(s) - ms}. \tag{3.3}$$

In Equation (3.3), $\tilde{v}(s)$ stands for the Laplace transform of the velocity and $\tilde{\zeta}(s)$ of the memory function dependent on frequency $s$. The next step relates the mean squared displacement of the particle's motion to the memory function via the Laplace transform of the MSD:

$$L_u\left\{\left\langle \Delta r^2(t)\right\rangle\right\} = \frac{6}{s^2}\left\langle \tilde{v}(s)v(0)\right\rangle. \tag{3.4}$$

With Equation (3.3), the memory function is

$$L_u\left\{\left\langle \Delta r^2(t)\right\rangle\right\} = \frac{6}{s^2}\frac{k_B T}{\tilde{\zeta}(s) - ms}. \tag{3.5}$$

The main idea is to get an insight about the mechanical properties of the medium. Hence the complex shear modulus has to be in relation to the mean squared displacement. For the next step the assumption has to be made that the particle is surrounded by a continuum. This holds when the particle size $a$ is bigger than the length scales of the structures inside the medium. As mentioned before, a polymer network also is a viscoelastic medium. Therefore the length scales in the network - the mesh sizes - have to be small compared to the particle size. Furthermore, the flow around the particle is assumed to be laminar which holds for small frequencies. Both assumptions allow the usage of the Stokes relation of a particle with sticky boundary conditions and a known drag in a purely viscous fluid. For a slippery boundary condition, the Stokes relation has to be modified [80]. A further assumption allows the memory function to be proportional to the complex bulk viscosity $\tilde{\eta}$ which is dependent on the frequency [73]:

$$\tilde{\eta}(s) = \frac{\tilde{\zeta}(s)}{6\pi a}. \tag{3.6}$$

With this formula the complex shear modulus can be determined and related to the memory function. The usage of $\tilde{G}(s) = s\tilde{\eta}(s)$, the frequency dependent shear modulus, finally leads to the generalized Stokes-Einstein equation

$$\tilde{G}(s) = \frac{s}{6\pi a}\left(\frac{6k_BT}{s^2L_u\left\{\langle\Delta r^2(t)\rangle\right\}} - ms\right). \tag{3.7}$$

In literature (e.g. [83]) this formula can be found in dependency of $\omega$ where the upper equation's frequency $s$ is substituted with the complex $i\omega$ using analytic continuation. The formula can be rewritten as

$$G^*(\omega) = \frac{\omega}{6\pi ai}\left(\frac{6k_BT}{\omega^2L_u\left\{\langle\Delta r^2(t)\rangle\right\}} + im\omega\right). \tag{3.8}$$

For frequencies below the characteristic inertia-friction frequency the second term $im\omega$ can be neglected. This is a good approximation which leads to a simplification of Equation (3.8). For polystyrene particles of a given diameter of 1 µm and are located in water, the crossover frequency $f_{inertia} = 6\pi a\eta/m$ is around $1.7 \cdot 10^7$ Hz. The used high-speed camera is far from this frequency. Hence Equation (3.8) can be simplified to

$$G^*(\omega) = \frac{k_BT}{\pi ai\omega L_u\left\{\langle\Delta r^2(t)\rangle\right\}}. \tag{3.9}$$

For measurement systems, where polymer networks are part of the medium, compressional modes (Poisson ratio $< 0.5$) have to be kept in mind. At high frequencies the viscous solvent and the polymer network are coupled through the solvents viscous drag, but at lower frequencies this fails. Hence the crossover frequency $f_{\text{compress}}$ becomes important. The estimated crossover frequency $f_{\text{compress}} = G\xi/(\eta a)$ for a polymer network with mesh size $\xi$ of 50 nm, a storage modulus $G'$ of 0.5 Pa, an effective viscosity of 200 mPa s and a particle diameter of 1 µm is 0.25 Hz [84], [85]. The frequency range covered by the high-speed camera is around 0.3 Hz to 2500 Hz for measurements up to 3 sec and therefore suitable for this model.
The complex shear modulus can be divided into two parts - storage and loss modulus. These parts are the real and imaginary parts of the complex shear modulus.

The real part is named storage modulus and describes the elastic response of the medium to the excitation via the particle. The imaginary part is the loss modulus, the dissipative energy in the examined system [87].

$$\begin{aligned} G'(\omega) &= \Re(G^*(\omega)) \\ G''(\omega) &= \Im(G^*(\omega)). \end{aligned} \tag{3.10}$$

Both are coupled via the Kramer-Kronig relation, because causality claims that the in-phase response $G'$ is followed by an out-phase response $G''$ [73]. Hence by the knowledge of one of the two it is possible to calculate the other part via

$$G'(\omega) = \frac{2}{\pi} P \int_0^\infty \frac{\zeta G''(\zeta)}{\zeta^2 - \omega^2} d\zeta \tag{3.11}$$

where $P$ is the principal value integral [75]. Hence, only when the complete frequency range is known it is possible to determine $G'$ out of $G''$ and vice versa, without losing information about the medium. Partial knowledge of one of the moduli introduces artifacts at the calculation of the other.
The same problem appears when Equation (3.8) is regarded. For determining the complex shear modulus, a Laplace or Fourier transform of the mean squared displacement is obligatory. This transform can only be performed exactly without errors, if the mean squared displacement of the whole time range from zero to infinity is known or can be measured. In reality this is not possible. Furthermore the mean squared displacement datasets have discrete values, and both the Laplace and the Fourier transform claim a continuous mean squared displacement. Both drawbacks inhibit the correct calculation of the complex shear modulus.
In the past, several methods were developed to circumvent these constraints with mathematical approaches. Two of these methods are discussed in the next section. The newly-developed method to calculate $G^*$ is presented in Chapter 5.

### 3.1.2 Conventional Methods

The classical estimation method for the dynamic shear modulus was introduced by Mason *et al.* in 1995. The information about the mechanical properties is a result

of the combination of the generalized Stokes-Einstein equation (GSE) and an unilateral transform which relates time and frequency domain. For the transformation into the Laplace domain the transform is estimated by expanding the mean squared displacement locally around the frequency of interest $s$ or $\omega$ and the usage of a power law (exponent $\alpha$) which describes the logarithmic slope of the mean squared displacement. This slope is the logarithmic derivative of the mean squared displacement in time and is assumed to be located between zero for the absolute elastic case and one in the case of a viscous medium, which leads to

$$\alpha(\omega) = \frac{\partial \ln \left\langle \Delta r^2 \left(\frac{1}{t}\right) \right\rangle}{\partial \ln \frac{1}{t}}. \tag{3.12}$$

The evaluation of the Laplace transformation of the power law can be related to the gamma function which shows a good approximation in case the slope of the mean squared displacement does not vary much. For the estimation in the Fourier domain, an analogous procedure leads to a similar approximation by the usage of the gamma function $\Gamma(\alpha)$:

$$G^*(\omega) = \frac{k_B T}{\pi a \left\langle \Delta r^2 \left(\frac{1}{t}\right) \right\rangle \Gamma[1+\alpha(\omega)] i^{-\alpha}}. \tag{3.13}$$

This model provides an easy way to determine the dynamic shear modulus by avoiding the direct calculation of the unilateral Fourier transform. Therefore it is simple to implement and faster than the FFT. An approximation for the gamma function $\Gamma[1+\alpha] = 0.457(1+\alpha)^2 - 1.36(1+\alpha) + 1.90$ for the range of $\alpha$ between zero and one, represents at most a 12 % correction. Storage modulus $G'$ and loss modulus $G''$ can be described as

$$\begin{aligned} G'(\omega) &= |G^*(\omega)| \cos \frac{1}{2}\pi\alpha(\omega) \\ G''(\omega) &= |G^*(\omega)| \sin \frac{1}{2}\pi\alpha(\omega). \end{aligned} \tag{3.14}$$

The approximation shows worst results when the slope of the mean squared displacement varies most rapidly and the power law representation is an oversimplification. Thus, the overall error of this method is less than 15 % which is the value of the

worst case scenario [79]. This indicates that the usage of an approximation via the gamma function amplifies errors when the slope varies a lot. Since the Brownian motion of a particle is a random motion the mean squared displacements are always noisy and therefore the calculation of $G'$ and $G''$ is susceptible to errors.

Another method was developed by Evans *et al.* in 2009. Evan's method tries to bypass the approximation of the slope of the mean squared displacement with the usage of a direct conversion of the rheological data into storage and loss modulus. Hence the usage of fitting functions and an approximation is avoided due to their possible uncertainties. The derived dynamic shear modulus consists of three terms. The first term handles the initial compliance for $t = 0$. A second term is the sum of piecewise functions that are the linear interpolations between each data points of the compliance. For the third term an additional parameter has to be introduced - the steady state viscosity which includes an extrapolation of the MSD for $t = \infty$. This is required because of the finite number of the experimental data. The steady state viscosity ensures that the mean squared displacement is defined for all positive times $t$. Hence the sum of terms leads to the resulting formula for $G^*(\omega)$

$$\begin{aligned}\frac{i\omega}{G^*(\omega)} &= \frac{e^{-i\omega t_N}}{\eta} + \\ &+ iC\omega \left\langle \Delta r^2(0) \right\rangle + C(1 - e^{-i\omega t_1}) \frac{\langle \Delta r^2(t) \rangle - \langle \Delta r^2(0) \rangle}{t_1} + \\ &+ \sum_{k-2}^{N} \left( C \frac{\langle \Delta r^2(t_k) \rangle - \langle \Delta r^2(t_{k-1}) \rangle}{t_k - t_{k-1}} \right) \left( e^{-i\omega t_{k-1}} - e^{-i\omega t_k} \right). \end{aligned} \tag{3.15}$$

The equation provides a direct link between the experimental mean squared displacement $\langle \Delta r^2(t) \rangle$ or creep compliance $J$ and the complex dynamic shear modulus. The steady state viscosity is denoted as $\eta$, $C$ being a calibration constant and $\langle \Delta r^2(0) \rangle$ is the mean squared displacement at the initial time ($t = 0$). Parameters like the radius of the particle and the temperature are located in $C$. A closer look at Equation (3.15) shows that the single terms calculate the slope between each data points, which leads to an amplification of the noise in case of a Brownian motion measurement. Additionally, another problem of this method is that the creep compliance $J_0$ or $\langle \Delta r^2(0) \rangle$ for the initial time has to be known. Another difficulty is introduced by the usage of the steady state viscosity. For a polymer network this viscosity only

can be estimated and not determined accurately. The advantage of this method is the fast evaluation and the avoidance of a fitting function [86].
For both methods, simulations were performed to show whether there are weak points at the method. At the publication of Evans an exemplary compliance function is used to confirm the quality of the method. Hence, the first simulation shown here is the compliance function to prove that the the simulations and the preset parameter are correct. Values like the initial compliance are taken from the publication.

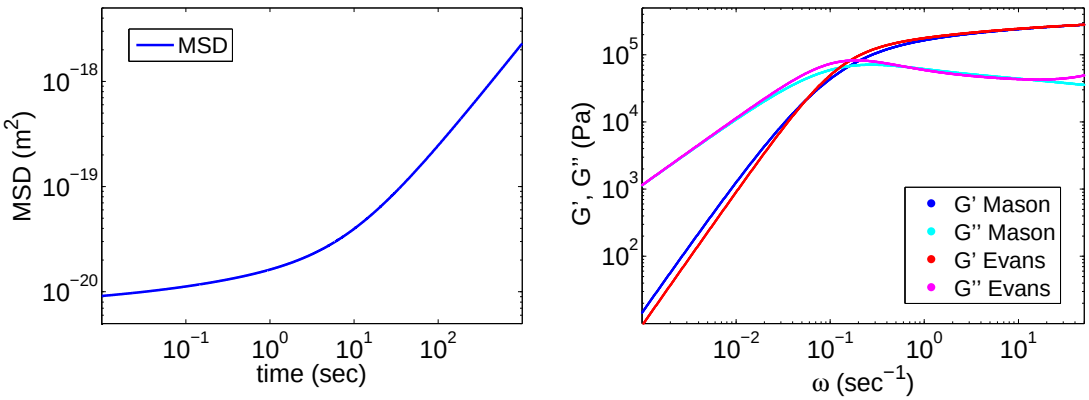



Figure 3.1: Simulation of a MSD behaving like the compliance function in [86]. Left: The MSD in $m^2$ shows the curvature of a typical compliance measurement. The MSD can be converted from the compliance as described in [77]. Right: The resulting shear moduli calculated via both the Evans and Mason method are in accordance to each other. The Evans storage and loss modulus conforms to the curves in the publication.

Figure 3.1 shows on the left side the MSD which corresponds to the compliance function given from the publication. The conversion from compliance to MSD is possible and illustrated in [77]. This MSD was used to calculate the storage and loss modulus of as well as the Evans and the Mason method. The shear moduli with the Evans method exactly could be rebuilt. Hence, the simulation were reliable and additional tests could be performed.
In the next simulation, a Gaussian white noise was added to the upper MSD. Since both methods use the derivative of the MSD where the the slope of neighboring points is determined, the noise gets amplified. The influence on the calculations of the shear modulus is shown in Figure 3.2. The noise which was added to the upper compliance function changes the storage and loss moduli in a dramatic way. The

noise added had a SNR of 40 and at the MSD hardly is recognized. The amplification due to the derivation of the MSD makes the output become useless.

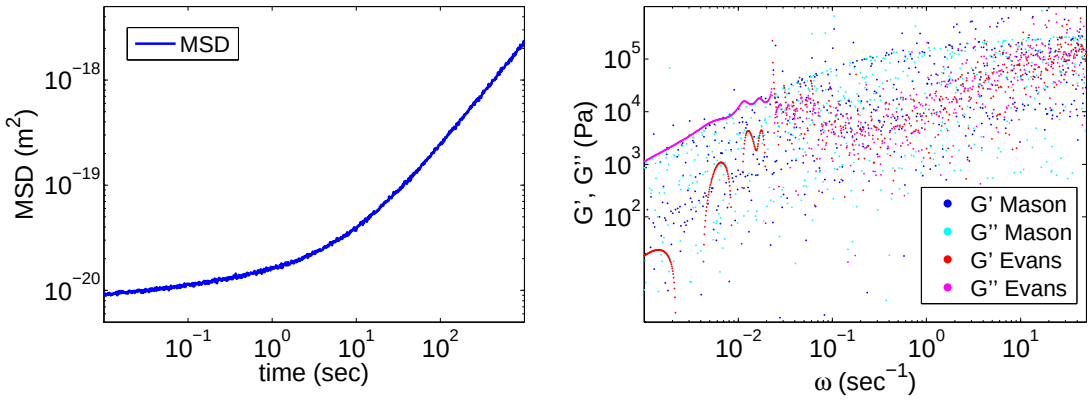



Figure 3.2: Simulation of a MSD behaving like the compliance function in [86]. Left: A Gaussian white noise is added to the MSD in $m^2$. The SNR is chosen to a value of SNR= 40. Right: The resulting shear moduli calculated via both the Evans and Mason method. Both result in a huge amplification of the noise.

In addition to the compliance function simulations with and without noise, tests were performed for the extreme cases when the medium is a pure viscous fluid and a complete elastic solid. Figure 3.3 shows the pure viscous fluid case, whereas Figure 3.4 illustrates the output for an elastic body. For the calculations at the viscous case the viscosity of water ($\eta = 1\,\mathrm{mPa\,s}$), a temperature of 23 °C, a bead radius of 500 nm and a measurement frequency of 5000 Hz were taken into account. Hence, the MSD is of constant slope dependent on the chosen parameter. Although the MSD is without noise and the slope is independent on the time, the Evans method introduces artifacts for both the storage and loss modulus. The storage modulus, which is predicted to be zero, is in the same range than the loss modulus. This is not correct and cannot be referred to a false calculation, because the latter MSD of the typical compliance was similar to the publication. The Mason method in contrast shows a correct loss modulus. The storage modulus is very noisy, but in a region of $10^{-20}$ Pa and can be neglected. Hence, for this case the Mason method produces correct outputs whereas the Evans method fails. The conversion of the MSD from $m^2$ to $nm^2$, which changes the numeric values to larger numbers to decrease probable rounding artifacts, does not influence the outputs.

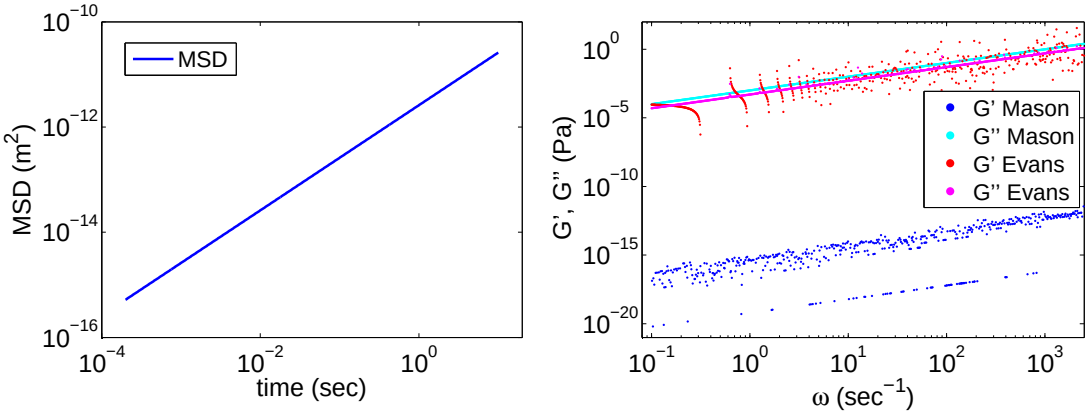



Figure 3.3: Simulation of a MSD at the viscous fluid case. The MSD shows a constant slope. The resulting storage modulus therefore should become zero whereas the loss modulus increases linearly.

For the elastic solid simulations an elasticity of 1 Pa and the same parameters as for the viscous case were used. The MSD as well as the predicted storage modulus are time-independent. The loss modulus should vanish.

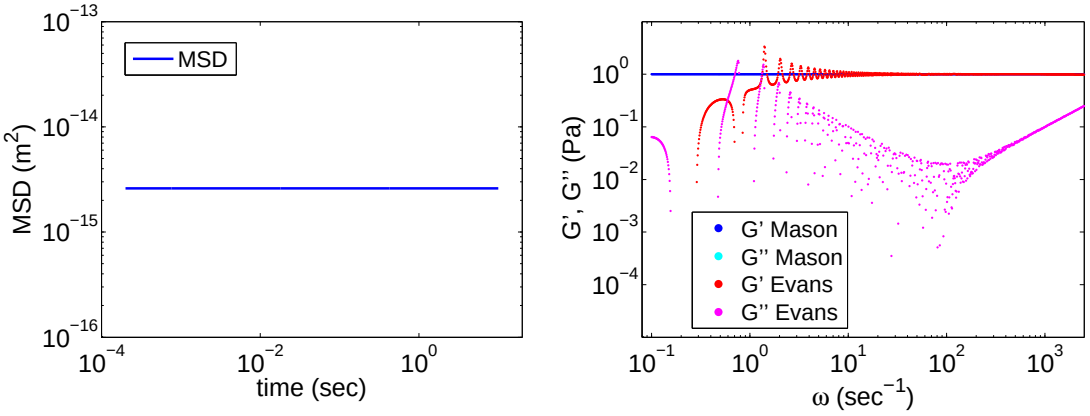



Figure 3.4: Simulation of a MSD behaving like an elastic solid. The predicted curve for the storage modulus should be independent on the frequency. The loss modulus in this case is predicted to be zero over all frequencies.

The Mason method again produced correct values for $G'$ and $G''$, but the Evans method failed again. At high frequencies the curvature for the storage modulus at the Evans method approached the correct value, but with huge artifacts at the low frequencies. $G''$ is very noisy and hence it is very difficult to interpret the data.

By adding noise to the simulations both methods failed and no reasonable information could be gathered. Since the measurements of Brownian motion in networks always are noisy it not possible to say something about the result unless the data is manipulated, e.g. by smoothing roughly. This modification changes the complete curvature which then leads to misinterpretations. Because of these drawbacks it is feasible to derive a new method. This method is introduced below (Chapter 5).
There are some additional constraints which affect the accuracy of the determination of the particles' motion. For example acoustical noise in the measurement system or oscillations of the devices can change the calculated mean squared displacement and therefore evoke misleading interpretation of the measurement. Therefore, Two-Point microrheology was introduced by Crocker *et al.* in 2000 where the correlation between the motion of two particles is determined and subtracted of the motion. This leads to a particle motion without noise which refers to the system's vibration [88],[89]. Although this is a promising method, the drawback is that particle motions, which are not dependent on the systems vibrations, but are correlated due to the viscoelastic medium, also get subtracted. In that way collective motions are eliminated, although they would give insight to additional features of the medium. In this work single particle microrheology was used. The noise of the system compared to the motion of the particles in the cell networks or in the *in vitro* assembled ones was smaller so that the result is not influenced by the vibrations. The idea to compare single particle to two-point microrheology and additionally to conventional rheology where the bulk modulus of a medium sheared by two plates is measured, often evokes discussions in science. The discussion about one point and two-point microrheology is not important for this work and for more details, the work of Buchanan *et al.* [90] can be taken into account.

## 3.2 Active Microrheology

This section describes another way to determine the mechanical properties of a viscoelastic system. In contrast to passive microrheology where the Brownian motion of particles is recorded, at the technique active microrheology the observed particle is excited by an external force at a specific frequency, amplitude and direction. The advantage is that the motion of the particle is not purely random, and the response is observed at the frequency of the excitation.

In this part the common way of active microrheology is explained, whereas in Chapter 6 a novel method, which allows to get more information out of the measurement, is presented. For both the common and the new way an additional device which provides the external force for the particles embedded in the medium is necessary. Hence, there are two major possibilities: One is the excitation of magnetic beads with a magnetic field inside the medium. The other one is the usage of an optical tweezers which excite the particles to oscillations. In the case of the optical tweezers a system which can steer the laser beam has to be used. This is either a piezoelectric mirror, a holographic plate or an acousto-optical modulator [93]. Dependent on the choise, different frequency ranges are accessible. Although there are differences in the setup, the theory behind it is similar and showed briefly in the following.
The particle of radius $a$ which gets oscillated by the optical tweezers (OT) force with spring constant $k_{\mathrm{OT}}$, responses to this excitation dependent on the medium's mechanical properties. Since the medium is viscoelastic, the motion of the particle at a frequency $\omega$ will be influenced by the medium's viscosity $\eta(\omega)$ and its elasticity $k(\omega)$. Hence the equation of motion includes a springlike force dependent on the optical trap and a viscous force because of the drag through the medium [91],[92]

$$m^*\ddot{x} + 6\pi\eta^* a\dot{x} + (k_{\mathrm{OT}} + k)x = k_{\mathrm{OT}} A\cos\omega t. \tag{3.16}$$

Variable $A$ denotes the amplitude of the oscillating optical trap at time $t$. Since the inertial effects are considered, both the mass of the particle $m$ and the viscosity of the medium are corrected so that an effective viscosity $\eta^*$ and effective mass $m^*$ follows [91]. The effective mass can be expressed by the particle bare mass $m$, its radius and its density $\rho$. Furthermore, $\eta^*$ is given by

$$m^* = m + \frac{2\pi}{3}a^3\rho + 3\pi a^2\sqrt{\frac{2\eta\rho}{\omega}}$$

with

$$\eta^* = \eta\left(1 + \sqrt{\frac{a^2\rho\omega}{2\eta}}\right). \tag{3.17}$$

The theory described here uses the idea of a dual optical tweezers and therefore one trap oscillates whereas the other trap measures the response of the particle. The second trap is chosen much weaker ($< 0.6\,\mathrm{mW}$, [75]) so that its force does not

influence the oscillation of the first trap and the particle.
A possible solution of the differential Equation (3.16) for the steady-state case is

$$x(t) = D(\omega)\cos\omega t - \delta(\omega) \tag{3.18}$$

with $D(\omega)$ being the response amplitude and $\delta(\omega)$ as the phase shift due to the existence of the surrounding medium. Both can be described by the trap stiffness, effective mass and effective viscosity which leads to

$$D(\omega) = \frac{k_{\mathrm{OT}}A}{\sqrt{(k_{\mathrm{OT}} + k(\omega) - m^*\omega^2)^2 + m^*\beta^2\omega^2}}$$

$$\delta(\omega) = \arctan\frac{m^*\beta\omega}{k_{\mathrm{OT}} + k(\omega) - m^*\omega^2} \tag{3.19}$$

where $\beta$ is

$$\beta = \frac{6\pi\eta^* a}{m^*}. \tag{3.20}$$

The amplitude $D(\omega)$ and the phase shift can be measured by the setup and consequently, the unknown viscosity and elasticity of the medium can be determined. With the knowledge of both the in-phase storage modulus and out-of-phase loss modulus can be derived

$$G'(\omega) = \frac{k(\omega)}{2\pi a}$$

$$G''(\omega) = \omega\left(\eta(\omega) - \eta_{\mathrm{solvent}}\right). \tag{3.21}$$

This is the common way to determine both storage and loss modulus by usage of a dual optical trap. In Chapter 6 this method will be extended by regarding several directions of excitement and therefore new insights in the observed medium can be gathered.

# 4 Setup of the Optical Tweezers

In this chapter the setup of the used instruments is described. The different applications - the passive and active microrheology - make usage of several devices which have to run synchronously or interact with each other.
The optical tweezers in general is built of a light microscope with a high numerical aperture of the objective that resolves the examined surface and focuses the laser beam for trapping objects. For visualizing the surface the illumination with a light source is needed, and a camera that records the enlightened surface. Since it is easier for many applications, the microscopes are inverted so that the laser beam can be coupled into the objective from below. Thus, the beam is recorded above the condenser with the quadrant photo diodes. To increase the trap stiffness, the laser beam gets broadened with a lens system and deflected via mirrors or an acousto optical deflector (AOD). In the following the specific parts of the custom-built setup are described.
The first section shows the setup of the light microscope with the high speed camera used for passive microrheology. In this section a further add-on, the incubator system, is briefly mentioned which allows to perform measurements with living cells.
In the second section the setup of the optical tweezers is shown. To ensure the active microrheology technique, an acousto-optical deflector is used which steers the laser beam.
In the third part an additional setup is explained. A total internal reflection fluorescence (TIRF) microscope allows to measure the dynamics of fluorescent labeled biopolymer networks. It also can be used in combination with the optical trap or the high-speed camera.

## 4.1 Light Microscope and Components

The setup of the light microscope is shown in Figure 4.1. The microscope is inverted, so that the illumination light is located at the upper side of the setup. The observation of the sample is performed with the camera below the objective with high numerical aperture (Nikon®ApoTIRF 100x, NA= 1.49). For the illumination of the sample a cold light projector (Karl Storz GmbH, Techno Light 270) is used.

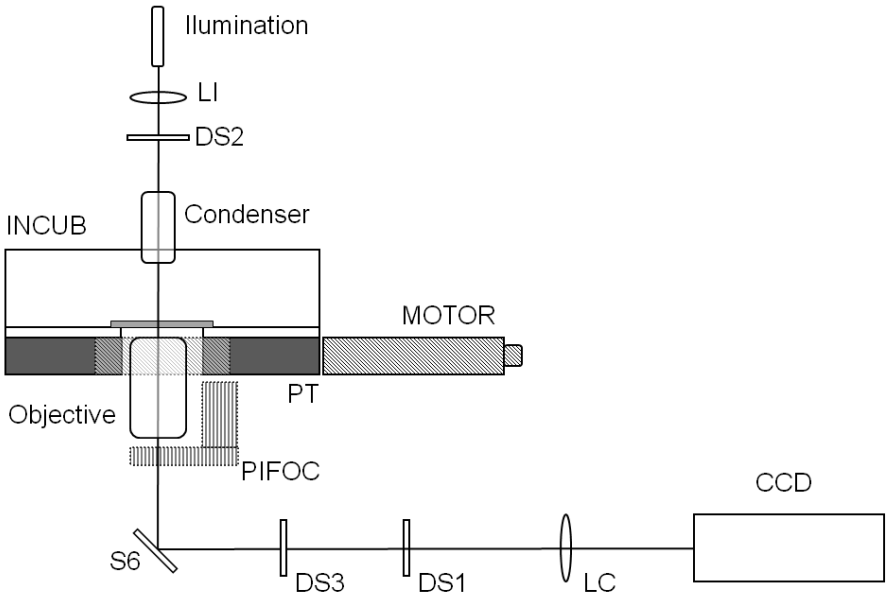



Figure 4.1: Sketch of the principal setup of the light microscope used for passive microrheology and live-cell imaging. The dichroic mirrors (DS1, DS2 and DS3) allow to include additional light beams like the optical trap laser or the TIRF-illumination and filter out the laser light for the detection (DS2). LI and LC are the lenses which focus the illumination light in front of the glass fiber and the camera (CCD). Objective and Condenser build the microscope with the piezoelectric table (PT), the micro-step motors (MOTOR) and the piezoelectric stage (PIFOC) for the axial displacement of the objective. The piezoelectric stage is surrounded by a incubation system (INCUB) to hold temperature, air humidity and $CO_2$ level in the sample.

The light projector ensures a high intensity of light and a stable illumination, which is important for measurements at high frequencies with short exposure times. The illumination light reaches the microscope via a glass fiber, gets collimated via lens

(LI), and passes the dichroic mirror (DS2). The condenser, a 16× Nikon®objective (NA= 0.65), focuses the light into the sample. For measurements with living cells, a dip-in objective (Leitz, 25×, NA 0.65) can be used to increase the contrast and to avoid water droplets on the surface of the objective. Below the condenser the illumination light passes through the sample which is mounted on a piezoelectric table (PI-561-3DD, Physikalische Instrumente, Controller E-710). On the piezoelectric table, a warming plate is located to heat up the incubation chamber (custom-built, [94]) to temperatures of 37 °C for live cell measurements and to test the transition range of polymer solutions. The piezoelectric table can be moved in a range of $45 \times 45 \times 15\,\mu m$ with a high precision in the nm range. This is necessary for applications such as the approach to the sample surface, oscillation of the sample and focus on the sample surface.
For larger distances two micro-step motors (OWIS®PS90, LTM 60) can move the piezoelectric table laterally in the range of few µm to several mm with a positioning accuracy of around 3 µm. The objective, which is below the sample, is mounted on a piezoelectric stage (PIFOC, P-720.00, Physikalische Instrumente, Controller E-503, E-509 C3) to be moved in axial direction in a range of 100 µm. The objective has a high magnification (100×) as well as a high numerical aperture (NA= 1.49) to ensure an accurate tracking of the particles at the microrheology applications and a high force for a stable trapping of particles in the optical trap. A correction ring allows to correct for specific glass slide thicknesses and temperatures (measurements at room temperature and up to 37 °C).
While passing through dichroic mirrors (DS3 and DS1) the illumination light gets focused via a lens (LC) on the CCD chip of the high-speed camera (Imaging Solutions, MotionPro X4). The high-speed camera offers the possibility to record pictures of $512 \times 512$ pixel size at a frame-rate of 5000 Hz. This is necessary to measure the particles' motion at a high temporal resolution. For both applications, passive and active microrheology, this improves the accuracy of the measurement. The lens can be aligned along the optical axis to change the field of view of the sample surface. The current field of view is $51.2 \times 51.2\,\mu m$. The usage of the micro-step motors in combination with the PIFOC, the piezoelectric table (PT) and the high-speed camera (CCD) allows a complete scan of the sample surface which is needed to get an overview of the sample when the field of view is limited to a small proportion of the sample. During the scan the function of the PIFOC is to ensure the sample surface stay in the focus, although the sample is slightly tilted (Appendix A).
The incubation system includes a regulated heating unit, a $CO_2$ supply and a humidity control device. This system ensures a physiological environment for living

cell experiments. The detailed description and reference measurements concerning the incubation system can be found in [94]. The warming plate consists of four conventional heat slides which are above the piezoelectric stage and via aluminum in contact with the sample. For the regulation of the temperature a PT-100 probe, embedded in the plate, and a controller (Eurotherm, temperature controller) are used. A (custom-built) PMMA box on the warming plate allows to hold the temperature constant. The mixing of $CO_2$ and air at a rate of 5% of $CO_2$ is most suitable for the health of the cells. A sensor (Vaisala CARBOCAP® Sensor, GMT 221) monitors the rate of $CO_2$ which is piped into the chamber. For the experiments a high humidity ($> 85\,\%$) is needed to keep the amount of cell medium constant and prevent indriectly a change of the pH of this medium. Via a bubbling system (Thermo Electron Corporation, Haake DC 10) the air-$CO_2$ mixture gets nearly saturated in water before reaching the chamber.
The sample, located on a cover slide ($24 \times 24\,\text{mm}$, Thermo Fisher Scientific, Menzel-Gläser), is mounted on a holder like depicted in Figure 4.2.

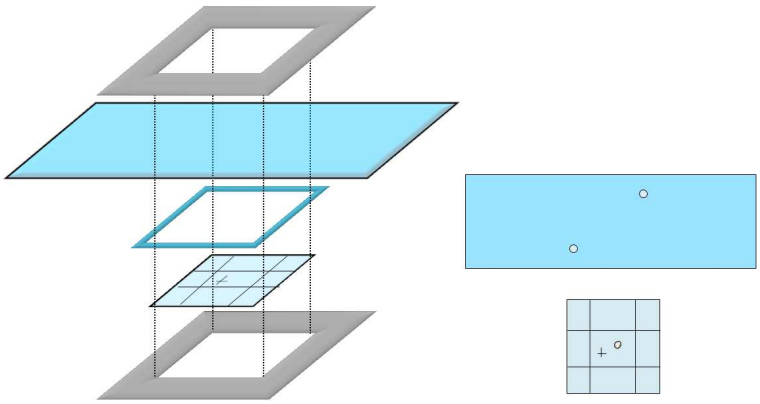


Figure 4.2: Sample holder for the cover slips. A PDMS ring seals the chamber and prevents the sample of drying out. A specimen holder with holes allows to refill the chamber with solution/medium if necessary.

The sample is placed in an aluminum ring which builds the basis of the sample holder. Dependent on the application, the aluminum ring is of circular (sealing the chamber downwards, for high humidity and constant temperature) or rectangular geometry. Onto the sample cover slip a PDMS layer is located which is the lateral sealing of the chamber. Additionally a circular PDMS layer of $0.5\,\mu\text{m}$ thickness (custom built, [95]) is used to seal the incubation system. A specimen holder with two holes builds the cover for the chamber. Via the holes the amount of buffer fluid,

culture medium or solvents is regulated in the chamber. At the top of the specimen holder a second aluminum ring closes and fixes the sample holder. In case of living cell measurements, the specimen holder is replaced by an aluminum plate with a larger aperture and a tray for a higher volume of medium. The aperture allows to use the dip-in objective mentioned above.
For some applications it is necessary to mark the position of the measurement. Therefore a cover slip is scarified with several scratches which, on the one hand, allow to break the glass for the usage in the electron microscope and on the other hand mark a coordinate system. In Appendix A this application is described in more detail (correlative Microscopy).

## 4.2 Optical Tweezers Setup

The setup of the optical tweezers is included in the inverted light microscope. Hence, the high-speed camera, the positioning system and the incubation system can be used for optical tweezers applications as well. In Figure 4.3 the laser beam path of the optical trap is shown.
The laser beam of a Nd:YAG diode laser (Coherent®Compass 1064-500) at a wavelength of 1064 nm is used to build a single, double or multiple trap. The intensity of the single mode laser ($TEM_{00}$) with a diameter 1/e of about 0.9 mm can be tuned up to a intensity of 500 mW [96]. Filter F1 is used to exclude the pumping light (wavelength 800 nm) out of the beam path. Mirrors S1, S2, S3 which have a special coating for the used wavelength, to align the laser beam onto the optical axis. There a telescope system of lenses (L1 and L2) and a pinhole (diameter 20 µm) expand the beam and remove possible additional modes out of the beam. Since the beam is linearly polarized via a rotating polarizer (LP) plate, beam splitter ST1 divides the beam into two parts where each part of the beam has a specific intensity dependent on the angle of the polarizer.
In that way the vertical polarized part of the beam passes an acousto-optical deflector (AOD, AA Opto-Electronic DTSXY-400), whereas the horizontal part only passes two mirrors (S4, S5) and beam splitter ST2. The acousto-optical device deflects the laser beam in both lateral directions with a maximal angle of 48 mrad at at resolution of $400 \times 400$ steps.

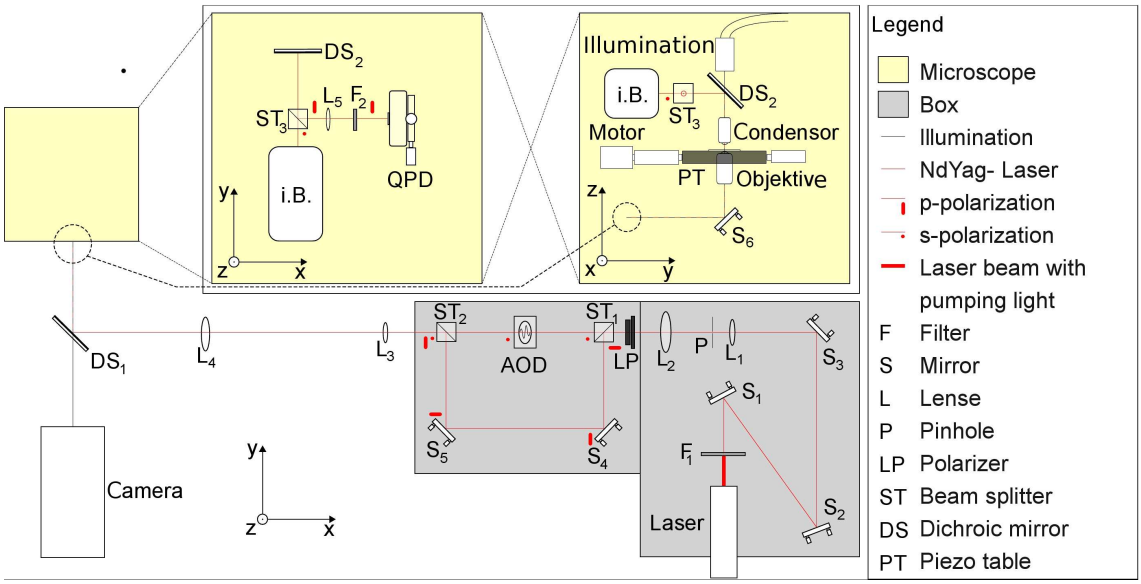



Figure 4.3: Optical tweezers setup for applications with two or more traps. The yellow box shows the inverted microscope with two photodiodes (QPD, i.B). The gray box includes the laser light source with lenses (L1-L2), mirrors (S1-S5) and a pinhole P to manipulate and steer the beam. An acousto-optical device AOD with two beam splitters (ST1, ST2) and a polarizer plate LP are used to separate the laser beam into two innocent beams - a static and a dynamic one. Lenses L3 and L4 outside the box expand the beam to enhance the trapping force.

The maximal frequency which can be applied is up to 30 MHz. Hence, one laser beam pass builds a steerable dynamic and the other a fixed, static trap. At beam splitter ST2 both beams get together with conserved polarization which ensures that the beams do not influence each other. By rotating LP it is possible to increase or decrease the intensity of both, the dynamic and the static laser beam. This leads to an increase or decrease of the strength of the specific traps. Two function generators (Stanford Research Systems, DS345) control the AOD and therefore the movement of the dynamic laser beam. By applying a specific voltage to the device the laser beam gets deflected in lateral direction. The superposition of sinusoidal voltages applied to the single deflectors for the lateral directions enables an oscillatory movement of the laser beam with specific frequency and amplitude. This is important for applications like active microrheology or multiple trapping. An additional function generator manipulating the output intensity of the beam at the AOD could be used to steer the trap in axial direction.

When ST2 is passed, both beams are expanded by the lenses L3 and L4. A dichroic mirror DS1 deflects the beam into the direction of mirror S6 and the high numerical objective to get focused. The alignment and focal length of the lenses make the beams overfill the objective which ensures a high and stable trapping force. Additionally the dynamic trap passes the optical axis at the back focal plane of the objective so that the trap focus stays at a fixed height above the objective while moving laterally [96], [97], [53].
At the sample holder, which is described in Section 4.1, both laser beams build two optical traps which are used for the applications shown in Chapter 7.3 and Appendix C. Above the sample holder, the condenser collects the laser light and dichroic mirror DS2 deflects the laser beams out of the optical axis. Beam splitter ST3 separates the perpendicular polarized beams so that both can be independent monitored with two four quadrant photo diodes (QPD, Hammamatsu Photonics, InGaAs 6849 series). Lenses L5 and L6 focus the beams on the specific QPD and filters F2 and F3 block the illumination light. The alignment of these lenses ensures a back focal plane detection of the QPD [96]. To record the motion of trapped particles, the QPD are connected to a AD/DA data acquisition device (Keithley Instruments Inc., K-USB 3116) which is controlled by the lab computer. The measurement device has 16 analog inputs as well as four analog outputs and an additional digital I/O. The maximal scanning rate at this device is 500 kHz for all channels. Operating with a single four quadrant photo diode needs four channels resulting in a scanning rate of at approximately 125 kHz for every channel. As explained in the theoretical part, by the usage of the optical trap it is possible to observe the particles' motion with a high spatial and temporal resolution. Further information about the lens basics, the description of the AOD and the setup of optical tweezers can be found in [60] and [96].

## 4.3 Total Internal Reflection Fluorescence Microscope Setup

In addition to the optical tweezers setup, a Total Internal Reflection Fluorescence Microscope (TIRFM) can be realized by using a separate laser beam. The setup is described in Figure 4.4. The laser beam of 532 nm wavelength (Coherent®Compass 315M CW DPSS laser system, around 80 mW power)is aligned onto the optical axis via mirrors M1 and M2 and expanded with the lenses L7 and L8. The lens L9 can be

moved laterally to displace the laser beam parallel to the optical axis. Furthermore, the lens focuses the beam into the back focal plane of the lower objective after having been deflected at mirrors M3, DS3 and S6. At DS3, which is a dichroic mirror, only light of the wavelength 532 nm gets deflected.

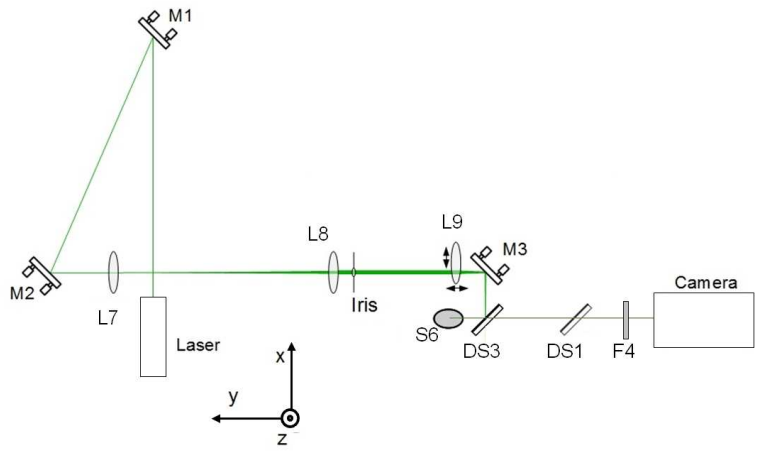



Figure 4.4: Setup of the TIRF Microscope. A laser at the wavelength of 532 nm is focused at the back focal plane of a TIRF objective. The plain wave illuminates the sample and causes a near field at the sample surface [98].

Other wavelengths like those of the illumination light can pass the filter. Focusing onto the back-focal plane allows to get a parallel laser light above the objective. The collimated laser beam passes through the immersion oil below the sample up to the examined surface. This ensures a constant illumination of the surface. The lateral displacement of lens L9 change the angle of incidence of the laser at the sample. This change increases or decreases the depth and intensity of the near field at the sample surface. Hence, it allows the transition from epifluorescence to total internal reflection fluorescence. If the sample surface is labeled with fluorescent markers, the near field excites the sample which emits light of different wavelength dependent on the marker. The emitted light passes DS2 and the dichroic mirror of the optical trap (DS1) and can be observed with the high-speed camera. Partially reflected light of the excitation laser is filtered with filter F4.
This additional possibility opens several applications like single filament or network dynamics with labeled polymers, as well as cell dynamics when the focal adhesions of the cell are marked with fluorescent dyes. Further details are described in the work of T. Robel [98].

# 5 Conversion of the Mean Squared Displacement into the Shear Modulus

As mentioned in Chapter 3.1, the calculation of the complex shear modulus is only exact for two conditions. The Laplace or Fourier transform has to be known from initial $t = 0$ to infinite time, and the mean squared displacement (MSD) has to be a continuous function dependent on time. Since other approaches underly constraints or lead to errors in case of a noisy mean squared displacement - and indeed the MSD of a thermally driven particle is noisy - a new method was developed to improve the calculation of the shear modulus and the understanding of viscoelastic systems. In the first section the new method and its principles are introduced and described. In the second section simulations are shown which demonstrate the functionality of the method on the one hand, and on the other hand give insight to the physical meaning of the single parts of the model.

## 5.1 Introduction to the New Method

The idea behind the new method is a model-based approach to characterize the mean squared displacement that allows to transform it without constraints into the dynamic shear modulus.
In theory the mean squared displacement of a particle moving in a viscoelastic medium or a polymer network has a slope of $\alpha = 3/4$ for short measurement times and reaches a saturation in the mid-time regime. For longer times the saturation value will stay constant, if the polymer network is cross-linked, and will increase again, if the network is entangled [100]. Figure 5.1 shows the master curve for the MSD of a particle in a viscoelastic medium.

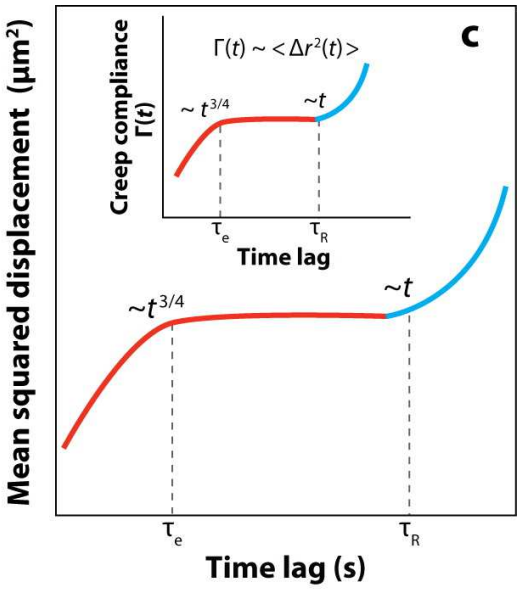



Figure 5.1: The mean squared displacement of a particle in a viscoelastic medium in theory [99], [100]. For short times, the MSD shows a power law behavior with $\alpha = 3/4$. In mid-time regimes, the MSD saturates and later increases if the network is entangled. The creep compliance, which is proportional to the MSD, underlies the same behavior (inset) [77]. $\tau_r$ is the relaxation time and $\tau_e$ the entanglement time [102].

If the polymer network is sheared, it can relax the stress for short times because of the thermal fluctuations of the filaments. For longer timescales the motion is limited by the lack of an overall filament motion which leads to a plateau in the mean squared displacement. At larger time scales, after the relaxation time, the network diffuses to relax the remaining stress [100], [101]. For a particle in a network the situation looks similar. At short time ranges the particles undergoes the thermal motion which dominates the movement. For longer times it reaches the limiting borders of the network. When the network moves via diffusion, the particle embedded in the network has to follow this motion. The model-based approach, which is used to develop a fitting function for the MSD, makes usage of these three circumstances for the particle motion in the network. Therefore the fitting function consists of three terms.
Regarding a particle embedded in an elastic gel-like network, the mean squared displacement of the motion becomes independent of time. This means, if the particle moves in one direction via thermal motion, it gets repelled by the medium.

Consequently, the mean squared displacement is dependent on the temperature and elasticity of the medium

$$\left\langle \Delta r^2(t) \right\rangle = \frac{k_B T}{K} = A. \tag{5.1}$$

In Equation (5.1), $k_B$ is the Boltzmann constant, $T$ the temperature and $K$ the elasticity of the medium. Since all values are constant, they are substituted by parameter $A$.
For a pure viscous fluid the mean squared displacement shows a power law dependency with the power law exponent $\alpha = 1$. This stands for an object which is thermally driven by the Brownian motion underlying a random walk. By using the Langevin equation of Chapter 3.1, the thermal motion of the particle that leads to the mean squared displacement, is

$$\left\langle \Delta r^2(t) \right\rangle = 2nD_{\mathrm{SE}}t = 2n\frac{k_B T}{6\pi\eta a}t = Bt. \tag{5.2}$$

The diffusion constant $D_{\mathrm{SE}}$ is the slope of the mean squared displacement. It contains the viscosity $\eta$ of the medium, the radius $a$ of the particle moving in the medium and the temperature $T$ of the medium. This is the Stokes-Einstein relation with the assumption of laminar flow around a round particle with sticky boundary conditions. $n$ is the number of dimensions in which the motion is observed in. For the description of the method, $n$ and $D_{\mathrm{SE}}$ are chosen to be constant, and therefore it can be rewritten with parameter $B$.
Additionally the particle motion in a confined cage is observed. The particle is thermally driven and freely moving in the medium, until it reaches the borders of the cage which limit its motion. Because of this the MSD increases linearly up to the point when the boundaries limits the motion. The mean squared displacement saturates and no higher displacements can be reached. The equation is given by

$$\left\langle \Delta r^2(t) \right\rangle = C(1 - e^{-\frac{t}{D}}), \tag{5.3}$$

where $D$ is the relaxation time (also $\tau$) and $C$ the saturation value. The longer the time, the more the mean squared displacement approaches the value of $C$. The

time, when saturation starts, is dependent on parameter $D$.
If a polymer network is seen as a viscoelastic medium, the three terms describe the complete medium with the motion of the particle inside. If this assumption holds, the total mean squared displacement is the superposition of the three terms. This leads to

$$\left\langle \Delta r^2(t) \right\rangle = A + Bt + C(1 - e^{-\frac{t}{D}}). \tag{5.4}$$

The calculation of the complex shear modulus out of Equation (5.4) can be performed by using the Laplace transform of the single terms. This is valid because on the one hand the Equation (5.1), Equation (5.2) and Equation (5.3) are analytical functions and on the other hand the linearity principle of the Laplace transform allows the superposition of separately transformed functions. Hence the resulting Laplace transform is

$$L_{tot} = L\{A\} + L\{Bt\} + L\left\{C(1 - e^{-\frac{t}{D}})\right\}, \tag{5.5}$$

which leads to

$$L_{tot} = \frac{B + BDs + s(A + C + ADs)}{s^2(1 + Ds)} \tag{5.6}$$

The resulting complex shear modulus is obtained, when Equation (5.6) is applied to Equation (3.8) of Chapter 3.1. The usage of analytic continuation allows to substitute the Laplace frequency $s$ by the Fourier frequency $i\omega$

$$G^*(\omega) = \frac{-k_{\mathrm{B}}T\omega^2(1 + iD\omega)}{\pi a i\omega \cdot (B + iBD\omega + i\omega(A + C + iAD\omega))}. \tag{5.7}$$

The complex shear modulus is dependent on the parameters $A$, $B$, $C$ and $D$ which are determined by fitting Equation (5.4) to the mean squared displacement measured in the experiment. The fitting method used in this work was the nonlinear least-squares method with weighting, so that values of longer times contribute less compared to those of short times scales. The parameters used for fitting are listed in Table 5.1.

If the mean squared displacement shows a particle in a pure viscous fluid, which has a constant slope, parameters $A$ and $C$ approach to zero and $B$ will be a nonzero value. If the particle moves in an elastic body, the parameter $B$ and $C$ get negligible

Table 5.1: Table of used parameters for the fitting of the MSD.

| Nonlinear least squares fitting | | |
|---|---|---|
| Fit function | | $A + Bt + C(1 - e^{-t/D})$ |
| Fit parameter | Method | Levenberg-Marquardt |
| | Confidence Level | 95 % |
| | Maximal Iterations | 10000 |
| | Weighting | $1/t$ |

small.
In some cases the fitting leads to a wipe-out of the terms, because the fitting terms are oppositional. To prevent this, the parameters are substituted by an exponential function of other parameters $a$, $b$, $c$ and $d$. This makes the method less susceptible to errors and the fitting function becomes

$$\left\langle \Delta r^2(t) \right\rangle = e^a + e^b t + e^c(1 - e^{-e^d t}). \tag{5.8}$$

In the polymer network, especially in the keratin 8/18 network used in this work, the motion of an embedded particle is composed of the limited caged motion inside the meshes of the network, a viscous drag which represents the thermal motion of the network itself and an elastic part which shows the ability of the network to store and release energy to the particle at future times. Since the fitting parameter are not smaller than zero at the measurements, an exponential function of the parameters is reasonable. The network is described by these parameters, and the complex shear modulus can be distinguished. Inserting Equation (5.8) into Equation (5.7) leads to

$$G^*(\omega) = \frac{-k_\mathrm{B}T\omega^2(1 + ie^d\omega)}{\pi a i\omega \cdot (e^b + ie^b e^d\omega + i\omega(e^a + e^c + ie^a e^d\omega))}. \tag{5.9}$$

The complex dynamic shear modulus $G^*$ can further be separated into the storage modulus $G'$ and loss modulus $G''$ which represent the real part and imaginary part of the complex shear modulus. Hence $G'$ and $G''$ can be rewritten as

$$G'(\omega) = \frac{K_{\mathrm{M}}\omega\left(e^{a}w + e^{c}w + e^{a+2d}w^{2}\right)}{e^{2b} + e^{2a}w^{2} + e^{2c}w^{2} + 2e^{a+c}w^{2} + 2e^{b+c+d}w^{2} + e^{2b+2d}w^{2} + e^{2a+2d}w^{4}} \quad (5.10)$$

$$G''(\omega) = \frac{K_{\mathrm{M}}\omega\left(e^{b} + e^{c+d}w^{2} + e^{b+2d}w^{2}\right)}{e^{2b} + e^{2a}w^{2} + e^{2c}w^{2} + 2e^{a+c}w^{2} + 2e^{b+c+d}w^{2} + e^{2b+2d}w^{2} + e^{2a+2d}w^{4}} \quad (5.11)$$

with $K_{\mathrm{M}} = (k_{\mathrm{B}}T)/(\pi a)$ being a constant for both moduli. By the determination of storage and loss moduli via the fitting with parameters $a$, $b$, $c$ and $d$, insights into the mechanical properties of the measured viscoelastic medium can be gained. To prove the validity of the method the next section depicts simulations, which show possible applications and test the functionality of the method.

## 5.2 Simulations

In order to test the data analysis method suggested in the last chapter, numerical simulations of idealized situations were performed. These simulations should show the accuracy of the fitting and the rightness of the physical meaning for the chosen situation. Moreover, simulated Brownian motions of particles with or without boundaries of a limiting symmetric cage should show if the physical interpretation of the third term of Equation (5.8) is valid. Additionally, the Brownian motion in a non-symmetric cage was performed to see the consequences of the simulation.
The simulation can be performed by applying a normal distributed random number which is linked to physical parameters like the viscosity, the temperature, particle radius and a trap stiffness. For the simulations used here the modeling of a particle motion inside an optical trap and inside a cage is investigated. In the first simulations, and the sake of simplicity, the cage is a cube. Hence the particle can move freely inside the cube until it reaches the borders where it bounces of the wall elastically. To investigate the particle motion inside the viscoelastic fluid without optical trap, the trap stiffness is equal to zero for all spatial directions. The Langevin equation in one dimension is

$$m\ddot{x}(t) + \gamma\dot{x}(t) + \frac{dV}{dx} = F(t) \tag{5.12}$$

with $m$ being the mass of the bead and $\gamma$ the drag coefficient. The assumption for this is that there is laminar flow around the particle and a linear dependency of the friction force on the velocity of particle motion. The trap potential $V(x)$ is assumed to be a harmonic potential with the force constant $k$. By neglecting the inertia of the particle it follows

$$\dot{x}(t) = -\frac{k}{\gamma}x + \gamma^{-1}F(t). \tag{5.13}$$

Since the thermal motion is assumed to lead to a random force $F$, it can be described by a Gaussian white noise process with mean zero and a variance depending on the drag coefficient and the temperature. That means $\langle F(t)\rangle = 0$ and $\langle F(t)F(t+\Delta t)\rangle = 2\gamma k_B T\delta(\Delta t)$. $\Delta t$ is the time the particle needs for one single step. With the requirement that $\langle F(t)^2\rangle = 2\gamma k_B T/\Delta t$, the numerical simulation of the Langevin equation and the step-wise integration leads to a recursive function [59]

$$\left[x(t+\Delta t) - x(t)\right]/\Delta t = -\frac{k}{\gamma}x(t) + \sqrt{\frac{2k_\mathrm{B}T}{\Delta t\gamma}} \cdot N\left(0, 2\frac{k_\mathrm{B}T}{\Delta t\gamma}\right). \tag{5.14}$$

The parameter $N$ indicates that the Brownian motion is normal distributed. The magnitude of the size of one time step $\Delta t$ can be described with a frequency $f = 1/\Delta t$. This frequency is chosen to be the same as the sampling frequency for a measurement of a particle in a network. Hence, the simulation and the measurement are comparable. Regarding the simulation in three uncoupled spatial directions it is feasible that Equation (5.14) can be used for each direction separately. The resulting motion can be written as

$$r(t+1/f) = r(t) - \frac{k}{\gamma f}r(t) + \sqrt{\frac{2k_\mathrm{B}T}{\gamma f}} \cdot N(0, 2k_\mathrm{B}Tf/\gamma). \tag{5.15}$$

### Cubic confinement

As mentioned above the simulations include a spatial confinement for the particle's motion which simulates the motion inside a cage. If a particle hits the wall under the assumption that the collision with the confinement wall is totally elastic, the position the particle would take outside the cage gets mirrored to the inside. Since the simulations are performed by MATLAB or Mathematica this feature can be added in one line of code inside the simulation loop. The resulting motion only takes place inside the confinement and the trajectory can be used for calculating the MSD. The MSD can be compared to measured data and carefully linked to the mesh size of the network.

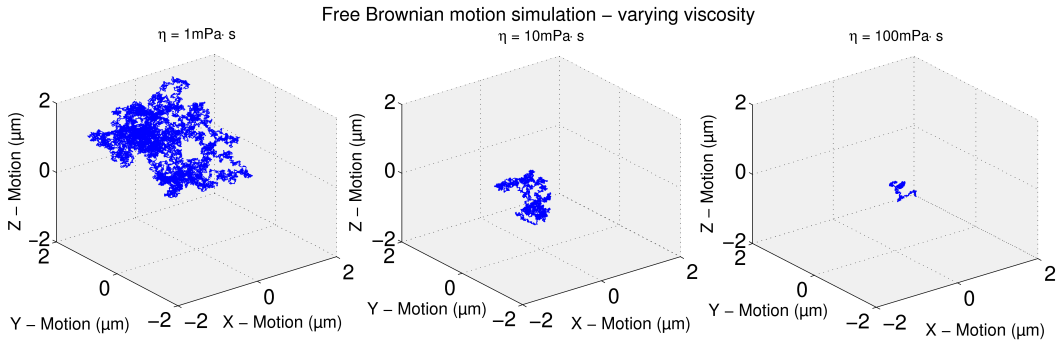



Figure 5.2: Simulation of the motion of a particle in purely viscous fluids with varying viscosity (blue line). The corresponding viscosity is shown above the graphs. The more viscous the fluid the smaller is the step size of the particle during its motion. The viscosity of 1 mPa s (left graph) is equal to the viscosity of water at 20 °C.

Figure 5.2 shows the simulation of a particle without spatial limits. The three graphs show motions for varying viscosities: $\eta = 1\,\mathrm{mPa\,s}$, $\eta = 10\,\mathrm{mPa\,s}$ and $\eta = 100\,\mathrm{mPa\,s}$. The more viscous the fluid the less is the distance the particle can move. For the simulations a sampling frequency of 5000 Hz, and a particle radius of 500 nm at a temperature of 296.15 K was chosen. These conditions were comparable with those of the measurements performed in the lab. This simulation showed that a free particle diffusion worked with the upper theoretical aspects. The slope of the resulting MSD for the simulations was dependent on the diffusion coefficient. Furthermore, the MSD was linear in time. The diffusion coefficient is indirectly proportional to the viscosity. Thus, the higher the viscosity the lower the slope of the MSD is. The

next simulations showed the behavior of a free particle (without optical trap) in spatial confinements with varying confinement size in three directions. Confinement size in this case meant the length $l$, width $w$ and depth $d$ of a cuboid, first with $l = w = d$ and the parameter varied from $l = 500\,\text{nm}$ to $l = 15\,\text{nm}$.

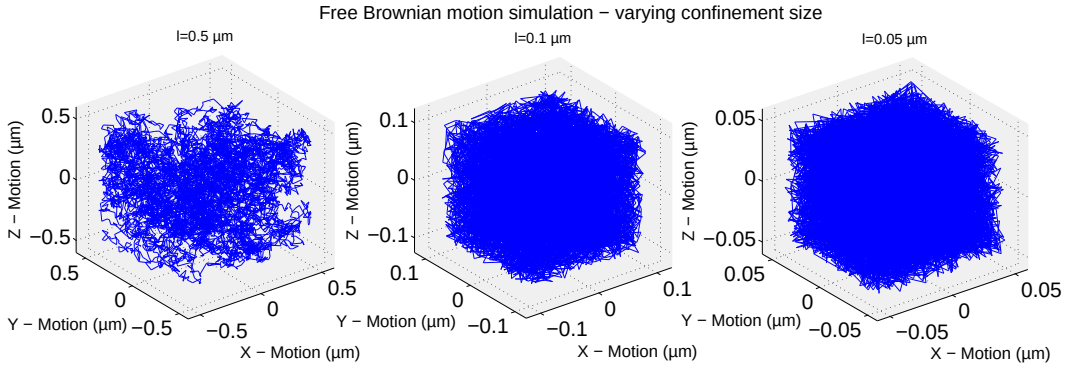



Figure 5.3: Brownian motion of a particle in a water-like fluid with spatial confinements of varying size (e.g. 500 nm, 100 nm, and 50 nm). The confinements chosen were of cubic geometry so that every direction has an equal limit. If the particle hit the wall, it got deflected elastically. The size of the confinement is located above the corresponding graphs.

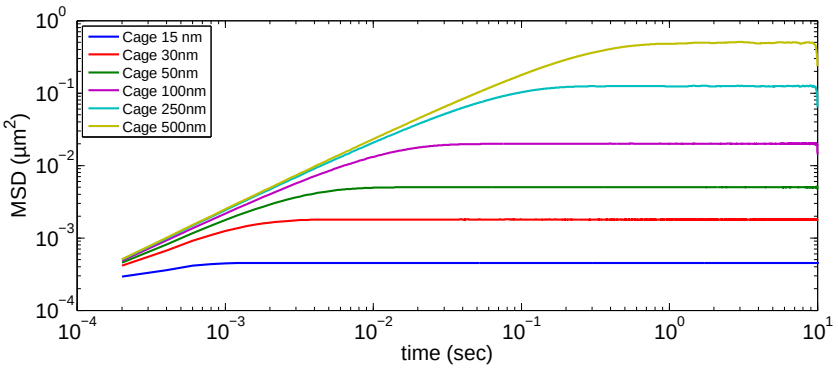



Figure 5.4: Mean squared displacement of the particle motion with varying confinement size. The smaller the cage the faster the particle reached the walls, got deflected and its MSD got saturated. The saturation value was lower the smaller the confinement was. The different colors of the curves indicated a varying cage size.

Figure 5.3 shows exemplary trajectories of the simulations for the varying cage sizes (500 nm, 100 nm, and 50 nm). The viscosity of the medium is comparable to water, $\eta = 1\,\mathrm{mPa\,s}$, with a temperature of $T = 296.15\,\mathrm{K}$. The used sampling frequency is $f = 5000\,\mathrm{Hz}$ (equal to the passive microrheology measurements). The number of steps was chosen to 50000 and the simulation was repeated 100 times. The particle's motion was a free Brownian motion which always got deflected when hitting the confinement wall. The smaller the confinement the earlier the particle reached the boundary. This influenced the MSD of the particle motion. In Figure 5.4 the averaged MSD for every confinement size is shown.
As the simulations showed, the MSD's saturation time changed due to the limited motion of the particle. The MSD could be fitted to the third term of Equation (5.8) to test if the theoretical ideas matched with the simulations. It can be seen that the fit had low residues and consequently, theory and simulations were in good agreement. Furthermore, a dependency of the fit parameters $C$ and $D$ on the cage size was distinguished. Equation (5.16) shows the behavior of cage size $l$, $\alpha$ and $\beta$ dependent on fit parameters $C$ and $D$.

$$C = \alpha \cdot l^2 \qquad D = \beta \cdot l^2 \tag{5.16}$$

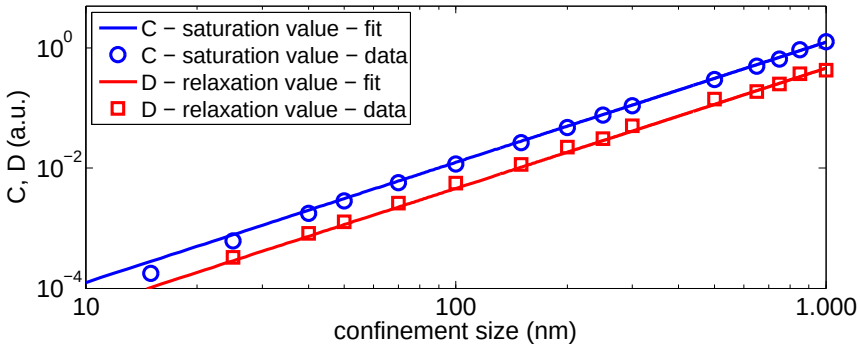



Figure 5.5: By fitting the upper MSD with the third term of Equation (5.8), the saturation value $C$ and relaxation value $D$ were determined. A varying cage size changed both the saturation and relaxation in a power law behavior with a factor of 2 multiplied by a constant. The graph shows double logarithmic plots of $C$ and $D$ dependent on the confinement (circles and squares) with the specific harmonic fit (colored lines).

In Figure 5.5 the simulated averaged fit parameter $C$ and $D$ are plotted over the specific confinement size. The parabolic behavior can be identified clearly because

the double logarithmic plot has a constant slope. The $R^2$ values of the fits were in both cases $R^2 > 0.998$ which indicated an accurate fit with low residuals. Hence, in a cube confinement in three dimensions $\alpha$ and $\beta$ were

$$\alpha = 1.244 \cdot 10^{-6} \qquad \beta = 4.588 \cdot 10^{-7}.$$

Fit parameter $C$ in this equation stands for the saturation value which is the value the MSD can reach. The parameter $D$ is equivalent to the relaxation time. In general the idea is that if the MSD of the measurement is fitted by Equation (5.8), the parameters of the third term can be linked to the cage size. This gives an idea of how much the particle in the network is able to move, and might lead (with additional steps) to the mesh-size of the network.

### Cuboid confinement

Another simulation shows the resulting mean squared displacements for an anisotropic confinement ($l \neq w \neq d$). The measurements (Chapter 7) indicate that the motion of the particle is not the similar for different directions. Figure 5.6 shows an exemplary simulation trajectory on the left hand side with $l = 75\,\text{nm}$, $d = 40\,\text{nm}$ and $w = 35\,\text{nm}$, and the comparison of the MSD of several varying confinement sizes on the right side.

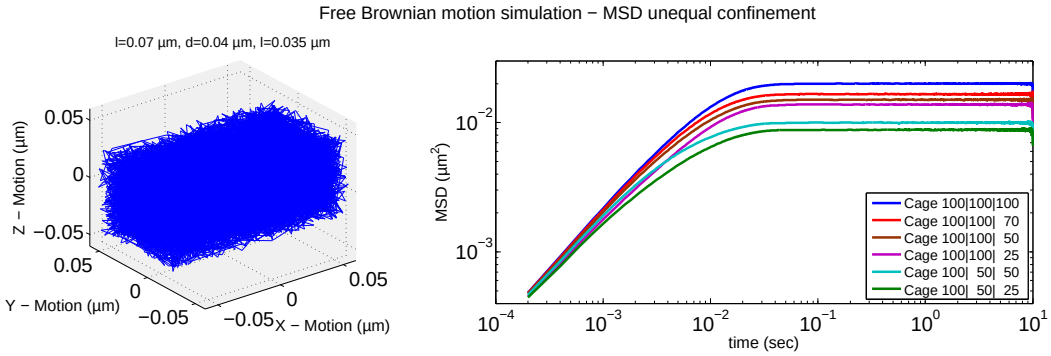



Figure 5.6: MSD for simulations when the particle moved in an confinement with different spatial limits. Left: Exemplary Brownian motion. Right: The unequal confinement size changed the saturation value but not the edge of the mean squared displacement. Measurement in assembled networks indicated that a confinement is not symmetric in all spatial directions. The legend shows the different length scales of the confinement in nm.

For these simulations it was seen that the edge and the saturation was shifted to higher or lower values by conserved curvature of the mean squared displacement. For measurements in networks this behavior indicated that the network was not isotropic, homogeneous and the cage not symmetric. In addition to the motion in a static confinement, simulations were performed in a dynamic cage. The particle can move freely inside a cage which is moving with a spatial drift by diffusion. To ensure a correct simulation two scenarios were tested. In the first scenario at every step of the particles' motions it was checked whether they hit the wall of the drifting confinement. In the second scenario the calculations were performed as described above without drifting confinement, and after that a linear function was added to the complete trajectory of the particles. The linear function corresponded to the diffusive motion of the confinement. The simulations were performed with the same parameters as above plus a drift of $dr = 0.05\,\mu\text{m}$ for the complete motion.

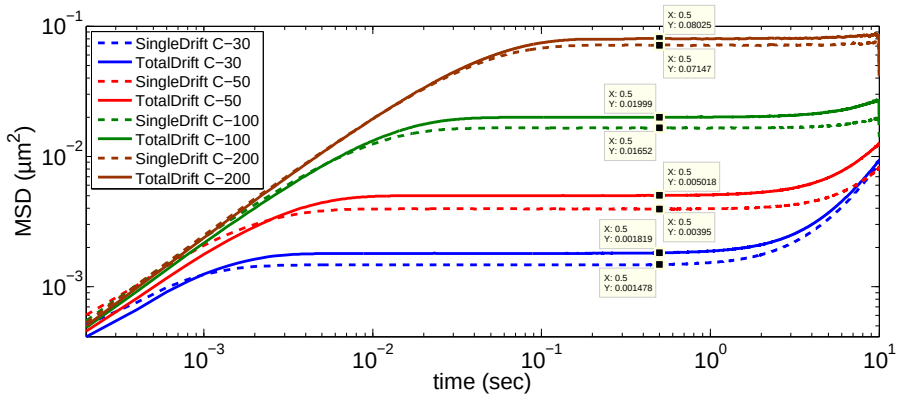



Figure 5.7: Comparison of the MSD of both the step-wise drift (dashed line) and the drift added after the simulation of the Brownian motion (line). As the confinement was smaller the influence of the drift to every single step increased and hence the difference to the totally added drift decreases. The boxed values show the values of the corresponding MSD at a time value of 0.5 sec and different colors mark different cage sizes.

Figure 5.7 shows the different MSDs of the two scenarios for four different confinement sizes. The smaller the confinement the more the trajectory of the particle was influenced by the drift of the confinement. At the plateau at $t = 0.5\,\text{sec}$ the values of the corresponding MSDs are included in the graph. At small confinement sizes the difference of the MSD for both scenarios could be neglected. Due to the assumptions of Chapter 3, the particle should be larger than the mesh size. Therefore every

step is dependent on the motion of the confinement and consequently, the addition of a linear function is allowed. For computations of the trajectories the addition of a linear function as drift is much easier compared to a step wise calculation of the confinements influence. Especially when the confinement is of complicated geometry. Overall by adding a linear drift, the viscous part of the fitting function can be simulated, and its physics described. When the whole network moves with the embedded particle, there is a increase of the MSD for long times [100]. This becomes more obvious when the network is entangled, because there the filaments can slip along each other and thus move the cage. In the cross-linked case, the network's filaments are bound to each other and therefore the cage does not move much.

**Ellipsoidal confinement**

In a next step the geometry of the confinement was changed. The latter cuboid cage as an approach to the motion in a network was not that close to reality. Measurements that are shown in Figure 5.8 reveal that the trajectories were close to an ellipsoid.

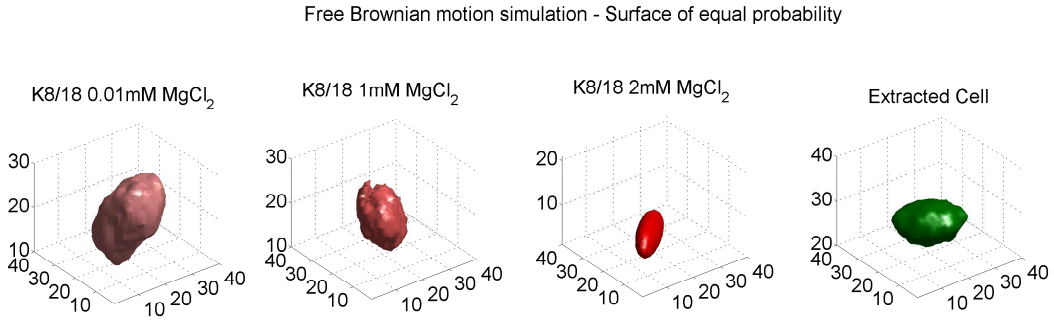



Figure 5.8: Exemplary surfaces of equal probability of measurements performed at different cross-linker concentrations of *in vitro* assembled keratin 8/18 networks and extracted cells. The axes describe the binning of the motion (40 bins in each direction). The surfaces of equal probability revealed that the confinement, the particle moved in, was of ellipsoidal shape. The higher the cross-linker concentration the more obvious was the ellipsoidal shape. For measurements at cells this became clearer the closer the particle was to the cell nucleus.

Hence, in this part the motion was simulated for an ellipsoid as spatial confinement. The results from above allowed that the confinement drift was added after simulat-

ing the motion. The ellipsoid size was defined by the lengths of the semi-principal axes in all spatial directions. If $l = w = d$ was chosen, the motion was located in a sphere, otherwise if $l \neq w \neq d$ the particle moved inside an ellipsoid.

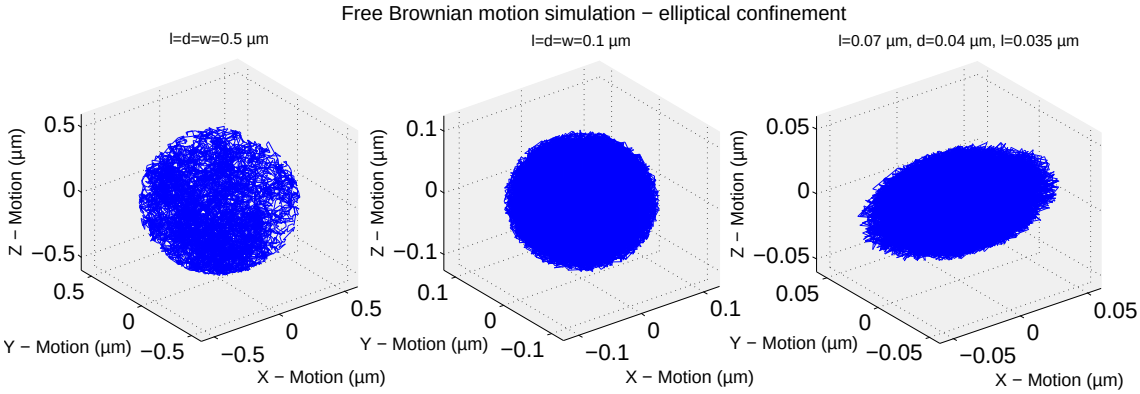



Figure 5.9: Simulations of Brownian motion in an ellipsoidal confinement. The varying parameters allowed motions of different distances depending on the direction of motion.

In Figure 5.9 three exemplary trajectories are illustrated. The left graph shows the motion in a confinement with $l = w = d = 500\,\text{nm}$, in the middle the confinement size is changed to $l = w = d = 50\,\text{nm}$. On the right side the situation of an unequal elliptical cage $l \neq w \neq d$ with $l = 75\,\text{nm}$, $d = 40\,\text{nm}$ and $w = 35\,\text{nm}$ is illustrated.

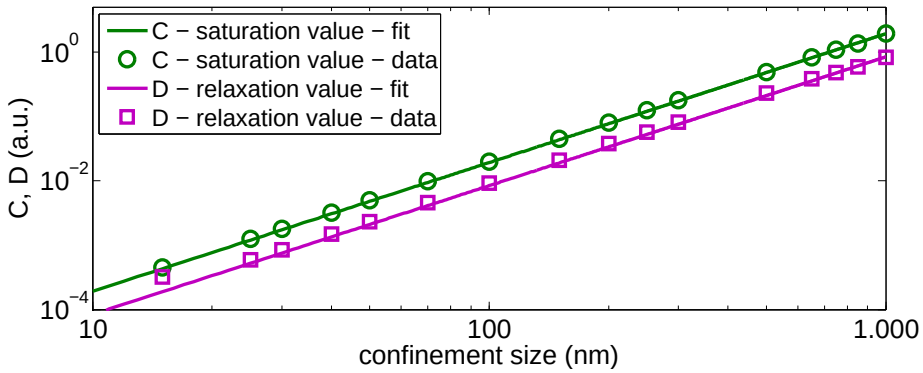



Figure 5.10: Dependency of C, the saturation, and D, the relaxation value, on the confinement size was similar to the cuboid confinement, but with a different values of constants $\alpha$ and $\beta$.

When the particle hits the wall, it gets reflected elastically like in the upper simulations. The comparison of the MSD of the cuboid and elliptical confinements showed that the saturation began at earlier times and the saturation value was smaller, because the particle earlier reached the confinement wall for the elliptic case. By fitting with the third term of Equation (5.8), the fit parameters for the saturation value and the relaxation time were determined for a spherical confinement. Similar to the cube confinement, both the saturation and the relaxation value behaved like a parabolic function with varying cage size. The equation can be written as

$$C = \alpha \cdot l^2 \qquad D = \beta \cdot l^2, \tag{5.17}$$

with

$$\alpha = 1.922 \cdot 10^{-6} \qquad \beta = 8.407 \cdot 10^{-7}.$$

Figure 5.10 shows the dependency of saturation value $C$ and relaxation value $D$ on the confinement size. For the simulations several spherical confinements were tested and the resulting MSDs were an average of 100 simulations. The viscosity, particle radius and temperature were chosen similar to the cube confinement simulations.

**Additional trap potential**

In the latter section the fit function was described to contain three terms - the confined motion term, the viscous term, which was the drift of the network, and the elastic part that represented the elastic behavior of the network towards the particle. As mentioned above, the simulation can be performed with an additional force of the optical trap which has a harmonic potential. In that way the particle is pulled into the trap while following the thermal motion. If one assumes that the network, in which the particle is embedded, has also a harmonic potential, it is possible to introduce a force constant for the network. The parameter $k$ - the trap force constant - can be used as influence of the surrounding network for the simulations of the Brownian dynamics and be denoted as network force constant. Figure 5.11 shows the potential over displacement of a particle which passively moved in an extracted cell network. By fitting a parabolic function it becomes obvious that the network potential is a parabolic function.

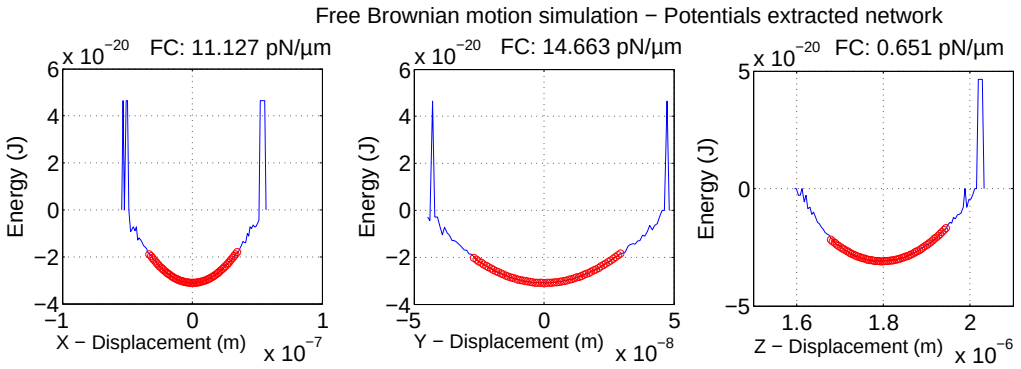



Figure 5.11: By determination of the distribution of particle positions and Boltzmann's law the potential of the network can be developed. The potential can be approached to a harmonic potential for small displacements of the particle. It is obvious that the harmonic fit is in accordance to the measured data in an extracted cell.

With this result, it is possible to assume a harmonic potential for the network and use the parameter $k$, the network force constant. Consequently, simulations were performed with an additional network force constant describing the elasticity of the network. At the simulations, the other parameters were not modified.

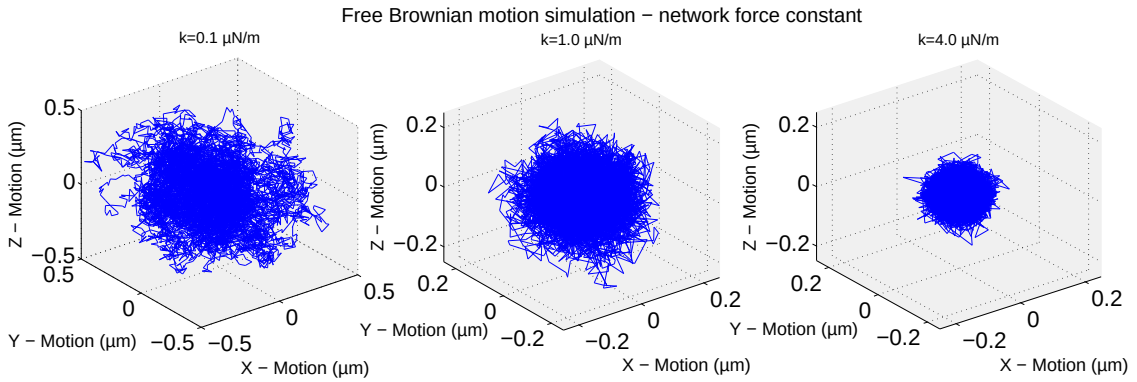



Figure 5.12: Brownian motion of particles with a repelling force of the network. The assumption that the network has a harmonic potential led to a network force constant and a behavior like in an optical tweezers. The figure shows the Brownian motion with varying network force constants.

In Figure 5.12 three exemplary simulated Brownian motions are shown. For these simulations the cage size was chosen to be large ($l = d = w = 4\,\mu\text{m}$), so that it

did not influence the particle motion. For the calculation, different network force constants were chosen, $k_1 = 1 \cdot 10^{-7}$, $k_2 = 1 \cdot 10^{-6}$ and $k_3 = 4 \cdot 10^{-6}$. For each direction the same repelling force was used. In the simulation shown in Figure 5.12, the particle motion was not strictly limited to a certain volume, but the repelling force pulled the particle back to the center of motion. The lower the force is, the more the particle can move. By applying a high force, the particle's motion becomes more and more limited.
For the next simulations a varying confinement size is added to a specific network force constant.

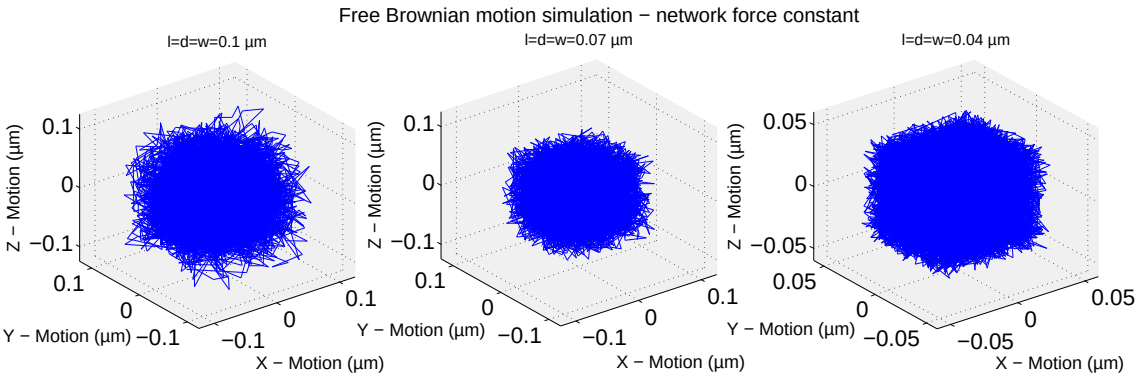



Figure 5.13: Brownian motion of particles in a cuboid confinement with added repelling force by the network. The particle was trapped in a harmonic potential and additionally hit the cage walls when it got displaced too much.

Figure 5.13 illustrates a Brownian motion with network force constant $k = 2.6\mu\mathrm{N/m}$ (determined by measurement) in cuboid confinements $l = w = d = 100\,\mathrm{nm}$, $l = w = d = 70\,\mathrm{nm}$ and $l = w = d = 40\,\mathrm{nm}$. One can clearly see that the particle often passed the center of the confinement because of the elastic forces of the network. The smaller the cage the bigger was the influence of the confinement. In the same way as for the unequal confinement, further simulations could be performed with unequal force constant for the spatial directions. This increases the amount of possible simulations and would be too much to show at this point. In general the forces that act in real networks are not equal, which can be seen at Figure 5.11.

### Predetermined MSD

The considerations of this section illustrate that simulations of a viscoelastic medium lead to fitting Function 5.8. The three terms show different characteristics which

can describe the complete viscoelastic behavior of a medium like a polymer network. Further simulations with given MSDs proof that the model based fitting function can be applied to real measurements and for the extreme case shows better results compared to other methods (Mason, Evans, described in Chapter 3.1).
For the first simulation the compliance function, which Evans used in his publication [86], was used to confirm that the novel method for this case gave reasonable results. As shown in Chapter 3.1, both other methods worked for this scenario. The following Figure 5.14 shows the fitting of the MSD and the resulting storage and loss modulus. The storage and loss modulus resulting of the fitting with Equation (5.8) are in accordance with the results of Evans and Mason. This confirms that the methods work for compliance measurements with similar curvature.

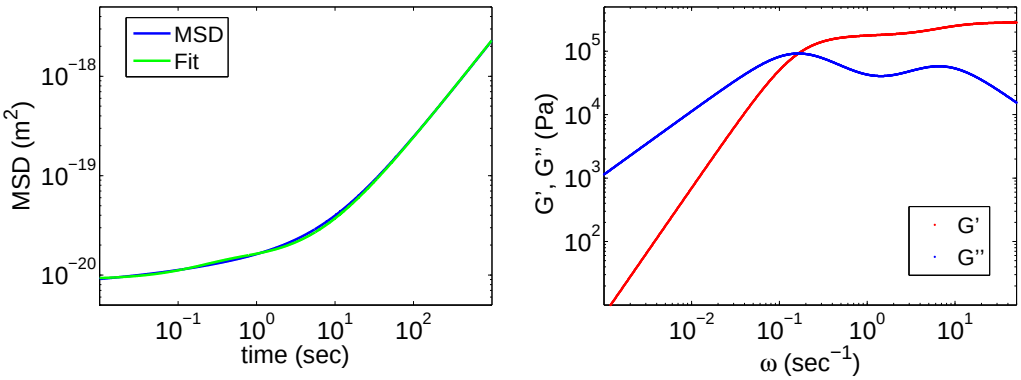



Figure 5.14: MSD of Evan's compliance function. On the left side the MSD (blue) with its fit (green) is shown. The fit is in accordance with the MSD. On the right side the resulting storage (red) and loss modulus (blue). Both show a similar curvature compared to those of the Evans and Mason methods.

As a second test, the same MSD was used and Gaussian white noise added. The other methods failed at this scenario with an amplification of the noise. Figure 5.15 shows MSDs with noise (SNR= 40, SNR= 10) and the resulting $G'$ and $G''$. The MSD with noise (SNR= 40) had almost the same curvature compared to the MSD of Figure 5.14. Since the SNR is high the noise is very small and could hardly be recognized. For this case the output, the storage and loss is not influenced by the noise. In the other case the SNR is small and the MSD noisy. The fitting also worked in this scenario and produced the same output compared to a low noise. In that way the novel method showed, independent on the amount of noise, the same curvature of the compliance data compared to Evans's publication. The other methods failed

at this point whereas the new method does not amplify the noise and does not lead to unreasonable storage and loss moduli.

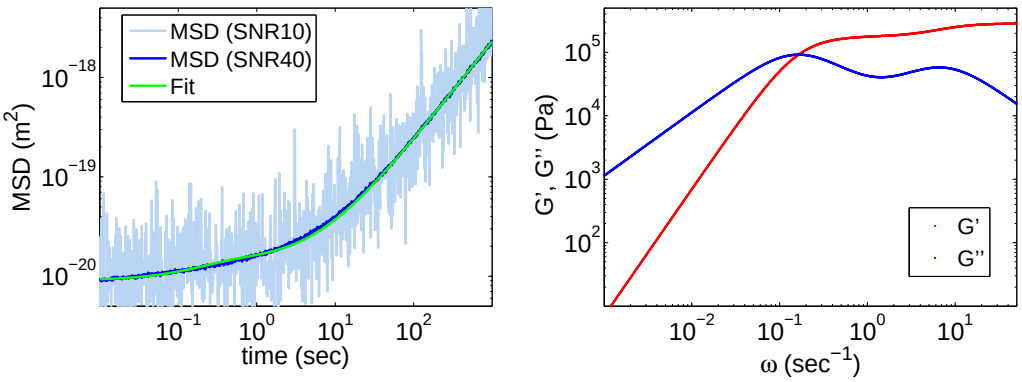



Figure 5.15: MSD of Evan's compliance function with noise. On the left side the MSD with noise of a SNR= 40 (blue) and a SNR= 10 (light blue) with its fit (green) is shown. The fit is in accordance with both MSDs. On the right side the resulting storage (red) and loss modulus (blue). Both show a similar curvature compared to those of the Evans and Mason methods. In this case the output does not change even if the noise is really large (SNR= 10)

As a third scenario a MSD of an absolute viscous fluid is taken into account. The MSD has a constant slope over time. For this case theory predicts that the first and the third term of Equation (5.8) will disappear. Furthermore, if the shear moduli of this scenario are calculated via the Laplace transformation of the MSD fit, the elastic part $G'$ will be zero because in a viscous fluid no elasticity exists. The loss modulus $G''$ on the other hand will have a linear increasing behavior. Additionally the other extreme case - the case of an elastic solid - is simulated. In this case the MSD is independent of time and therefore constant over the whole time range. The expected storage modulus $G'$ is also independent of time and the loss modulus $G''$ should be zero over the whole frequency range. Figure 5.16 shows the simulated MSD within the fitted function. Figures 5.17 and 5.18 the resulting shear moduli for both scenarios. Both fits for the viscous and elastic case work properly (Figure 5.16). That means the terms, which do not benefit to the specific case, have parameters which almost disappear. In the case of a viscous fluid the first and third term of the fitting function have to vanish and at an elastic solid the second and third term have no influence on the MSD. The conversion to the dynamic shear modulus leads

to the results shown in Figure 5.17.

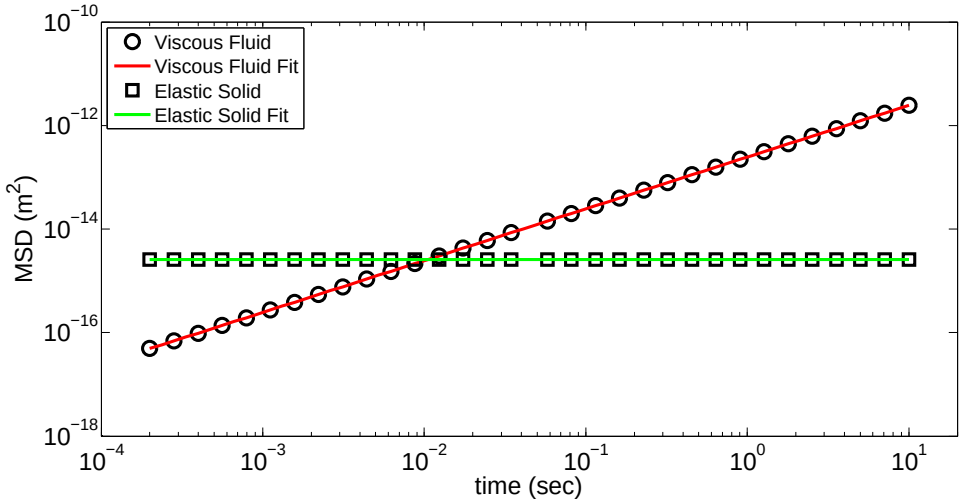



Figure 5.16: The given MSD of the totally viscous fluid (circles) and rubber like elastic solid (squares) are fitted by Equation (5.8) (line, red and green). The fit can completely follow the MSD because of the viscous term and/or the elastic one. The third term disappears for both cases.

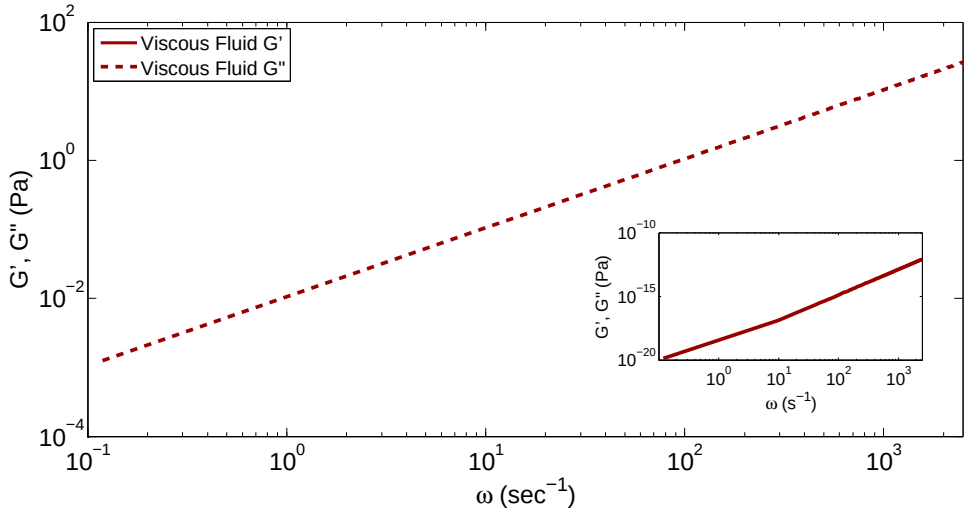



Figure 5.17: Storage modulus $G'$ and loss modulus $G''$ for the case of a viscous fluid. The storage modulus is shown in the inset and is at the order of $1 \cdot 10^{-15}$ because of calculation artifacts (the fitting parameters never become exactly zero).

As mentioned above, for the viscous fluid scenario the storage modulus disappears

because of a lack of elastic response to an external pressure. This can be seen in Figure 5.17. The remaining loss modulus is in the theoretically predicted range and the storage modulus is in the order of $1 \cdot 10^{-15}$ which is an artifact because the fitting program does not allow parameters to be equal to zero. Consequently, the values are very small and the result is a negligible storage modulus.
In case of an elastic solid, the simulation and calculations of the shear modulus are similar to the upper viscous fluid scenario. As predicted in theory, the loss modulus is negligible small because of the fitting artifact and the storage modulus is independent on the frequency.

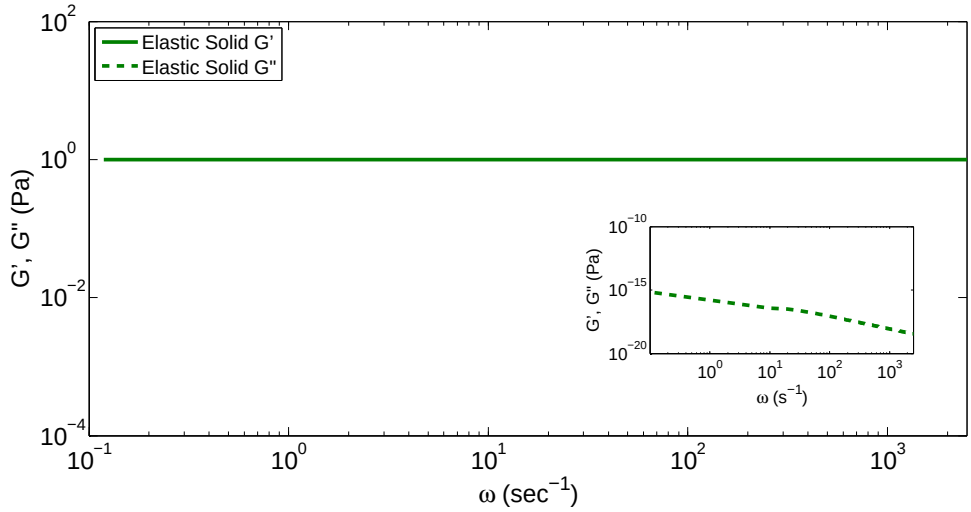



Figure 5.18: In an elastic solid scenario the storage modulus $G'$ is constant and the loss modulus $G''$ disappears. $G''$ is very small (inset) and does not completely vanish because of the calculation artifacts already mentioned above.

Hence, the model based fitting function leads to correct results for both extremes. Therefore the resulting storage and loss moduli are reasonable and can be used for the MSDs of the simulations. With this a better insight towards the physical aspects and the dependency on the three terms is gained.

### Shear moduli of varying parameters

In the following calculations of the shear moduli are shown. The shear moduli are a result of the simulated MSD. The simulations will vary in viscosity, drift and network stiffness. Hence, the goal is to imitate a measurement of an *in vitro* assembled network to gather more information about its dynamics and behavior.

Figure 5.19 shows a simulation of a Brownian motion in an elliptical confinement with $c = (0.100, 0.100, 0.100)\,\mu\text{m}$, a viscosity $\eta = 1.0\,\text{mPa s}$, an additional drift of $dr = (0.050, 0.050, 0.050)\,\mu\text{m}$ and a network force constant which varies relative to the normalization force $k_0 = 1.0 \cdot 10^{-6}\,\text{N/m}$ (in that way $r_k = 20$ means $k = 20 \cdot 10^{-6}\,\text{N/m}$). The influence of the repelling force of the network changes both the storage modulus and the loss modulus. Hence, the higher the network force constant the higher the storage modulus because the particle's motion underlies a higher repelling force. The loss modulus is changed in that way that the minimum is shifted to higher frequencies and to a higher value. The maximum at low frequencies behaves in a similar way.

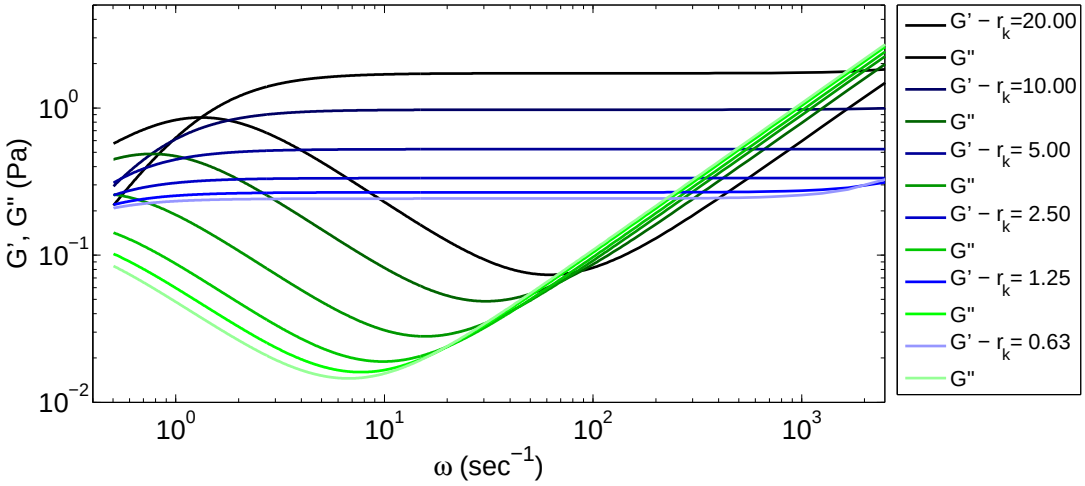



Figure 5.19: Dynamic shear modulus of Brownian motion simulation with varying network force constants. $r_k$ denotes the ratio of the varying network force constant and $k_0 = 1.0 \times 10^{-6}\,\text{N/m}$. Blue lines show the storage modulus and green lines represent $G''$.

If - in another simulation - the network force constant is equal to zero and the relation between the total drift and the confinement size is varied, a modified dynamic shear modulus is observed. Figure 5.20 shows this simulation. The variable $r$ denotes the ratio of total drift to confinement size. For $r = 4$ the drift is four times higher than the confinement size. That means that the particle at every step is pushed into the direction of the drift and the free Brownian motion is dominated by the drift. In this case the MSD ends up in a curve with constant slope and therefore the resulting $G'$ disappears and $G''$ increases linearly. Vice versa, if the drift is apparently equal to zero ($r = \infty$) the MSD depends on the confinement size and the resulting $G'$ and

$G''$, too.

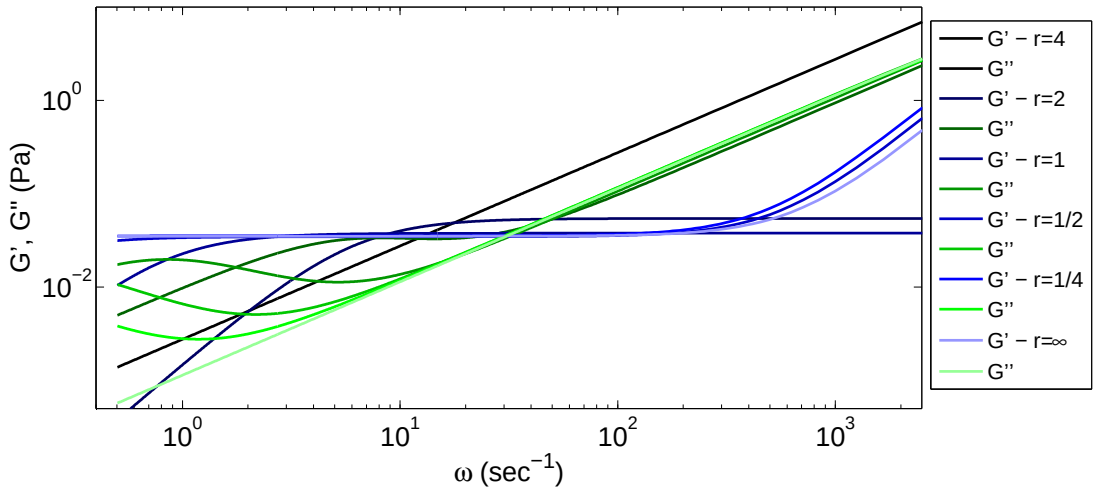



Figure 5.20: Dynamic shear modulus of Brownian motion simulation with varying drift of the network. $r$ denotes the ratio between confinement size and added drift.

For intermediate ratio the loss modulus' minimum shifts to higher frequencies and higher values, if the influence of the drift rises or dominates. The storage modulus remains unaffected in value and the plateau moves to lower frequencies.
At a third simulation the viscosity of the medium in the network was modified and related to the viscosity of water ($\eta_0 = 1\,\mathrm{mPa\,s}$). In this case the loss modulus increases if the particle moves in a more viscous material. The minimum moves of $G''$ to lower frequencies for higher viscosities. The storage modulus $G'$ changes its curvature at the upper end of the simulated frequency range, increases with $r_\eta > 1$ and decreases in the opponent case.
In summary with a variation of either the viscosity, the confinement size, the drift or the repelling force the dynamic shear modulus is changed in curvature and in absolute value. A superposition of the modification of those parameters leads to additional possible values and location of the minimum for $G''$ and the plateau of $G'$ in the simulated frequency range.

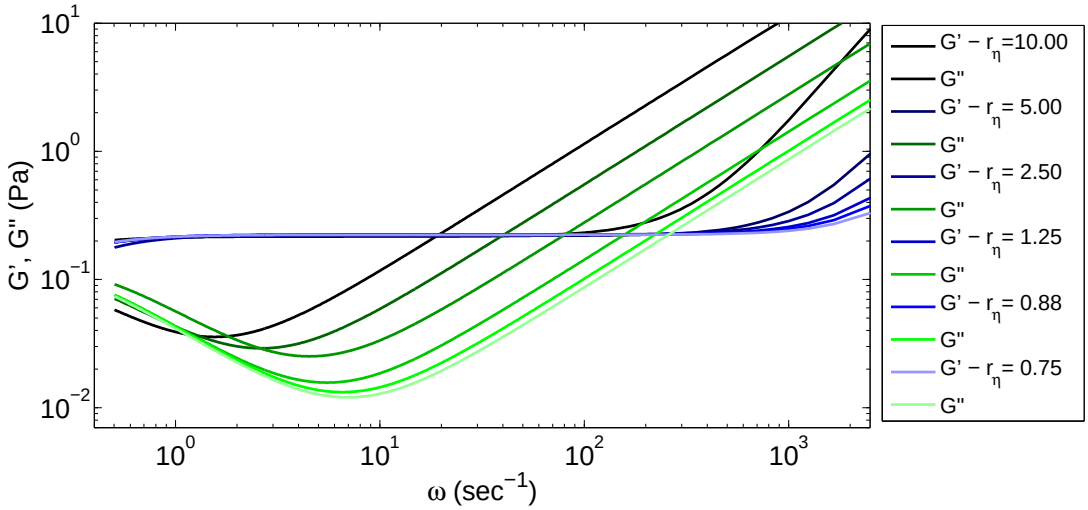



Figure 5.21: Dynamic shear modulus of Brownian motion simulation with varying viscosity in the network. The change in the ratio of the medium compared to water ($r_\eta$) influences the loss modulus' minimum.

Furthermore, a change in the confinement shape and the usage of unequal values for the parameters in different spatial directions opens a wide field of manipulations which influence the dynamic shear modulus. In general the simulation of the three terms introduced for this method allow to rebuild the MSD and the shear modulus of the measurements and, in that way, offers insight into the network properties.
The simulations show that the method is valid for determining the mechanical properties of viscoelastic media, confirmed by the correct reproduction of theoretically predicted curvature and magnification, of both the MSD and the dynamic shear modulus. This was tested for a purely viscous medium, an elastic body and viscoelastic materials of varying properties. In Chapter 7 the method will be applied to measurements of varying media to underline the functionality of the method.

# 6 New Insights for Active Microrheology - the Lock-In Method

In this chapter a second novel method to describe the mechanical properties of networks is introduced. This method uses optical tweezers to apply an external stress to the examined viscoelastic medium or network. The response of the medium gives an insight into its dynamics and its mechanical behavior in case of stress. In the first part the general theory for deformations of isotropic and elastic bodies is described. The novel method is explained in a following part. Afterwards, simulations concerning the method and the theory are given.

## 6.1 Deformation of an Isotropic, Elastic Body

In this section the theory behind the deformation of an isotropic, elastic body is illustrated. This background is needed because in the next section the transfer tensor is introduced and measurements are compared to the theory.
The information about the displacement of a point in a medium, when the medium gets stressed, can be expressed by a force and the Green's tensor. The stress applied to the medium can be a shear, a dilatation or a compression. The Green's tensor contains the properties of as well as the viscous and elastic medium. To gain knowledge about the Green's tensor, several assumptions have to be made and the strain tensor and the stress tensor are introduced [103]. The deformation of the medium - as a first assumption - is always small. Hence, the theory is valid when the change of the distance of two points in the medium is small compared to their distance. Regarding a point with the distance $\vec{r}$ to the origin, with its position being influenced by a deformation, so that the new position is $\vec{r}'$. The difference of both is denoted by the displacement vector $\vec{u}$. Considered in one dimension, it is

$$u_i = x_i' - x_i, \qquad i = \{1, 2, 3\}, \tag{6.1}$$

with the specific direction being $i$. If two neighbor points have a distance $dx_i$ before deformation, the distance is $dx_i'$ after deformation and the change is $du_i$. For all dimensions the distance is $dl'$, the square root of the sum of all squared $dx_i'$.

$$\begin{aligned} dl'^2 &= dx_i^{'2} \\ &= (dx_i + du_i)^2 \\ &= \left(dx_i + \frac{\partial u_i}{\partial x_k} dx_k\right)^2 \\ &= dl^2 + 2\frac{\partial u_i}{\partial x_k} dx_k dx_i + \frac{\partial u_i}{\partial x_k}\frac{\partial u_i}{\partial x_l} dx_k dx_l. \end{aligned} \tag{6.2}$$

If the indices $i$ and $k$ are swapped in the second term and $k$ and $l$ in the third term the equation can be rewritten as

$$\begin{aligned} dl'^2 &= dl^2 + \left(\frac{\partial u_i}{\partial x_k} + \frac{\partial u_k}{\partial x_i}\right) dx_i dx_k + \frac{\partial u_i}{\partial x_k}\frac{\partial u_i}{\partial x_l} dx_l dx_k \\ &= dl^2 + 2u_{ik} dx_i dx_k. \end{aligned} \tag{6.3}$$

Then the strain tensor is defined as

$$u_{ik} = \frac{1}{2}\left(\frac{\partial u_i}{\partial x_k} + \frac{\partial u_k}{\partial x_i} + \frac{\partial u_l}{\partial x_k}\frac{\partial u_l}{\partial x_i}\right), \tag{6.4}$$

with a symmetric tensor $u_{ik} = u_{ki}$. This is the strain tensor in the general case. For small deformations the third term is negligible. Consequently, the strain tensor becomes

$$u_{ik} = \frac{1}{2}\left(\frac{\partial u_i}{\partial x_k} + \frac{\partial u_k}{\partial x_i}\right). \tag{6.5}$$

In order to express the displacement via the Green's tensor using an external force, the stress tensor has to be related to the strain. If a body gets deformed, an external stress is assumed to act at the surface of a small part of the body and affect only this part. Internal stresses only become relevant at short ranges and therefore are taken to be zero. Short ranges mean that just the neighborhood of the point is affected by the internal stress. Macroscopic distances on the other side are considered to be large compared to the small distance in the molecular range. Thus, if several forces are applied at several parts of the body, the total force can be written as a sum of forces acting on all surface elements - a volume integral over force and volume element. This integral over the force at the small volume element can be rewritten via the Gaussian equation to a surface integral when the force $F_i$ is the divergence of the stress tensor $\sigma_{ik}$. With this the following equation holds

$$\int F_i dV = \int \frac{\partial \sigma_{ik}}{\partial x_k} dV = \oint \sigma_{ik} df_k \tag{6.6}$$

where $df_k$ is related to one component of the surface element. If the surface element is located in the $xy$, $xz$ or $yz$ plane, the component of the stress tensor becomes the $i$-component of the force per surface which is orthogonal to the $x_k$ axis. If a force acts towards the orthogonal surface of the $x$-axis, it can be divided into a normal force $\sigma_{xx}$ and tangential forces $\sigma_{yx}$ and $\sigma_{zx}$. In the case of hydrostatic pressure, the assumption can be taken into account that on every surface element the acting force is equal. The stress tensor is dependent on the pressure $p$ and the unit vector $\delta_{ik}$ with $\sigma_{ik} = -p\delta_{ik}$. In the general case the forces are not equal for every surface element and underly varying normal and tangential forces. Due to this the non-diagonal elements of the tensor become non-zero.
The deformation of a body for varying temperature shows a different behavior. Thus, the stress tensor is also dependent on temperature. In this theory a constant temperature is another assumption so that the deformation of the body is only from an external stress and not because of thermal influences. In the thermal equilibrium state the stress tensor is related to the free energy $E_\mathrm{F}$

$$\sigma_{ik} = \left(\frac{d\epsilon}{du_{ik}}\right)_S = \left(\frac{dE_\mathrm{F}}{du_{ik}}\right)_T. \tag{6.7}$$

If the isotropy $S$ of the system is constant, the stress tensor can be derived by the inner energy $\epsilon$. As mentioned before, the deformation can be regarded as small and so Hook's law can be applied to the theory. This enables relating stress tensor and strain tensor which are needed for explaining the deformation of an isotropic, elastic body. The free energy $E_\mathrm{F}$ is a scalar and therefore all terms in the expansion of $E_\mathrm{F}$ have to be scalars, too. Furthermore, all terms are dependent on the stress tensor which is assumed to be symmetric. Hence, the expansion of $E_\mathrm{F}$ with two second-order terms of $u_{ik}$ is

$$E_\mathrm{F} = E_{\mathrm{F}_0} + \frac{1}{2}\lambda u_{ii}^2 + \mu u_{ik}^2 \tag{6.8}$$

with $\lambda$ and $\mu$ the Lamé coefficients. $E_{\mathrm{F}_0}$ is an additional constant for the free energy without deformation. The Lamé coefficients separate the free energy into two parts, one part concerning pure shear where the deformation does not change the volume of the body (affine dformation), and the other part where the volume is not changed, but the shape due to a compression of the whole body. By involving an identity for $u_{ik} = \left(u_{ik} - \frac{1}{3}\,\delta_{ik}u_{ll}\right) + \frac{1}{3}\,\delta_{ik}u_{ll}$ into the formula, one can further generalize Equation (6.8). With this generalization further parameters can be introduced - the shear modulus (or modulus of rigidity) $G$ and the compression modulus (or bulk modulus) $K$. This leads to

$$E_\mathrm{F} = \frac{1}{2}Ku_{ll}^2 + G\left(u_{ik} - \frac{1}{3}\delta_{ik}u_{ll}\right)^2. \tag{6.9}$$

Parameter $E_{\mathrm{F}_0}$ is neglected because the free energy of the deformation is important for this case and not the energy of an undeformed body. The second parameter of the Lamé coefficients is equal to the shear modulus ($\mu = G$) and the compression modulus can be related to $G$ and $\lambda$ with $K = \lambda + \frac{2}{3}G$. Regarding Equation (6.9) it becomes obvious that both, the shear modulus and the compression modulus, underly the necessary condition that they are positive values. The whole equation is positive because of the squared terms. If $u_{ik}$ is chosen that $u_{ll}$ disappears, only the first part remains. If $u_{ik} = const \cdot \delta_{ik}$, the second term remains. For this both, $K$ and $G$, have to be positive.
If Equation (6.7) is considered and the total differential of the free energy is taken into account, a relation of the stress tensor to the strain tensor can be derived. $dE_\mathrm{F}$

is given by

$$dE_F = K u_{ll}\, du_{ll} + 2G \left( u_{ik} - \frac{1}{3} u_{ll}\delta_{ik} \right) d \left( u_{ik} - \frac{1}{3} u_{ll}\delta_{ik} \right) \tag{6.10}$$

where $du_{ll}\delta_{ik}$ is equal to zero and vanishes. The total differential of the free energy can be inserted into Equation (6.7) and for the stress tensor follows

$$\sigma_{ik} = K u_{ll}\, \delta_{ik} + 2\mu \left( u_{ik} - \frac{1}{3}\, \delta_{ik} u_{ll} \right) \tag{6.11}$$

$$u_{ik} = \frac{1}{9K}\delta_{ik}\sigma_{ll} + \frac{1}{2\mu} \left( \sigma_{ik} - \frac{1}{3}\, \delta_{ik}\sigma_{ll} \right). \tag{6.12}$$

A further assumption is that the deformation is homogeneous which means that every volume of the body in case of external stress gets stressed equally. A good example for a homogeneous deformation is the deformation of a rod. In this case the relative elongation $\sigma_{zz}$ is dependent on the coefficient of elasticity and the Young's modulus $E$. The Young's modulus can be rewritten with the usage of the shear modulus and the compression modulus

$$E = \frac{1}{\frac{1}{3}\left(\frac{1}{G} + \frac{1}{3K}\right)} = \frac{9KG}{3K + G}. \tag{6.13}$$

Another parameter can be introduced - the Poisson ratio which denotes the ratio between axial and lateral strain $\nu = -u_{xx}/u_{zz} = -u_{yy}/u_{zz}$. If $K$ and $G$ are positive which is necessary in thermal equilibrium, it follows that the Poisson ration lies between $-1$ (when $K = 0$) and 0.5 (when $G = 0$) for different elastic materials. The relation of strain and stress tensor of Equation (6.12) can be rewritten as

$$\sigma_{ik} = \frac{E}{1 + G} \left( u_{ik} + \frac{\nu}{1 - 2\nu} u_{ll}\delta_{ik} \right). \tag{6.14}$$

In the special case of an isotropic body and the situation of equilibrium the following equation is valid

$$\frac{\partial \sigma_{ik}}{\partial x_k} + \varrho g_i = 0. \tag{6.15}$$

The gravity is included to keep the equation more general. Hence, the parameter $\varrho$ is the density of the body and $g_i$ the gravitational acceleration. The equation is correct, if the internal forces of the body are compensated for longer times. If Equation (6.14) is applied to the upper Equation (6.15) and the general Equation (6.5) for the strain tensor is implemented one gets

$$\frac{E}{2(1+\nu)}\left(\frac{\partial^2 u_i}{\partial x_k^2} + \frac{\partial^2 u_k}{\partial x_i \partial x_k}\right) + \frac{E\nu}{2(1+\nu)(1-2\nu)}\left(\frac{\partial^2 u_l}{\partial x_i \partial x_l} + \frac{\partial^2 u_l}{\partial x_i \partial x_l}\right) + \varrho g_i = 0. \tag{6.16}$$

A further step is to exchange $\partial^2 u_i / \partial^2 x_k$ by components of a vector $\Delta\vec{u}$ (Laplace operator of $\vec{u}$. This also changes $\partial u_l / \partial x_l = \text{div } \vec{u}$ and therefore the whole equation to

$$\Delta\vec{u} + \frac{1}{1-2\nu} \text{ grad div } \vec{u} = -\varrho\vec{g}\frac{2(1+\nu)}{E}. \tag{6.17}$$

As mentioned above, the term on the right side of the equation denotes the gravitational influence on the body. For our purpose the gravitational force is neglected and replaced by a punctual force which deforms a small part of the body. An additional assumption at this point is that the deformation is much smaller than the regarded part of the body where the force is applied. Hence, the complete body can be seen as infinite in the spatial directions and Equation (6.17) becomes

$$\Delta\vec{u} + \frac{1}{1-2\nu} \text{ grad div } \vec{u} = -\frac{2(1+\nu)}{E}\vec{F}\delta(r) \tag{6.18}$$

where $\vec{F}$ is the force which stresses the body at the origin of the coordinate system. Since an infinite body is assumed, the force has to approach zero for large distances to the origin of the coordinate system. The solution for the upper Equation (6.18), which was derived by Thomson in 1848, has to be found to gather the displacement dependent on the distance $r$ to the center of excitation. By using a solution like $\vec{u} = \vec{u_0} + \vec{u_1}$, with the assumption that the solution has to be zero at infinity, $\vec{u_0}$ becomes

$$\vec{u_0} = \frac{1+\nu}{2\pi E}\frac{\vec{F}}{r}. \tag{6.19}$$

Since the rotation of Equation (6.18) leads to $\Delta \mathrm{rot}\, \vec{u}_1 = 0$, and for infinity the condition is that $\mathrm{rot}\, \vec{u}_1 = 0$, this leads to $\vec{u}_1 = \mathrm{grad}\, \phi$, and

$$\mathrm{grad}\,(2(1-\nu)\Delta\varphi + \mathrm{div}\ \vec{u_0}) = 0 \tag{6.20}$$

which is valid at infinity. For the whole space the equation can be written as

$$\Delta\varphi = -\frac{\mathrm{div}\ \vec{u_0}}{2(1-\nu)} = -\frac{1+\nu}{4\pi E(1-\nu)}\vec{F}\ \mathrm{grad}\ \frac{1}{r}. \tag{6.21}$$

At this point another variable is introduced - $\Psi$ which is the solution of the equation $\Delta\Psi = 1/r$. In the case of no singularity, $\Psi$ becomes $r/2$ and $\vec{u}_1$ is

$$\vec{u_1} = \ \mathrm{grad}\ \varphi = \frac{1+\nu}{8\pi E(1-\nu)}\frac{(\vec{F}\vec{n})\vec{n} - \vec{F}}{r} \tag{6.22}$$

with $\vec{n}$ being a unit vector in the direction of $r$. A general result with $\vec{u} = \vec{u_0} + \vec{u_1}$ is

$$\vec{u} = \frac{1+\nu}{8\pi E(1-\nu)}\frac{(3-4\nu)\vec{F} + \vec{n}(\vec{n}\vec{F})}{r}. \tag{6.23}$$

If a force $\vec{F}$ is applied to an isotropic elastic infinite body, the displacement $u$ can be calculated. It is obvious that $\vec{u}$ is dependent on the Young's modulus, Poisson ratio and the distance to the place the force acts. The higher the Young's modulus is, the lower is the displacement. That is reasonable because the higher the Young's modulus of a body, the stiffer is the body and the more force is needed to get a similar displacement. In the case $K = 0$ for a body, the Poisson ratio reaches $\nu = -1$ and an external stress leads to zero displacement because the deformation cannot be passed through the body. To generalize Equation (6.23) the Green's tensor is introduced and the Young's modulus is replaced by the shear modulus.

This can be done because both are in relation to each other via the Poisson ration. In the end the Green's tensor $G_{ik}$ is

$$G_{ik} = \frac{1}{4\pi G}\left[\frac{\delta_{ik}}{r} - \frac{1}{4(1-\nu)}\frac{\partial^2 r}{\partial x_i \partial x_k}\right]. \tag{6.24}$$

If a force is applied to the body, the displacement $u_i$ is

$$u_i = G_{ik}(x, y, z)F_k \tag{6.25}$$

with $G_{ik}$ the Green's tensor and a force $F_k$ in direction $k$. In this work, the Green's tensor is used in a Cartesian coordinate system and can explicitly be expressed as

$$G_{ik} = \frac{1}{4\pi G r}\begin{bmatrix} 1 - \frac{1}{2b} + \frac{1}{2b}\frac{x^2}{r^2} & \frac{1}{2b}\frac{xy}{r^2} & \frac{1}{2b}\frac{xz}{r^2} \\ \frac{1}{2b}\frac{yx}{r^2} & 1 - \frac{1}{2b} + \frac{1}{2b}\frac{y^2}{r^2} & \frac{1}{2b}\frac{yz}{r^2} \\ \frac{1}{2b}\frac{zx}{r^2} & \frac{1}{2b}\frac{zy}{r^2} & 1 - \frac{1}{2b} + \frac{1}{2b}\frac{z^2}{r^2} \end{bmatrix} \tag{6.26}$$

where $b = 2(1-\nu)$ and $x$, $y$ and $z$ denote the spatial directions. This leads to $r = \sqrt{x^2 + y^2 + z^2}$. By applying a force in a specific direction it is possible to calculate the displacement at every position close to the stress origin. This derivation of the Green's tensor is the Thomson solution which is valid in case of a viscous, elastic body [103].

## 6.2 Lock-In Method and Transfer Tensor

The novel active method is introduced in this section. Since it is an active method, an external force is necessary to deform the medium or the network. In principle this is possible with an optical tweezers, a magnetic field or an external shear. In this work an optical trap, combined with tracer particles, is used to apply the deformation to the measured system. The idea behind the method is the usage of the functionality of a Lock-In amplifier [104].
In the viscoelastic medium several particles are located and connected to each other

via the medium. Due to this connection, the movement of one particle in this group leads to a response of the other particles. By analyzing the motion of all particles it is possible to gather information about the medium. Hence, the relationship of response amplitudes, phase shifts of the motion and frequency changes to higher harmonics can be determined. These information are reliant on the position of the particles and the distances to each other. Furthermore, the behavior of the medium changes when the amplitude and frequency of stress vary and also if temperature or medium properties are different. Overall there are a lot of parameters which play a role for determining the mechanical properties. In a group of particles (a group constitutes at least two particles) one particle - the reference particle $R$ - gets trapped by the optical tweezers and excited with function $f(t)$. The excitation with $f(t)$ leads to sinusoidal oscillations at specific frequency $\omega$, with an amplitude $A$ and a specific direction $\theta$. The total motion of the particle is a superposition of thermal noise and the oscillation of the optical trap. In a similar way Lock-In amplifiers work [104], the response motion of the other particles in the network is also a superposition of thermal noise and the same sinusoidal function. Dependent on the network characteristics, amplitude and frequency of the oscillation, several terms of the sinusoidal function with doubled, three-fold to $n$-fold frequencies determine the response motion. These are the higher harmonics of the systems which appear when the medium gets excited. If a sinusoidal motion is added to the reference particle, the motion of the response particle can be written as

$$\begin{aligned} s_n(t) = \frac{a_0}{2} &+ a_1\cos(\omega t) + a_2\cos(2\omega t) + ... + a_n\cos(n\omega t) \\ &+ b_1\sin(\omega t) + b_2\sin(2\omega t) + ... \\ &+ b_n\sin(n\omega t). \end{aligned} \tag{6.27}$$

In this equation $\omega$ is the frequency of excitation, $a_0$ to $a_n$ and $b_1$ to $b_n$ the Fourier coefficients for the single terms which are dependent on the $k$-fold frequency. The multiplication of the excitation function $f(t)$ with sine and cosine, and its time averaging leads to the Fourier coefficients

$$a_k = \frac{2}{T}\int_0^T f(t)\cos(k\omega t)dt = \frac{2}{T}\int_{t_0}^{t_0+T} f(t)\cos(k\omega t)dt \tag{6.28}$$

$$b_k = \frac{2}{T}\int_0^T f(t)\sin(k\omega t)dt = \frac{2}{T}\int_{t_0}^{t_0+T} f(t)\sin(k\omega t)dt. \tag{6.29}$$

The whole response function can be expressed as a sum of sines under the assumption that the series converges for longer times. With the coefficients $a_k$ and $b_k$ the relationship of response amplitudes $x_k$ and phases $\phi_k$ to the reference can be gained

$$\begin{aligned} s(t) = \frac{a_0}{2} &+ a_1\cos(\omega t) + a_2\cos(2\omega t) + ... + a_n\cos(n\omega t) \\ &+ b_1\sin(\omega t) + b_2\sin(2\omega t) + ... + b_n\sin(n\omega t) \\ = \frac{a_0}{2} &+ x_1\sin(\omega t + \phi_1) + x_2\sin(2\omega t + \phi_2) + ... + x_n\sin(n\omega t + \phi_n) \end{aligned} \tag{6.30}$$

with

$$x_k = \sqrt{a_k^2 + b_k^2} \tag{6.31}$$

$$\tan(\phi_k) = \frac{a_k}{b_k} \tag{6.32}$$

In the end the response vector in all spatial directions is

$$\vec{r}_{i\theta}(t) = \begin{pmatrix} x_{i0\theta} + x_{i1\theta}\sin(\omega t + \phi_{xi1\theta}) + x_{i2\theta}\sin(2\omega t + \phi_{xi2\theta}) + ... + x_{in\theta}\sin(n\omega t + \phi_{xin\theta}) \\ y_{i0\theta} + y_{i1\theta}\sin(\omega t + \phi_{yi1\theta}) + y_{i2\theta}\sin(2\omega t + \phi_{yi2\theta}) + ... + y_{in\theta}\sin(n\omega t + \phi_{yin\theta}) \\ z_{i0\theta} + z_{i1\theta}\sin(\omega t + \phi_{zi1\theta}) + z_{i2\theta}\sin(2\omega t + \phi_{zi2\theta}) + ... + z_{in\theta}\sin(n\omega t + \phi_{zin\theta}) \end{pmatrix} \tag{6.33}$$

In this equation $x_{ik\theta}$, $y_{ik\theta}$ and $z_{ik\theta}$ denote the amplitudes of response particle $i$ for the specific spatial direction $x$, $y$ or $z$ when the excitation direction is $\theta$ at higher harmonic $k$. The phase information for a corresponding $k$ is $\phi_{xik\theta}$, $\phi_{yik\theta}$ and $\phi_{zik\theta}$. The transfer tensor $\bar{A}_i$, which contains information about the medium, links both the reference motion and the response motion.

$$\bar{Y}_i = \bar{A}_i \cdot \bar{X}_0 \tag{6.34}$$

$$\bar{X}_0 = \begin{pmatrix} x_{011} & x_{012} & ... \\ y_{011} & y_{012} & ... \\ z_{011} & z_{012} & ... \end{pmatrix} \qquad \bar{Y}_i = \begin{pmatrix} x_{i11} & x_{i12} & ... \\ y_{i11} & y_{i12} & ... \\ z_{i11} & z_{i12} & ... \end{pmatrix} \tag{6.35}$$

with $\bar{X}_0$ the reference matrix and $\bar{Y}_i$ the response matrix of particle $i$. The number of columns of both matrices are dependent on the amount of directions the particles were excited in.

To calculate the transfer matrix the solution of the linear equation is needed. Since all different directions of excitation $\theta$ are considered for the determination of the transfer matrix, the reference motion and the response motion are formed like a

$l \times m$ matrix where $l = 3$ (number of dimensions) and $m$ is the number of excitation directions $\theta$ (Equation (6.35)). Hence, the linear equation is overdetermined because $m > l$ and cannot be solved for $A_i$. This leads to the minimum least squares solution where $\bar{A}_i$ with the smallest residual norm is determined. To gather the unique solution Equation (6.34) is transposed and left-hand sided multiplied by the reference matrix.

$$\begin{aligned} \bar{Y}_i^T &= (\bar{A}_i \cdot \bar{X}_0)^T \\ \Leftrightarrow \bar{Y}_i^T &= \bar{X}_0^T \cdot \bar{A}_i^T \\ \Leftrightarrow \bar{X}_0 \bar{Y}_i^T &= \bar{X}_0 \bar{X}_0^T \cdot \bar{A}_i^T. \end{aligned} \tag{6.36}$$

If the reference matrix is left-invertible, the matrix product can be inverted and put on the other side of the equation. In that way a unique solution is found by least squares optimization [105]. This leads to

$$\bar{A}_i^T = (\bar{X}_0 \bar{X}_0^T)^{-1} \cdot X_0 Y_i^T. \tag{6.37}$$

The transfer tensor describes the change of the excitement vector to the response vector of the particles. Regarding the transfer tensor $\bar{A}$ a further assumption was made. In general the obtained matrix $\bar{A}$ is a combination of $\bar{E}_0 \bar{A} \bar{E}_i$ with $\bar{E}$ the elastic modulus which links stress and strain. $\bar{E}$ is in general a 4th order tensor which can be minimized via symmetries in the medium. The assumption taken for the case of the transfer tensor is that the network elastic modulus is independent on the position of the particles. This holds when the network is homogeneous in the range where the particles move. For the reference particle the stress is given by the product of strain and elastic modulus $\vec{\sigma}_k = \bar{E}_k \vec{\epsilon}_k$. For $\bar{E}_0 \bar{A} \bar{E}_i$ follows $\bar{E}_0 = \bar{E}_i$ which leads to the upper used transfer matrix (Equation (6.37)) without the elastic tensors.

## 6.3 Simulations

The following simulations check that the measurement system and the idea behind the method is suitable to perform measurements at real media. Furthermore, the

simulations give insight how the method behaves for changing circumstances. The simulations are divided into two parts: one part handles simulations to test the Lock-In method. In the other part, simulations of the elastic body theory are presented.
The test system contains two particles with a reference particle fulfilling a sinusoidal oscillation of known frequency $f = 10\,\mathrm{Hz}$ with an amplitude of $a_{\mathrm{amp}} = 1\,\mu\mathrm{m}$. The sampling rate of the observing system is 5000 Hz. The values are taken from the measurements which were performed in real systems. The second particle, the response particle, moves dependent on the first particle at a specific distance to the reference. In the following cases the reference particle's phase difference to itself and the transfer matrix compared to itself are not shown because the result leads to zero respectively an identity matrix. The second particle's position is shifted $2\,\mu\mathrm{m}$ in both lateral directions and no higher modes and phase shifts are assumed. Consequently, the reference and response matrices are both $3 \times 4$ matrices with each column the oscillation in a different direction (0°, 45°, 90° and 135°) with amplitude $a_{\mathrm{amp}}$. This leads to

$$\bar{X}_0 = \bar{Y}_1 = \begin{pmatrix} a_{\mathrm{amp}} & \frac{a_{\mathrm{amp}}}{\sqrt{2}} & 0 & \frac{a_{\mathrm{amp}}}{\sqrt{2}} \\ 0 & \frac{a_{\mathrm{amp}}}{\sqrt{2}} & a_{\mathrm{amp}} & \frac{-a_{\mathrm{amp}}}{\sqrt{2}} \\ 0 & 0 & 0 & 0 \end{pmatrix}.$$

Before calculating the transfer matrix a coordinate transformation is performed. In that way the connection-line between the particles is $X^*$, orthogonal to that $Y^*$ and the vertical direction $Z^*$. In this coordinate system the reference and response matrices are

$$\bar{X}_0 = \bar{Y}_1 = \begin{pmatrix} \frac{a_{\mathrm{amp}}}{\sqrt{2}} & a_{\mathrm{amp}} & \frac{a_{\mathrm{amp}}}{\sqrt{2}} & 0 \\ \frac{-a_{\mathrm{amp}}}{\sqrt{2}} & 0 & \frac{a_{\mathrm{amp}}}{\sqrt{2}} & -a_{\mathrm{amp}} \\ 0 & 0 & 0 & 0 \end{pmatrix}.$$

Since both matrices are the same, the resulting transfer matrix $\bar{A}_1$ leads to the identity matrix. For the computations the matrix contains non-numeric values (NAN), because of the z-direction being zero. To produce comparable results, white Gaussian noise in the range of several nanometer was added to the simulations in every direction. After that the simulation was performed 50 times. For an amplitude of $a_{\mathrm{amp}} = 1$ in each excitation direction the resulting matrices $\bar{X}_0$ and $\bar{Y}_1$ are

$$\bar{X}_0 = \begin{pmatrix} 0.7071 & 1.0000 & 0.7071 & 0.000 \\ -0.7071 & 0.0000 & 0.7071 & -1.000 \\ 0.0069 & 0.0069 & 0.0069 & 0.0069 \end{pmatrix} \qquad \bar{Y}_1 = \begin{pmatrix} 0.7071 & 1.0000 & 0.7071 & 0.000 \\ -0.7071 & 0.0000 & 0.7071 & -1.000 \\ 0.0001 & 0.0001 & 0.0001 & 0.0001 \end{pmatrix}.$$

Via the upper introduced method the transfer matrix for every simulation was calculated. The resulting averaged transfer matrix is

$$\bar{A}_0 = \begin{pmatrix} 1.0000 & 5.2900 \times 10^{-8} & -2.0580 \times 10^{-11} \\ -3.0575 \times 10^{-8} & 1.000 & -3.4985 \times 10^{-11} \\ -4.7038 \times 10^{-5} & -3.2351 \times 10^{-5} & 1.0240 \end{pmatrix}.$$

The computation led to the identity matrix as a transfer matrix. This was predicted and additionally showed, that the simulation script worked properly for both the simulation without and with noise. With the added noise another important insight is gained. By the magnitude of noise added to both the reference motion and the response motion, the values in the third row of the transfer matrix can completely change and lead to unreasonable results. As examples several simulations with varying signal-to-noise ratio (SNR) for both the reference and response matrices were investigated. The start value is a SNR of 5 which leads to a motion of decades of nanometers. The end value is a SNR of 80 which is a non-resolvable noise in the sub nanometer region. Figure 6.1 shows the change of entries of the third row dependent on the ratio of SNR. If the noise of the response is lower than the reference noise, the matrix entry $\bar{A}_1^{z,z}$ is zero (for plotting at a logarithmic scale, one was added to the values), which is not correct in case of a pure rotation of the motion of the response particle or a deformation of the medium. If the noise of the response is higher (with a lower signal to noise ratio), the matrix entry increases to values in the $10^3$ range. Obviously this is not a property of the medium itself. The correct values with small variations are reached by a SNR ratio of 1. For real measurements with particles in a network these artifacts can only be decreased with varying positions in the network because the network can differ locally and therefore the values of the matrix vary a lot.

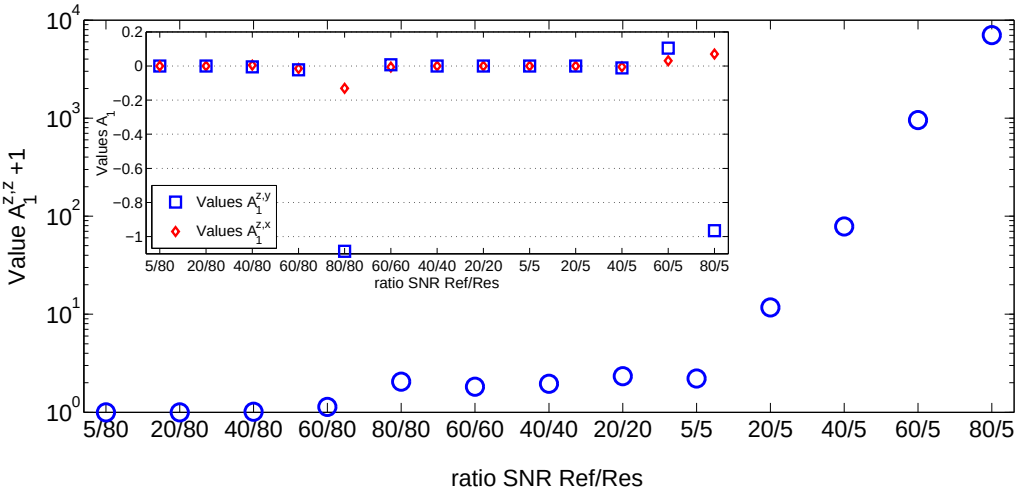



Figure 6.1: Transfer matrix values with varying magnitudes of SNR. The ratio of $\mathrm{SNR}_{Reference}$ and $\mathrm{SNR}_{Response}$ can change the values of the transfer matrix drastically. The circles (blue) show the $z, z$ value of the transfer matrix. Inset: The values of the $z, x$ (red triangles) and $z, y$ entry (blue rectangles) of the transfer tensor with varying SNR-ratios.

The force acting on a point in an elastic body leads to a deformation of the body with a displacement that can be determined dependent on the observed position. The simulation should give insight how the deformation changes due to a varying stiffness of the medium and for different magnitudes of the applied force. The results can be compared to the measurements at the *in vitro* assembled keratin network and the extracted cell. The displacement is derived via the product of the Green's tensor and the force vector.

$$G_{ik} = \frac{1}{4\pi G r} \begin{bmatrix} 1 - \frac{1}{2b} + \frac{1}{2b}\frac{x^2}{r^2} & \frac{1}{2b}\frac{xy}{r^2} & \frac{1}{2b}\frac{xz}{r^2} \\ \frac{1}{2b}\frac{yx}{r^2} & 1 - \frac{1}{2b} + \frac{1}{2b}\frac{y^2}{r^2} & \frac{1}{2b}\frac{yz}{r^2} \\ \frac{1}{2b}\frac{zx}{r^2} & \frac{1}{2b}\frac{zy}{r^2} & 1 - \frac{1}{2b} + \frac{1}{2b}\frac{z^2}{r^2} \end{bmatrix}.$$

$G_{ik}$ is the Green's tensor. Since the Possion ratio $\nu = 0.5$ is constant, the parameters which influence the displacement are the force vector $\vec{F_k}$ and the shear modulus $G$. To gather insight about the absolute displacement at a specific point, several simulations where performed with varying force and shear moduli. For all simulations the force acted at the origin of the coordinate system, and pointed to the $x$-direction. The region the displacement is observed reaches from 1 µm to 10 µm distance to the

origin in both lateral directions.

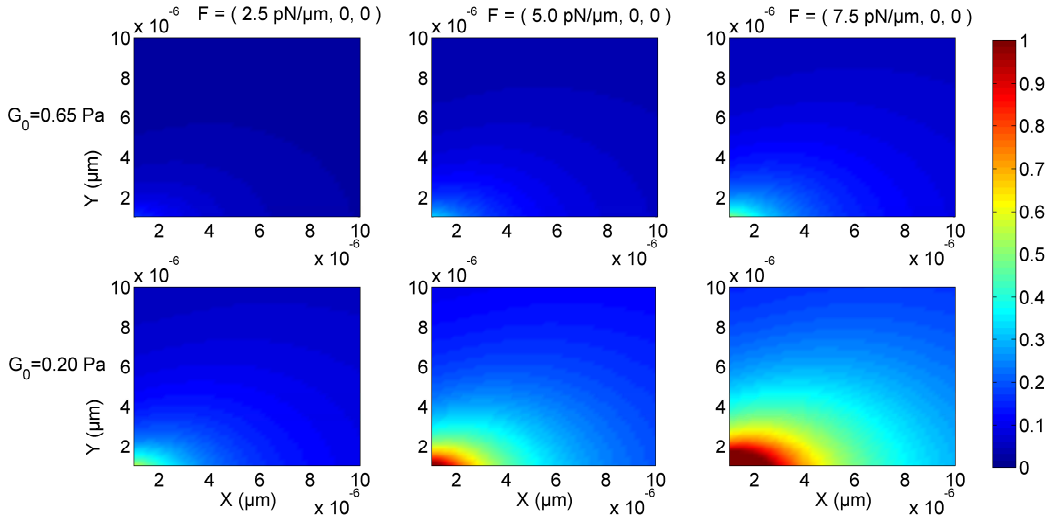



Figure 6.2: Elastic body with different forces (2.5 pN/µm, 5.0 pN/µm and 7.5 pN/µm) acting on the body of varying stiffnesses (0.65 Pa and 0.20 Pa). For each column the specific force is illustrated and for each row the specific shear modulus. For the case of a stiff medium and a low force (upper left) almost no displacement can be recognized at a distance of 2 µm. In the other case, when the force is high and the stiffness low (lower right), the displacement is more than 3 times higher as for the upper case in a distance of 10 µm. Since the force acts along the $x$-axis, the deformation in this direction is higher.

The values for the plateau moduli $G_0$ were taken from passive microrheology measurements. The high value stands for a plateau modulus close to the cell nucleus, and the low value $G_0$ for a distance of 8 µm to the rim of the nucleus. The values of the forces applied to the elastic body were taken from the calibration data of the optical tweezers. Therefore the 2.5 pN/µm refer to the optical trap with a laser power of 30 mW whereas the highest applied force was achieved by a laser power of 100 mW. As a result, the simulations show that at a stiff medium a high force is needed, so that the displacement can be measured at a distance of more than 2 µm in force direction (Figure 6.2, upper right corner). A lower force hardly displaces the medium at short distances, and even less at higher ones (upper left surface plot). For a medium of lower stiffness a strong displacement, even for higher distances, is calculated (lower row). Hence, when the force is applied at the origin of the coordinate system (here in $x$-direction), it deforms the elastic body along this axis

with an additional component of deformation in the other direction ($y$-axis). This displacement in this direction is smaller compared to the $x$-direction. In Chapter 7.3 measurements are presented which can be compared with this results.
The calculation of the displacement at a fixed position, dependent on a varying force acting at the origin of the coordinate system, is simple if the force vector has only one entry. In this case the displacement increases linearly when the force gets larger. In addition, the displacement to shear modulus dependency is reciprocal: the lower the shear modulus the higher the displacement. An interesting fact comes up if the displacement is observed when the force is directed in other directions, too. By adding only a small force, the displacement changes at a fixed point in a significant way. Figure 6.3 shows the results of the simulations.

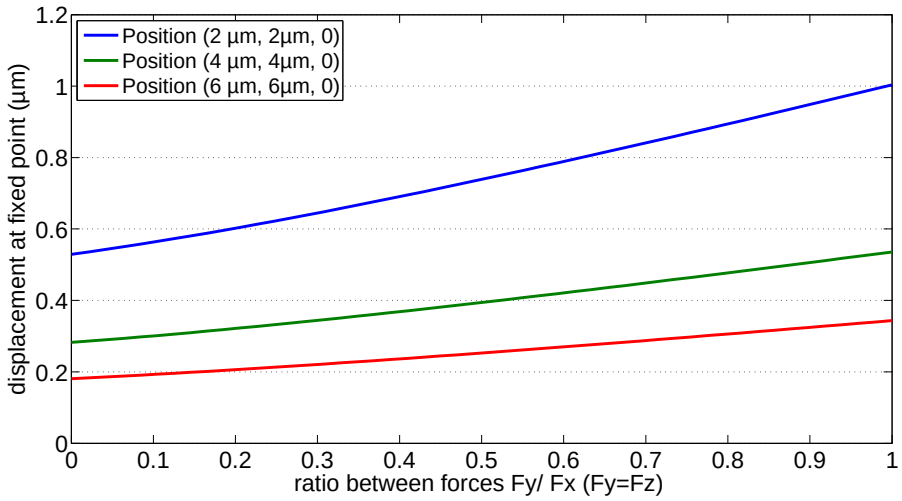



Figure 6.3: Displacement dependent on the ratio of forces acting in lateral directions. The forces in $y$ and $z$ directions are equal, but the ration toward the force in $x$ direction varies. Three positions are shown: P at (2,2,0) in blue, P at (4,4,0) in green and P at (6,6,0) in red. Even when only a small force is acting in an additional direction, the overall displacement enlarges.

The displacement increases when the ratio between the forces increase. With regard to measurements, where the optical trap applies a force in one direction on a particle, the response due to the network might change in direction. Particles at a specific distance then are affected by a force which is not only along one axis. This has to be considered for the comparison of the measurement and the theoretical displacement.

With the displacement of the reference particle during a measurement one can calculate the force on this particle or the medium. That leads (by assuming an isotropic and elastic body) to a displacement of a response particle at a specific point. Via the Lock-In method the theoretical transfer tensor can be compared with the measurements, shown in Chapter 7.

# 7 Applications of the Developed Tools

## 7.1 Sample Preparation and General Parameters

The preparation of the samples is described in this section. For the measurements on the one hand *in vitro* assembled keratin 8/18 networks were produced and on the other hand extracted pancreatic cancer cells were prepared. The first part contained the synthesis and purification of human keratins K8 and K18. The purification as well as the synthesis process were performed in the DKFZ in Heidelberg. The details are described by Herrmann et al in [106], [38]. To obtain an *in vitro* assembled network of K8 and K18, an equimolar mixture of K8 and K18 had to be dialyzed. Keratin 8/18 was stored at 5 mM Tris, 8 M Urea, 1 mM EDTA, 0.1 mM EGTA and a pH 7.5 at −80 °C. Before use it had to be dialyzed to 2 mM Tris, 1 mM DTT and pH 9 in order to enable assembly. Especially the Urea had to be removed. The exact steps in which the dialysis was performed [107], can be seen in the following table.

Table 7.1: Preparation methods for the dialysis.

| Dialysis | |
|---|---|
| Old preparation method (all pH 8.5) | New method (all pH 9.0) |
| 4 M Urea, 10 mM Tris, 2 mM DTT<br>2 M Urea, 10 mM Tris, 2 mM DTT<br>0 M Urea, 10 mM Tris, 2 mM DTT<br>2 mM Tris, 1 mM DTT, pH 9<br>at 4°C overnight | 8 M Urea, 2 mM Tris, 1 mM DTT<br>6 M Urea, 2 mM Tris, 1 mM DTT<br>4 M Urea, 2 mM Tris, 1 mM DTT<br>2 M Urea, 2 mM Tris, 1 mM DTT<br>1 M Urea, 2 mM Tris, 1 mM DTT<br>0 M Urea, 2 mM Tris, 1 mM DTT<br>2 mM Tris, 1 mM DTT<br>at 4°C overnight |
| Endbuffer | 2mM Tris, 1mM DTT, pH 9 |

There are two dialysis protocols which were used during this work. Both of them

lead to the same assembly of intermediate filament networks. The first method was used for the passive microrheology measurements. In the meantime, the preparation steps were changed, and the active microrheology measurements were performed after dialysis with the new method. After these steps the assembly was ready to start, which was achieved by the addition of an equal volume of 2 x assembly buffer (20 mM Tris, pH 7.0). In that way a filament network was obtained by waiting long enough (approx. 1 h). The network was an entangled network without the addition of $MgCl_2$. If the salt of an amount of $0-2$ mM $Mg^{2+}$ is added to the K8 and K18 solution, the network became cross-linked. The K8/K18 solution for all measurements was chosen to be at a concentration of 0.5 mg/ml, as determined by the Bradford test [85], [4].

For the measurements at the extracted cells, the cells of type Panc-1 of pancreatic carcinoma cells (American Type Culture Collection, Manassas, Va, USA) were grown on a cover-slip and splitted two days before the measurement. At the day of the measurement, the cells were prepared and hence all non-keratin components were extracted. For the details and the protocol the reference is [25]. For the passive and active microrheology measurements polystyrene particles with a diameter of 1 µm (Cat No. 4009A , Thermo Fisher Scientific, Waltham, MA, USA) were added to gather 1% of weight. Concerning the *in vitro* assembled K8/K18 networks the mixed suspension was put on a glass slide for filament assembly with the particles which later were embedded in the assembed network. After that either the cells on the cover slide or the assembled networks were placed in the sample holder. The sample was sealed with a PDMS ring or layer prepared for the measurements. The stainless steel ring of the sample holder closed and fixed the chamber.

In both types of measurements - the passive and active method - the high-speed camera recorded at a sample-rate of 5000 Hz, and measured from 1 to several seconds dependent on the screen size. The trajectories were determined out of recorded pictures via a particle tracker algorithm described in [108]. The temperature was always room temperature at about $T = 23\,^{\circ}\mathrm{C}$ and the illumination intensity together with the screen size (51.2 µm×51.2 µm) was chosen to be constant during all measurements. The sections, where the measurements of the specific systems are presented, give additional information about the values of the used parameters.

After a measurement of either filaments or extracted cells the samples were fixed with an equal volume of 2.5% glutaraldehyde and 1% saccharose in filament buffer (10 mM Tris, 0.5 mM DTT, pH 7.4). To ensure that the network could be displayed at the electron microscope, the samples had to be dried in advance. Therefore, the samples were first contrasted with Osmium and washed with PBS. After that

by a gradually dehydration in 30%, 50%, 70%, 90% and 100% propanol steps the medium with the filament suspensions were critically-point dried (Critical Point Dryer CPD 030, BalTec, Liechtenstein). Afterwards the sample was rotary coated with a $2 - 3.5\,\mathrm{nm}$ layer of platinum and visualized with a Hitachi S-5200 inlens scanning electron microscope (Hitachi, Tokyo, Japan) [123]. The platinum coverage on the filaments and the cells helped to calibrate the electron microscope to gain the highest possible amount of details in a picture. The small grains of the $2 - 3.5\,\mathrm{nm}$ layer of platinum had to be made visible to ensure a good image quality.

## 7.2 Passive Microrheology

In this chapter the method which was introduced in Chapter 5 was applied to real microrheology applications. In these measurements particle motions in systems of different mechanical and physical properties were recorded. For all particle motions the mean squared displacement was determined and afterwards fitted with Function 5.8. The resulting fit parameters were used to calculate the dynamic shear modulus - the storage modulus and the loss modulus. In the latter section the parameters for the measurements are listed which were usually used for all measurements.
The first section shows the passive microrheology measurements of *in vitro* assembled keratin 8/18 networks. In [85], it is shown that the networks dependent on the added salt concentration $MgCl_2$ get stiffer for the storage modulus and more inhomogeneous in the mesh size. Due to the collaboration with A. Leitner, it was possible to use parts of already measured microrheology data to verify that the new method can be applied to both *in vitro* assembled and extracted cell networks. Hence, it was shown that resulting storage and loss moduli could be evaluated of the measurements. The plateau modulus $G_0$ as a second step was determined to allow a comparison between the networks of different salt concentrations. A first estimate about these was presented by Köster *et al.* [109]. The second section presents the microrheology application at pancreatic cancer cells line Panc-1. The cell measurements were performed to measure the mechanical properties dependent on the distance to the rim of the cell nucleus, and to test whether the new method is stable or not. The cells, as already mentioned above, were extracted so that only the nucleus and the intermediate filament network of these cells remained. In this way the intermediate filament network, which builds the scaffold of the cell, could be examined.

The third section shows measurements and results of measurements at human granulocyte cells. Here the addition of colchicine changes the stiffness of the cell and its motility. Passive microrheology was performed by particles which were added to stick at the membrane of these cells. In that way the stiffness of the membrane and the integrins was measured. The results could be related to the stiffness of the actin network.
Before these measurements were performed, measurements of particles in a pure viscous fluid and a fluid-like viscoelastic medium were investigated.

### 7.2.1 Well-known Media

#### Bi-distilled water

For the measurements in a purely viscous medium polystyrene particles (1 µm diameter) were put into bi-distilled water. The motions of the particles were recorded with the CCD high-speed camera. The distance to the glass surface was chosen to be larger than 8 µm to decrease the influence of the substrate. The measurement was repeated several times to get the motion of many particles and to minimize the statistical errors. The total number of particles measured at this medium was $n = 110$.

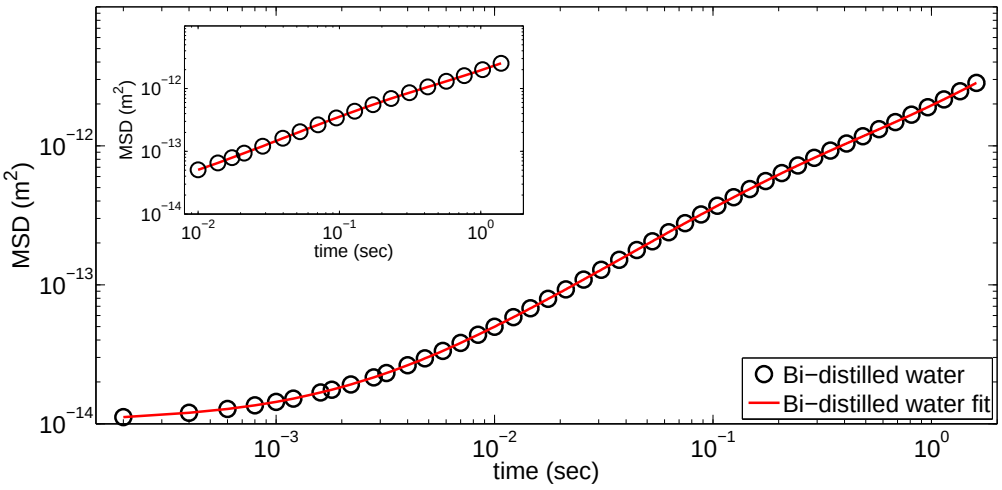



Figure 7.1: Double-logarithmic plot of the averaged MSD for particles of 1 µm diameter in bi-distilled water (circles) and its fit (red line). Inset: The MSD for a particle motion recorded at lower sample frequency (circles) and the fit (red line).

After determining the MSD of each particle, an average of all particle MSDs was calculated. This average was fitted by the fitting function (Equation (5.8)), which led to the fitting parameter $a$, $b$, $c$ and $d$. Figure 7.1 shows the resulting averaged mean squared displacement with the fitted function. For long time scales ($> 10^{-3}$ sec) the particles' MSD showed a behavior of a single relaxation time Maxwell fluid. The slope of the MSD in this regime was almost constant. At small times this was not the case, because the particle entered into the ballistic regime, where the particles moved only few steps and did not get hit by any molecules [110]. When measurements were performed at lower sample frequencies, this ballistic regime did not become obvious. By fitting a linear function at the MSD, the viscosity of the medium could be determined. This viscosity was $(1.0 \pm 0.1)$ mPa s which is in good agreement with the theoretical value at 23°C. The red line denotes the fitted curve with the fitting function (Equation (5.8)). The goodness of the fit could be derived by the residuals of the fitting function and the measured MSD. The residuals are shown in Figure 7.2.

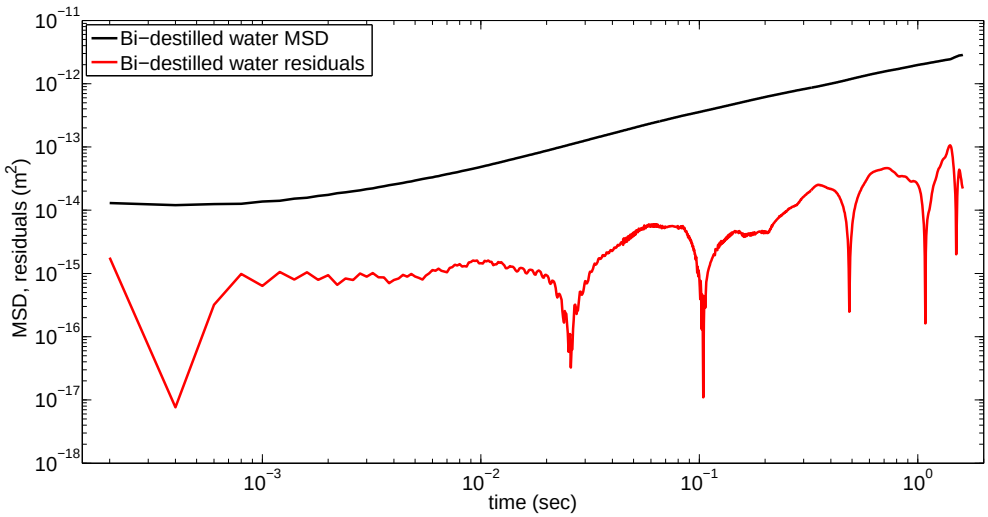



Figure 7.2: Double logarithmic plot of the averaged MSD for particles of 1 µm diameter in bi-distilled water (black line) and the residuals of fitting (red line).

In Figure 7.2 it becomes obvious that the residuals were small compared to the averaged MSD. This indicated a high goodness of the fit (GoF). The drop-downs of the residuals showed that the fitting function crossed the MSD and therefore the residual became zero. This could be achieved by the exponential functions of the

fitting parameters, which prevented the fitting function to drift off. To improve the fitting, further terms could be added to the fitting function. The physical meaning of these additional terms would have to be discussed. In addition the $R^2$ value also

Table 7.2: Results of the fitting of the MSD of bi-distilled water. A $R^2$ value of 0.9991 led to a high goodness of the fit.

| Fitting results | | |
|---|---|---|
| Goodness of fit | $R^2$ | 0.9991 |
| Fit parameter | $a$ | -4.5890 |
| | $b$ | 0.3716 |
| | $c$ | -0.7031 |
| | $d$ | 1.6500 |
| Standard Error | $\Delta a$ | 0.0174 |
| | $\Delta b$ | 0.0037 |
| | $\Delta c$ | 0.0098 |
| | $\Delta d$ | 0.0108 |

gave an idea about the goodness of the fit. $R^2$ is the ratio of the squared deviation of the fitting function to the total mean value of the MSD, and the squared deviation of the MSD to the total mean value of the MSD. If $R^2 = 1$, a perfect fit is observed. A value of zero indicates a poor fit and the fitted curve does not reflect the MSD.
At Table 7.2, the parameters give insight into the observed values of the fitting. Each fitting parameter describes the weight of the specific fitting term. The parameter $a$ was the parameter of the elastic part of the fitting function. Since this part in a viscous fluid in theory is zero, this parameter tends to be small. In Chapter 5 it is described that, for the sake of stability of the fitting, an exponential function is applied to every fit parameter. Hence the more negative a parameter gets, the closer to zero the corresponding term is. Therefore the weight of the term in respect of whole fitting function is small. With $a = -5.64$ the elastic part did not play a role for this viscous fluid. Additionally the parameter $c$ was smaller than parameter $b$, which means that the major part describing the MSD was the viscous part. Thus the measurements were in accordance with the theoretical predictions. Moreover the $R^2$ value was close to the perfect fit ensuring a high GoF.
The MSD is a sum of single terms as described in Chapter 5. Figure 7.3 shows the single terms and how their combination resulted in the fitted MSD.

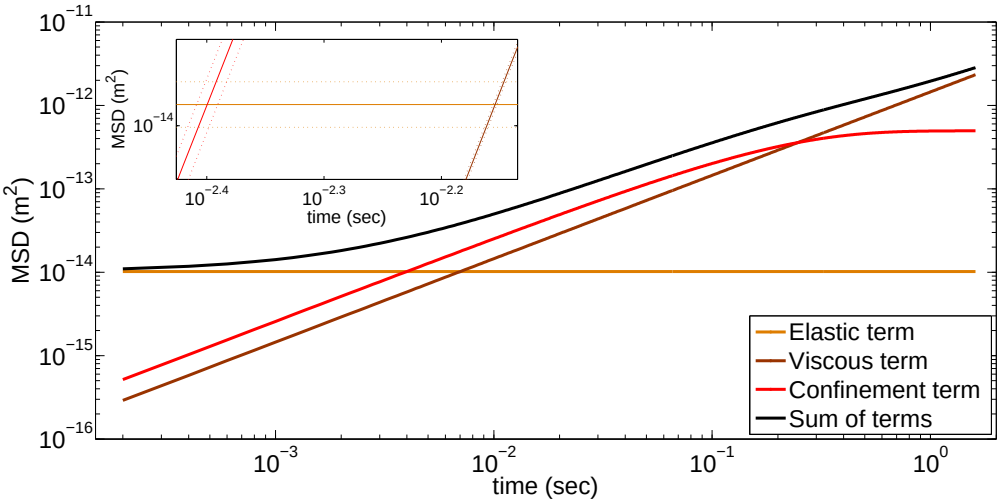



Figure 7.3: Double logarithmic plot of the single fitting terms of the MSD. The MSD (black line) was the sum of the elastic term (orange line), the viscous term (brown line) and the term corresponding to the confinement (red line). The inset shows the 95% confidence intervals for the fitting parameters beside the terms.

At low times the viscous term and also the confinement term were of low values. In this regime the constant part - the elastic term - dominated the other terms and therefore, the total MSD flattened for small times. This fitted to the ballistic regime described in [110]. At mid-time regime both the viscous and the confinement term increased linearly which led to a increasing slope of the whole MSD. At large times the confinement term got into saturation and this made the whole MSD flatten slightly until the viscous part dominated. The inset of the figure shows the 95 % confidence intervals for the parameters $a$, $b$, and the combination of $c$ and $d$. The intervals could hardly be recognized due low standard error of the parameters. For parameter $a$, the fit parameter of the elastic term, the absolute value of the term was $1.016 \times 10^{-14}\,\mathrm{m}^2$, and the intervals $1.034 \times 10^{-14}\,\mathrm{m}^2$ and $9.988 \times 10^{-15}\,\mathrm{m}^2$. For the other parameter the confidence interval was smaller.

Based on the fitting parameters of Table 7.2 and Equation (5.9) the shear modulus was determined. The storage and loss modulus ($G'$, $G''$) display the real and imaginary part of the complex shear modulus $G^*$. Since the particle in this case moved in a viscous fluid, the storage modulus in theory is zero over the whole frequency range up to the ballistic regime. In Figure 7.4 the storage modulus and loss modulus are shown at the measured frequency range.

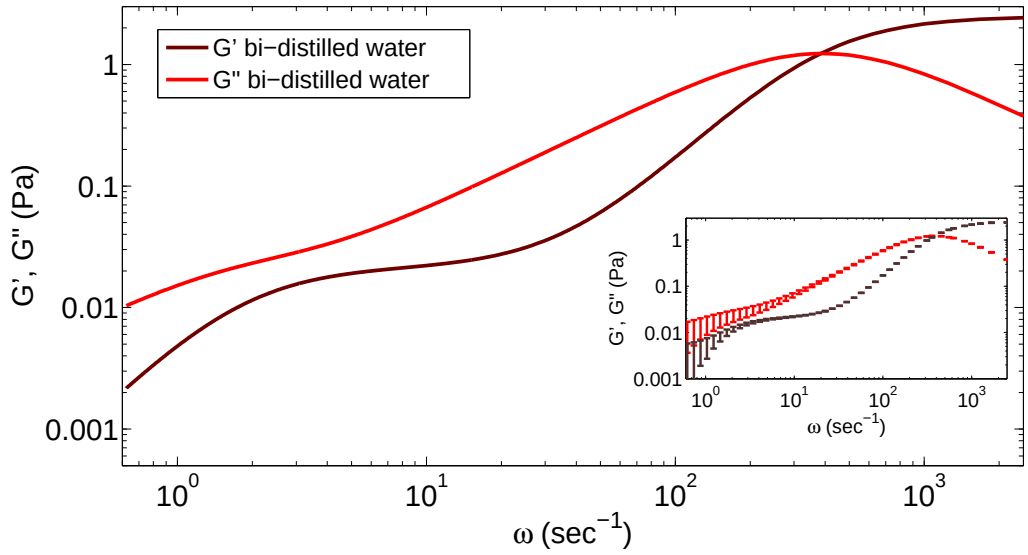



Figure 7.4: Double logarithmic plot of storage (dark red line) and loss modulus (light red line) in bi-distilled water. The inset shows values for the error of propagation dependent on the frequency.

The storage modulus (dark red) was smaller than the loss modulus over the frequency regime up to a frequency of $f = 300\,\mathrm{sec}^{-1}$. This matched to the theoretical predictions. At higher frequencies, when the ballistic regime was reached, the storage modulus ran into saturation. The loss modulus started to decrease and both moduli crossed.

Although bi-distilled water is a purely viscous fluid in theory, the measurement showed that the MSD has not a constant slope for longer times. This is due to the calculation algorithm that determined the MSD. For longer times the amount of averaged MSDs decreases. For the longest time value the averaged MSD is equal to the amount of particles measured. Therefore the uncertainty of the MSD for high times is higher compared to lower times. To reach the results of the theory, it is recommended to perform either an infinite number of measurements or measurements of infinite length (hypothesis of ergodicity). Thus, the storage modulus did not disappear completely.

Overall, the new method worked good at the experiment in bi-distilled water. This was confirmed by a $R^2$ value close to one, small residuals of the fitting function and small errors for G' and G". The next measurement was performed on a solution of saccharose - a fluid-like viscoelastic material [112].

**Saccharose solution**

In the same way as before, the particles were put into the solution of saccharose. The solution had a value of 50 % brix, with 50 g of saccharose dissolved in 100 g saccharose/water solution at a purity of 99 %. The distance to the surface was about 7 µm, and the total number of particles measured was 160. The resulting MSD was the average of each of the particle's MSD. Since it is known that the saccharose solution is a fluid-like viscoeastic material, the MSD is predicted to saturate for long times. In [112], this indirectly can be seen via the shear moduli for different solutions. The averaged MSD, its fit, and the MSD of bi-distilled water is shown in Figure 7.5.

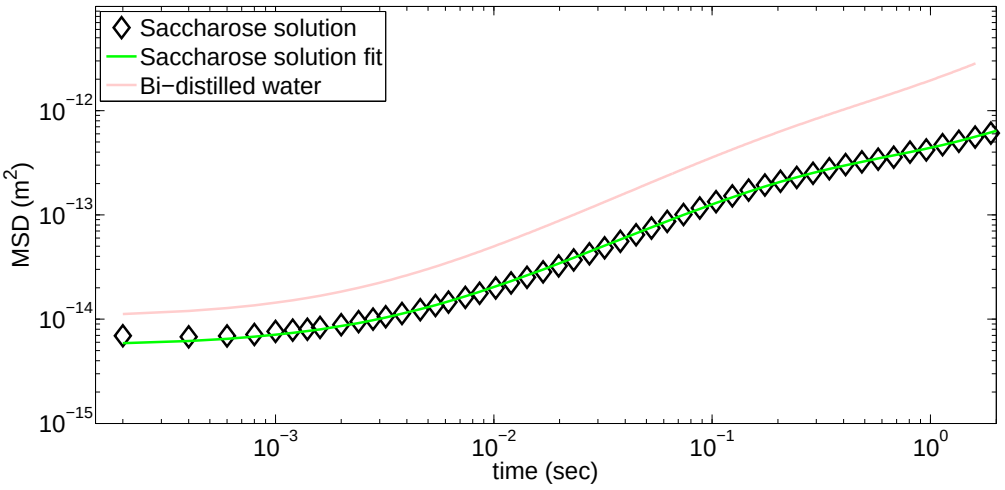



Figure 7.5: Double-logarithmic plot of the averaged MSD for particles of 1 µm diameter in saccharose solution (diamonds) and its fit (green line). The MSD of the water measurements is added for comparison.

Compared to the bi-distilled water measurements, when the slope of the MSD remained almost constant, the slope of the MSD of the saccharose solution slightly started to decrease for time values higher than 0.1 sec. This indicated a saturation which is typical for viscoelastic systems. As mentioned in Chapter 5, an additional drift or flow of the medium leads to a further increase at time scales which could not be resolved at the measurements. Hence, because of the short measurement time only the begin of the saturation/drift process was measured. Since the MSD was lower than the MSD of bi-distilled water, the saccharose solution was of higher viscosity. For short times the ballistic regime became obvious.

Via $R^2$ and the residuals of the fit, the quality of the fitting was determined. The residuals are shown in Figure 7.6.

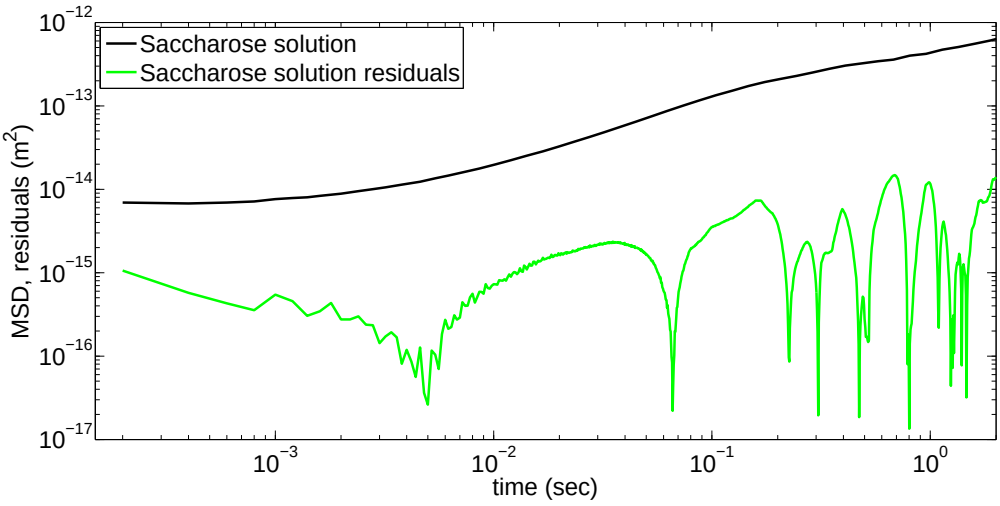



Figure 7.6: Double logarithmic plot of the averaged MSD for particles of 1 µm diameter in saccharose solution (black line) and the residuals of fitting (green line). Similar to the measurements of bi-distilled water, the residuals remained small compared to the averaged MSD.

Table 7.3: Results of the fitting of the MSD of saccharose solution.

| Fitting results | | |
|---|---|---|
| Goodness of fit | $R^2$ | 0.9988 |
| Fit parameter | $a$ | -5.1886 |
| | $b$ | -1.6179 |
| | $c$ | -1.4369 |
| | $d$ | 1.7075 |
| Standard Error | $\Delta a$ | 0.0117515 |
| | $\Delta b$ | 0.00468375 |
| | $\Delta c$ | 0.00465486 |
| | $\Delta d$ | 0.00620881 |

The residuals of the fitting were approximately two orders of magnitude smaller than the corresponding MSD. This indicated that the fitting worked fine, in the same way which was already observed at bi-distilled water. The $R^2$ value was smaller compared to water, but close to the perfect fit. This showed that the fitting also worked for a fluid-like viscoelastic medium. The fit parameter of Table 7.3 can be used to show

the weight of the single terms for the MSD. The values of the viscous term was smaller than in bi-distilled water. Hence, this led to a higher weighting of the elastic and the confinement term, which made the MSD start to saturate and to be lower in value. Furthermore, the smaller the viscous parameter was, the lower the diffusion of the particle, and the higher was the viscosity of the medium.
The total MSD and the single terms of the model-based fitting are shown in Figure 7.7

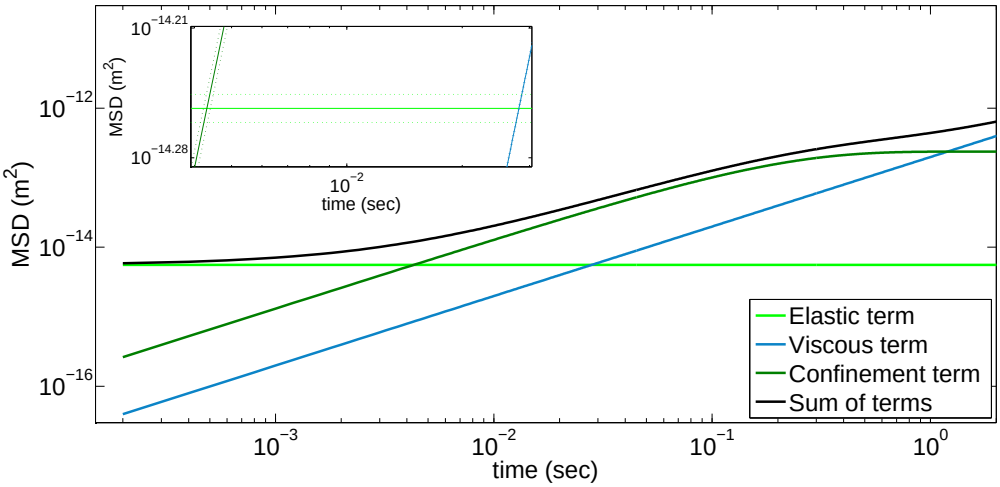



Figure 7.7: Double logarithmic plot of the single terms of the MSD. The MSD (black line) is a sum of an elastic term (light green line), a viscous term (blue line) and the term corresponding to a confinement the particle moves (dark green line). The inset shows the 95% confidence intervals around the terms.

Compared to Figure 7.3 the MSD terms showed a similar curvature. Thus, for small time ranges the elastic part dominated which was due to the ballistic behavior. For longer times the confinement term dominated which made the total MSD start to saturate. At times longer than 1 sec the confinement term remained constant and the viscous term made the total MSD increase linearly. For the determination of the long time viscosity, the viscous term was taken into account, because both the elastic and the confinement term were constant. The slope of the viscous part led to the diffusion coefficient and via the assumption that the Stokes-Einstein relation is valid, the long time viscosity was determined. For the saccharose solution the viscosity was $\eta_{LT} = (13.12 \pm 0.08)\,\mathrm{mPa\,s}$. A rough estimation at [111] led to a theoretical value of $\eta_{Th} = 13.77\,\mathrm{mPa\,s}$ at a temperature of $T = 23\,^{\circ}\mathrm{C}$ (the measured

temperature inside the solution). If a temperature of $T = 24\,°\mathrm{C}$ was assumed, the theoretical viscosity changed to $\eta_{Th} = 13.17\,\mathrm{mPa\,s}$. This led to two interpretations - on the one hand the temperature might vary locally due to the illumination light. On the other hand the theoretical value discriminates between different types of sugar (saccharose, dextrose, glucose, etc.). The reference did not clearly define for which type of sugar the calculation is valid.
Further on, with the fitting parameter the shear modulus was determined. The resulting $G'$ and $G''$ are illustrated in Figure 7.8.

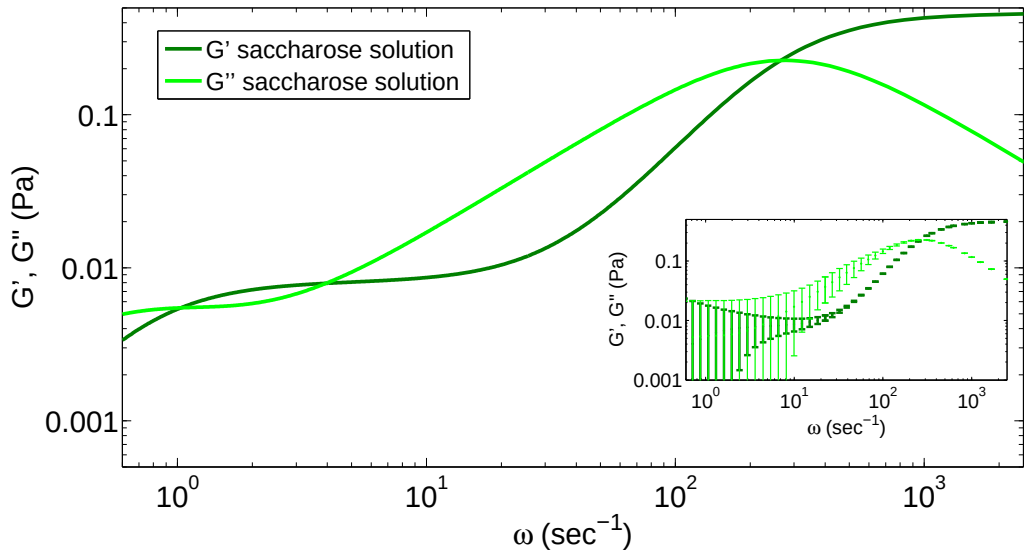



Figure 7.8: Double logarithmic plot of storage (dark green line) and loss modulus (light green line) in saccharose solution. The inset gives an insight about the propagation of error of the shear modulus.

The saccharose solution is a fluid-like viscoelastic system, and theory predicts that large parts of the storage modulus are lower than the loss modulus. In Figure 7.8 this can be seen for the mid-frequency regime. At high frequencies both the storage and loss modulus showed the typical behavior of a medium in the ballistic regime. The loss modulus decreased to zero whereas the storage modulus stayed constant. At lower frequencies the storage modulus reached a plateau which indicates the presence of a viscoelastic material. The plateau of the storage modulus was at a frequency of 5 Hz with a measured value $G_0 = (0.008 \pm 0.003)\,\mathrm{Pa}$.
These measurements at well-known media showed that the new method could be applied to viscous as well as to fluid-like viscoelastic media. The observed values for

the long-time viscosity are in accordance to the theoretical values. This indicates that the system is well-calibrated and the results of the measurements are meaningful. In the next subsection the measurements at *in vitro* assembled networks are presented. Those are gel-like viscoelastic media dependent on parameters like the protein or salt concentration.

### 7.2.2 In Vitro Assembled Keratin 8/18 Networks

The *in vitro* assembled keratin 8/18 network without cross-linkers like magnesium-dichloride or plectin is an entangled network. By adding a cross-linker the former physical connection between the filaments changes to a chemical one. This change of the connections has an effect on the viscoelasticity of the whole medium, and can be described by the dynamic shear modulus. Dependent on the concentration of the cross-linker, the network changes from a soft to a stiffer one, and the mesh-size decreases. A particle embedded in the network moves in a spatial confinement which is related to the mesh-size. Thus, the motion gets more and more limited if the concentration of the cross-linker increases. Additionally the stiffness is dependent on the protein concentration used for the assembly and parameters like the temperature, assembly time and buffer viscosity. For the measurements all parameters apart from the cross-linker concentration were held constant.

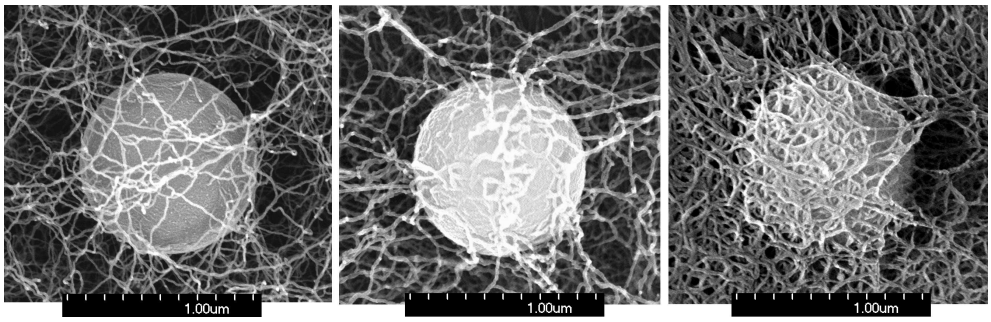



Figure 7.9: SEM images of the *in vitro* assembled K8/18 networks with a protein concentration of 0.5 mg/ml. Left: Without cross-linker. Center: 0.5 mM $MgCl_2$. Right: 2.0 mM $MgCl_2$ [40].

Furthermore, the particles' motions were analyzed with the Mason method and the results are described in [85], [40]. This section shows the results of the calculations

with the new method which used the data of the measurements of [85].
The changes in the networks depending on the cross-linker concentrations are shown in Figure 7.9. Without cross-linker the network consisted of large meshes and loose entangled filaments. The increase of the $MgCl_2$ concentration reduced the mesh-size and the filaments became chemically bound to each other. A further increase led to thick bundles of filaments which sticked together. The mesh-size reached a minimum. For the microrheology measurements the particles embedded in the network were chosen to be similar to the water and sugar measurements (a diameter of 1 µm, polystyrene as material). The particles' motion led to the MSDs, which varied for different cross-linker concentrations. The number of measured particles for each concentration was in the range of 20 to 80. The protein concentration for all measurements was constant at a value of 0.5 mg/ml.
The MSDs were fitted by Equation (5.8) and both the fits and the corresponding MSDs are shown in Figure 7.10 and Figure 7.11. Both figures reveal the MSDs for different salt concentrations. The $MgCl_2$ concentration of 0.5 mM is shown in both figures for a better understanding of the changes in the MSDs. In Figure 7.10 it can be seen that the fitting functions fit worse the higher the amount of $MgCl_2$ is, whereas the fits get better (Figure 7.11) for the highest concentrations.

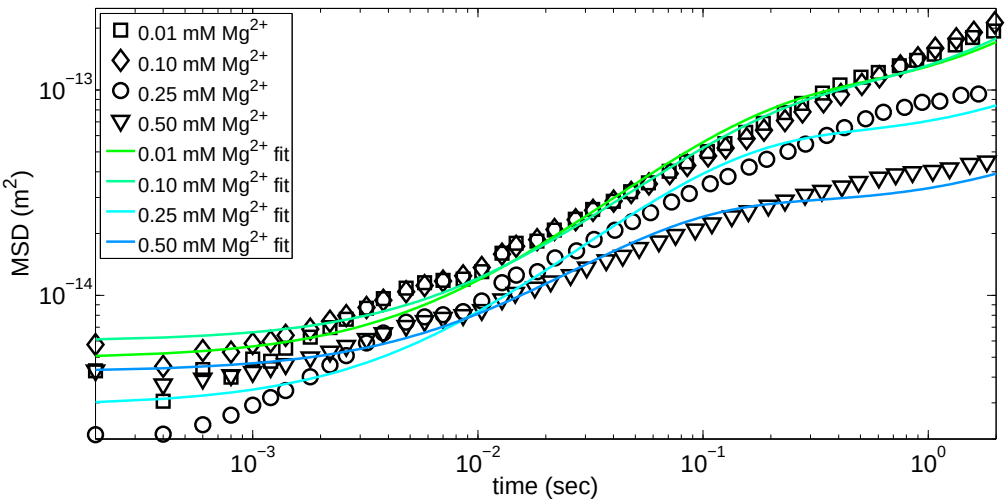



Figure 7.10: MSD in keratin 8/18 networks of varying cross-linker concentrations (part1 - up to 0.5 mM $MgCl_2$) with the corresponding fits (lines). For a lower $MgCl_2$ concentration, the MSD showed a fluid-like character. By further reducing the $MgCl_2$ from 0.1 mM to 0.01 mM the change in the MSD decreases due to the low amount of salt.

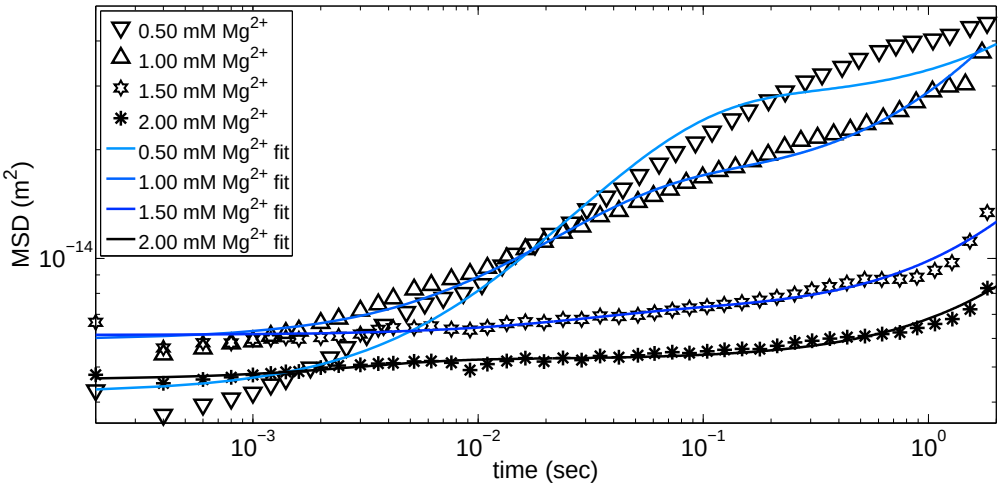



Figure 7.11: MSD in keratin 8/18 networks of varying cross-linker concentrations (part2 - up to 2.0 mM $MgCl_2$) with the corresponding fits (lines). For the highest $MgCl_2$ concentration (2 mM) the slope of the MSD becomes small. This indicates a gel-like viscoelastic behavior.

The resulting fitted functions showed a lower MSD and an earlier saturation of the MSD for higher concentrations. This means, referring to Chapter 5, that the confinement size was smaller for higher salt concentrations. Consequently, there were more cross-linked filaments, the network was stiffer and the mesh-size smaller. Table 7.4 shows the fit parameter and the standard errors. Regarding the goodness

Table 7.4: Results of the fitting of the MSD of *in vitro* assembled keratin 8/18 networks.

| Fitting results | | | | | | | | |
|---|---|---|---|---|---|---|---|---|
| $C_{MgCl_2}$ (mM) | | 0.01 | 0.10 | 0.25 | 0.50 | 1.00 | 1.50 | 2.00 |
| GoF | $R^2$ | 0.982 | 0.935 | 0.857 | 0.881 | 0.976 | 0.947 | 0.947 |
| Fit parameter | $a$ | -5.312 | -5.119 | -5.840 | -5.075 | -5.124 | -5.094 | -5.380 |
| | $b$ | -3.202 | -3.072 | -4.306 | -5.129 | -4.359 | -5.892 | -6.467 |
| | $c$ | -2.466 | -2.529 | -2.912 | -3.769 | -4.589 | -6.953 | -7.351 |
| | $d$ | 2.078 | 1.998 | 2.327 | 2.898 | 3.476 | 3.511 | 5.772 |
| Std Error | $\Delta a$ | 0.0280 | 0.0239 | 0.0377 | 0.0087 | 0.0034 | 0.0021 | 0.0017 |
| | $\Delta b$ | 0.0331 | 0.0305 | 0.0715 | 0.0888 | 0.0149 | 0.0379 | 0.0213 |
| | $\Delta c$ | 0.0293 | 0.0343 | 0.0300 | 0.0239 | 0.0071 | 0.0458 | 0.0145 |
| | $\Delta d$ | 0.0464 | 0.0540 | 0.0491 | 0.0404 | 0.0152 | 0.1004 | 0.0428 |

of the fit, the measurements showed that in the mid-regime of the concentrations

the fit is of smallest $R^2$ value. This means that Equation (5.8) did not fit to the measured data exactly, which on the one hand could be due to a low number of measurements performed for these concentrations. On the other hand an additional term in the fitting function would increase the goodness of the fit. Consequently, an additional term would reveal further mechanical properties of the observed network like a second relaxation process.
By comparing the fitting parameters with those of the saccharose solution, it became obvious that the elastic parameter was of similar value. The parameter $b$ was smaller as for saccharose, which indicated of lower slope of the MSD and therefore a higher viscosity at the keratin network. In addition to that the higher the concentration of $MgCl_2$, the smaller the slope was. The other parameters, $c$ and $d$, showed the same tendency as parameter $b$. For a higher $MgCl_2$ concentration parameter $c$ became smaller which led to lower saturation value. Vice versa the increase of parameter $d$ dependent on the $MgCl_2$ concentration was related to a decreased relaxation process.

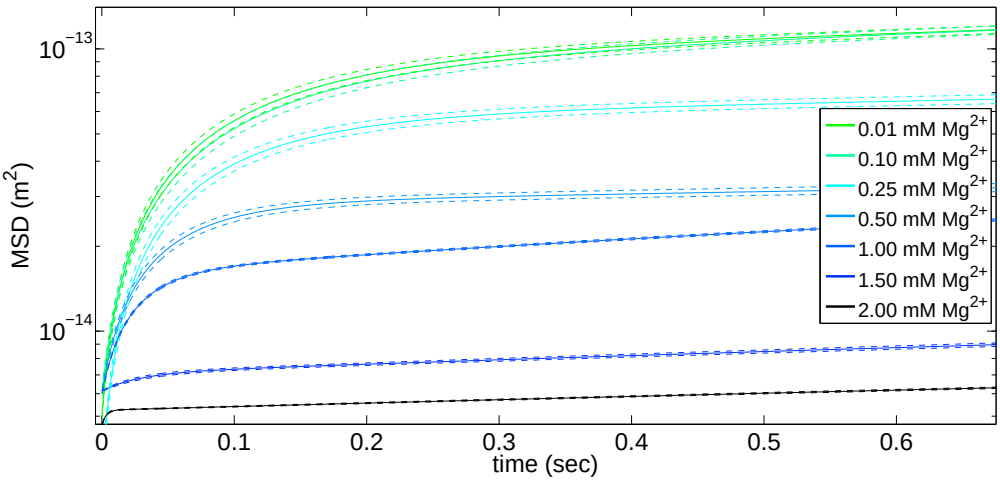



Figure 7.12: Fitting functions of the MSD of keratin 8/18 networks with 95% confidence intervals in semilogarithmic graph. The saturation behavior dependent on the salt concentration can clearly be seen in the graph. The uncertainty of the fitting parameter is denoted by the dashed lines. Between 0.25 mM and 0.5 mM $MgCl_2$ the uncertainty is higher compared to the other measurements.

In total the MSD became smaller, which consequently led to higher constraints in the motion of the particle. The confinement parameter indicated a growing stiffness of the network by increasing amount of $MgCl_2$.

The 95% threshold uncertainties are illustrated in Figure 7.12. For a concentration between 0.25 mM and 0.5 mM $MgCl_2$ the uncertainties are higher compared to the other concentrations. The higher uncertainty can be referred to a weaker fit of the MSD. To reduce this error, as already mentioned above, an additional fitting term could be applied or the number of measured particle motions has to be increased. The calculation of the shear modulus for the corresponding salt concentration leads to the information about the stiffness of the network and its diffusive properties. Hence, one obtains the storage as well as the loss modulus for varying concentrations. Figure 7.13 shows the real part of the complex shear modulus.

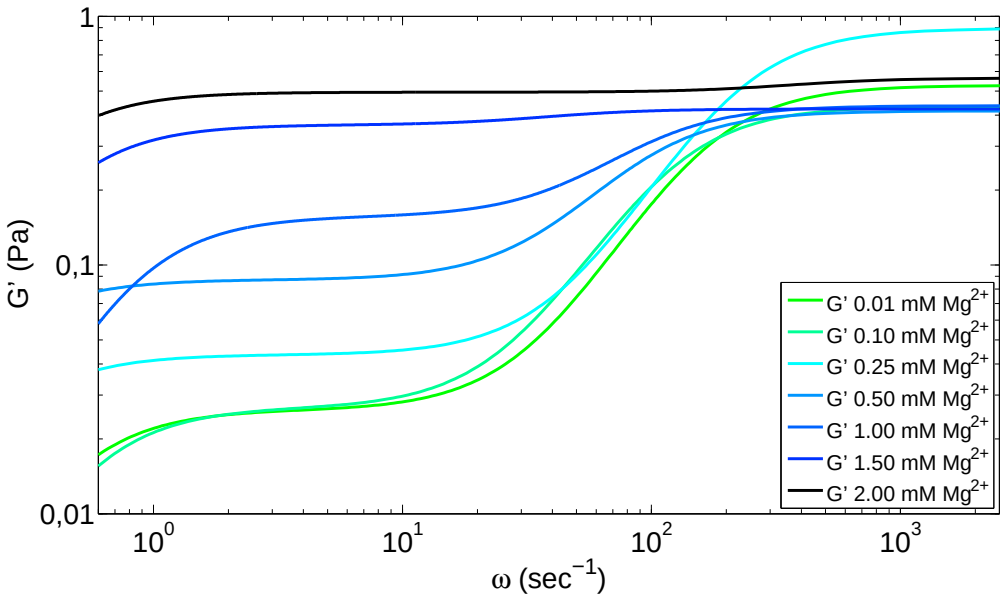



Figure 7.13: Storage moduli for varying salt concentrations. The higher the salt concentration, the stiffer is the network.

For a higher salt concentration the storage modulus increased. This can be related to the higher number of cross-links in the network (Figure 7.9) which minimized the mesh-size. Thus the particle was placed in a small confinement where its motion was tightly limited. All storage moduli showed a plateau for the frequency range of $2 - 8$ Hz. The higher the $MgCl_2$ concentration, the plateau became broader until the complete measured frequency range was at a constant value. In that way one can extract the plateau values for the keratin 8/18 networks. The values are taken

from the frequency $\omega = 5\,\mathrm{Hz}$.

$$\begin{aligned} G_0^{0.01\,mM} &= (0.026 \pm 0.056)\,\mathrm{Pa} & G_0^{0.10\,mM} &= (0.027 \pm 0.044)\,\mathrm{Pa} \\ G_0^{0.25\,mM} &= (0.044 \pm 0.073)\,\mathrm{Pa} & G_0^{0.50\,mM} &= (0.088 \pm 0.023)\,\mathrm{Pa} \\ G_0^{1.00\,mM} &= (0.151 \pm 0.005)\,\mathrm{Pa} & G_0^{1.50\,mM} &= (0.363 \pm 0.016)\,\mathrm{Pa} \\ & & G_0^{2.00\,mM} &= (0.493 \pm 0.005)\,\mathrm{Pa}. \end{aligned} \tag{7.1}$$

The plateau modulus increased for higher $MgCl_2$ concentrations, which is due to a stiffer network. The uncertainty of the plateau decreased, the higher the stiffness of the plateau was. For low concentrations the uncertainty reached a maximum, which as mentioned above can be related to a missing fitting term. Compared to the Mason method (data shown in [85]) the plateau moduli were in accordance to each other at lower concentrations. At higher concentrations the Mason method overestimated the plateau value. The frequency ranges $G_0'$ was located were similar for both methods (1 Hz - 3 Hz versus 2 Hz - 8 Hz).
The loss modulus of the measurement gives insight into the diffusive properties of the network. The figure 7.14 shows the loss moduli in relation to the concentration of $MgCl_2$.

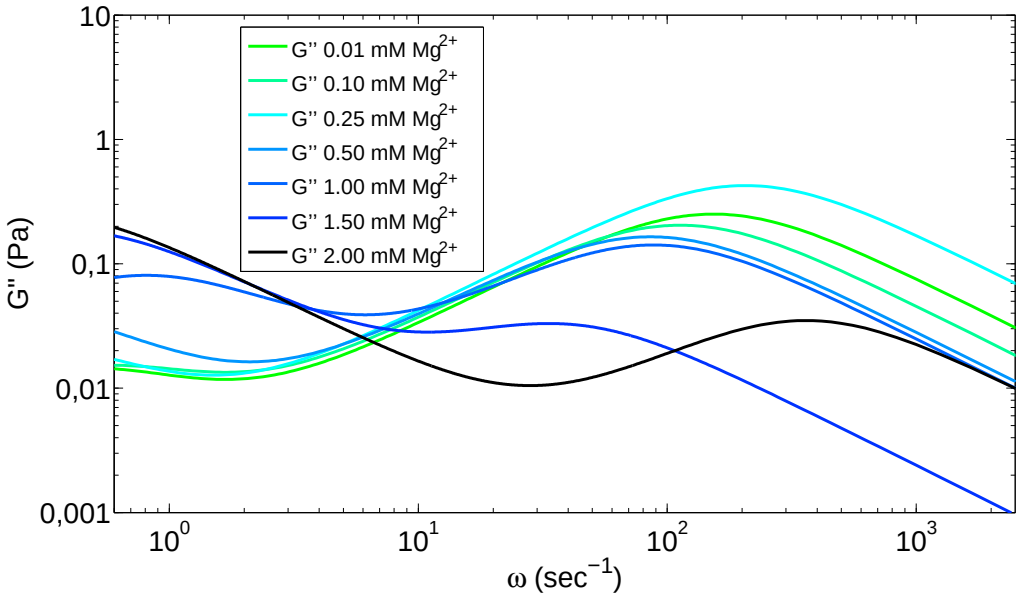



Figure 7.14: Loss moduli for varying salt concentrations.

The minimum of $G''$ shifted to higher frequencies when the $MgCl_2$ concentration increased. This was already observed for actin networks [113]. Regarding the simulations described in Chapter 5, the ratio of confinement size and drift changed at the higher concentrations. This made the minimum shift towards higher frequencies. Consequently, the higher the repelling force, the higher the frequency of the minimum of $G''$ was. This is in accordance with a higher stiffness of the network.
The loss modulus of high salt concentrations was lower than the storage modulus over the complete measured frequency range. In theory this is the case for gel-like viscoelastic material. For 0.01 mM $MgCl_2$ the relation between storage and loss modulus was similar to the measurements of the saccharose solution and therefore this network can be described as a fluid-like viscoelastic medium. This can be seen in the following figure.

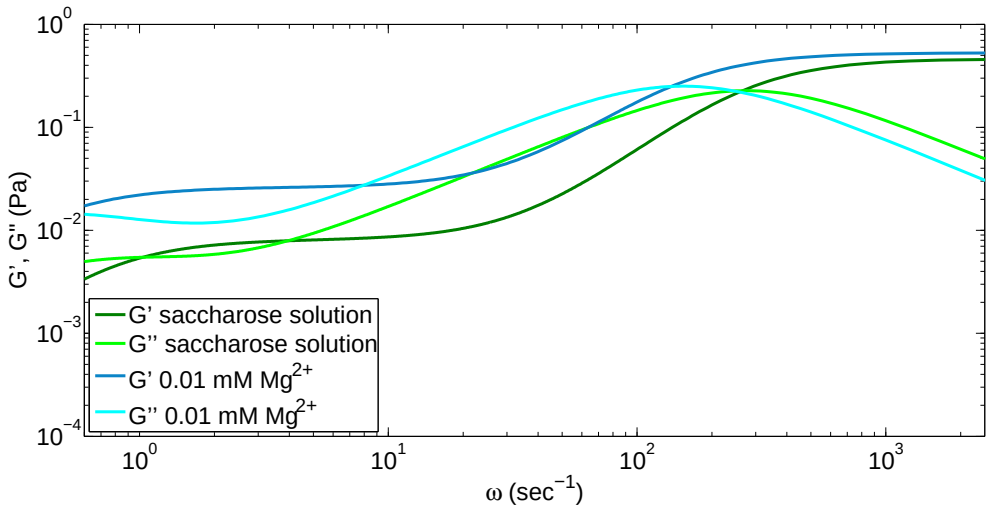



Figure 7.15: Comparison of the shear moduli. The storage and loss modulus of the 0.01 mM $MgCl_2$ concentration is compared to the shear moduli of saccharose.

The figure shows that both the saccharose solution and the keratin 8/18 assembly at 0.01 mM $MgCl_2$ behave like a fluid-like viscoelastic medium. The assembled keratin network is, since there are cross-links, stiffer than the saccharose solution.
The comparison to the simulations of Chapter 5 leads to theoretical confinement sizes of cages where the particle is located. For low concentrations therefore the confinement size is larger compared to high salt concentrations. The comparison of the simulations and the measurements were performed at a high salt concentration of 2.00 mM $MgCl_2$. The fitting of the MSD leads to a value of fit parameter $d = 5.77$.

With the value determined at Equation (5.18) of Chapter 5 the confinement size is $l = 60.89\,\text{nm}$ for ellipsoidal shape. This value can be used for a Brownian motion simulation in a confinement with additional repelling force and drift of the network. The resulting parameters with the best agreement in $G'$ and $G''$ were

Table 7.5: Results of the comparison to the simulated Brownian motion.

| Confinement size | | |
|---|---|---|
| $l_x = 0.065\,\mu\text{m}$ | $l_y = 0.065\,\mu\text{m}$ | $l_z = 0.09\,\mu\text{m}$ |
| Drift | | |
| $d_x = 0.045\,\mu\text{m}$ | $d_y = 0.045\,\mu\text{m}$ | $d_z = 0.045\,\mu\text{m}$ |
| Repelling force | | |
| $k_x = 2.0\mu\text{N/m}$ | $k_y = 2.0\,\mu\text{N/m}$ | $k_z = 2.0\,\mu\text{N/m}$ |
| Other | $\eta$<br>$T$ | $0.2\,\text{mPa s}$<br>$296.15\,\text{K}$ |

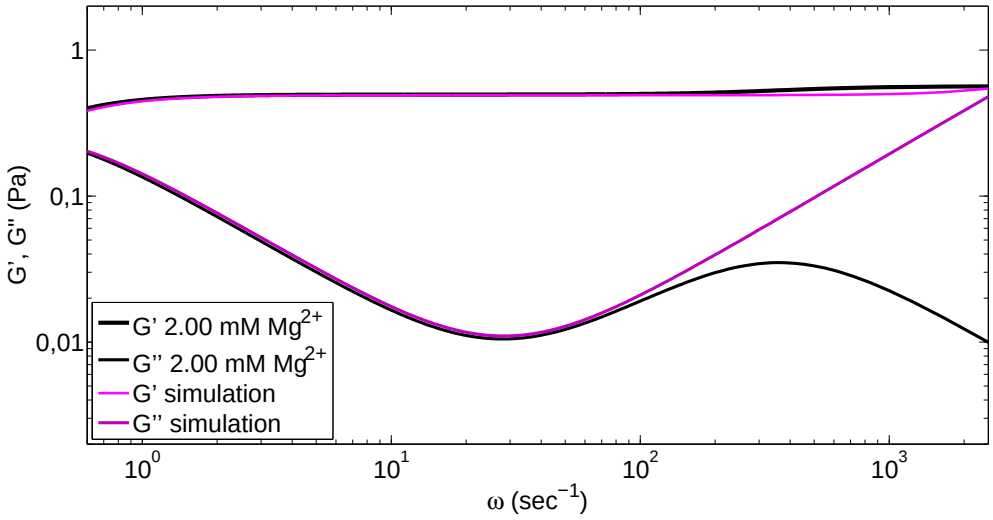



Figure 7.16: Comparison of a Brownian motion simulation in an elliptical confinement with the measurement.

In Figure 7.16 the resulting storage and loss moduli of the simulation and the measurement can be seen. The good agreement for low frequencies showed that the method can be used for achieving insight into values like the confinement size or the viscosity of the system. At high frequencies the simulation was not in accordance to the measurement because the ballistic behavior was not included so far. Another

interesting fact of the simulation in this case was a low value for the viscosity. It was unclear whether there is another combination of simulation parameters which also agree to the measurement and the viscosity is in the same order of magnitude as the buffer fluid. In addition to that, the simulation worked best for an anisotropic confinement. The motion in $z$-direction was small compared to the other directions. This indicates that for high magnesium concentration the networks collapse and therefore the mesh-size gets small.
In conclusion, it was shown that the fitting method works for the *in vitro* assembled keratin 8/18 networks. In the case of a fluid-like medium and for a gel-like medium it shows the correct physical meaning in sense of a higher loss modulus over for a mid-frequency range and vice versa. In the intermediate range, where the medium changes from fluid-like to gel-like, an additional parameter should be taken into account which further improves the fitting of the MSD and leads to more insight into the network mechanics. First tests of a modified viscous term showed an improvement of the fitting. The idea, that also the confinement moves in a viscoelastic medium, leads to a second exponential fitting term. Further tests will be performed on this issue.
The comparison of the plateau moduli of both the Mason and the new method showed similar results for low frequencies, whereas at higher frequencies the Mason method overestimated $G_0'$.

### 7.2.3 Pancreatic Cancer Cells

Pancreatic cells of line Panc-1 were measured with the passive microrheology method. The goals of these measurements were on the one hand to gather information about the mechanical properties of the intermediate filament network of the cytoskeleton, and on the other hand to test whether the method introduced in Chapter 5 was applicable to this kind of system.
Before the measurements were performed, the particles of 1 µm diameter were put into the medium, where the cells were located. The cells were splitted before ([114]) and ingested the particles via phagocytosis. This procedure took 48 hours and after that the particles were embedded in the cell intermediate filament network. At the day of the measurement the cells were extracted so that only the cell nucleus and the intermediate filament networks remained with the embedded particles. The extraction was performed in steps according to [25]. The goal to gather information

about the network stiffness in general is dependent on the density of the network. This dependency varies by the distance of the particle to the rim of the nucleus. In Figure 7.17, a picture of an extracted cell is shown (electron microscope, SEM). To allow the imaging of the extracted cell, it had to be prepared for the electron microscope. This preparation is described in Section 7.1. Figure 7.17 shows the cell nucleus in the center with the keratin network around it. Particles of 1 µm diameter are embedded in the network, and are located at different distances to the nucleus.

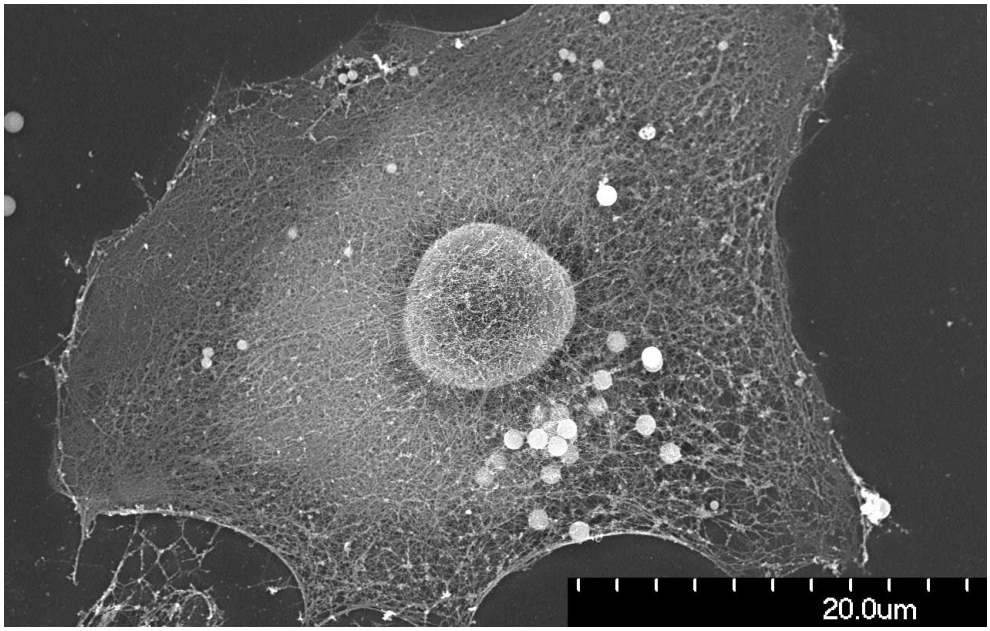



Figure 7.17: Electron microscope image of an extracted cell of line Panc-1.

An important issue for the measurements of cells is that the network changes if the cell moves. Therefore the density of the network differs from cell to cell dependent on the direction of movement and the arrangement of the network because of external stress [115]. Figure 7.18 shows an overview of several cells and the constitution of their networks. When the particles are embedded inside the network, the mesh-size has to be larger than the particle size. That is an assumption behind the theory of passive microrheology. Only if this assumption holds, the network around the particle can be seen as a continuum. The particles shown in Figure 7.18 are located in the network, but only for two of them a measurement would lead to reasonable results. Because of the invisibility of the network, it is complicated to decide during the measurements whether the particle is surrounded by the network. Correlative microscopy, where the measured particle is identified afterwards in the electron

microscope, solves this problem. Up to now the preparation for electron microscopy removes more than 50 % of the cells ([116]) and makes it difficult to improve the measurements with the help of correlative microscopy.

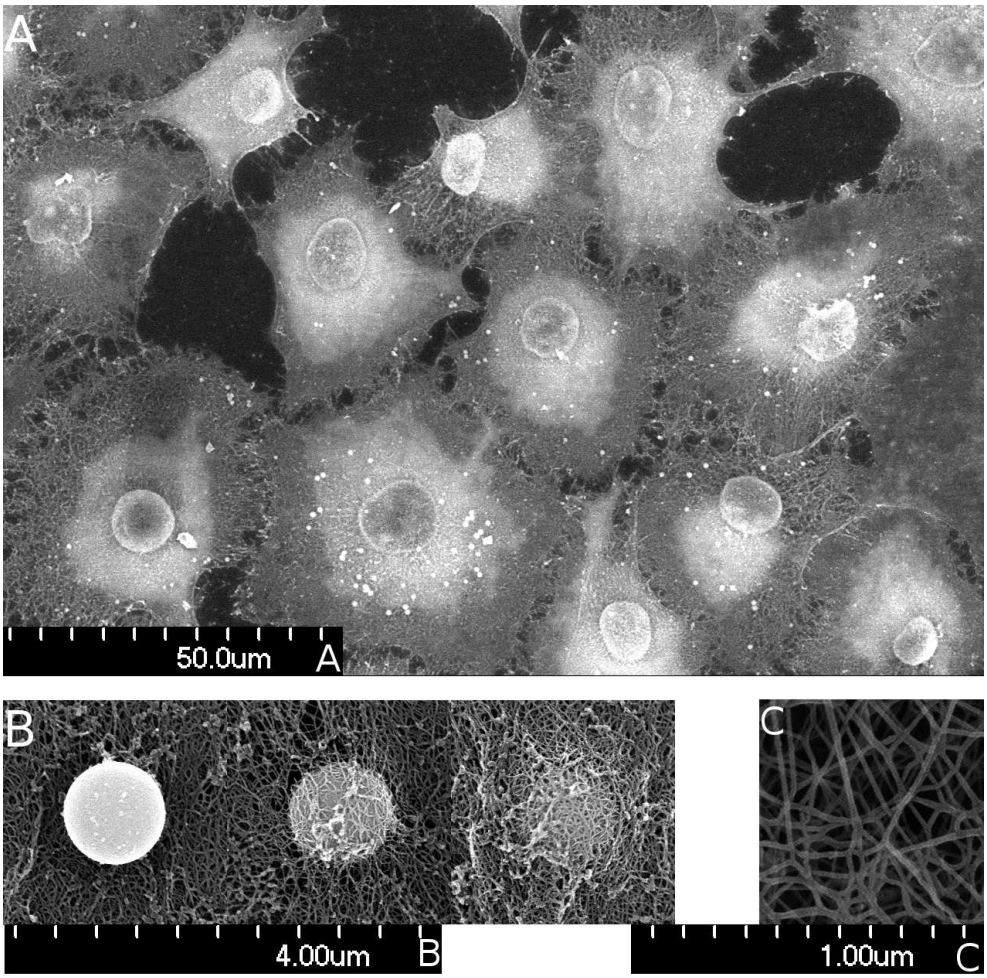



Figure 7.18: Electron microscopy image of extracted cells. A) The network constitution is different for every cell. This depends on the direction of motion as well as on the external stress applied to the cells. B) The particles embedded in the cell network. The deeper the particle is inside the network, the better are the results of microrheology measurements. C) Cell intermediate filament network without remaining agglomerates of the extraction process which disturbs the measurements.

In Appendix A the method and its drawback are described. For the cell measurements presented in this chapter, the motion of a large number of particles was

analyzed and its result averaged.
As mentioned above the motion of the particle is dependent on the distance of the particle to the rim of the nucleus. Since the networks assembles radially around the cell nucleus, a cylindrical coordinate system was chosen instead of the Cartesian. In this coordinate system the cell nucleus is located in the origin and the particles' motion is determined by the radial, tangential and vertical motion. Thus, each particle motion was transferred into the cylindrical system, and afterwards the calculation of MSD and the shear moduli was performed. This is reasonable when a radial constitution of the cell network is assumed. The extracted cell network in Figure 7.19 consists of radial and tangential components, and therefore confirms this assumption.

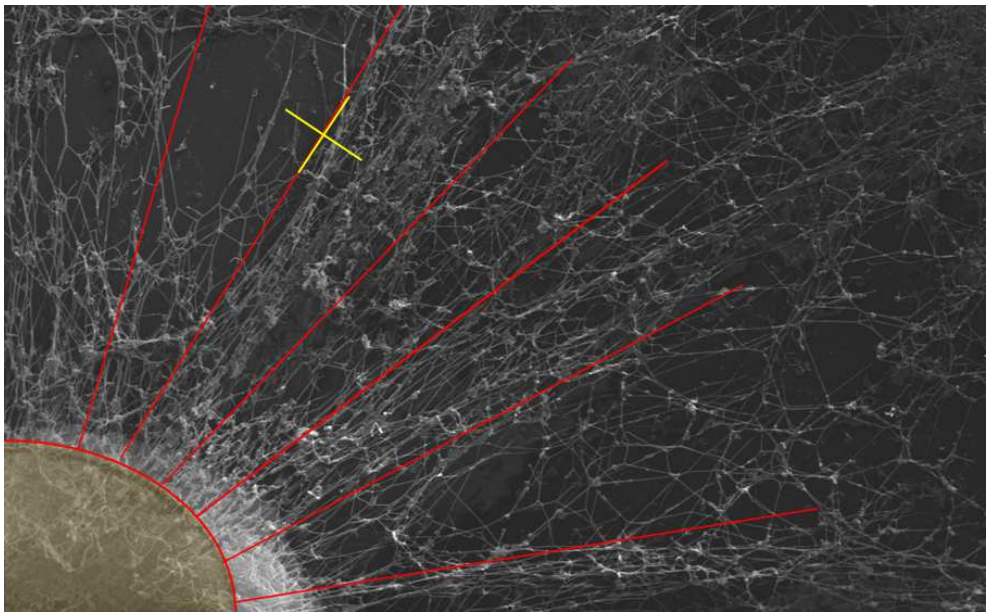


Figure 7.19: Electron microscope image of an extracted cell showing the radial alignment of the intermediate filament network.

The yellow transparent area marks the cell nucleus, whereas the red lines show the radial alignment of the filaments in the network. Hence, the radial component is the x-direction and the tangential component is the y-direction (yellow cross). The vertical direction (z-direction) is perpendicular to the other directions. The radially stressed network refers to the motion of the cell, and due to the directed assembly of the cell network. This is a difference to the *in vitro* assembled networks which are randomly assembled.
During the measurement the particle position and the distance to the nucleus rim

was recorded. Distances between 1 µm and 30 µm were observed. As in the previous sections the trajectory of the particles lead to the MSD which was fitted by the fitting function of Chapter 5. The higher the number of measurements, the less uncertain the resulting shear moduli are. Therefore, a high number of particle were tracked (> 900), and categorized into distances to the nucleus. Figure 7.20 shows a histogram with the number of particles divided by distance.

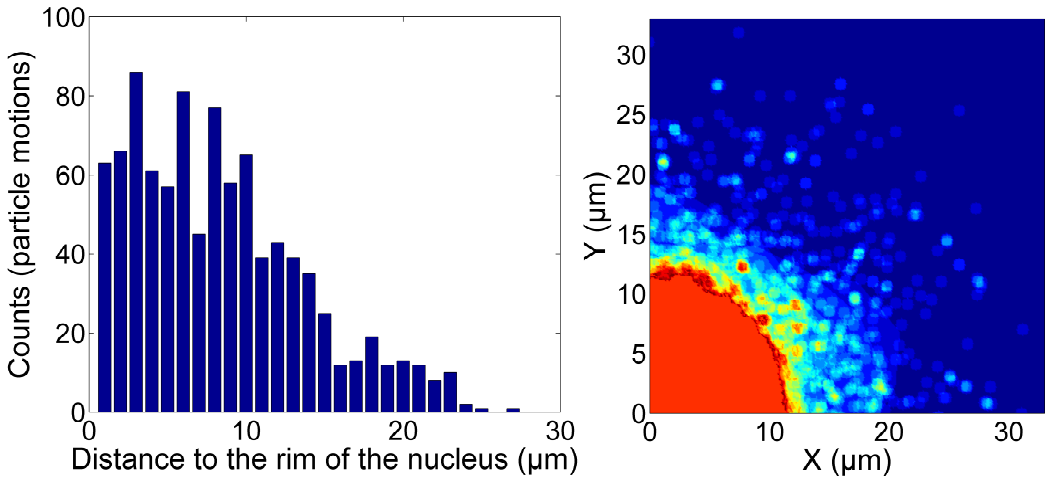



Figure 7.20: Sum of particle positions located in the cytoskeleton. Left: A histogram gives an overview of all measured particle motions dependent on the distance to the nucleus. Right: The cell nucleus (orange) and the counted particles inside one quarter of the cytoskeleton. The number of particles close to the nucleus is higher than for growing distances.

In Figure 7.20 the total number of measured particles is shown in a histogram. The distance of 30 µm was divided in 1 µm steps. The right picture is a superposition of all measurements the cell nucleus and its particles. For this an overview picture of each measurement was taken, the nucleus centered and all images superimposed. In that way an overview picture about the particle locations was created. It can be seen that the number of particles, that are located close to the cell nucleus, is higher than the number of larger distances.
For passive microrheology the trajectories were determined with the same method compared to the latter sections. Thus, 1 µm particles of polystyrene were embedded in the network and its trajectory recorded at a frame-rate of 5000 Hz for few seconds. After particle tracking a coordinate transformation was performed as ex-

plained above. Similar to the distribution of the histogram, the calculated MSD were separated into groups dependent on the distance to the rim of the nucleus. After the calculation of the single particle MSDs, an averaged MSD was determined for every group. Those MSD were used for the fitting with Equation (5.8) and the determination of $G'$ and $G''$.
The next Figures (7.21, 7.22 and 7.23) show the averaged MSDs with the corresponding fits. The MSD of distances larger than 12 µm are not included. Since the diameter of the cell in general is between 40 µm and 50 µm, and the nuclei diameter accounts for 10 µm to 20 µm, the network only exceptionally spans over higher distances than 15 µm to 20 µm. This exception occurs in case of a stretched network, which happens when the cell is stressed by an external force. The number of particle measured at these distances was low, so that the data was disregarded. The first figure shows the averaged MSD for particles close to the nucleus (up to 4 µm).

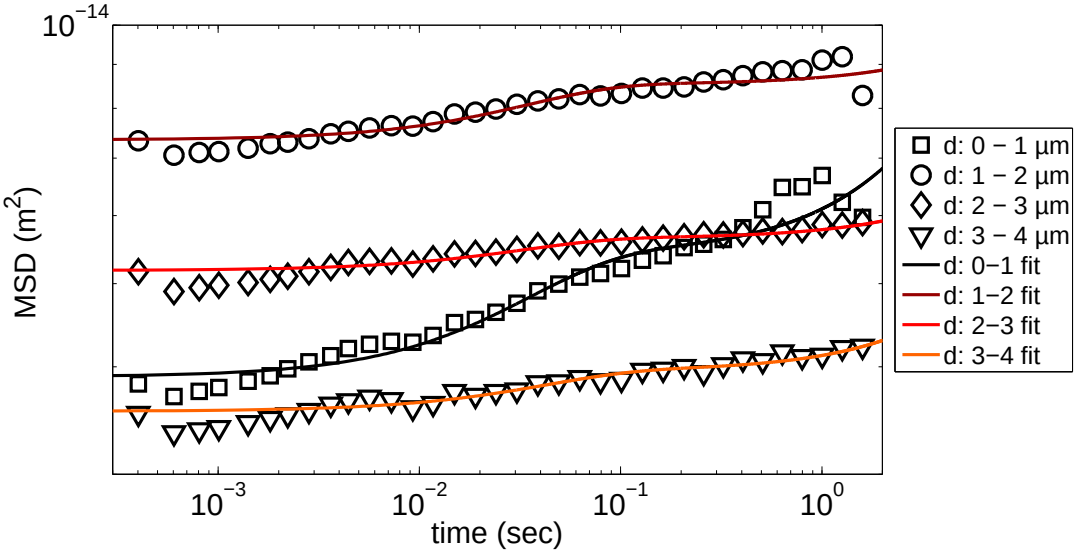



Figure 7.21: MSD in extracted cell keratin 8/18 networks with varying distances to the rim of the nucleus (part1 - up to 4.0 µm distance) and its corresponding fits (lines).

The MSD increased between the first two steps ($0 - 1\,\mu m$, $1 - 2\,\mu m$ ). After the second step the MSD decreased, which could be related to a smaller confinement the particle moved in. Since the slope of all MSDs, apart from close to the nucleus, were low compared to those of saccharose, a network which is gel-like viscoelastic can be assumed. The MSDs for larger distances (Figure 7.22) increased until a maximum

in value could be recognized. This indicated that the particles' motions were less limited by the network.

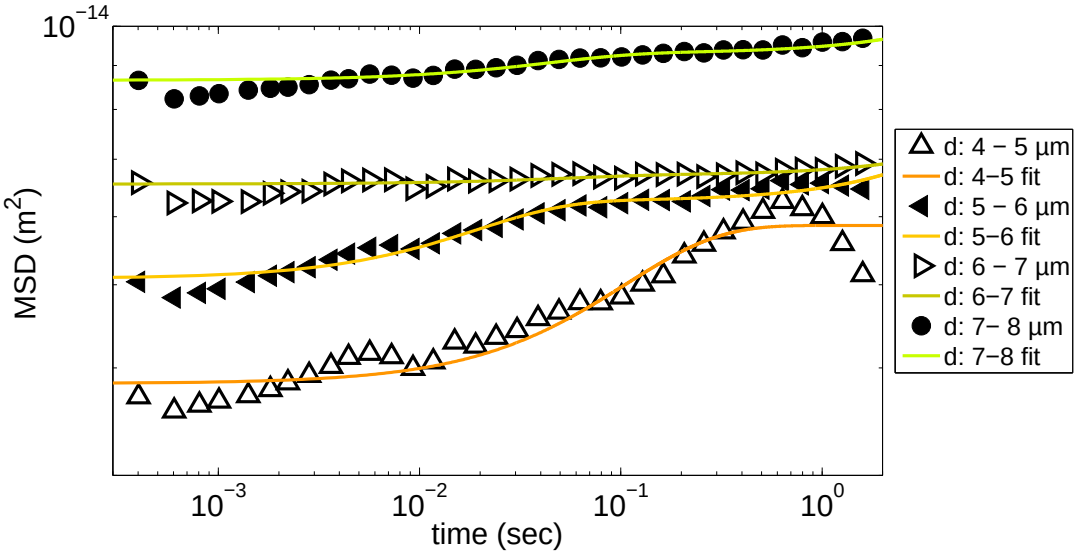



Figure 7.22: MSD in extracted cell keratin 8/18 networks with varying distance to the rim of the nucleus (part2 - up to 8.0 µm distance) with the corresponding fit (lines)

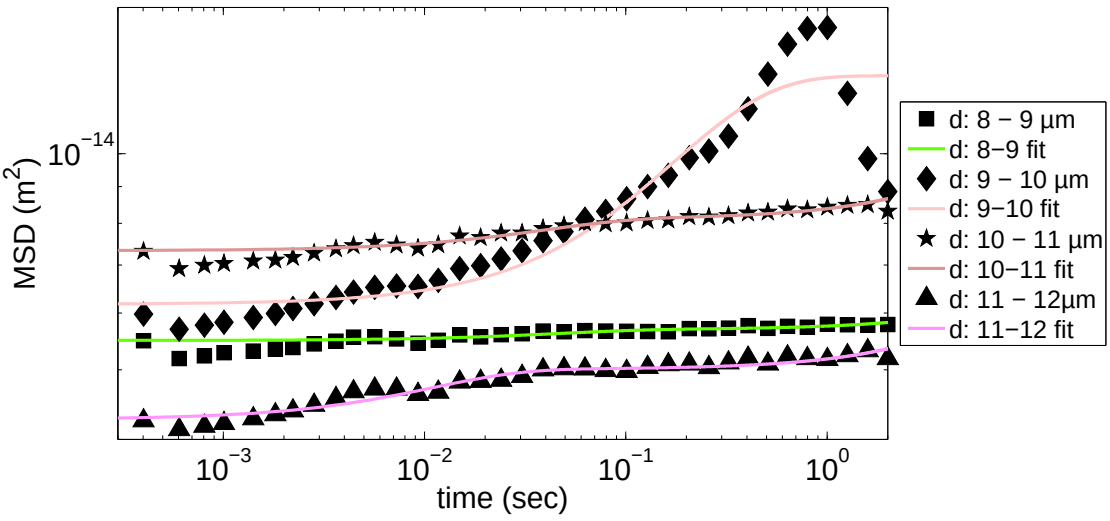



Figure 7.23: MSD in extracted cell keratin 8/18 networks with varying distance to the rim of the nucleus (part3 - up to 12.0 µm distance) with the corresponding fit (lines)

For distances up to 12 µm (Figure 7.23) the MSDs stayed in the same range than before, but with a small tendency to decrease. Table 7.6 shows the results of the fitting with the model-based function. The $R^2$ values were lower compared to the measurements in the *in vitro* assembled network which was due to the different constitution of the cells at each measurement. This introduced uncertainties for the fitting because the MSD varied much at the long times range and this resulted in

Table 7.6: Resulting fitting parameter $a$, $b$, $c$ and $d$ dependent on the distance to the rim of the nucleus. The $R^2$ value shows the goodness of the fit.

| Fitting results - part1 | | | | | |
|---|---|---|---|---|---|
| Fitting parameter | | | | | |
| Distance | $R^2$ | a | b | c | d |
| $0-1$ µm | 0.689 | -5.5480 | -7.2621 | -6.4952 | 3.2480 |
| $1-2$ µm | 0.513 | -4.9131 | -8.6821 | -6.7470 | 3.3159 |
| $2-3$ µm | 0.926 | -5.2629 | -8.9056 | -7.6785 | 3.3938 |
| $3-4$ µm | 0.905 | -5.6404 | -8.6845 | -7.816 | 3.1366 |
| $4-5$ µm | 0.754 | -5.5631 | -943.3160 | -6.2023 | 2.0974 |
| $5-6$ µm | 0.736 | -5.2821 | -8.3754 | -6.7498 | 3.8729 |
| $6-7$ µm | 0.759 | -5.0282 | -9.1771 | -8.7834 | 2.9232 |
| $7-8$ µm | 0.924 | -4.7501 | -8.6220 | -7.3485 | 3.1167 |
| $8-9$ µm | 0.924 | -5.2042 | -9.6141 | -8.5511 | 3.0513 |
| $9-10$ µm | 0.731 | -5.0881 | -895.1020 | -5.0093 | 1.4846 |
| $10-11$ µm | 0.935 | -4.916 | -8.2023 | -7.1518 | 3.2229 |
| $11-12$ µm | 0.769 | -5.4575 | -8.6732 | -7.2061 | 4.4581 |

high residuals. The parameter table shows two exceptions for the fitting parameter. The value of parameter $b$ at a distance of 3 µm to 4 µm and 9 µm to 10 µm was in the order of $-1000$. Fit parameter in general $b$ belongs to the viscous part of Equation (5.8) with the slope $e^b$. If $b = -1000$, the value for the exponential function is equal to zero and therefore this term vanishes. Thus for the fitting of the measured MSD only an elastic and a confinement term remained.
The parameter Table 7.7 shows the standard error of the fitting parameter provided by the fitting algorithm. The standard errors $\Delta a$ of the elastic parameter $a$ are smaller compared to the standard errors $\Delta b$ and $\Delta c$. The other values had a higher uncertainty, apart from the exceptions seen in Table 7.6 which were values of $10^{-18}$. The errors of the fitting parameter lead to an estimation how accurate the storage and loss modulus can be specified. Since the fitting parameter $a$ was larger than parameter $b$ and $c$ for all cases, the elastic part dominated at the MSD.

Table 7.7: Resulting standard errors of the fitting parameter $\Delta a$, $\Delta b$, $\Delta c$ and $\Delta d$ dependent on the distance to the rim of the nucleus.

| Fitting results - part2 | | | | | |
|---|---|---|---|---|---|
| Standard Error | | | | | |
| Distance | | Δa | Δb | Δc | Δd |
| 0 – 1 µm | | 0.0010 | 0.0198 | 0.0057 | 0.0154 |
| 1 – 2 µm | | 0.0006 | 0.0884 | 0.0078 | 0.0214 |
| 2 – 3 µm | | 0.0001 | 0.0879 | 0.0156 | 0.0433 |
| 3 – 4 µm | | 0.0007 | 0.0504 | 0.0135 | 0.0355 |
| 4 – 5 µm | | 0.0009 | 0.0000 | 0.0049 | 0.0129 |
| 5 – 6 µm | | 0.0007 | 0.0431 | 0.0049 | 0.0145 |
| 6 – 7 µm | | 0.0007 | 0.1725 | 0.0781 | 0.1953 |
| 7 – 8 µm | | 0.0006 | 0.1088 | 0.0195 | 0.0511 |
| 8 – 9 µm | | 0.0007 | 0.2108 | 0.0472 | 0.1222 |
| 9 – 10 µm | | 0.0018 | 0.0000 | 0.0069 | 0.0154 |
| 10 – 11 µm | | 0.0007 | 0.0690 | 0.0151 | 0.0404 |
| 11 – 12 µm | | 0.0006 | 0.0379 | 0.0049 | 0.0153 |

For the storage moduli, shown in Figure 7.24, the exceptions had no effect - the curvature did not exhibit any special features, and were of typical curvature. That means, it had a positive slope for small frequencies and a plateau in the mid-frequency regime.

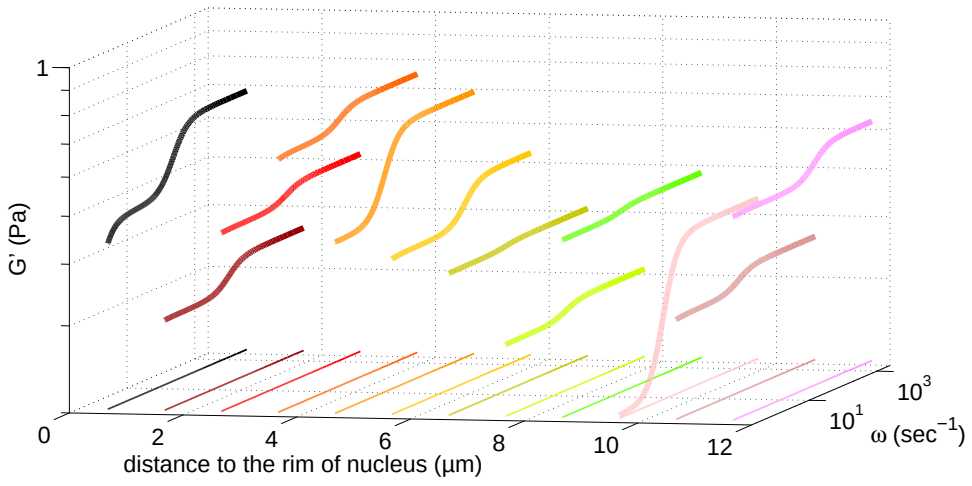



Figure 7.24: G' in extracted cell keratin 8/18 networks with varying distance to the rim of the nucleus, up to 12.0 µm distance

At higher frequencies, an increase of the storage modulus could be observed as well as a saturation due to the ballistic regime. The distance to the nucleus played an important role. The closer to the nucleus the particle was located, the higher got the storage modulus. Consequently in this region the network was stiffer compared to larger distances. For distances between 4 µm and 8 µm the storage modulus decreased, reached a minimum and increased again for distances up to 12 µm. The higher the distance was, the more unsteady the storage moduli were dependent on distance. This could be explained by an artifact corresponding to the sample surface. The determined plateau modulus $G_0'$ clarified these aspects.
Regarding the exceptions of parameter Table 7.6, the loss moduli showed a different curvature in comparison to the other curves. The minimum was shifted to lower frequencies and hence, did not appear in the measured frequency range. As shown in Chapter 5 the relation of the viscous part and confinement size is responsible for the location of the minimum of the loss modulus.

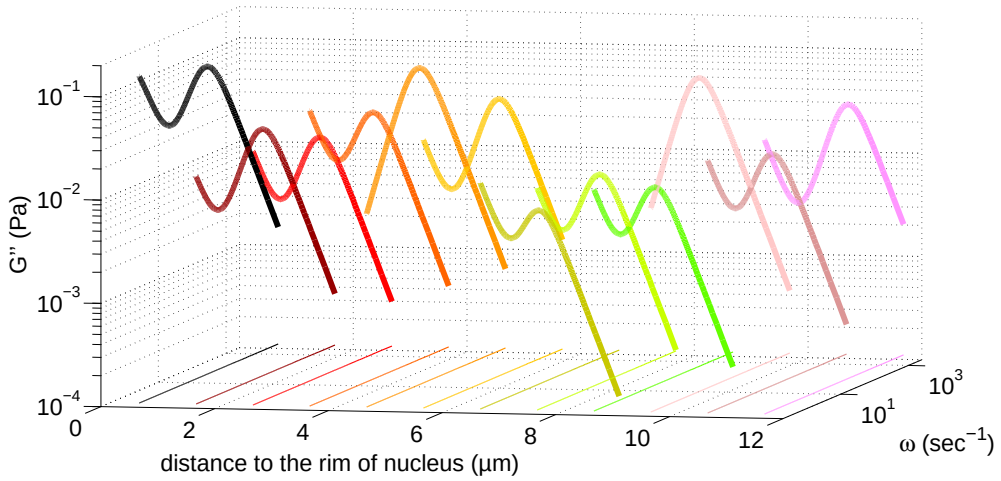



Figure 7.25: G" in extracted cell keratin 8/18 networks with varying distance to the rim of the nucleus, up to 12.0 µm distance.

The loss moduli $G''$ gave insight into the lost energy of the particle moving in the network. The dependency of the absolute value on the distance to the nucleus rim was not as clear as for the storage moduli. Compared to the *in vitro* assembled networks the minima of the loss moduli were in the range of low $MgCl_2$ in the networks (Frequency below 10 sec$^{-1}$).
In the same way as for *in vitro* assembled keratin 8/18 networks a plateau modulus $G_0'$ and its corresponding $G_0''$ can be determined. At Figure 7.24 for a distance of

0 µm to 1 µm the plateau can be seen more clearly compared to the storage moduli at other distances. Hence, the plateau is determined to be at around 1 Hz frequency. At the following figure the storage and loss modulus at a frequency of 1 Hz are shown.

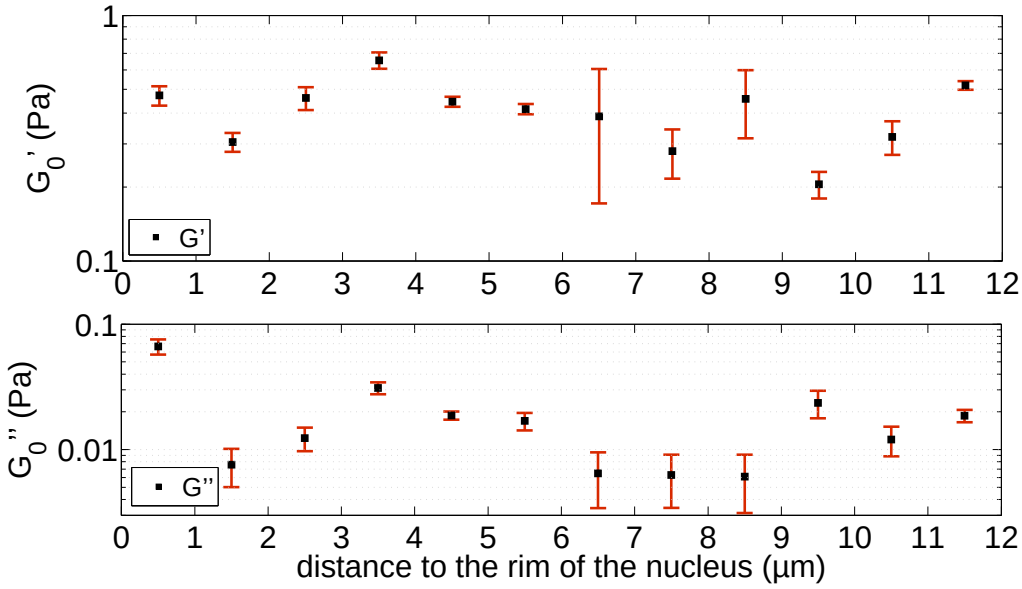



Figure 7.26: Plateau storage and loss moduli $G_0'$ and $G_0''$ dependent on the distance to the rim of the nucleus. The storage modulus decreases first for low distances and then reaches a maximum. For higher distances the stiffness becomes smaller and the influence of the substrate below the network increases.

Close to the nucleus the plateau value $G_0'$ had a value of 0.47 Pa and decreased at a distance between 1 µm and 2 µm. The plateau value close to the nucleus was influenced by the much stiffer nucleus itself. The larger the distance the lower this influence was. Therefore the plateau modulus decreased in the first steps. At larger distances (3 µm - 4 µm) the modulus reached a maximum which corresponds to the stiffest part of the intermediate filament network. In Figure 7.17 the cell nucleus and the area around it with its networks show the same feature. For higher distances between 5 µm and 8 µm the network got softer and the plateau modulus was smaller. The particle motion in that region was more and more influenced by the substrate which was located below the network. The increasing errors for that distances showed that the measured particle motion varies a lot depending on the network constitution and the substrate roughness. For distances from 9 µm to 12 µm it was difficult to interpret the values of the modulus because during a measurement the

network was not resolvable without changing its constitution (e.g. with labeling). The influence of the substrate was one aspect which explained the increase of the plateau modulus.
The loss plateau modulus behaved almost the same way as the storage plateau modulus. That means that close to the nucleus the loss of energy due to friction was high, then decreased because the network was less stiff and for higher distances increased. It reached a maximum because the particle lost energy in the slightly stiffer network. Since the network got softer for higher distances, the energy loss decreased until the influence of the substrate played a role.
Overall the measurements at pancreatic cancer cells showed that on the one hand the method also in this scenario is suitable to determine the mechanical properties of the viscoelastic medium. On the other hand the mechanical properties in sense of the storage modulus give insight about the stiffness of the network dependent on the distance to the rim of the nucleus. The decrease of the storage modulus close to the nucleus can be explained by the disassembly of the intermediate filament network in the living cell. In addition to that the stiffest part of the network appears at slightly larger distances and is due to the movement of the network towards the nucleus before it gets disassembled.

### 7.2.4 Human Granolyzytes

Human granulozytes are part of the white blood cells which can be separated into several groups depending on their function. The neutrophilic granulozytes or neutrophils are one of these groups and were in the focus of this work. The motility of the cells is controlled by the microtubules, the actin network and the stiffness of the whole cell. The ability to get infected by a disease therefore is up to the motility of the cells to reach the damaged tissue. The treatment with colchicine, an alkaloid used for curing artrithis, of a specific amount reduces the deformability which leads to reduced motility. The colchicine binds to tubulin and stops the polymerization to microtubules in the cell. Furthermore, it increases the amount of cortical actin filaments [121]. The aim of the investigations of passive microrheology was to confirm the optical stretcher measurements which showed an increasing cell stiffness for the treatment of 10 ng/ml.
Particles coated with fibronectin of $r_1 = 1\,\mu\text{m}$ or $r_2 = 0.5\,\mu\text{m}$ were added to the cells half an hour before the measurement was started. The observation of the particles' motion located on the membrane of the cell was performed at both granulozytes

with and without colchicine. In case of a treatment with colchicine it was added to the cells one hour before the measurement took place. The average of several MSDs of the particles motion lead to the dynamic shear modulus. After that the storage and loss modulus were extracted out of the dynamic shear modulus. The method used is explained in Chapter 5 and the application to this system should (beside the medical aspects) underline the functionality of the method. The averaged MSDs of the measurements are shown in the following figure. The measurement was performed at room temperature ($T = 296.13\,\mathrm{K}$) with the high-speed camera at a frame rate of $f = 5000\,\mathrm{Hz}$.

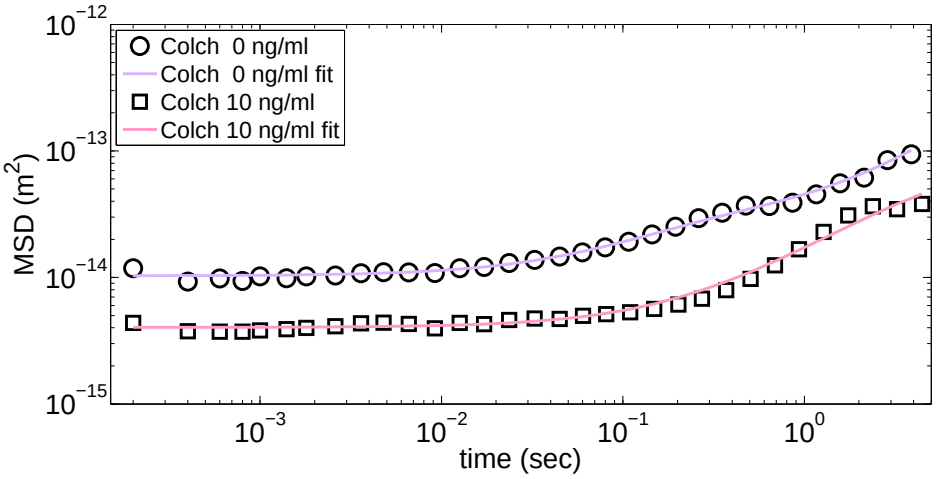



Figure 7.27: Double-logarithmic plot of the averaged MSD for particles of 1 µm and 0.5 µm diameter on neutrophils without treatment (circles) and its fit (light purple line). Neutrophils with treatment are shown by squares and the corresponding fit in light magenta.

Both MSDs show a similar curvature which means that for higher time scales the slope of the MSDs increases slightly. The curve of the treated neutrophils is located below the curve of the untreated granulozytes. Thus the particle movement is more limited in case of the treated cells. The fitting function at first sight is in good agreement for both cases. The fit residuals, shown in Figure 7.28, and Table 7.8 with the fitting parameter give more information about the goodness of the fit.

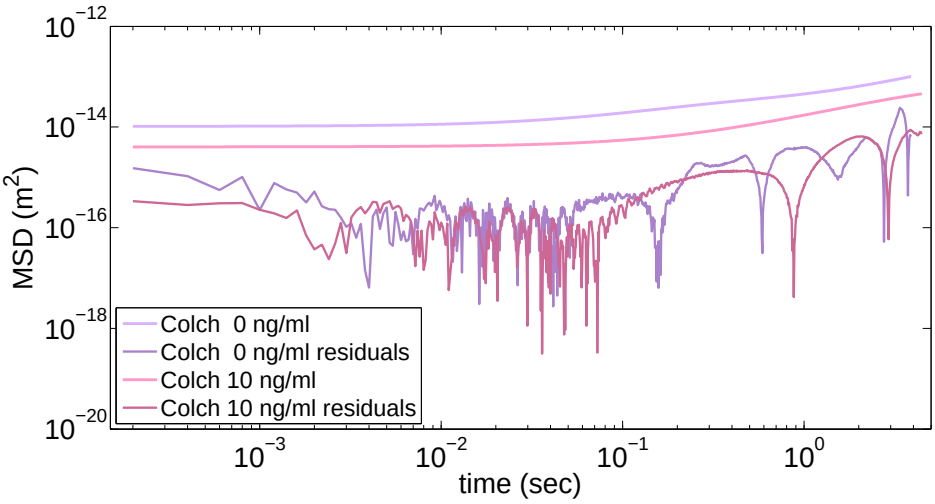



Figure 7.28: Residuals plot of colchicine treated and untreated neutrophils.

Table 7.8: Results of the fitting of the MSD at treated and untreated human granulozytes.

| Fitting results | | | |
|---|---|---|---|
| Colchicine concentration | | 0 ng/ml | 10 ng/ml |
| Goodness of fit | $R^2$ | 0.9752 | 0.9500 |
| Fit parameter | $a$ | -4.5756 | -5.5141 |
| | $b$ | -3.9506 | -38.1657 |
| | $c$ | -4.1438 | -2.7057 |
| | $d$ | 1.7330 | -1.5141 |
| Standard Error | $\Delta a$ | 0.0034 | 0.0033 |
| | $\Delta b$ | 0.0213 | 0.0000 |
| | $\Delta c$ | 0.0335 | 0.0543 |
| | $\Delta d$ | 0.0465 | 0.0667 |

The goodness of the fit described by the $R^2$ value is for both the untreated and treated cells higher than 0.9 and therefore the fit results is good. The fitting parameter and their errors lead to the dynamic shear modulus for both cases. The shear modulus can be separated into storage and loss modulus, which give insight to the stiffness and viscous behavior of the interplay between the cell membrane, the actin network and microtubules inside the cell. The resulting moduli are shown in Figure 7.29. The storage modulus of granulocytes, when colchicine was added one hour before the measurement, showed an increased stiffness over the whole frequency range compared to the normal granulocytes. That means that colchicine bound to the microtubules and increased the amount of expressed actin which led to the higher

overall strength of the cell.

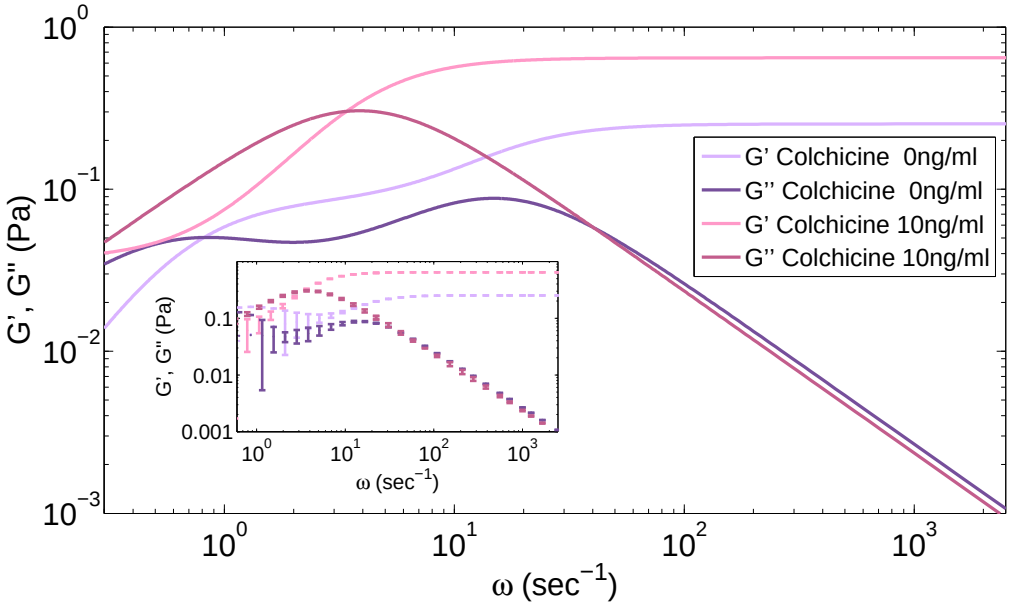



Figure 7.29: Storage and loss modulus of treated and untreated cells.

The loss modulus of the untreated cells was larger than the storage modulus for a small frequency range at the lower frequencies. The cell acted like a gel-like viscoelastic medium. In the case of treated cells it was vice versa, the loss modulus was higher than the storage modulus for a wider frequency range. The error-bars at all curves showed a higher error for lower frequencies, so that the determination of fluid-like and gel-like was difficult. The reason for this was a low number of measurements. If the number of averaged MSDs is low, the high times range is inaccurate. Thus, the fit becomes uncertain, which has an influence on the standard errors of the parameter.
In sum the method showed a reasonable result, and the observations of the optical stretcher were confirmed [121].

## 7.3 Active Microrheology

The application of the method introduced in Chapter 6 to viscoelastic media like the *in vitro* assembled keratin 8/18 network and the extracted pancreatic cell network is presented in this chapter. For the measurements the optical tweezers setup described in Chapter 4 was used to excite one particle to oscillations in the specific media. Other particles which were located around the reference particle, responded to the excitation dependent on the composition of the surrounding network. The Lock-In method allowed to determine the resulting motion of the response particles without the disturbing noise (Brownian motion). Additionally, the response amplitudes of the first, and several higher harmonics of the given excitation frequency were determined. Furthermore, the phase differences between reference and response, dependent on the higher orders of the excitation frequency, followed from the calculations. In the end the transfer tensor of the viscoelastic medium was derived and compared to the theory.
In the first section the measurements in bi-distilled water are shown because of the simplicity of the system. After that the results of the measurements at the *in vitro* assembled network are presented. For cell measurements first insights are described.

### 7.3.1 Bi-distilled Water

The measurement in bi-distilled water was performed to show the functionality of the system. The water itself is a purely viscous medium and therefore, if a particle gets excited to oscillations at low frequencies by the trap, it will follow the motion of the trap. At these measurements the motion and response of only one particle was observed, because there were no particles which can respond to the excited one. This was because of the lack of interactions provided by the viscoelasticity of the surrounding medium.
Hence, in bi-distilled water, the expected values of the response amplitude for different angles should always be the same as the excitation amplitude. This is valid if the oscillation frequency is small so that the viscosity of the medium does not influence the particle motion. Since the response particle phase is always in dependency on the reference particle phase, the expected value should lead to zero for bi-distilled water, because the response particle is the reference particle at the computations. This is an additional test if the written analysis script works correctly. Furthermore,

the calculated transfer matrix is predicted to be the identity matrix because of the calculation with equal matrices. The calculation of the amplitudes corresponding to the higher frequency modes leads to zero because only the first harmonic is expected.

At the measurements for this test, the optical trap oscillated with an amplitude of 1.275 µm peak-to-peak (pp), a oscillation frequency of 10 Hz and four angles of excitation 0°, 45°, 90° and 135° in the Cartesian coordinate system ($x$,$y$ and $z$) of the CCD camera. The optical trap had a laser intensity of 180 mW which led to a force constant of around 9.8 pN/µm. The measurements were performed at 10 µm distance to the surface to minimize effects of the substrate. The sampling frequency of the high-speed camera was at 5000 Hz. Figure 7.30 shows the resulting motion separated in the three directions of the coordinate system, which means that the $X^*$-direction is the connection line between reference and response particle, $Y^*$-direction its orthogonal and the $Z^*$-direction the vertical direction.

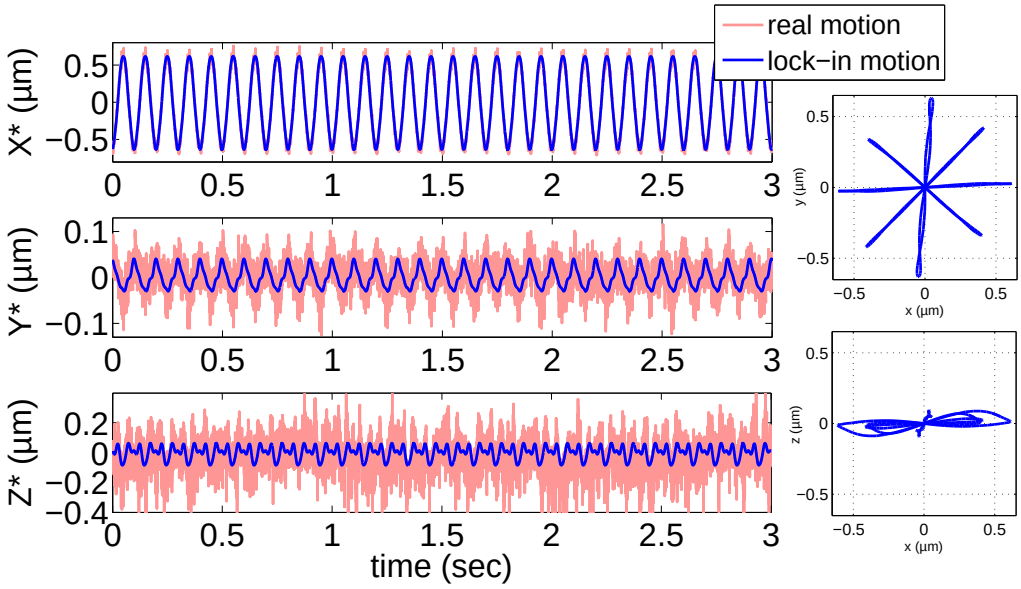



Figure 7.30: $X^*$,$Y^*$ and $Z^*$ Lock-In (blue) and real motion (light red) of the reference particle with an excitation angle in $x$-direction (0°) and 0.6375 µm amplitude. On the right side the Lock-In motion is shown ($x$-$y$- and $x$-$z$-plane) for all excitation directions. The particle always follows the optical trap with low displacement in the $z$-direction.

For this case if only one particle is observed, the coordinate system with $X^*$, $Y^*$ and $Z^*$ is equal to the CCD coordinate system with $x$, $y$ and $z$. The measured

particle motion was in accordance with the calculated particle motion via the Lock-In method in the direction of excitation because the Brownian motion was small compared to the oscillations. The lateral motion of the particle can be seen as a superposition of the Brownian motion and a cross-talk due to the oscillation in $x$-direction. The lateral calculated motion in the theoretical ideal case is zero. Table 7.9 shows the input parameters and the resulting values for the amplitudes and phase differences.

Since the response and reference particle motions were the same, the phases were

Table 7.9: Response parameters of a particle excited in bi-distilled water.

| Input parameter | | | | |
|---|---|---|---|---|
| Medium | Osc. freq. | Osc. amp. | Distance | Sampling |
| bi-distilled | 10 Hz | 0.638 µm | 0 µm | 5000 Hz |
| Result | | | | |
| | Order | $X^*$ | $Y^*$ | $Z^*$ |
| 0°-Excitation | 1st Amp | 0.617 | 0.030 | 0.033 |
| | 2nd Amp | 0.002 | 0.003 | 0.047 |
| | 3rd Amp | 0.007 | 0.004 | 0.016 |
| | 4th Amp | 0.016 | 0.004 | 0.014 |
| | 1st Phs | 0 | 0 | 0 |
| | 2nd Phs | 0 | 0 | 0 |
| | 3rd Phs | 0 | 0 | 0 |
| | 4th Phs | 0 | 0 | 0 |
| 45°-Excitation | 1st Amp | 0.414 | 0.422 | 0.028 |
| | 2nd Amp | 0.001 | 0.002 | 0.012 |
| | 3rd Amp | 0.001 | 0.001 | 0.016 |
| | 4th Amp | 0.013 | 0.006 | 0.001 |
| 90°-Excitation | 1st Amp | 0.049 | 0.632 | 0.077 |
| | 2nd Amp | 0.001 | 0.010 | 0.022 |
| | 3rd Amp | 0.002 | 0.001 | 0.023 |
| | 4th Amp | 0.014 | 0.007 | 0.001 |
| 135°-Excitation | 1st Amp | 0.402 | 0.348 | 0.027 |
| | 2nd Amp | 0.005 | 0.008 | 0.036 |
| | 3rd Amp | 0.002 | 0.008 | 0.016 |
| | 4th Amp | 0.010 | 0.003 | 0.008 |

zero and the algorithm of computation was correct. The amplitudes of the higher orders in the excitation direction were small compared to the first mode, and they were an artifact due to the laser motion in this case. In the other direction without excitation an amplitude of around 30 nm could be recognized. This was due to the crosstalk of the trap motion. The particle followed with small deviations the excitation of the trap.

The motions in the directions of 45°, 90° and 135° showed a similar behavior for the phase which is reasonable because of the comparison of the same particle with itself. The results of the calculated amplitudes is also shown in Table 7.9. The diagonal oscillations (45°, 135°) led to smaller amplitudes in $X^*$ and $Y^*$ because the oscillation amplitude was $a_{\text{amp}}/\sqrt{2} = 0.4508\,\mu\text{m}$. Hence, the measured values were in accordance with theory. The amplitude in non-excited direction always resulted in minor values which shows that the method works in the case of a viscous fluid. Furthermore, the higher orders of the amplitude were negligibly low in value, which was predicted in theory.
As already could be seen in the theoretical description of the method and the simulations, the transfer tensor $\bar{A}_0$ was expected to be equal to the identity matrix because the reference matrix $\bar{X}_0$ and response matrix $\bar{Y}_0$ were equal.

$$\bar{X}_0 = \begin{pmatrix} 0.617 & 0.414 & 0.049 & 0.402 \\ 0.030 & 0.422 & 0.632 & 0.348 \\ 0.033 & 0.028 & 0.077 & 0.027 \end{pmatrix} \mu\text{m} \qquad \bar{Y}_0 = \begin{pmatrix} 0.617 & 0.414 & 0.049 & 0.402 \\ 0.030 & 0.422 & 0.632 & 0.348 \\ 0.033 & 0.028 & 0.077 & 0.027 \end{pmatrix} \mu\text{m}$$

$$\bar{A}_0 = \begin{pmatrix} 1.000 & -3.335 \times 10^{-8} & 0.000 \\ 0.000 & 1.000 & 5.189 \times 10^{-8} \\ 0.000 & 3.196 \times 10^{-6} & 1.000 \end{pmatrix}$$

The columns of matrix $\bar{X}_0$ and $\bar{Y}_0$ are the amplitudes of the first harmonic - the excitation frequency itself - for the different oscillation angles. The resulting transfer matrix shows the predicted values apart from rounding artifacts which are in the range of $10^{-6}$ to $10^{-8}$. Hence, the identity matrix is a result for this measurement and shows that the principle and computations behind the method work. The next section shows the measurement of the *in vitro* assembled keratin 8/18 network.

### 7.3.2 In Vitro Assembled Keratin 8/18 Networks

The *in vitro* assembled keratin 8/18 network was prepared in a similar way as for the passive microrheology measurements. The polystyrene particles were added during the polymerization and were embedded in the network. At the beginning, the sample was scanned and searched for a suitable place for the measurement - a place where several particles were aligned in almost the same plane. In addition to that varying distances to each other to gather as much particle motions as possible with one record of the high-speed camera was preferred. The sampling rate was 5000 Hz and the optical trap was calibrated via the optical potential method. That

led to a force constant of 9.8 pN/µm at $I = 180$ mW. The high strength of the trap was needed to apply enough force to the network and to reduce the Brownian motion inside the trap. The distances of observed particles was between 1 µm and 20 µm, with the latter distance was assumed to be too large to gather reasonable results. The reference particle was excited by the laser oscillating at an amplitude of 255 nm pp and a frequency of 10 Hz. The angles of excitation were at 0°, 45°, 90° and 135° in reference to the CCD camera coordinate system ($x$, $y$ and $z$). The measurements presented in this work were performed in the keratin 8/18 networks of two different $MgCl_2$ concentrations. The first one had a concentration of 0 mM $MgCl_2$ and the other one a concentration of 1 mM $MgCl_2$. Both types of *in vitro* assembled networks had a protein concentration of 0.5 mg/ml.
The reference particle's response to the laser deformed the network, and this led to a response of the particle. The laser oscillation, which excited the reference particle, was always at an amplitude of 127 nm, but the response of the reference particle often did not follow the oscillation of the optical trap due to the limitations of the surrounding network.

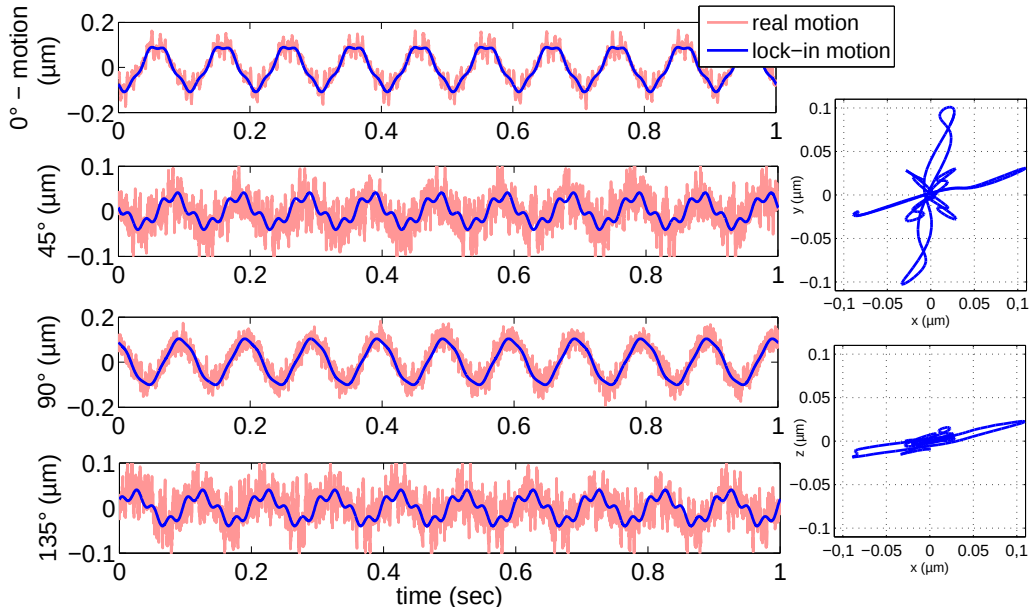



Figure 7.31: Lock-in (blue) and real motion (light red) of the reference particle with excitation angles in 0°, 45°, 90° and 135°-direction and a 127 nm amplitude. The graphs on the right depict the particle motion for the four angles in the $x$-$y$- and the $x$-$z$-plane.

The Figures (7.31 and 7.32) show exemplary motions of a reference particle and the response motion of a particle at a distance of 3.72 µm in a network with a salt concentration of 1 mM $MgCl_2$. The light red line stands for the motion which was observed via the tracking program whereas the calculated motion of the Lock-In method is shown in blue. The tracked motion of the reference particle and the calculated motion with the lock-in method showed that the curves were in good agreement. The amplitude of the reference particle (99.8 nm) was smaller compared to the excitation amplitude of the laser which showed that the network restricts the displacement of the particle. Regarding the shift of the angle between laser motion direction and reference particle motion direction the network allowed the particle to move in a slightly different direction. The motion into the $z$-direction is also due to the network surrounding the particle. This change of excitation angle due to the network was important for the calculation of the response particle, because not the laser beam deformed the network, but the reference particle. Dependent on the reference motion, the Lock-In motion for the response particle was calculated.

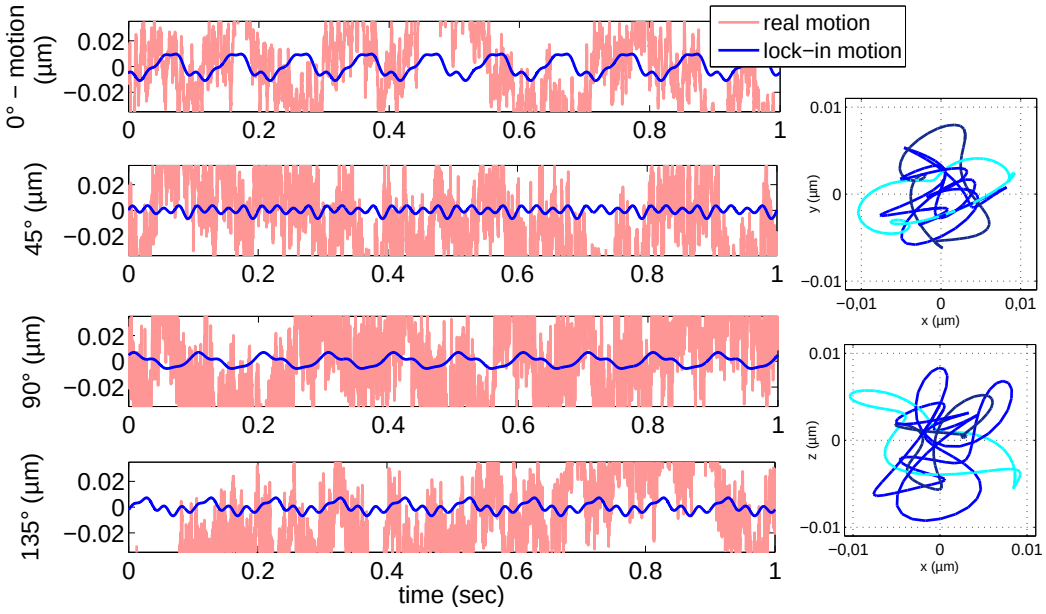



Figure 7.32: Lock-In (blue) and real motion (light red) of the response particle with excitation angles in 0°, 45°, 90° and 135°-direction and a 127 nm amplitude. The graphs on the right depict the particle motion for the four angles in the $x$-$y$- and the $x$-$z$-plane. The motion of the 0° and 90° excitation are highlighted (dark blue, light blue) to clarify the response curves.

In that case the reference particle was the source of the deformation of the network which influenced the motion of the response particle. In Figure 7.32 it became obvious that the response of the particle at the excitation frequency and the higher modes was small compared to a high signal due to the Brownian motion. Nevertheless, the Lock-In method results in a correct response for the specific excitation angle, which can be seen on the right part of Figure 7.32 considering the motion in the $x$- and $y$- plane. The motion of the reference particle, and therefore the deformation of the network in the $z$-direction, led to a response of the motion into this direction.
As can be seen in the upper figures, neither the reference nor the response particles moved the complete oscillation amplitude at 1 mM $MgCl_2$. For the networks without $MgCl_2$ the response of the reference particle to the oscillation of the laser was higher due to a looser network.

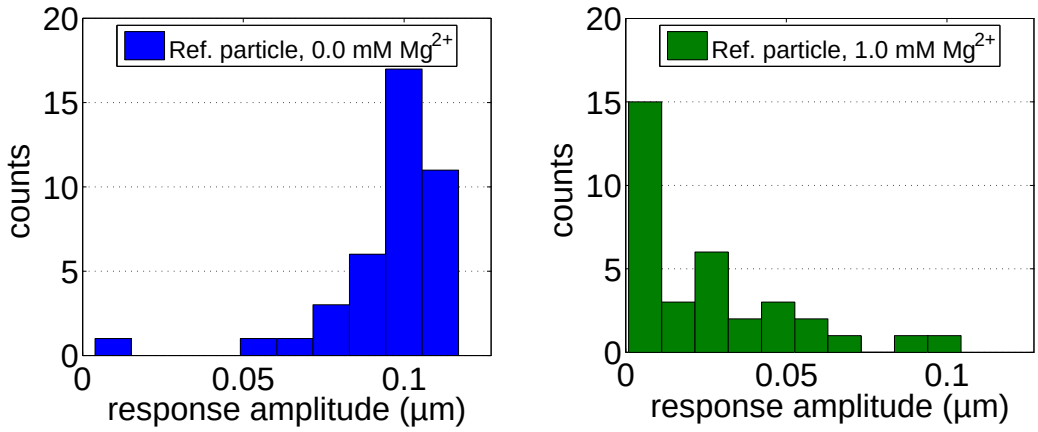



Figure 7.33: Response of the reference particle to an oscillation of the laser with the amplitude of 127 nm. On the left side the histogram at 0 mM $MgCl_2$, on the right side a $MgCl_2$ concentration of 1 mM.

The histogram of the amplitudes of the reference particles (Fig. 7.33) indicated that the higher the concentration of $MgCl_2$, the lower the amplitudes got. This is an important fact, because the motion of the reference particle is crucial for the deformation of the network and for the response of the other particles. Because of the higher distance to the excitation position, the oscillation of the response particle amplitudes in general are smaller than the reference particle and the calculated transfer tensor's entries are in a range around one and below. For the exemplary

measurement the transfer tensor was calculated and became

$$\bar{A}_i = \begin{pmatrix} 0.105 & 0.169 & 0.451 \\ 0.066 & 0.114 & 0.125 \\ 1.134 & 0.875 & 2.124 \end{pmatrix}$$

As can be seen at transfer tensor $\bar{A}_i$, the transfer matrix contained entries which were larger than one. This came up when the reference motion was more noisy than the response motion (simulations in Chapter 6). The general case for the measurements at 1 mM $MgCl_2$ was that the transfer matrices contained high entry values. Over a larger amount of data, there were high variations of values and thus a large standard deviation.
The transfer tensors of the networks were separated dependent on the distance of reference and response particle. Afterwards a displacement of arbitrary amplitude $a_i$ in the $X^*$ or $Y^*$-direction was chosen to calculate the output vector. The output vector $\vec{r_o}$ was determined via the multiplication of the arbitrary vector $\vec{r_p}$ and the average transfer tensor $\bar{A}$ at a specific distance of particles.

$$\begin{aligned} \bar{A}\vec{r_p} &= \vec{r_o} \\ \begin{pmatrix} A_{xx} & A_{xy} & A_{xz} \\ A_{yx} & A_{yy} & A_{yz} \\ A_{zx} & A_{zy} & A_{zz} \end{pmatrix} \begin{pmatrix} a_1 \\ a_2 \\ a_3 \end{pmatrix} &= \begin{pmatrix} A_{xx}a_1 + A_{xy}a_2 + A_{xz}a_3 \\ A_{yx}a_1 + A_{yy}a_2 + A_{yz}a_3 \\ A_{zx}a_1 + A_{zy}a_2 + A_{zz}a_3 \end{pmatrix} \end{aligned} \tag{7.2}$$

As ratio the absolute values of preset and output vectors were taken into account and weighted by the standard deviation.

$$\frac{|\vec{r_o}|}{|\vec{r_p}|} = \frac{\sqrt{(A_{xx}a_1 + A_{xy}a_2 + A_{xz}a_3)^2 + (A_{yx}a_1 + A_{yy}a_2 + A_{yz}a_3)^2 + (A_{zx}a_1 + A_{zy}a_2 + A_{zz}a_3)^2}}{\sqrt{a_1^2 + a_2^2 + a_3^2}} \tag{7.3}$$

The error was determined via the standard deviation of the transfer matrices and the propagation of error. The resulting ratios were compared to the theoretically derived values. The theoretical derived values used a shear modulus which was observed at the passive method for the corresponding $MgCl_2$ concentration. In addition to that a theoretical curve was computed which fitted to the curve of the measurement. This gave an idea of how large the difference between the theory and the experiment was. The following figure shows the resulting ratios of as well as the theoretical and the experimentally calculations - in this case of the measurements in the network with a concentration of 0 mM $MgCl_2$. By taking the plateau modulus of $G'_0 = 0.02$ Pa for

a network with a low salt concentration into account (Section 7.2), the theoretical curve was higher than the curve of the measurements. If a theoretical value of $G_0' = 0.1\,\text{Pa}$ was applied to the theoretical calculations, the curve matched better to the measurement data, which indicated that, for the moment, both methods - the passive one and the active one - are not comparable.

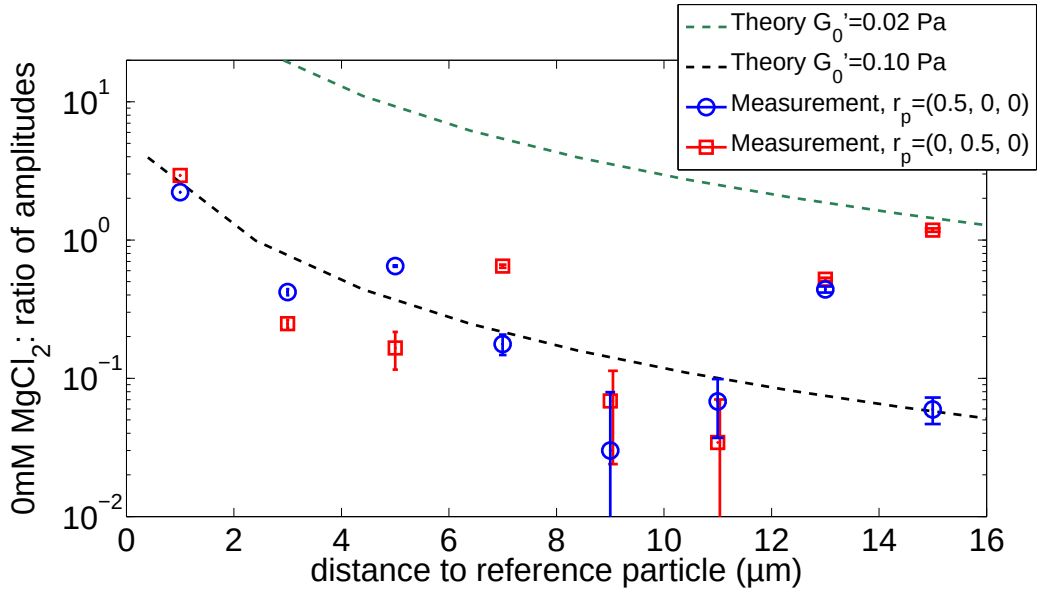



Figure 7.34: Excitation in $X^*$ and $Y^*$ of amplitude $a = 0.5\,\mu\text{m}$ at $0\,\text{mM}$ $MgCl_2$. Calculation of response amplitude of the measurement (blue circles) in $X^*$ and $Y^*$ (red squares) and the theoretical values (dashed green for $G_0' = 0.02\,\text{Pa}$, dashed black for $G_0' = 0.1\,\text{Pa}$) dependent on distance to the reference particle.

For larger distances to the reference particle, the ratio of amplitudes decreased which means that the displacement of the particle got smaller the further away the response particle was from the origin of deformation. This behavior is comparable to the theoretical predictions. For the measurements at $0\,\text{mM}$ $MgCl_2$ this can be seen for both curves - for excitation in axial ($X^*$) and lateral direction ($Y^*$) - but it is difficult to recognize a faster decrease of the amplitude ratio with larger distance for the lateral excitation. The larger the distance, the higher the error became because the deformation propagation was highly dependent on the morphology of the network. Hence, for larger distances the probability that the filaments channeled the force not directly to the response particle was higher, especially if the network mesh sizes were large.

For the measurements with $1.0\,\text{mM}$ $MgCl_2$ the prediction is that the response of

the network is lower for short distances, assuming that the deformation force is the same as above. The displacement of positions at larger distances therefore are hardly appreciable due to the low deformation. Figure 7.35 depicts the theoretical as well as the measured curves.

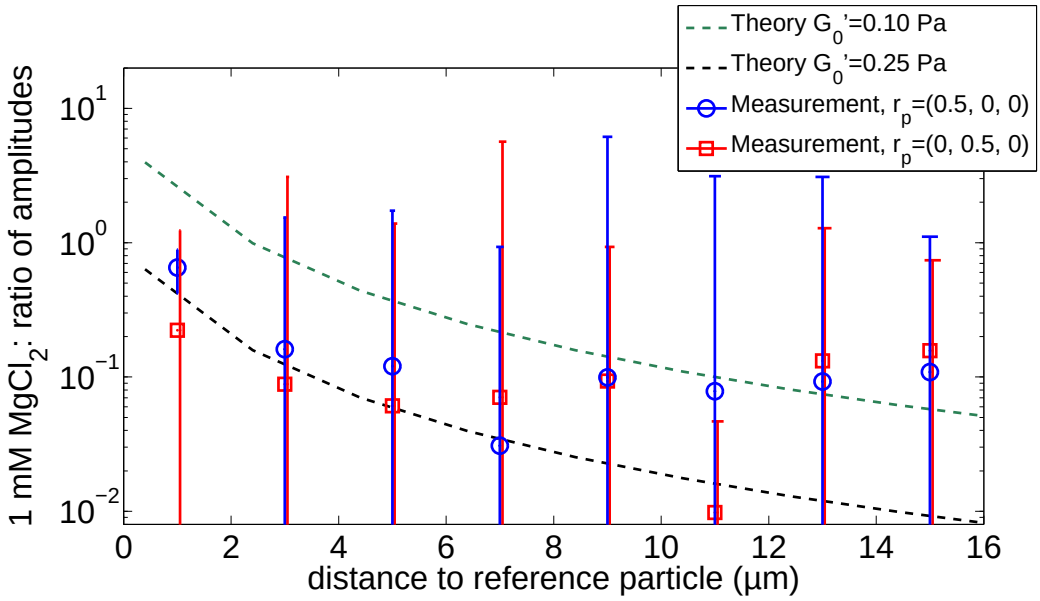



Figure 7.35: Excitation in $X^*$ and $Y^*$ of amplitude $a = 0.5\,\mu\text{m}$ at 1 mM $MgCl_2$. Calculation of response amplitude of the measurement (blue circles) in $X^*$ and $Y^*$ (red squares) and the theoretical values (dashed green for $G_0' = 0.1\,\text{Pa}$, dashed black for $G_0' = 0.25\,\text{Pa}$) dependent on distance to the reference particle.

It is obvious that the errors were very high for the 1 mM $MgCl_2$-network. This was on the one hand due to the low amplitudes of the reference particle which deformed the network (Figure 7.33). That led to a high ratio of reference SNR and response SNR which introduced high entries at the transfer tensor like shown in Chapter 6. From measurement to measurement the entries in the transfer matrices varied a lot and this resulted in the high uncertainties. On the other hand it was observed in [40] that the higher the salt concentration is, the more often bundles occur in the sample. Then the assumption of an isotropic medium is not valid any more and for every position it is not known if the response particle is located in a bundle or beside the bundle and how the network behaves. Thus, the comparison of the specific directions of excitement and the fit to a theoretical curve are not reasonable for this case. To improve the results and decrease the error it might be recommended to additionally investigate the amplitudes of the higher harmonics of the measurement.

If those amplitudes are comparable to the first harmonic, additional effects play a role which complicate the interpretations. The histograms (Figure 7.36 and Figure 7.37) show the higher modes for a low $MgCl_2$ concentration and an amplitude of 127 nm.

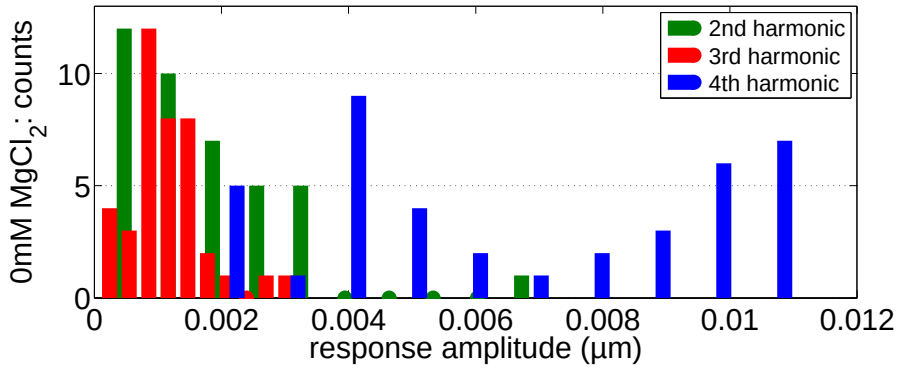



Figure 7.36: Histogram of the amplitudes of the higher harmonics (2nd - green, 3rd - red, 4th - blue) due to the oscillation of the optical trap for the amplitude of 127 nm at a network with 0 mM $MgCl_2$ concentration.

For the network without $MgCl_2$ the higher harmonics do not play a role at this amplitude. The highest value observed at the 4th harmonic was only 1/10 of the excitation amplitude of the laser. Compared to the amplitudes of the first harmonic (Figure 7.33) the ratio is also around 1/10 for the highest occurring value.

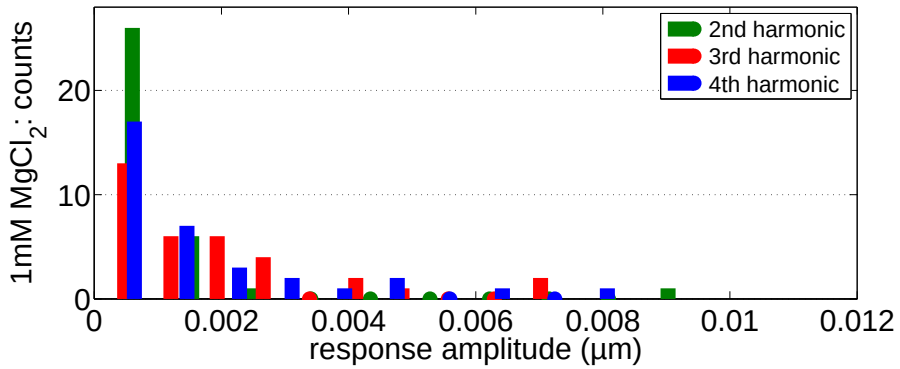



Figure 7.37: Histogram of the amplitudes of the higher harmonics (2nd - green, 3rd - red, 4th - blue) due to the oscillation of the optical trap for the amplitude of 127 nm at a network with 1 mM $MgCl_2$ concentration.

The higher harmonic amplitudes measured at the 1 mM $MgCl_2$-network were in the same range or even smaller compared to the upper 0 mM $MgCl_2$ case, but compared to the first harmonic they are half the size or about 1/5. Hence, it might be the case that the amplitude of the excitation was chosen too large and higher harmonics influenced the result and led to significant errors.
Further measurements in the already investigated networks should give more insight to the dynamics of the networks and show up novel results which are also interesting for measurements at cells. The observation of the change in phase during the motion dependent on the distance is another information which can be extracted out of the motion of reference and response particle.
Furthermore, measurements were performed at extracted pancreatic cancer cells. For an oscillation of the optical trap at the tangential direction respective to the cell nucleus the reference particle response was measured higher compared to the response for radial oscillation with the same amplitude. This indicates that the observations shown in Section 7.4 are correct. Since these observations are derived from a low number of measurements further discussions are avoided in this context. Measurements in the future certainly will give more information about this topic.

## 7.4 Further Results

In this section further results obtained by the measurements of particle motions in the extracted Panc-1 cell networks are described and discussed. With the motions of the particles more information about the networks can be gathered. This is important for the understanding of the constitution and the functionality of the intermediate filament network. As seen before the stiffness of the network depends on the distance to the rim which has amongst other the function of a shielding of the nucleus. As shortly discussed in Chapter 5 there are two additional ideas how to describe the networks behavior towards stress. On the one hand the network can be compared to a mass-spring system with a harmonic potential. Then the network force constant can be determined dependent on the distance to the rim and the direction of the network. On the other hand the particles motion can be described by the surface of equal probability which gives insight of how the network or in other words the confinement is constructed. Both ideas lead to helpful values for the simulations as already mentioned in Chapter 5 and new insights into the network.

### 7.4.1 Network Potentials

The potential of the particles motion in the network can be derived in the same way as the trap stiffness of the optical tweezers. This is described in Chapter 2 as one of the force calibration methods and named optical potential analysis [53]. Thus the particle, which is seen to be located in a potential follows a Boltzmann distribution in the network and this potential is considered to be harmonic. In that way the particle positions during its motion can be separated into the bins of a histogram. The histogram has a Boltzmann distribution, hence the logarithm of the histogram's values is multiplied by the thermal energy and resulting in the potential of the particles motion. Since it is assumed that there is no external force or anything else acting on the particle apart from the network itself, the potential is the potential of the network. A further assumption is that the network potential is harmonic and therefore the network force constant can be derived to gather the force for a specific displacement.
In Section 7.2.3, when the measurements at pancreatic cancer cells were introduced, it was mentioned that the particle's motion is transformed into cylindrical coordi-

nates to reveal the x-movement as radial component and the y-movement as tangential part. This is an important step to show the network force constants in radial, tangential and vertical ($x$,$y$, and $z$) direction and get insight into the physics of the cell. An exemplary result of the calculation of the network force constant was already shown in Chapter 5. At Figure 5.11 the network force constants (nfc) were determined of a particle at the distance of $d = 1.6\,\mu m$. The motion in the z-direction for this example is less limited and therefore the distribution wider than for radial and tangential direction. Thus, the network force constant is lower compared to the other directions.
For a more detailed insight all measurements performed at the cell networks were taken into account. Hence, the network force constants were separated in the direction (x - radial, y -tangential, and z - vertical) and in the distance to the rim of the nucleus. In Figure 7.38 the averaged notwork force constants can be seen.

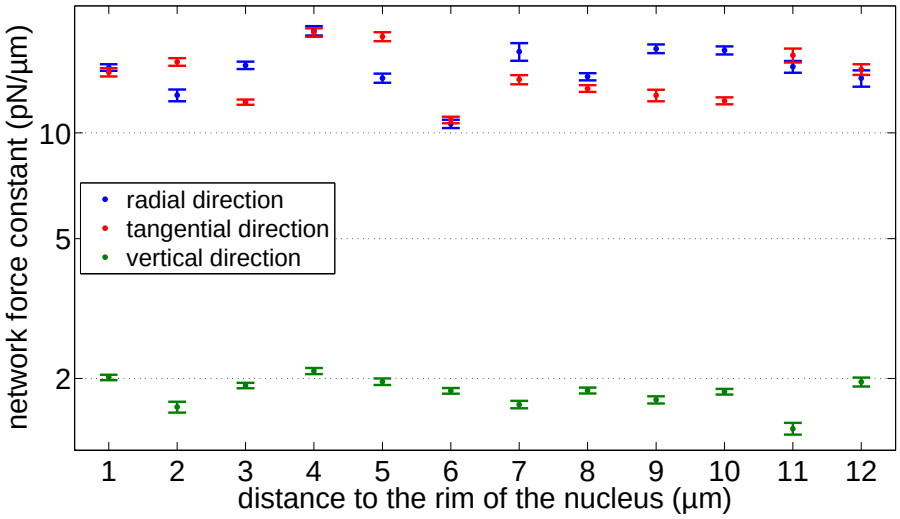



Figure 7.38: Semi-logarithmic plot of the averaged network force constant (nfc). The motion is divided into radial, tangential and vertical components leading to these three values for the nfc depending on the distance of the rim of the nucleus

The measurement parameters like temperature and particle size were the same as for all presented cell measurements. As already seen at the exemplary measurement (Figure 5.11), the motion in z-direction was larger compared to the the other directions. Hence, the network force constant was smaller in that direction. This fact was recognized over all distances from 1 µm to 12 µm. The force constants in radial and tangential direction were in the same range but differed for the specific distances.

The tangential component behaved almost like the storage modulus although at about $5 - 6\,\mu m$ a minimum appears. The number of measurements performed in this region were around 60, and therefore an artifact as reason seemed implausible. Additionally at this distance the radial component followed this behavior. In general the higher the distance the lower the network force constants in tangential direction get which can be linked to the decreasing density of the network. For distances above $10\,\mu m$ the influence of the substrate could be recognized. In the radial direction the network force constant underlies a permanent change of higher to lower value and vice versa. In the vertical direction the stiffness constant got smaller at short distances and increases until, at $4\,\mu m$ distance, a decrease in value appears. This can be seen similarly for the storage modulus (Section 7.2.3). At a distance of $6\,\mu m$ the value is not significantly smaller compared to the other values and the other directions. Thus, the minimum only appears at the horizontal plane. The $R^2$ value of the fitting of an harmonic potential showed the goodness of the fit. For all averaged histograms resulted from the measurements the $R^2$ value was determined dependent on motion direction and distance to the rim of the nucleus. The values for the goodness of the fit were calculated and can be seen in Figure 7.39.

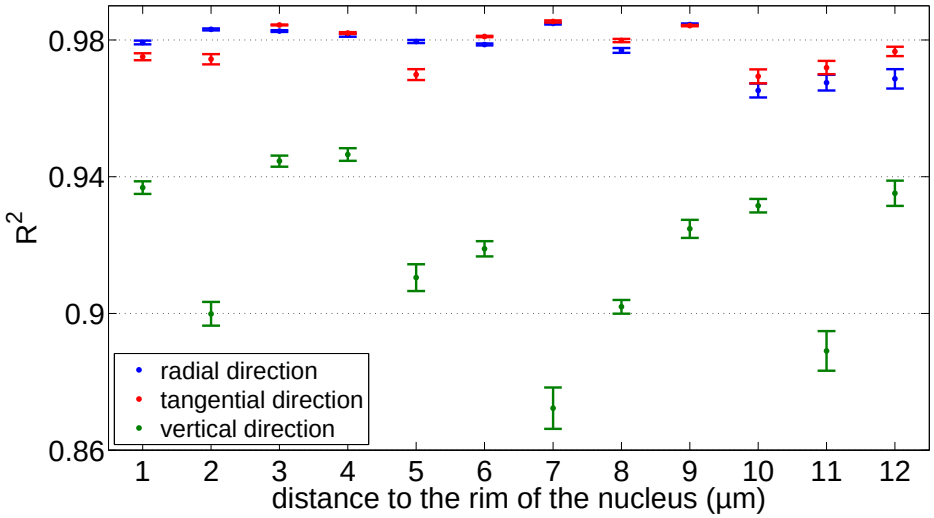



Figure 7.39: The $R^2$ values show the goodness of the fit for the three directions in a cylindrical coordinate system.

The fits for the horizontal directions are in the range between 0.96 and 0.98 with small uncertainties at short distances. The higher distance show higher uncertain-

ties which can be explained by the substrate influence and the low density of the network. The $R^2$ in vertical direction shows a high variation depending on the distance and a lower goodness of the fit compared to the other directions. Hence, the harmonic fit was not always in good accordance with the histogram determined by the measurement. A possible reason for this is the influence of the distance of the network to the substrate. Whereas in the *in vitro* assembled networks a distance of several µm could be chosen, at the adherent cell this was not possible. Consequently, the network is not as stiff as in the lateral directions, and depends on the connection to the surface.
In total, the introduction of a network force constant out of a harmonic potential, which fits to the particle motion distribution, leads to a good additional information about the network and can be used to fulfill Brownian motion simulations in confinements with repelling forces.

### 7.4.2 Surface of Equal Probability

The Brownian motion simulations can be performed either in a cuboid confinement or in any other geometry which limits the particle motion. For setting up a simulation, which should be as close as possible to reality, a cuboid confinement seems not to be sufficient and a good solution for the simulations. The idea presented in Chapter 5 to use an ellipsoidal confinement is based on the observations during the measurements of particles in the pancreatic cancer cell network and in the *in vitro* assembled networks. The particles positions during the motion in the network were used to determine a surface which spans over a specific volume. Therefore a three-dimensional histogram of the positions is calculated that is described by a $N \times N \times N$ array. Each entry corresponds to a probability of a position that shows how likely the particle moved to this position. The isosurface or surface of equal probability is the surface that results from the connection of all entries with the same probability. The probability is given by the density value. If a low density value of 0% is chosen, all probabilities of the histogram are included in the surface, because at the largest distance to the arithmetic average of the particle motion, the probability is zero. Thus, at a density value of 50% only those positions are included, if the probability to find particles at this position is higher than 50%. The higher the density value is, the lower the amount of included positions. The geometry of the observed isosurface gives an idea about the motion of the particle. This geometry can be related to the confinement geometry that are used for the simulations. Additionally, with

this method a classification of the network type - entangled or cross-linked - can be derived [40].
Figure 7.40 shows different measurements with their surfaces of equal probability.

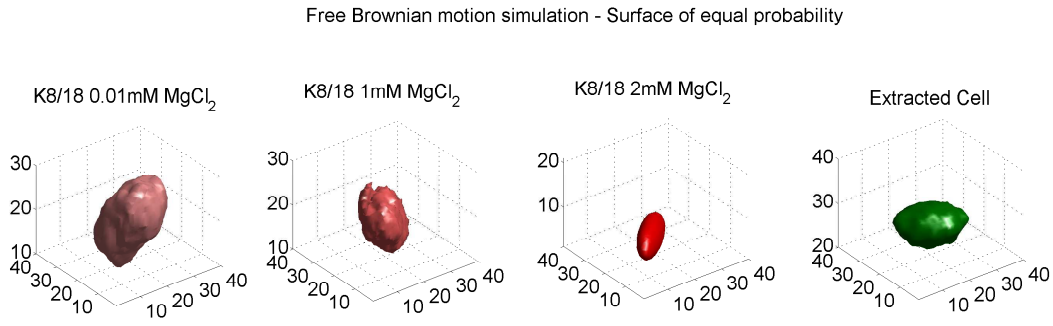



Figure 7.40: Exemplary surfaces of equal probability of measurements performed at different cross-linker concentrations of *in vitro* assembled keratin 8/18 networks and extracted cells. The surfaces of equal probability reveals that the confinement the particle moves in is of ellipsoidal shape. The higher the cross-linker concentration the more obvious is the ellipsoidal shape. At cells this becomes clearer the closer the particle is to the cell nucleus.

At first sight it is clear that the surfaces of equal probability look like ellipsoids. The size of the confinement for these surfaces of equal probability play a major role. By determining the length of the semi-principal axes of the ellipsoid, it is possible to relate the measurement and the simulation. All data points of the surface of equal probability are known, and hence a system of equations can be set up with unknowns, the semi-principal axes. In case of an overdetermined system a least-squares optimization solves the set of equations for these three parameters. An optional way to determine the unknowns is to calculate the volume and the surface area of the isosurface. In addition, with the equation for ellipsoids three equations for the three unknowns are determined. For this method there is the constraint that the calculation of the surface area only can be performed with an approximation (Knud-Thomson formula).
Another problem causes the determination of the density used for the calculation of the isosurface, because the semi-principal axes lengths are dependent on the density value. By increasing the density the semi-principal axes get smaller and applied to the simulations. That means a smaller confinement size which might underestimate

the real value. Figure 7.41 shows the calculation of the surface area dependent on the density value and the distance to the rim of the cell.

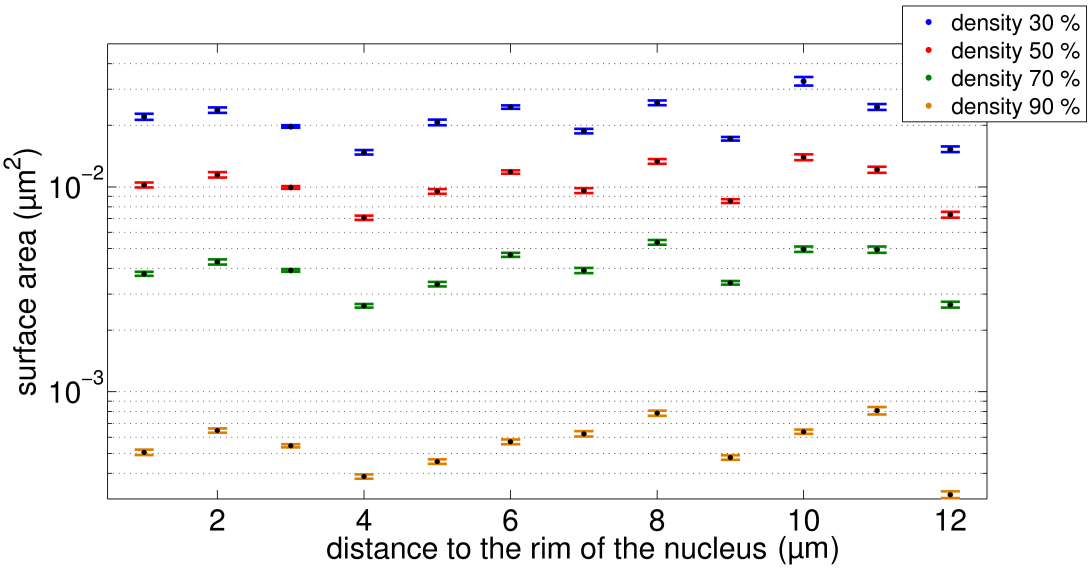



Figure 7.41: Surface area of the isosurface dependent on density value and distance to rim of the nucleus. Densities of 30% (blue), 50% (red), 70% (green) and 90% (orange) are shown.

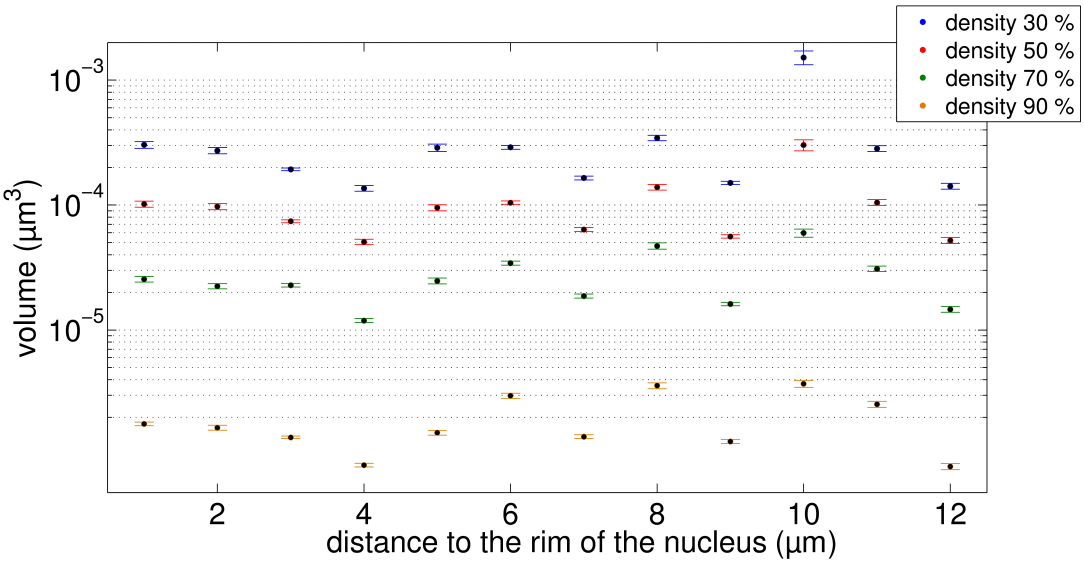



Figure 7.42: Volume included of the isosurface dependent on density value and distance to rim of the nucleus with the shown densities of 30% (blue), 50% (red), 70% (green) and 90% (orange).

The higher the distance to the rim of the nucleus, the larger the surface area is, if a decreasing network density is assumed. The particle moves further in the network because of larger meshes. For a low density this is difficult to observe at the measurements, because the particles position included for the calculation of the isosurface vary too much so that a tendency is not clear. At a density value of 90%, if only a small amount of particle positions are included for the surface area calculation, a tendency can be observed. Thus, for low distances to the rim the surface area first sligthly increases and then decreases due to the increasing stiffness of the network and the limitation the particle's motion underlies. For higher distances the area increases because the network density becomes smaller. As already observed at the dynamic shear modulus, the higher distances are difficult to interprete because of the substrate's influence.
The changes of the isosurfaces' volume are in principle similar to the observations seen for its surface area (Figure 7.42). The tendencies to decrease and increase are reasonable for the first 6 µm distance to the rim of the nucleus. For larger distances a high variation of the volume appears, although the surface areas do not change in this manner. A probable explanation for this can be the change of eccentricity of the ellipsoid.
The calculation of the averaged semi-principal axes in dependency on the density can be used to gather an estimation value for the confinement for this type of cells. As mentioned in the latter section, the coordinate transformation was also considered for the calculation of the isosurfaces and its semi-principal axes. In that way the axes $x$, $y$ and $z$ are the radial, tangential and vertical components in the cylindrical coordinate system. The dependency on the distance to the rim of the nucleus is shown in Figure 7.43, with the semi-principal axes at values of 70% density. The errors observed can be explained by the fitting of the ellipsoid to the isosurface. The radial semi-principal axis is slightly smaller compared to the other directions. That means that the particles can move less into the radial direction. This implies a network which is stiffer in the radial direction because in this direction the filaments are pre-stressed whereas in the tangential direction the network is looser connected. The calculation of the surface of equal probability gives additional insight of how the shape of the confinement can be assumed and also helps to gather the semi-principal axes of the fitted ellipsoids. A further improvement for the simulation would be a direct insertion of the shape of the isosurface which definitely is possible but requires more knowledge in programming.

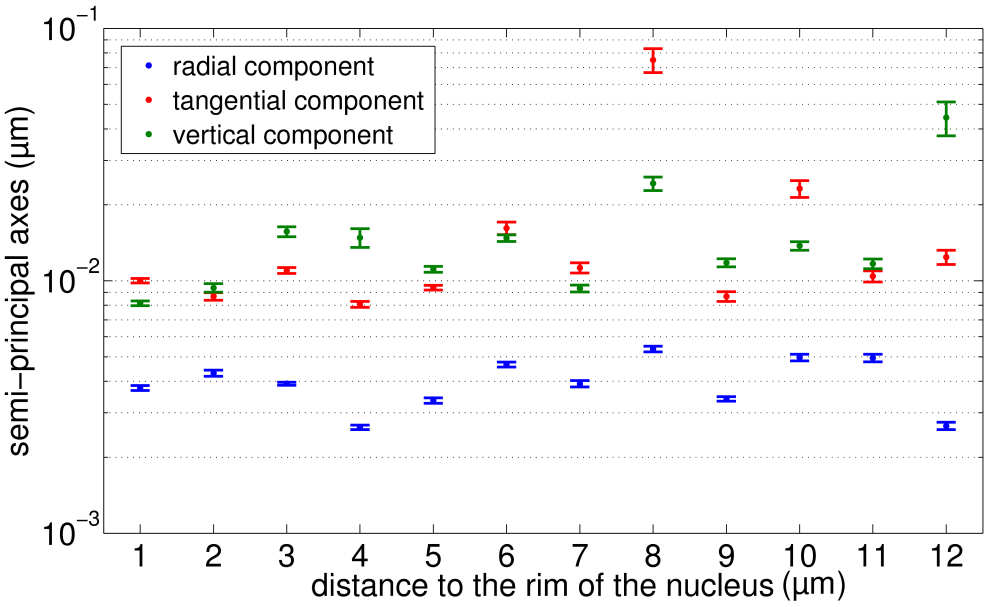



Figure 7.43: Semi-principal axes fitting an ellipsoid to the isosurface. In radial (blue), tangential (red), and vertical (green) direction the dependency of the semi-principal axes on the distance to the rim of the nucleus is shown.

Overall, the calculation of the surface of equal probability gives information about the geometry of the confinement. In case of an ellipsoidal confinement the determination of the semi-principal axes leads to information about the sphericity of the confinement. In that way a preferred direction of the particle motion can be revealed. In the end it can be shown how inhomogeneous or stressed the networks are. The ellipsoidal geometry furthermore is useful for the simulations of the Brownian motion in a confinement.

# 8 Summary

At this work two new methods for the analysis of mechanical properties have been introduced. The first method shows an alternative way to determine the shear modulus out of the mean squared displacement. The mean squared displacement is determined via the Brownian motion of particles that are embedded in the medium. The method uses a model-based approach which allows the fitting to the noisy MSD and an exact conversion into the frequency dependent shear modulus. The second method gives insight about the transfer tensor of the medium, when a reference particle is excited to oscillations. The resulting motion of the response particles is determined via the Lock-In method. A least-squares optimization leads to the transfer tensor which describes the mechanical properties of the medium.
This thesis showed that both introduced methods are suitable to describe the mechanical properties of viscoelastic systems. The system investigated were the *in vitro* assembled biopolymer networks, the extracted cell networks and the whole living cell. Additionally, the methods help in understanding the propagation of mechanical forces in the networks and the response due to the forces.
The investigated improvements, performed at the setup of the optical tweezers built the basis for all the measurements which were done at this work. For this purpose the acousto-optical deflector and a high-speed camera were added and the micro-step motors supplemented to allow an accurate positioning at the sample. Furthermore, a piezoelectric stage, implemented at the setup and the rebuilt electrical circuit for two four quadrant photo diodes, was important to increase the possible field of measurements. Signals of the photo diodes recorded with the integrated data acquisition card were directly transferred to the renewed PC system. The control and synchronization of all devices was enabled by the programs written during this work. The software (Mathworks®MATLAB) offered many features which allowed to start the analysis of the measurements directly during or after the measurement. With all this, a powerful setup was constructed, allowing a high variety of applications.
In the theoretical chapters, which introduced the novel methods, also simulations

were shown which were performed to support the ideas behind the methods and to help in understanding the results of the measurements. The development of the methods was divided into two chapters - one for the passive and the second for the active microrheology. In the first chapter the simulations of a particle motion in a cage of varying geometries and sizes explained the saturation behavior of the MSD at viscoelastic systems. An additional introduced network force constant led to a back pulling force into the center of the network. This force is responsible to the shift of the storage modulus and the shift of the minimum appearing at the loss modulus. The third part of the model-based fitting function was described by the drift occurring in the network. Therefore, the MSD increases for larger time scales. With these simulations the passive method was described - an idea to circumvent the drawbacks of the other methods namely the noise amplification by taking the derivative of the noisy MSD. Hence, a way was developed to exactly perform the unilateral Laplace transformation without any approximations. The fitting function has a reasonable physical basis and its transformation leads to reasonable storage and loss moduli and consequently, is a good way for the determination of mechanical properties.

In the second theoretical chapter another novel method was introduced and explained by simulations. The general idea to excite one reference particle in the network to oscillations and record the response of the other particles in the network offers information about properties like the network morphology, force propagation, phase change and stiffness of the network. The simulations on the one hand provided information about possible errors which occurred at the measurements and on the other hand showed how the displacement at the reference position changed the motion dependent on the distance to the reference. The error calculations compared signals with an added Gaussian white noise of specific signal-to-noise-ratios. In the case that the reference signal had a higher noise compared to the response signal, the matrix entries of the transfer tensor got larger than one which means that the result is less meaningful. Thus, the average transfer matrix was prone of errors due to high variations of the entries. Additional information could be gathered by varying the parameters like stiffness of the network or the direction of excitement.

In the experimental part of this work the application of the developed methods to real measurements was described. Since there were two new methods, the chapter was divided into two sections dealing with the passive method and the active method and a third section with further important results of the measurements which support the simulations.

The media in the first part of passive microrheology - bi-distilled water and the sac-

charose solution - were chosen because of their simplicity. On the one hand water as a viscous fluid and on the other hand saccharose as a fluid-like viscoelastic system. The resulting shear moduli of water clearly showed a storage modulus below the loss modulus without crossing each other apart from the region of a high frequency when the ballistic regime played a role. For longer times the MSD of water showed a constant slope and the calculation of the viscosity out of this slope was in the range of 0.9 mPa s to 1.1 mPa s which is comparable to the predicted value of water at room temperature.
The measurements in saccharose solution, a fluid-like viscoelastic medium, resulted in a MSD with a slightly decreasing slope for long times and a lower magnitude than water. The calculated effective viscosity was at 10.9 mPa s with a theoretical value of 12.6 mPa s. The difference between the two values might be based on wrong temperature values or false assumptions for the ratio of the saccharose-water mixture. The resulting shear moduli showed correct results meaning the diffusive part of the shear modulus is higher for the major part of the frequency range, but gets crossed by the storage modulus at a lower and a higher frequency. Again the ballistic regime could be resolved.
Those tests showed that the method works for simple systems. Therefore the measurements were performed at the *in vitro* assembled networks, which are entangled when no magnesium chloride is insert and cross-linked, when an amount of $MgCl_2$ fixes the contact points of the filaments. The cross-linked networks were gel-like viscoelastic media and therefore a plateau modulus for G' appeared in the mid-frequency regimes. In the same frequency range the loss modulus G" reaches a minimum which gets shifted due to parameters like the salt concentration, the viscosity and the network force constant. The measurements showed an increasing plateau modulus for an increasing amount of $MgCl_2$ in the range of 0.02 Pa up to 0.50 Pa. The introduced model-based function was fitted to the MSD and resulted in a goodness of the fit provided by the $R^2$-value of at least 0.88. This showed a good accordance to the function, although, at concentrations of around 0.5 mM $MgCl_2$, the fitting function could be improved with additional terms. The result of the measurements showed that the model-based method is suitable for the *in vitro* assembled intermediate filament networks.
The investigation at extracted pancreatic cell networks leads to insights to the dependency of the plateau modulus on the distance to the rim of the nucleus. Additionally the goodness of the fit reflected the quality of the method. The $R^2$ values determined by the fit were lower compared to the values of the *in vitro* assembled networks. This could be explained by the high diversity of the morphology of the

cells. The dependency on the direction the cell moved before extraction and how this influences the network was neglected completely. Most likely this introduced errors which decreased the goodness of the fit. Although the goodness of the fit was lower, the measurements clearly showed that the network stiffness decreases for larger distances to the rim of the cell. The observed plateau moduli were in the range of 0.65 Pa for the stiffest case and lower for large distances. The assembly of intermediate filaments at the rim of the intermediate filament network and the corresponding disassembly at the rim of the nucleus leads to a less dense network around the nucleus like discussed in literature. The measurement of the stiffness showed this region in the cells and therefore confirmed this assumption.
The passive method was also applied to measurements at human granulocytes. There the particles were placed on the membrane of the living cells and their motion recorded. Although the motion on the cells membrane is not a suitable application for the model conditions - especially the continuum around the particle assumption did not hold - the method worked good in sense of the goodness of the fitting and the physical meaning behind the measurements. Thus, the addition of colchicine stiffened the cells and changed the motility. This behavior was observed by both the measurements in the optical stretcher and the passive microrheology showed in this work.
To confirm the model-based passive method simulations were performed which simulated the three terms of the fitting function. A physical interpretation for each of the terms could be found with the calculations described in the last part of the chapter. The elastic part of the network was approached by the assumption that an intermediate filament network has a harmonic potential. This leads to a repelling force applied by the network at the particle. The force constant or spring constant could be derived and added to the simulations. The resulting network force constants were in the range of 1 pN/µm to 20 pN/µm, which is also the range of the optical tweezers force constant. Another term, the third term of the fit function, was described by the calculations of the motion of the particles. The motion of the particles in an ellipsoidal confinement led to the saturation of the MSD. The usage of so-called isosurfaces confirmed that mostly the confinement has an ellipsoidal shape. The viscous term, to complete the fitting function, was assumed to describe the drift the network is exposed during the measurement. This part leads to an increase of the MSD for long times.
The active microrheology measurements were also divided into two measured media. On the one hand with the oscillation of the particle in bi-distilled water, the requirement that the optical tweezers setup really works was proofed and on the

other hand the measurements in two *in vitro* assembled K8/18 networks should give insight into the dynamics of the observed media. The amplitude given by the oscillation of the dynamical optical trap led to a correct response of the particle which was excited. Since the medium was water, the particle should follow the trap without constraints as long as the frequency of the oscillation is low and the trap stiffness is high so that friction is negligible. The analysis of the displacement of the particle confirmed the predicted behavior and the calculation of the transfer matrix resulted in the identity matrix. Another important result was that the oscillating trap did not steer the particle along the axial direction, but only in the lateral directions since the displacement only can be performed in the $x$-$y$-plane.
The measurements at the *in vitro* assembled intermediate filament networks were analyzed with the result that the higher the added $MgCl_2$ concentration, the lower the response of the reference particle which deforms the network. Without salt the given amplitude of 127 nm could be followed for the most cases and the response of the reference particle was at around 100 nm amplitude. Thus, the deformation of the network resulted in a displacement of particles with a specific distance. The transfer tensor between the motions could be calculated and the dependency of the amplitude ratio on the distance of the particles be determined. A clear tendency could be observed that these ratios decrease with distance, that is also predicted in theory. The theoretical curvature was shown with a value of the plateau modulus that fit to the measurements. This plateau modulus did not fit to the passive microrheology measurements, which indicates that the two methods are not comparable yet. The measurements at the higher $MgCl_2$ concentration showed that the reference particle almost never followed the optical trap because of the stiffness of the network. In that way the small amplitudes of the reference and the occurring bundling introduced huge variations of the transfer matrices with high uncertainties. Those uncertainties made it very difficult to interpret the data and confirm a tendency that the higher the distance is, the higher the decay of the response motion. Additionally the faster decay of the response of motions perpendicular to the excitation compared to the in-excitation direction could be observed, but was handled with care because of the high errors. In both kinds of networks the higher harmonics were lower than the first, but for higher salt concentration the first harmonics amplitude is double the size of the higher order. Hence, the denser the network is, the more higher harmonics were introduced at this excitation amplitude. The preliminary measurements with this method proofed that the method is a suitable tool to measure the dynamics and the force propagation in the *in vitro* assembled networks. Further measurements in cell networks are also possible and have a high content of new insights helping to

understand the cells dynamics and force propagation.

In the end the interplay between the built setup, the introduced methods, the simulations and the measurements improved the understanding of the physical network properties of intermediate filament networks which are located on a sample assembled *in vitro* or in the extracted cell. Only if theory, the experiments and the simulation operate in accordance, the work has a meaningful output.

# 9 Outlook

The treatment of the pancreatic cancer cell and the *in vitro* assembled K8/K18 networks as a viscoelastic medium and the introduced methods open a huge field of possible applications. These applications should lead to a further understanding of the networks in sense of their morphology, assembly, the dynamics due to stress and the function in the whole cell. Some of these ideas are presented in this chapter as an outlook for future works.

For the *in vitro* assembled networks it was seen that for some $MgCl_2$ concentrations the derived fitting function fitted not perfectly for the intermediate time scales. This might be due to additional relaxation modes the networks contain. Hence the fitting function has to be extended with additional terms describing this behavior of the network. In this sense additional terms may be exponential functions with varying relaxation times or the introduction of a power law with specific factors. In general it is not challenging to increase the number of terms to gain a better fitting, but a crucial point is to explain the physics behind the function in a correct way.

Regarding the measurements of the *in vitro* assembled networks and the passive microrheology, the temperature dependency and the temporal development of the assembly are of larger interest. Moreover, the system to control the temperature shown in Chapter 4 could be used to perform microrheology at specific temperatures. The temporal development of the assembly could give insight if and how the networks change from an viscous-like fluid to a gel-like solid and how all parameters influence the formation of the gel-point.

The active microrheology method which was developed during this work can be used in the future to, one the one hand, increase the number of measurements which improves the goodness of the statistics for varying parameters like $MgCl_2$, temperature, protein concentration and angles of excitation. Additionally the influence of the laser intensity might play a role at the determination of the transfer tensor. On the other hand, the dynamics of the network can be investigated in sense of phase shifts dependent on the distance of reference and response, velocity of the

signal passing through the network and the propagation of the force in the network. The latter point is interesting regarding the measurements in cells. A theoretically predicted force channeling ([117]) could be confirmed or declined, if the particles were located radially in the network. For this it would be a challenge to find a way to place particles as wished or find a dependency of particle size and particle position in the cell network.
The passive microrheology method applied to extracted cells on varying substrates like gold or fibronectin could give information whether the network meshes are smaller and thus the network denser, or whether the morphology completely changes with a different substrate. As already shown in [118] and [119] measurements in living cells are possible, but have to be handled with care, because inside the living cell it's apparatus influence the motion of the particles. Since the microrheology is difficult at this point, there are other interesting applications like the alignment of the inserted particles dependent on the direction of the cells motion. Here the idea is to track the particle position for cells moving in a known direction. If there is a dependency, one could determine the direction of motion by the alignment of particles which helps at the extracted cell network to develop a model for the shear modulus in the cell dependent on radial position and angle to the cells main axis. This possible application can be realized with the usage of a particle coated with attractants and the dynamic optical trap.
Since 2005 when Woell *et al.* showed the dynamics of the keratin filament network with its formation at the outer part of the cell, a drift towards the nucleus and a disassembly at the rim of the nucleus ([120]), an application which could lead to interesting results, is the manipulation of the assembly or disassembly of the keratin network. This could be performed by a disturbing oscillating of particles at the nucleus rim or close to the outer part of the intermediate filament network. With an optical tweezers setup and multiple traps which can oscillate in several directions that can be realized. This oscillation could change the behavior of the cells and disturb their growth or even animate them to faster division.
In the end the resumé is that with the introduced methods there are plenty of new opportunities and challenges to gain newer and more important results and information about the keratin networks morphology, the dynamics and their role in life.

# 10 Acknowledgements

In this part I want to thank all the persons who helped or supported me during this work by working actively at my project as well as by providing important information via fruitful discussions. Additionally I want to thank those who braced me for the work and gave me the feeling to do things right. Special thanks go to

- **Prof. Dr. sc. nat. ETH Zürich Othmar Marti** who offered me the thesis and already at this point had the confidence that I can manage it. During the whole four years the discussions and his excellent supervision always helped a lot and provided new ideas which wouldn't be realized otherwise. With his wide-ranging expertise he steered me into the right direction, supported my own ideas and stopped me before running into a blind alley. I also want to thank him because of the nice atmosphere he creates in the department, the feeling to be involved and to be a part of the team.

- **Prof. Dr. Michael Beil** who always welcomed discussions about work and therefore improved the results and brought up new ideas which opened new perspectives. He supported me in my decisions and often gave me the chance to contact many people. This helped a lot because I always got new information, could exchange opinions and therefore, develop new ideas.

- **Prof. Dr. Kay Gottschalk** who, especially in the last year, opened his door to discuss problems, referred his knowledge and improved the atmosphere during work.

- **Dr. Manuel Gonçalves** who supervised my diploma thesis and since that time, always has been prepared for any question which came up. For the best choice of instruments purchased he provided his knowledge. Additional thanks for the discussions concerning the thesis itself.

- **Tamara Stadter** who is one of the most important persons in the department. She has known how to handle contracts, billings, the management of trips and everything around that. She has offered a nice atmosphere and made life in the department delightful.

- **Thomas Fröhlich** who helped a lot in improving the setup and writing the scripts for controlling the devices. The current possibilities to measure with synchronous working instruments and having a nice GUI wouldn't have been possible without his support and his diploma thesis.

- **Hans-Jörg Drotleff** who improved the upper part of the setup and supported the permanent advancement of the optical tweezers. The discussions opened a lot of new ideas for improving the measurements.

- **Dennis Müller** who investigated the possibilities for the calibration and analysis of the optical tweezers and helped me improving the setup at additional tasks.

- **Samuel Vollmer** who did a lot of measurements during his bachelor thesis which improved the statistics and opened new insights into the mechanics of the cell. I want to thank Thomas, Hansi, Dennis and Sam for the nice atmosphere they brought into the department and for their excellent work as a team.

- **Ulla Nolta** who very very often explained the biological background of the cells and their networks. Her reliable way to work in the S1 lab and to provide the cells for the measurement was a big relief during the work.

- **Dr. Anke Leitner** whose collaboration and discussions led to good results and helpful insights into *in vitro* assembled networks.

- **Andreas Häußler** whose expertise during the diploma thesis opened first insights towards single filament dynamics. The discussions helped a lot to improve the system and being a good friend made a good collaboration.

- **Ines Martin** for her help providing the *in vitro* assembled networks for the measurements and her collaboration concerning the supervision of the students. In addition I want to thank her for proofreading this work.

- **Dr. Stefan Fischer** who always exemplary provided his wide-ranging knowledge - not only to help me during my work, but to everyone who needed help. Additionally I want to thank him for proofreading the thesis.

- **Dr. Manuela Pluntke** who helped with her fruitful discussions and gave me insight to her field of work which finally bore fruits. Also a big thanks for her kind associate to everyone. I especially want to thank the latter five, **Dr. Christian Holzheu**, **Dr. Alexander Schmatulla** and **Dirk Doser** for the warm welcome they offered me when I started my thesis and the good time we all had during the first years.

- **Thorsten Robel**, **Sandra Bührdel**, **Eva Liebald** and **Christoph Meschenmoser** who did a lot of pioneering work both at the setup to further improve it and to open a huge field of new applications which would not be possible without them. Their fruitful discussions, their works and friendship showed that progress can only be achieved with more than two hands. Additional thanks to the first two for the proofreading of my work.

- **Martin Müller** who did a great job in repairing things we broke. Additionally he always supported me at technical decisions and helped at the development of several parts at the optical tweezers. Additional thanks to Thorsten and co. (with **Frank Zocholl** and **Reiner Keller**) for the last year in which we really had a good atmosphere.

- **Peter Schützner**, **Maryse Lapierre-Landry** and **Tobias Pusch** who did a lot of programming and measurements for a better statistics and functionality of the optical tweezers.

- **Iris Mayer** for being always there for me especially when work didn't work the way I wanted to have it. I want to thank her for the excellent support and for giving me the encouragement to manage the thesis and whole life. Additionally I want thank her for proofreading the thesis which helped a lot because of her knowledge about English grammar.

- **Alexander Gerstmayr** for sharing 25 years of life-time to be there as the best friend one can have. Big thanks for supporting and keeping me in a good mood during the work, during free-time and everywhere else. Furthermore, I want to thank him for the discussions about the thesis.

- **Tobias Bleher** and **Jenny Führer** for the proofreading of the thesis although it is very difficult for someone who is completely outside of the subject area. Additional thanks for the immediate attendance to help me at the this.

- my **parents** and my brother **Florian Paust** who always stood behind me and supported me at everything I did in my whole life. Furthermore I want to thank them for the many hours they listened to my stories about work and the university.

- my **friends**, especially **Stefan Staib**, **Sandro Strazzeri**, the **soccer clubs** and the upper mentioned (Iris, Alex, Velasco, Jenny) who, through all the years, gave me the power to reach for the stars, because they showed interest, friendship and the willingness to understand me. In addition they helped me to free up my memory if needed.

- **Dr. Masoud Amirkhani** for the interesting discussions about our works and his knowledge about dynamic light scattering which helped me in understanding this topic.

- **Patrick Paul** and **Karin Fluhr** who gave me during the supervision of their works new insights to other interesting fields and helped to get an overview and knowledge about these. Their discussions often opened the eyes for improvements which could also be realized at all kinds of setups. Thanks to Patrick for the correction of the thesis.

- **Prof. Dr. Harald Herrmann**, **Dr. Norbert Mücke**, **Prof. Dr. Sarah Köster** and **Stefan Winheim** for the good collaboration, the interesting discussions and the support at the *in vitro* assembled keratin 8/18 networks.

- **Prof. Dr. Paul Walther** who helped a lot at the interpretation of the SEM pictures and gave excellent instructions for the usage of the electron microscope which provided absolute incredible pictures of the nano-world which supports the macro-world.

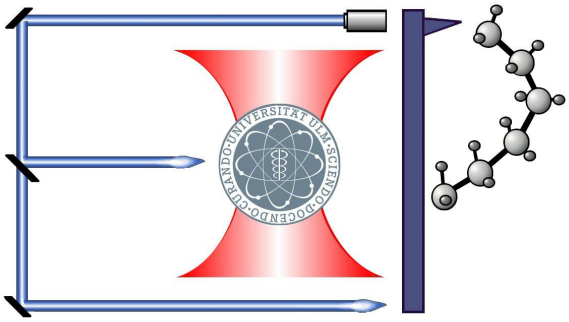
- **Anne-Marie Saier**, **Monika Asbach**, **Maria Hammer**, **Elke Wolff-Hieber** and **Iris Repple** who always immediately helped at technical questions, problems and decisions.

- the whole **Institute of Experimental Physics**. It became a second family for me because of the nice atmosphere and the good discussions.

- the **mechanics workshop** and **electronics workshop** for giving us the chance to realize all the parts the setup needed for improvement.

- the **SFB518** and **SFB569** for the financial funding through the four years.

I want to thank everyone who supported me, not only during my work, but also in all situations during life which helped making every day's life easier.

# A Correlative Microscopy

The optical tweezers setup presented in the latter sections was built by Maghelli [122]. The improvements of the setup during this work contained the attachment of the high-speed camera (with illumination device), the incorporation of the microstep motors and the piezoelectric stage. Furthermore, for dual trap applications the AOD was included and a second QPD added. For recording the QPD signals the data acquisition card was involved into the setup. Since all devices used separate software to control the corresponding device a commercial programming and data analysis software (Mathworks®MATLAB, varying versions) was implemented to control and synchronize the specific devices. The applications shown in the following and in chapter 7 make use of the self-made programs and scripts developed in this work.

Correlative microscopy describes the method to perform a measurement at the same sample or object with two different devices. In that way the results of two methods or devices are comparable or in a second case, one device can be used for verifying the results of the other method. In correlative microscopy two microscopes are used to examine the same region or the same position of a sample, which was the challenging part in case of the optical tweezers and the electron microscope used in this work. The microrheology measurement was performed at several specific cells in the sample, but only a small number in comparison to all could be observed. To verify the result of the measurement the same cell was to be identified in the electron microscope.

Before the measurement at the optical trap the cells were prepared an put on a cover slip ($24 \times 24\,\mathrm{mm}$) which then was mounted on the sample stage inside the sample holder presented above. The cover slip was scratched with six scratches before the cells were grown on it. The alignment of the scratches on the cover slip was chosen to limit the area of cells measurable. The area is of the size comparable to the sample size of the electron microscope. For this four scratches were necessary. After the measurement the sample was treated with fixative and an alcohol series to prepare it for the electron microscope [123]. After fixation the cover slip was

broken along the scratches and the remaining small glass ($5 \times 7$ mm) fitted into the electron microscope. The other two scratches built the axes of a coordinate system on the small glass. The origin of this coordinate system was placed in one corner and due to the rectangular geometry of the small glass the positions of the cells were well-defined.

The position of a cell on the glass inside the sample was determined via the coordinate system and with an overview scan performed by the micro-step motors, the PIFOC, and piezo-electric table and the high-speed camera. These devices were needed because a sample inside the microscope is always slightly tilted (around 5 µm in height difference for 1 mm distance). Therefore the scanning via the micro-step motors for an area of several mm led to an overview over the surface. Since this overview is of a large tilted area, the step motors alone would run out of focus. Hence, the PIFOC simultaneously changed the height of the objective during the scan. Via three determined heights of the sample and a fitted plane representing the substrate tilt, the focus correction was performed. Additionally the piezo-electric stage analyzed the images recorded with the CCD camera and adjusted the correct height for each picture. In the end the single recorded pictures were stitched together to an overall overview where the scratches and the coordinate system were determined. This led to the information of the position of the cells needed for the electron microscope. The following pictures show a measurement of a substrate containing pancreatic cancer cells and a test sample with Fisher projection patterns (FPP, [124]), where significant structures were determined in both the optical tweezers and the scanning electron microscope.

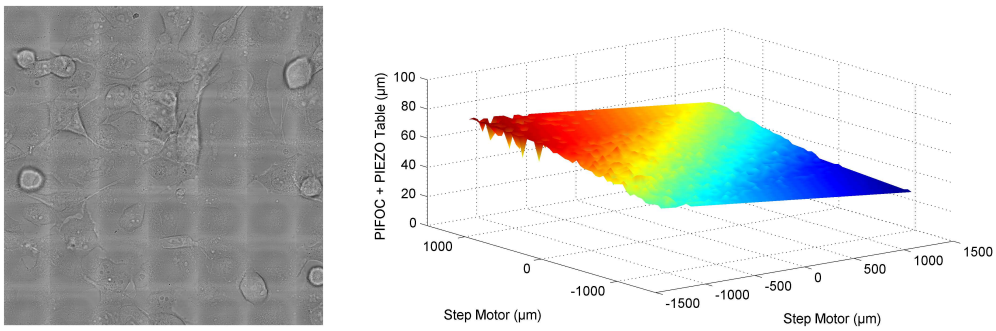



Figure A.1: The overview picture of a sample scan at the optical tweezers. Left: Only a small part of the whole scan is showed to illustrate the principle of the surface scan. Right: During the scan the tilt of the sample is recorded. The cover slip is slightly bended due to the contact with the lower objective.

On the left side the surface with cells is shown. Independent on the position on the sample the surface is in the right range for the focus. Since all images are a series of single pictures, the resolution is not decreased and hence, no structural information is lost. Here a small part of the surface is shown to illustrate the method. The complete scan was over an area of $1500 \times 1500\,\mu m$. The right graph depicts the tilt of the sample determined during the scan. The fact that the cover slip is not only tilted but also slightly bended underlines the importance of the piezo-electric stage which adjusts the height.
With the significant structures (dislocations) of the FPP and their positions identified at the optical tweezers and in the electron microscope the deviance between the points at both systems were determined. This gives an idea if cells can be relocated and how accurate this is.

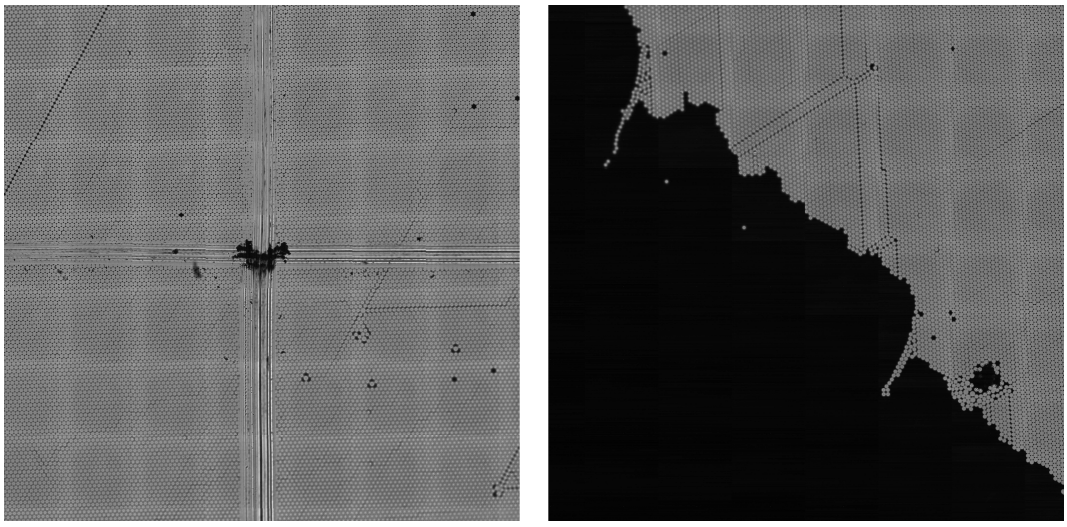


Figure A.2: The overview picture of a sample scan at the optical tweezers. Left: The FPP shows dislocations which are a good reference for the determination how accurate positions can be relocated. The origin of the coordinate system is marked by a scratch. Right: Rim between mono-layer of the FPP and several layers without transmitted light [125].

The left picture of Figure A.2 shows the FPP and the small errors due to the image stitching and varying foci. The radius of the cavities was $3\,\mu m$ and the scan range $500 \times 500\,\mu m$. In the center the scratch can be seen which is the coordinate system's origin. On the right side an additional overview scan is presented for illustration.
The chosen unique structures for testing their location are shown in Figure A.3. At both systems the optical tweezers and the electron microscope the dislocations can

clearly be identified. Thus the distance of the center of the origin to the center of the dislocation was determined with the help of the micro-step motors of the optical tweezers and the electron microscope.

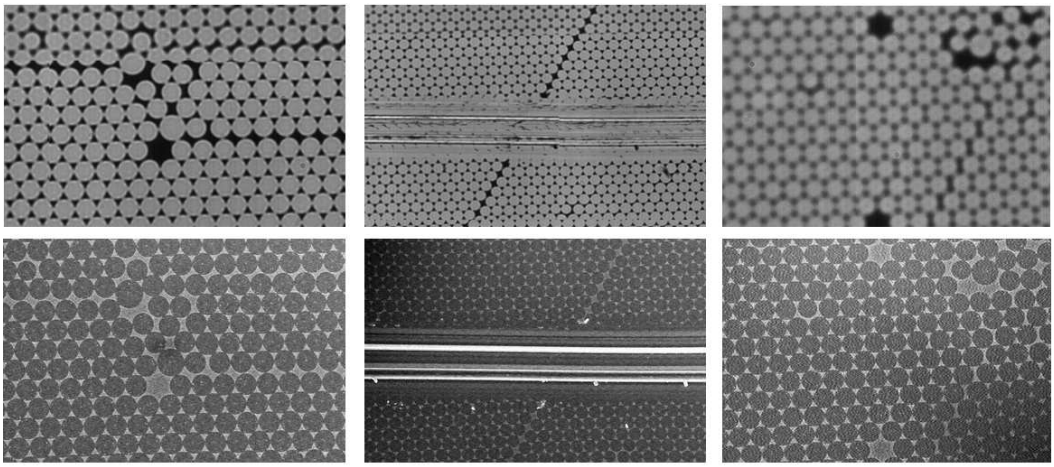


Figure A.3: Dislocations of the pattern in the optical trap and the electron microscope. The upper line illustrates screenshots at the light microscope of the optical tweezers. The lower row shows the same dislocations in the electron microscope.

The positions of the dislocations were determined as distance to the origin of the coordinate system with its $x$-and $y$-components. With this distance a position regarded in the light microscope can be found in the electron microscope with an accuracy of 10 µm. Since the cell size is about 25 µm, a cell in principle could be found in the electron microscope. At real measurements is was difficult to find the cell. This could be explained by a loss of cells during the preparation process, and by a morphylogical change of the cell, e.g. a shrinking during the preparation. These are problems which should be solved with several measurements and a improvement of cell preparation for the electron microscope. Overall, the correlative microscopy is helpful to determine whether measurements in *in vitro* networks and cells are reasonable, and to decrease the high uncertainty of the measurements.

# B Polymer Brushes

Considering the attachment behavior of cells on surfaces of biomaterials polymer brushes are used as a link between the cells and the biomaterial. Since the polymer brushes vary in its stiffness and the adsorption behavior dependent on the pH value of the medium, the attachment of cells or proteins changes. Hence, a better insight into the behavior and influence of the brushes towards other materials is gained by analyzing the interaction during approaching these materials [127],[128]. In this work an additional application implemented with the optical tweezers setup was to analyze the influence of the brushes towards polystyrene particle during approaching to the brushes field. The particles chosen for these measurements had a radius of 500 nm and were trapped in the optical tweezers setup described in Chapter 4. The intensity of the laser beam was at 30 mW which corresponded to a force constant of around 3 pN/µm.
The polymer brushes of interest were brushes containing polycarboxylate poly (methacrylicacid) (PMAA) as substrate coating with varying pH values (pH 7.3 and pH 5) of the buffer (PBS). The produced surfaces and the measurements were in collaboration with Annina Steinbach (of the Institute of Physics, Chair of Solid State & Materials Chemistry, Augsburg University). Since the polymer brushes fields were aligned in a pattern of 50 µm width with glass surfaces of 50 µm width in between, the interaction of the glass and particles additionally could be tested and compared to the brushes measurements.
The measurement process worked in several steps. First, a calibration of the optical tweezers was performed as described in Chapter 2, and afterwards a particle was trapped at a distance of around 2.5 µm above the glass or brushes surface. The interplay of the piezoelectric stage and the AD/DA measurement device allowed to record the motion of the the particle in the axial and lateral directions and in the mean-time approach to the surface in 5 nm steps. Out of the measured motion on the one hand the displacement of the particle in the trap could be detected and on the other hand the potential of the trap and surface was calculated for every

step during the approach. The displacement of the particle is the average value of the positions the particle was due to the Brownian motion inside the trap. When the optical tweezers moved towards the surface, there was an influence of it which displaced the particle out of the trap focus.

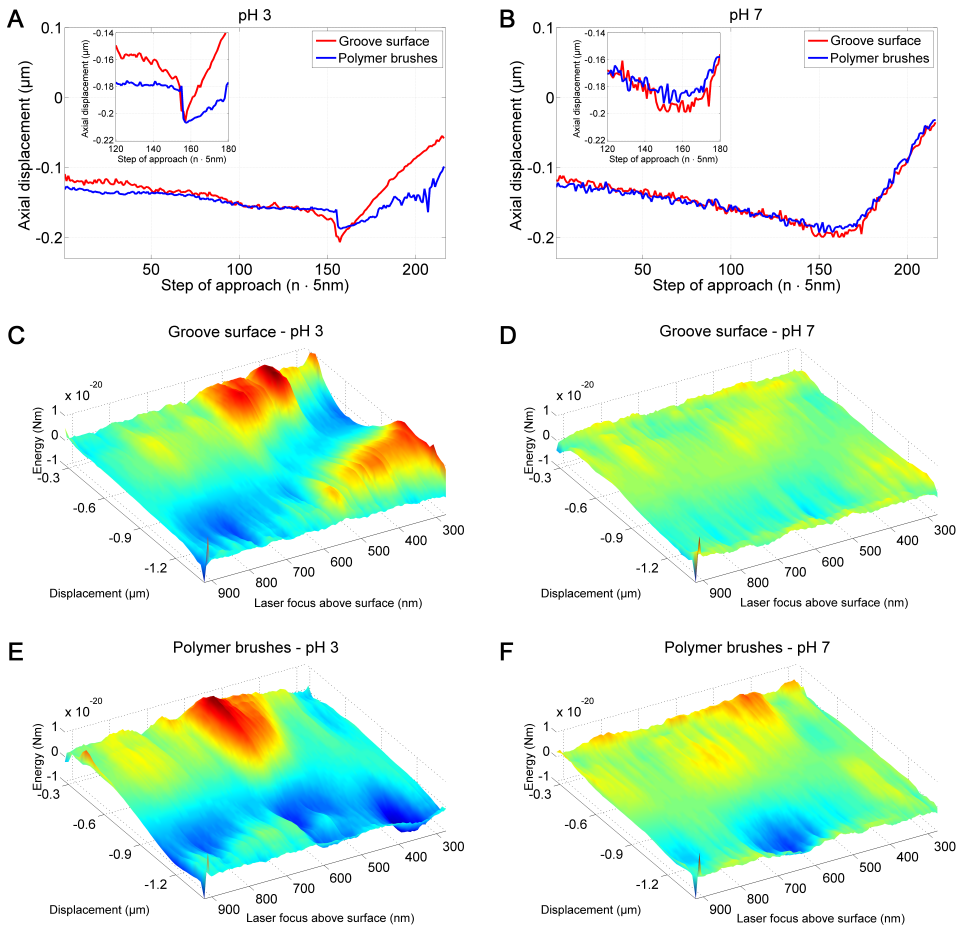



Figure B.1: Response of the particles upon approaching a PMAA coated polymer brush substrate and a groove surface at pH 3 (left) and pH 7 (right). A and B: The displacement of the particles due to the interaction between polymer brushes (blue) and groove surface (red). The insets depict a close-up of the snap-in for all cases. C-F: The potentials of the particles during the approach towards the substrate. The higher the potential (yellow to red), the lower is the probability of a displacement of the particles onto this region. Vice versa the lower the potential (green to blue), the more often the particles are located in that potential well.

Figure B.1 A and B show the change in displacement of the particle during the approach to a glass surface and the polymer brushes field with 5nm steps at a pH of 3 and 7.3. The inset shows a zoom into the snap-in region. For pH 3 the displacement minima were shifted towards each other to compare the strength of the snap-in of both cases. The change of the pH influences this displacement of the particle which leads the attractive forces for the particle. In Figure B.1 A, the curves were measured at pH 3 and show a point where the particle displacement changes drastically and reaches a minimum. This point is the snap-in, where the particle is pulled towards the surface due to the attractive forces. After the snap-in the curve for the glass surface and the polymer brushes field differed. When the particle was pushed towards the glass surface it could not follow the optical tweezers any more which further moved on decreasing the height above the surface. Relative to the trap focus the particle gets displaced in axial direction, linearly to the trap motion. In the case of a brushes field the particle also got pushed against the softer field, but here it could slowly flatten the brushes so that the displacement relative to the optical trap increases less. For the measurements at pH 7.3 (figure B.1 B) both curves showed the same behavior for both kinds of surfaces and compared to pH 3 less attractive forces. This is explained by regarding the charges the particle and the brushes which were both slightly negative. For the brushes this resulted in a swelling behavior which stiffened the field. Thus, a difference between glass and brushes could not be detected any more.
The potentials plotted in figure B.1 C-F give an overview of the energy landscape (z-axis) the particle is involved in during the approach (x-axis) dependent on the displacement in axial direction (y-axis). The energy landscape therefore only shows the influences of the surface - the potential of the optical tweezers is subtracted. As long there is no interaction between the glass or the brushes the energy should be the same independent on the displacement of the particle. In the case of interaction the particles motion in the trap is limited by an attractive or repulsive force and then the potential increases and builds a wall on one side of the displacement, because the probability to move there gets lower. At the measurements at pH 3 (C,E) the attractive forces of both polymer brushes and the glass surface could be recognized when the particle touched the surface. The potential wall increases immediately after the snap-in and the particles motion got strongly restricted. In the case of the glass surface the potential minimum shifted because the particle was pulled against the surface. Relative to the trap position the particle moved above the trap which was already explained at the displacement curves. At the polymer brushes the potential does not show a clear minimum because at the moment when the particle

got into contact it can move trough the brushes an the motion is less limited.
At pH 7.3 (D, F) the interactions are weaker compared to pH 3 which made the potential walls less steep. The behavior after the snap-in is similar to pH 3 which was not expected for the measurements. The repulsive force in case of pH 7.3 should be higher for the polymer brushes so that it could not be possible to approach to the field. A probable solution for the observations done during the measurement could be that the interactions are so weak that the particle mechanically sticks in the brushes field when gets attached to it.
The measurements at the polymer brushes showed that the optical tweezers beside the AFM is a suitable instrument to determine interactions between arrays of polymers. The change in pH value could be resolved and confirmed the measurements of the zeta potential described in [126]. As a possible alternative to the measurements of a trapped particle approaching to the surface one could use two particles coated with polymers and bring them slowly together with a dual optical trap based optical tweezers.

# C Multiple Optical Tweezers

In the outlook possible applications were mentioned where a multiple trap setup could be used to gather additional properties of the observed media like the *in vitro* assembled K8/K18 networks, the cytoskeleton or the membrane of a specific cell type or the interactions between particles covered with polymers. The multiple trap can be realized with different kinds of setups. An instantly apparent idea to realize a multiple trap is to use several light beams originating from several lasers. This method was already mentioned in [129] as easy but expensive method.
The usage of a spatial light modulator is a more up-to-date method. With this the phase component of an expanded laser beam is manipulated by the modulator which encodes the pattern for the information about size and positions of the traps. One of the drawbacks is that the realization of large trapping arrays causes errors and delays at the complex computation processes which make the traps unstable [130].
Holographic optical tweezers also can be used to gather a multiple trap system which is also a good method. A holographic plate controlled via a PC-system creates an arbitrary optical landscape which influences the laser beam. The real-time control and manipulation of the traps is a big advantage at this method [132], [131]. Some others are presented in [133].
In the setup used for the measurements presented in Chapter 7 and shown in Chapter 4 an acousto optical deflector system of two orthogonally aligned AODs was used. With these two AODs it is possible to steer the beam to several positions in the sample by modifying the angle of the outcoming beam. Depending on the frequency the angle changes it is possible to illuminate specific positions almost at the same time. A particle in the optical trap does not recognize the absence and the return of the laserbeam when the frequency is chosen high enough [134]. This method was tested beside the other measurements performed at this work. The two available function generators (Stanford Research Systems, DS345) were synchronized and with either a sinusoidal, a triangular or a rectangular signal sent to the AOD a steerable second trap could be realized. Additionally, the possibility to use an arbitrary

function provided by the computer made it possible to place the trap at several positions. By applying a high frequency to the AOD a multiple optical tweezers was ensured. The realization of several synchronous working traps is shown in Figure C.1.

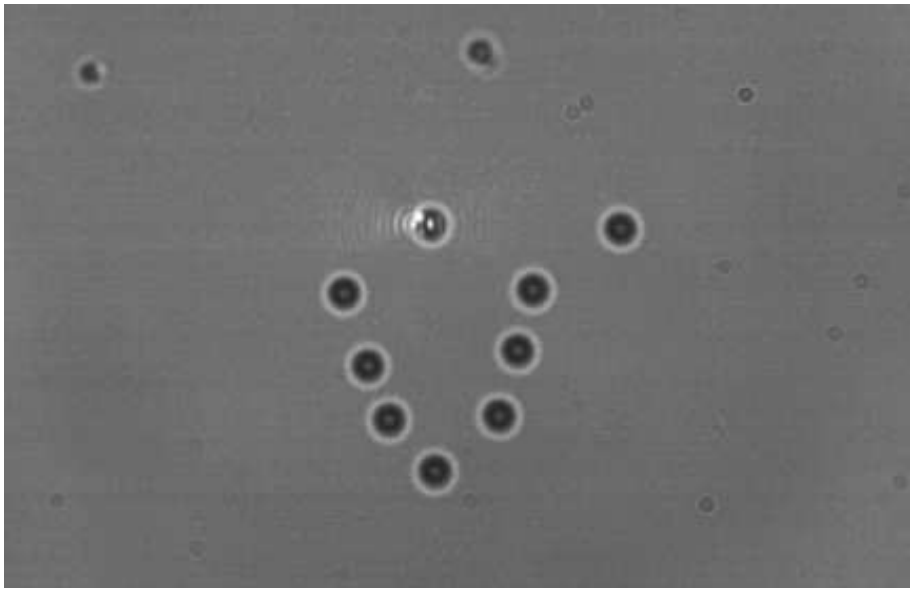


Figure C.1: Screenshot of particles of 1 µm diameter located in water. The laser beam jumps at a high frequency so that multiple traps can be generated. The laser beam of the static trap can be recognized in the center. The dynamic multiple optical trap are aligned as an 'V'.

In this figure the letter 'V' can be observed with a central trapped particle due to the static optical trap, written by the positions of the particles. The program running in the background allows to mark positions for the traps on the screen, and the AOD steers the beam to the specific positions. By changing the amplitudes of both function generators it is possible to wiggle the particles at their positions.
The usage of an multiple optical tweezers offers a lot of applications which can be used to further describe polymer networks, cell stiffnesses or polymer brushes field like the applications and methods used in this work already did.

# D MATLAB Programming

As mentioned in Appendix A the simultaneous usage of several devices of the setup allows complicated applications at the optical tweezers. The official software of the devices often do not support to synchronize one device with another. Therefore, one part of this work dealt with the programming of scripts to address each device and, dependent on the purpose, synchronize several devices. The programs written during this work made usage of Mathworks®MATLAB because of the simplicity to realize difficult issues and the possibility to perform further analysis during or after the measurement. In this chapter parts of the programs are presented. This will give an insight to the concepts used to keep a high performance at the devices.
The optical tweezers setup (described in Chapter 4) consists inter alia of the piezoelectric table, a piezoelectric stage, the step motors, the CCD camera, the laser, the photo diodes and the acousto-optical deflector. These devices can be controlled via graphical user interfaces (GUI) in MATLAB and can run simultaneously. The realization of the GUI-controller can be described in several steps and is similar for each device.

**Initialization**
As a first step, the initialization of the device has to be performed. This includes the connection to the devices and start them with default values. The initialization enables the usage of the specific device without further modification, and consequently, for every instrument a function was written to fulfill this step. MATLAB offers several commands for connecting to the device dependent on the type of connection. The easiest method for this is a predefined function of the manufacturer of the instrument, because the device directly can be addressed by the function. The CCD camera is used in this way. Listing D.1 shows the command which is used to open and initialize the CCD camera.

Listing D.1: Initialization of the CCD Camera

```
...
nInId = 0; % If one camera is used, the device ID always is 0
if exist('XStreamML.m')>0
  [nResult,CCD.CCDId]=XStreamML('OpenCamera',nInId);
       % 'OpenCamera' is used to connect to the camera

  propertyKey=X; % each parameter has a specific key number
  [nResult,exposure,nMinValue,nMaxValue]=...
    XStreamML('GetParameter',CCD.CCDId,propertyKey);
       % 'GetParameter' allows to get parameter X

  CCD.propertymax=nMaxValue;
  CCD.propertymin=nMinValue; % save parameter in main object

  propertyKey=X;
  [nResult]=...
    XStreamML('SetParameter',CCD.CCDId,propertyKey,propertyValue);
       % Set initialization values
  ...
  assignin('base','CCD',CCD); % Send object file to MATLAB workspace
else
  return;
end
...
```

The code first checks if the object file for the camera is available. A second command to connect to the camera leads to the camera identity number, which is used for further commands. By using `'GetParameter'` and `'SetParameter'` the current settings of the camera can be retrieved or modified. At the last step of the initialization, the `assignin()` command sends the device object variable `CCD` to the workspace. This allows to address the device with all other programs which can get the object variable from the workspace. All child programs of one MATLAB session have the permission to load this variable.

An other function (to control the acousto optical deflector via the function generators) is the `serial()` command. This command is predefined in MATLAB an connects the serial port with the specific device. In addition to this, commands like `analoginput()` and `analogoutput()` were used to address the photo diode via the AD/DA data acquisition instrument. With the latter commands the connection between the computer and both the piezoelectric stage and the laser was established.

Listing D.2 illustrates parts of the script for the initialization of the latter devices.

Listing D.2: Initialization with MATLAB commands

```
...
% Connection to function generators
FG=serial(sprintf('COM%i',com),'BaudRate',19200,'DataBits',8,'StopBits',2);
     % serial connection to COM Port com, with specific settings
fopen(FG); % open serial object FG
fprintf(FG,sprintf('CMND %.3f',val));
     % send command CMND with value val to the object FG
assignin('base',sprintf('FGCOM%i',com),FG);
...
% Connection to data acquisition card, piezoelectric stage, laser
% analog input control
AI = analoginput('dtol',id); % 'dtol': name of adaptor with ID id
addchannel(AI,i); % adds channel i for data transfer to object AI
getsample(AI,val); % get data of value val from object AI
assignin('base','AI',AI);
...
% analog output control
AO = analogoutput('dtol',id);
addchannel(AO,i); % adds channel i for data transfer to object AO
putsample(AO,V); % get data of value val from object AO
assignin('base','AO',AO);
...
```

The showed lines in principle have the same function. The first command creates and object and connects to the instrument. The second collects or sends data to the device. This allows to work with default values at the startup of the program. The last step ensures that other programs can communicate with the instrument via the workspace of the MATLAB session.
If only the dynamic libraries are available for a specific device, the script will contain commands which have to setup a device object. In this case the object is not an output of a predefined MATLAB script, but has to be developed by the programmer. For the initialization of the piezoelectric table and the step motors the device objects were defined by a custom-made script. Listing D.3 shows the script to built the device object of the piezoelectric table. This and other scripts were developed in collaboration with T. Fröhlich.

Listing D.3: Initialization with dynamic libraries

```
...
% Definitions of the device
c.DLLNameStub = 'E7XX_GCS_DLL';
c.libalias = 'E7XX';
c.ControllerName = [];
c.DLLName = [];
c = SetDefaults(c); % set default values for initialzation
if(~libisloaded(c.libalias)) % only load dll if it wasn't loaded before
  c = LoadGCSDLL(c);
end
c = class(c,'E7XX_GCS_Controller'); % define the class 'Controller'
...
%-------------------------------------------------------
function c = LoadGCSDLL(c)
% Search for dynamic library file
% its path in the windows registry
try
    gcspath = winqueryreg('HKEY_LOCAL_MACHINE','SOFTWARE\PI\GCSTranslator','Path');
catch
    gcspath = '';
end
% the dynamic library file itself
if(exist(gcspath,'dir')==7) %with the registry entry
    c.DLLName=[gcspath,'\',c.DLLNameStub,'.dll'];
else % with a predefined folder
  if(exist('c:\programme\pi\gcstranslator\','dir')==7)
    c.DLLName=(['c:\programme\pi\gcstranslator\',c.DLLNameStub,'.dll']);
  elseif(exist('c:\program files\pi\gcstranslator\','dir')==7)
    c.DLLName=(['c:\program files\pi\gcstranslator\',c.DLLNameStub,'.dll']);
  end
end
% import the corresponding header file
if strcmp(c.DLLNameStub , 'C843_PM_GCS_DLL')
    c.hfile = ['C843_GCS_DLL.h'];
else
    c.hfile = [c.DLLNameStub,'.h'];
end
% only load dll if it wasn't loaded before
if(~libisloaded(c.libalias))
  % load library
  [notfound,warnings] = loadlibrary (c.DLLName,c.hfile,'alias',c.libalias);
end
```

```
43 if(~libisloaded(c.libalias))
44   error('DLL could not be loaded');
45 else
46   % load the functions of the specific device, e.g. the MOVE command
47   c.dllfunctions = libfunctions(c.libalias);
48 end
49 end
```

The first part of the listing contains the definition of the name of the library which has to be loaded. Furthermore, the values for the initialization are arranged in function `c=SetDefaults(c)`. By calling the function `c=LoadGCSDLL(c)` the algorithm to import the dynamic library into MATLAB is started. Variable `c` denotes the device object variable, which has to be built step by step. In `LoadGCSDLL()`, first the dynamic library path is determined and afterwards loaded with function `loadlibrary()`. In between the header file for the library has to be imported. The functions the specific device can fulfill, e.g. the 'MOVE' command in case of the piezoelectric table, are listed in the dynamic library and have to be loaded to complete the device object variable. If the dynamic library is loaded correctly, the command `libisloaded()` will return with a 'TRUE' status.
With these different commands and function all devices could be addressed. Via the device object variable located in the MATLAB workspace it is possible for every script to access the object.

**Timer function and second MATLAB session**

In the setup of the optical tweezers the possibility to control the step motors, the piezoelectric table and the acousto optical deflector via a programmable joystick (Force 3D Pro PC Joystick, Logitech) was implemented. In contrast to the buttons used in the graphical user interface which use a callback function as trigger, the joystick actively has to be addressed and checked for status changes. In the case of a button, MATLAB sets up the trigger and the function calls. In case of the joystick, a loop has to be created which continuously checks status changes. A change of status means e.g. the tilt of the stick or a button press on the joystick. To realize the usage of the joystick a timer function was implemented into the MATLAB script. Hence, with the timer function the timer period could be chosen dependent on the connection and response speed of the device. Another advantage compared to a common loop function is that in the meantime several other timer objects can be

started. Since a function like `fork()` (language C) is not possible in MATLAB, the timer replaces this function. Moreover, the setup of the timer was used to allow a 'live' mode of the CCD camera and the photo diode via the AD/DA data acquisition card. Thus, further programs like live potentials, live particle detection and more could be realized by implementation in the timer function. Listing D.4 shows the setup of a timer function. This part of the script is similar for all timers used for the devices of the optical tweezers.

Listing D.4: Set up of the timer function

```
...
% set up of timer function
TimerName = timer('TimerFcn',{@Timer_Callback,handles},...
  'Period',TimerPeriod,'ExecutionMode','fixedDelay','BusyMode','drop');
  % 'TimerPeriod' is the time period of TimerFcn
  % 'fixedDelay', the timer starts after period and with
  % being the first entry at the MATLAB queue
  % 'drop' do not execute the function when sytem has no capacities
start(TimerName)
...
stop(TimerName)
```

In general there are three possibilities to built the timer function. In `'fixedRate'` mode, the next timer function starts directly after the execution of the current timer and the time period. In `'fixedDelay'` mode, before the next timer starts, the MATLAB queue has to be finalized. After that and the time period the timer is executed. In the third mode, `'fixedSpacing'`, the next timer function starts after the first ended plus the time period. For the custom-made scripts the second mode was used to allow to use the timer as fast as possible without exceeding the system's capacity. With the `start()` and `stop()` commands the timer can be started, which led to the execution of the `'TimerFcn'`, or stopped when the timer returns. The usage of several timer for different devices allowed to use their functionality in the same time. This was important e.g. for the measurements of the polymer brushes shown in Appendix B.

In case of a executing joystick controller, a photo diode controller and the CCD camera controller for the live view of the sample, three timer were running simultaneously. Since the CCD camera timer has to run at least with 25 Hz to allow a screening without buckling, and the shown signals of the photo diode at least with 10 Hz, the MATLAB session runs into capacity problems. A single MATLAB session does not completely use the whole memory of the system. This makes it possible

to run several MATLAB sessions which share the system's memory. Consequently, the two session work in parallel, do not influence each other and increase the efficiency in memory usage. For the upper purpose, to run the CCD camera without buckling, the CCD camera controller was outsourced to a second MATLAB session. For a communication between both MATLAB sessions, the second session has to be started by the first session. This can be performed via the `actxserver()` function. The return value of the function is a object variable which is used to address the client session. In the second session the CCD camera controller can be started and controlled via the link between both session. This is obligate if programs have to be synchronized. Listing D.5 shows the code to start and use two sessions.

Listing D.5: Usage of an activeX server

```
...
% commands at the host session
% start second session
OtherSession=actxserver('Matlab.Application'); % start second session
OtherSession.Visible=0; % make second session invisible - runs in the background
OtherSession.Execute(sprintf('cd(''bin'');')); % change folder in 2nd session
OtherSession.Execute('startup();'); % start the startup function in 2nd session
% start CCD camera controller
try CCD=OtherSession.GetVariable('CCD','base'); % try to get the camera
               % controller object from the second session's workspace
catch exception %if this wasn't successful
    OtherSession.Feval('CCD_Camera_Manager()',1,'2'); % execute camera controller
    return; % terminate the function
end
if ~CCD; % if there is an object, but the camera already closed
    result=OtherSession.Feval('CCD_Camera_Manager()',1,'2');
           % execute camera controller
else
    return; % terminate the function
end
...
```

In the host session the command `actxserver('Matlab.Application')` starts a client MATLAB session. In this way it also is possible to control e.g. a Microsoft Excel application. Since the second session can be controlled by the host, it can be made invisible and placed in the background. The variable `OtherSession` denotes the object of the client session. For every command concerning the second session the object has to be addressed. When the second session is executed, the paths of functions

which are not included in the main MATLAB folder are unknown to this session. Consequently, those functions cannot be started. Therefore while the second session starts up, a function has to be executed that includes the needed paths (command `startup()`). Afterwards the camera controller is started if there is no camera controller object. With the command `OtherSession.GetVariable()` variables between both sessions are transferred. The camera object variable is then a variable in the host's workspace. The function `OtherSession.Feval('CCD_Camera_Manager()',1,2)` is similar to `OtherSession.Execute` and starts the camera controller.
By the usage of several timer running simultaneously and a second session it was possible to ensure a smooth run of the applications. Another advantage was a better sharing of the computer memory to both session, which led to more efficiency.

### Graphical User Interface (GUI)

Every controller of the optical tweezers setup is shown in a separate figure with active control elements like buttons, sliders and edit fields. In that way the device can be controlled. The users do not have to know which steps are necessary and used to fulfill their commands. Especially for those users which are not familiar to programming scripts this makes it easy to work with the optical tweezers. The graphical user interfaces are similar in their principle. Beside the main function which is used to set up the figure and its objects, there are the callback functions which get executed when a specific button is hit or an edit field is changed. Moreover, axes can be implemented to show directly the output of a measurement. Via the objects' variables it is possible to change each object's properties in the program code. In Listing D.6 an exemplary GUI script is shown.

Listing D.6: script for a graphical user interface

```
1  % main GUI function, set up of the properties of the GUI
2  function varargout = CCD_Camera_Manager(varargin)
3  ...
4  gui_State = struct('gui_Name',    mfilename, ...
5                     'gui_Singleton', gui_Singleton, ...
6                     'gui_OpeningFcn', @CCD_Camera_Manager_OpeningFcn, ...
7                     'gui_OutputFcn', @CCD_Camera_Manager_OutputFcn, ...
8                     'gui_LayoutFcn', [] , ...
9                     'gui_Callback', []);
10 ...
11 end
12
```

```
% opening function, for changes before the GUI figure opens
% every callback contains the own object variable hObject and the handles
% of the figure. The opening function gets the input of the GUI - varargin.
function CCD_Camera_Manager_OpeningFcn(hObject, eventdata, handles,varargin)
...
% set up of a callback function, to use button with external program
set(handles.B_CCD_Init,'Callback',@B_CCD_Init_Callback);
% make a timer object for the usage of the camera, with specific options
ManTimr = timer('TimerFcn',{@Timer_Callback,handles},'Period',0.11,...
        'ExecutionMode','fixedDelay','BusyMode','drop');
...
end

function varargout = CCD_Camera_Manager_OutputFcn(hObject, eventdata,handles)
% Get default command line output from handles structure, GUI object variable
varargout{1} = hObject;
end

function Camera_Manager_CloseRequestFcn(hObject, eventdata, handles)
...
%close the CCD camera before closing the GUI
try help=XStreamML('CloseCamera',1);
catch exception
        disp('could not close');
end
...
end

% callback executed when the button B_Init is pushed
function B_Init_Callback(hObject, eventdata, handles)
...
end
...
```

Every GUI contains an 'opening' function and an 'output' function. These functions are important if predefined value should appear at the GUI and if specific values should be returned in case of a successful execution of the GUI. Furthermore, a 'closing' function is used when specific commands are executed before the GUI closes, e.g. the termination of a specific device or to stop a running timer. Every function ('opening', 'callback',...) within the script uses the variable defined as 'handles'. This variable contains all object variables and is passed to the function during

their call. By updating the status of the programs main object file, the handles are updated so that the next called function can use it. This is important in case of a running timer function, when parameters change during the execution. Another used feature is the possibility to address the GUI from a function which is not directly implemented in the GUI. Via the command `set(ButtonName,'Callback',@ProgName)` it is possible to call the figure object, extract the specific callback function and execute this function. This was used to steer the step motors with additional programs.

Overall by the usage of the embedded MATLAB and the custom-made MATLAB scripts it was possible to combine all devices which can be addressed via the computer. Furthermore, it offered a new way to several applications which use the functionality of the devices. At table D.1 a list of applications is shown, which use a specific device or a combination of several instruments.
ACF of table D.1 denotes autocorrelation function and PSD is the spectral power density. The current project 'Task Scheduler' allows to plan a schedule for the devices of the optical tweezers. Hence, for measurements of living cells specific positions are chosen where cells are located. The usage of the screen-shot and loop functions enable to screen the cells for long times with a high spatial resolution. If the microscope is out of focus at one specific cell, the autofocus function corrects the height and a sharp mapping of the cell is possible.
The usage of the function generators and the photo diodes made it possible to realize the active microrheology method (described in Section 3.2) to gather information about *in vitro* assembled keratin 8/18 networks. Details of this work are described in the thesis of S. Bührdel [135].

Table D.1: Overview of custom-made scripts.

| Controller for single devices | | |
|---|---|---|
| Name | Device | Applications |
| CCD Camera Manager | high speed camera | live screening, high sample rate measurements, long-time records, screen-shots, live particle detection |
| PiFOC Controller | piezoelectric stage | axial positioning in 100 µm range |
| Laser Controller | trapping laser | laser intensity variation |
| Photo Diode Manager | data acquisition card (for photo diodes) | live signal, laser position on photodiode, live position cloud, live potential, signal measurement, signal ACF, signal PSD |
| AOD Manager | function generators (for AOD) | trap position modulation, multiple traps, static trap shielding |
| **Controller for several devices** | | |
| Name | Devices | Applications |
| Joystick Controller | joystick<br>step motors<br>piezoelectric table<br>function generators (for AOD) | position control, position marking, beam steering, axial control (15 µm range), wave function motion, automatic height correction, coordinate system marking |
| MapRun Controller | step motors<br>high speed camera<br>piezoelectric table<br>PiFOC | sample scan (a range with several mm×mm range, autofocus, height correction, |
| Surface Approach Manager | piezoelectric stage<br>data acquisition card (for photo diodes) | approach particle displacement, approach energy landscapes, axial and vertical approach, |
| Task Scheduler | all devices | schedule applications, loops, time delays (beta) |

# Bibliography

[1] Maiman T.H., *Stimulated Optical Radiation in Ruby*, Nature **187**, 493-494, 1960.

[2] Ashkin A., Dziedzic J.M., Bjorkholm J.E., and Chu S., *Observation of a single-beam gradient force optical trap for dielectric particles*, Opt. Lett. **11**, 288, 1986.

[3] Binnig G., Quate C.F., and Gerber C., *Atomic force microscope*, Phys. Rev. Lett. **56**, 930-933, 1986.

[4] Bradford M.M., *A rapid and sensitive method for the quantitation of microgram quantities of protein utilizing the principle of protein-dye binding*, Anal. Biochem. **72**, 248-254, 1976.

[5] Borries B.V., and Ruska E., *Das Übermikroskop als Fortsetzung des Lichtmikroskops*, Verhandl. d. Ges. dt. Naturforscher und Ärzte **95**, 72-77, 1938.

[6] Flegler S., Heckman J., and Klomparens K., *Elektronenmikroskopie*, Spektrum Akademischer Verlag Berlin, 1993.

[7] U. Ulm, Sonderforschungsbereich 518 - Entzündung, Regeneration und Transformation im Pankreas, 2007).

[8] Deer E.L., Gonzalez-Hernandez J., Coursen J.D., Shea J.E., and Ngatia J., *Phenotype and genotype of pancreatic cancer cell lines*, Pancreas **39**, 425-435, 2010.

[9] Pantel K., Brakenhoff R.H., and Brandt B., *Detection, clinical relevance and specific biological properties of disseminating tumour cells*, Nat. Rev. Cancer **8**, 329-340, 2008.

[10] Alberts B., Johnson A., and Lewis J., *Molecular Biology of the Cell*, Garland Science New York **4th edition**, 2002.

[11] Sackmann E., and Merkel R., *Lehrbuch der Biophysik*, Wiley-VCH Weinheim **1st edition**, 2010.

[12] King, D., *Histology at SIU SOM. 'Epithelium Study Guide'*, 2010, `http://www.siumed.edu/~dking2/intro/epith.htm#simpcol`, 15.10.1012.

[13] Herrmann H., Bär H., Kreplak L., Strelkov S.V., and Aebi U., *Intermediate filaments: from cell architecture to nanomechanics*, Nat. Rev. Mol. Cell Biol. **8**(7), 562, 2007.

[14] Bernd, K., *Epithelial Cells*, Davidson College, Biology Department, 2010, `http://www.bio.davidson.edu/people/kabernd/BerndCV/Lab/EpithelialInfoWeb/index.html`.

[15] Githens, S., *Differentiation and development of the pancreas in animals*, The Pancreas: Biology, Pathobiology and Disease (eds Liang, V. and Go, W.), Raven Press Ltd New York, 21-55, 1993. `http://journals.lww.com/pancreasjournal/Pages/the-pancreas_bio_pathobio_disease.aspx`, 15.10.1012.

[16] Slack J.M., *Developmental biology of the pancreas*, Development **121**(6), 1569-1580, 1995.

[17] Bockman D.E., *Anatomy of the Pancreas*, The Pancreas: Biology, Pathobiology, and Disease(eds Liang, V. and Go, W.), Raven Press Ltd New York, 1095-1101, 1993, `http://journals.lww.com/pancreasjournal/Pages/the-pancreas_bio_pathobio_disease.aspx`, 15.10.1012.

[18] Bardeesy N., and DePinho RA., *Pancreatic Cancer Biology and Genetics*, Nat. Rev. Cancer **2**, 897-909, 2002.

[19] Hidalgo M., *Pancreatic cancer*, N. Engl. J. Med. **362**, 1605-1617, 2010.

[20] Chu G.C., Kimmelman A.C., Hezel A.F., and DePinho R.A., *Stromal biology of pancreatic cancer*, J. Cell. Biochem. **101**, 887-907. 2007.

[21] Adler G., *Has the biology and treatment of pancreatic diseases evolved?*, Best. Pract. Res. Clin. Gastroenterol **18**, 83-90, 2004.

[22] Kumar S., and Weaver V.M., *Mechanics, malignancy, and metastasis: the force journey of a tumor cell*, Cancer. Metastasis. Rev. **28**, 113-127, 2009.

[23] Wang N., and Stamenovic D., *Contribution of intermediate filaments to cell stiffness, stiffening, and growth*, Am. J. Physiol. **279**(1), C188-C194, 2000.

[24] Oshima R.G., Baribault H., and Caulin C., *Oncogenic regulation and function of keratins 8 and 18*, Cancer Metastasis Rev. **15**, 445-471, 1996.

[25] Beil M., et al., *Sphingosylphosphorylcholine regulates keratin network architecture and visco-elastic properties of human cancer cells*, Nat. Cell Biol. **5**, 803-811, 2003.

[26] Boal D., *Mechanics of the Cell*, Cambridge University Press Cambridge, 2002.

[27] Dominguez R., and Holmes K.C., *Actin structure and function*, Annu. Rev. Biophys. **40**, 169-186, 2011.

[28] Nogales E., *Structural insights into microtubule function*, Annu. Rev. Biochem. **69**, 277-302, 2000.

[29] Gittes F., Mickey B., Nettleton J., and Howard J., *Flexural Rigidity of Microtubules and Actin Filaments Measured from Thermal Fluctuations in Shape*, J. Cell Biol. **120**, 923, 1993.

[30] van den Heuvel M.G., de Graaff M.P., and C. Dekker, *Microtubule curvatures under perpendicular electric forces reveal a low persistence length*, Proc. Natl. Acad. Sci. USA. **105**, 7941-7946, 2007.

[31] Fuchs E., and Weber K., *Intermediate filaments: structure, dynamics, function, and disease*, Annu. Rev. Biochem. **63**, 345-382, 1994.

[32] Parry D.A.D., and Steinert P.M., *Intermediate Filament Structure*, Molecular Biology Intelligence Unit. R. G. Landis Co. Austin Texas, 1995.

[33] Nelson W., and Sun T.-T., *Keratin Classes: Molecular Markers for Different Types of Epithelial Differentiation*, J. Cell Biol. **97**, 244-251, 1983.

[34] Monteiro M.J., and Cleveland D.W., *Expression of NF-L and NF-M in fibrob-*

*lasts reveals coassemhly of neurofilament and vimentin subunits*, J. Cell Biol. **108**, 579-593, 1990.

[35] Steinert P.M., Chou Y.-H., Prahlad V., Parry D.A.D., Marekov L.N., Wu K.C., Jang S.-I., and Goldman R.D., *A high molecular weight intermediate filament-associated protein in BHK-21 cells is nestin, a type VI intermediate filament protein*, J. Biol Chem. **274**, 9881-9890, 1999.

[36] Chernyatina A.A., Nicolet S., Aebi U., Herrmann H., and Strelkov S.V., *Atomic structure of the vimentin central $\alpha$-helical domain and its implications for intermediate filament assembly*, PNAS **109**(34), 13620-13625, 2012.

[37] Herrmann H., Strelkov S.V., Burkhard P., and Aebi U., *Intermediate filaments: primary determinants of cell architecture and plasticity*, J. Clin. Invest. **119**, 1772-1783, 2009.

[38] Herrmann H., and Aebi U., *Intermediate filaments: molecular structure, assembly mechanism, and integration into functionally distinct intracellular scaffolds*, Annu. Rev. Biochem. **73**, 749-789, 2004.

[39] Lichternstern T., Mücke N., Aebi U., Mauermann M., and Herrmann H., *Complex formation and kinetics of filament self-assembly exhibited by the simple epithelial keratins K8 and K18*, J. Struct. Biol. **177**, 58-62, 2012.

[40] Leitner A., *Nanomechanische Eigenschaften von Keratin 8/18 - Von Einzelfilamenten zu Netzwerken*, Dissertation, Ulm University, Institute for Experimental Physics, 2011.

[41] Martin I., *Temperaturabhängige Eigenschaften von Keratin-Filamenten*, Diploma thesis, Ulm University, Institute for Experimental Physics, 2011.

[42] Winheim S., Hieb A.R., Silbermann M., Surmann E.-M., Wedig T., Herrmann H., Langowski J., and Muecke N., *Deconstructing the late phase of vimentin assembly by total internal reflection fluorescence microscopy (TIRFM)*, PLoS One **6**, 2011.

[43] Portet S., Muecke N., Kirmse R., Langowski J., Beil M., and Herrmann H., *Vimentin intermediate filament formation: In vitro measurement and mathe-*

*matical modeling of the filament length distribution during assembly*, Langmuir **25**, 8817-8823, 2009.

[44] Portet S., *Dynamics of length distributions- the in vitro intermediate filament assembly*, Preprint, 2011.

[45] Doi M., and Edwards S.F., *The Theory of Polymer Dynamics*, Clarendon Press Oxford, 1986.

[46] Graessley W.W., *Entangled Linear, Branched and Network Polymer Systems - Molecular Theories*, Adv. Polym. Sci. **47**, 1982.

[47] Ball R.C., Doi M., Edwards S.F., and Wagner M., *Elasticity of entangled networks*, Polymer **22**, 1010, 1981.

[48] Flory P., *Statistical Mechanics of CrossLinked Polymer Networks I. Rubberlike Elasticity*, J. Chem. Phys. **11**, 512, 1943.

[49] Rohrbach A., *Switching and measuring a force of 25 femtoNewtons with an optical trap*, Opt. Express **13**, 9695, 2005.

[50] Bockelmann U., Thomen P., Essevaz-Roulet B., Viasnoff V., and Heslot F., *Unzipping DNA with optical tweezers: high sequence sensitivity and force flips*, Biophys. J. **82**, 1537-1553, 2002.

[51] Wang M.D., Yin H., Landick R., Gelles J., and Block S.M., *Stretching DNA with optical tweezers*, Biophys. J. **72**, 1335-1346, 1997.

[52] Ashkin A., *Acceleration and trapping of particles by radiation pressure*, Phys. Rev. Lett. **24**, 1970.

[53] Block S., and Neuman K., *Optical Trapping*, Rev. Sci. Instrum. **75**(9), 2787-2809, 2004.

[54] Ashkin A., *Forces Of a Single-Beam Gradient Laser Trap On a Dielectric Sphere In the Ray Optics Regime*, Biophys. J. **61**(2), 569-582, 1992.

[55] Smith S.P., Bhalotra S.R., Brody A.L., Brown B.L., Boyda E.K. and Prentiss M., *Inexpensive optical tweezers for undergraduate laboratories*, Am. J. Phys. **67**,

26, 1999.

[56] Saleh B.E., and Teich M.C., *Fundamentals of Photonics*, Wiley Series in Pure and Applied Optics, Wiley New York, 1991, `http://www.emeraldinsight.com/journals.htm?articleid=1617051&show=html`,15.10.1012.

[57] Harada Y., and Asakura T., *Radiation Forces on a dielectric sphere in the Rayleigh Scattering Regime*, Opt. Commun. **124**(5-6), 529-541, 1996.

[58] Jackson J.D., *Classical Electrodynamics*, John Wiley & Sons Inc. Ney York **3rd edition**, 1999.

[59] Altmann S., *Single molecule mechanics - Linking structure and function of proteins*, Dissertation, Ulm University, Institute for Experimental Physics, 2002.

[60] Shaevitz J.W., *A Practical Guide to Optical Trapping*, 2006, `http://www.physics.sc.edu/~yar/Phys521_2010/tweezer_papers/Practical_Guide_to_Optical_Tweezers.pdf`, 15.10.1012.

[61] Novotny L., and Hecht B., *Principles of Nano-Optics*, Cambridge Univ. Press Cambridge, 2006.

[62] Cox A.J., DeWeerd A.J., and Linden J., *An experiment to measure Mie and Rayleigh total scattering cross sections*, Am. J. Phys. **70**, 620, 2002.

[63] van de Hulst H.C., *Light Scattering by Small Particles*, Wiley New York, 1957.

[64] Bohren C.F., and Huffman D.R., *Absorption and Scattering of Light by Small Particles*, Wiley New York, 82-129, 1983.

[65] Rohrbach A., and Stelzer E.H.K., *Trapping forces, force constants, and potential depths for dielectric spheres in the presence of spherical aberrations*, Appl. Opt. **41**(13), 2494-2507, 2002.

[66] Tolić-Nørrelykke S.F., Schaeffer E., Howard J., Pavone F.S., Juelicher F. and Flyvbjerg H., *Calibration of optical tweezers with positional detection in the back focal plane*, Rev. Sci. Instrum. **77**, 103101, 2006.

[67] Leach J., Mushfique H., Keen S., Di Leonardo R., Ruocco G., Cooper J.M., and

Padgett M.J., *Comparison of Faxén's correction for a microsphere translating or rotating near a surface*, Phys. Rev. E **79**, 026301, 2009.

[68] Florin E.-L., Pralle A., Stelzer E.H.K., and Hoerber J.K.H., *Photonic force microscope calibration by thermal noise analysis*, Appl. Phys. A: Solids Surf. **66**, 75-78, 1998.

[69] Mueller D., *Charakterisierung der Optischen Falle - Intensitaetsabhaengigkeit der Fallenstaerke*, Bachelor Thesis, Ulm University, Institute for Experimental Physics, 2011.

[70] Moffitt J.R., Chemla Y.R., Smith S.B., and Bustamante C., *Recent advances in optical tweezers*, Annu. Rev. Biochem, **77**, 205-228, 2008.

[71] Lang M.J., and Block S.M., *Resource Letter: LBOT-1: Laser-based optical tweezers*, Am. J. Phys. **71**, 201-215, 2003.

[72] Keen S., Leach J., Gibson G., and Padgett M., *Comparison of a high-speed camera and a quadrant detector for measuring displacements in optical tweezers*, J. Opt. A: Pure Appl. Opt. **9**, 264-266, 2007.

[73] Mason T.G., and Weitz D.A, *Optical measurements of frequency-dependent linear viscoelastic moduli of complex fluids*, Phys. Rev. Lett. **74**, 1252, 1995.

[74] Ferry J.D., *Viscoelastic properties of polymers*, John Wiley & Sons New York, 1980.

[75] Gittes F., Schnurr B., Olmsted P.D., MacKintosh F.C., and Schmidt C.F., *Microscopic Viscoelasticity: Shear Moduli of Soft Materials Determined from Thermal Fluctuations*, Phys. Rev. Lett. **79**, 3286, 1997.

[76] Mason T.G., Ganesan K., van Zanten J.H., Wirtz D., and Kuo S.C., *Particle Tracking Microrheology of Complex Fluids*, Phys. Rev. Lett. **79**, 3282, 1997.

[77] Xu J., Viasnoff V., and Wirtz D., *Compliance of actin filament networks measured by particle-tracking microrheology and diffusing wave spectroscopy*, Rheol. Acta. **37**, 387-398, 1998.

[78] Ward I.M., *The mechanical properties of solid polymers* Wiley New York, 1971.

[79] Mason T.G., *Estimating the viscoelastic moduli of complex fluids using the generalized Stokes-Einstein equation*, Rheol. Acta **39**, 371-378, 2000.

[80] Hansen J.P., and McDonald I.R., *Theory of Simple Liquids*, Academic London, 1986.

[81] Hess W., and Klein R., *Generalized hydrodynamics of systems of Brownian particles*, Adv. Phys. **32**, 173, 1983.

[82] Martin P.C., *Theory of Many-Particle Systems*, Lecture notes for P654, Cornell University, 2005.

[83] Mason T.G., Gang H., and Weitz D.A., *Diffusing-wave-spectroscopy measurements of viscoelasticity of complex fluids*, J. Opt. Soc. Am. A **14**, 139, 1997.

[84] Milner S.T., *Dynamical theory of concentration fluctuations in polymer solutions under shear*, Phys. Rev. E **48**, 3674, 1993.

[85] Leitner A., Paust T., Marti O., Walther P., Herrmann H., and Beil M., *Properties of Intermediate Filament Networks Assembled from Keratin 8 and 18 in the Presence of* $Mg^{2+}$, Biophys. J. **103**(2), 195-201, 2012.

[86] Evans R.M.L., Tassieri M., Auhl D., and Waigh T.A., *Direct conversion of rheological compliance measurements into storage and loss moduli*, Phys. Rev. E **80**, 012501, 2009.

[87] Bird R.B., Armstrong R.C., and Hassager 0., *Dynamics of Polymeric Liquids, Vol. I*, Fluid Mechanics John Wiley & Sons Ney York **2nd edition**, 1987.

[88] Crocker J.C., Valentine M.T., Weeks E.R., Gisler T., and Kaplan P.D., *Two-point microrheology of inhomogeneous soft materials*, Phys. Rev. Lett. **85**, 888-891, 2000.

[89] Crocker J.C., and Hoffman B.D., *Multiple-particle tracking and two-point microrheology in cells*, Methods Cell Biol. **83**, 141-178, 2007.

[90] Buchanan M., Atakhorrami M., Palierne J.F., and Schmidt C.F., *Comparing*

*Macrorheology and One- and Two-Point Microrheology in Wormlike Micelle Solutions*, Macromolecules **38**, 8840, 2005.

[91] Ou-Yang H.D., *Design and applications of oscillating optical tweezers for direct measurements of colloidal forces, Colloid-Polymer Interactions: From Fundamentals to Practice*, Wiley New York, 385-405, 1999.

[92] Gardel M.L., and Weitz D.A., *Microrheology, Microscale Diagnostic Techniques, ed. KS Breuer*, Springer Berlin, 1-50, 2005.

[93] Levine A.J., Lubensky T.C., *One- and Two-Particle Microrheology*, Phys. Rev. Lett. **85**, 8, 2000.

[94] Liebald E., *Konzept zum Bau einer Wärmekammer*, Zulassungsarbeit, Ulm University, Institute for Experimental Physics, 2012.

[95] Paul P., *Optimierung einer Vertreckeintrichtung zur Bestimmung mechanischer Eigenschaften biologischer Zellen*, Diploma thesis, Ulm University, Institute for Experimental Physics, 2012.

[96] Froehlich T., *Optische Doppelfalle- Konzeption, Aufbau, Verifikation*, Diploma thesis, Ulm University, Institute for Experimental Physics, 2011.

[97] Drotleff H.-J., *Zweikörpermikrorheologie an Zytoskelettsystemen*, Diploma thesis, Ulm University, Institute for Experimental Physics, 2011.

[98] Robel T., *Konzeption, Aufbau und Anwendung eines TIRF-Mikroskops in Verbindung mit fluoreszenzgelabelten Zytoskelettkomponenten*, Master thesis, Ulm University, Institute for Experimental Physics, 2012.

[99] de Gennes P.-G. *Scaling Concepts in Polymer Physics*, Cornell Univ. Press Ithaca, New York, 1991.

[100] Wirtz D., *Particle-tracking microrheology of living cells: principles and applications*, Annu. Rev. Biophys. **38**, 301-26, 2009.

[101] Morse D.C., *Viscoelasticity of concentrated isotropic solutions of semiflexible polymers. 1. Model and stress tensor*, Macromolecules **31**, 7030-7043, 1998.

[102] Morse D.C., *Viscoelasticity of concentrated isotropic solutions of semiflexible polymers. 2. Linear Response*, Macromolecules **31**, 7044-7067, 1998.

[103] Landau L.D., and Lifshitz E.M., *Theory of Elasticity*, Pergamon Press Oxford, 1986.

[104] Marti O., and Plettl A., *Vorlesungsskript Physikalische Elektronik und Messtechnik*, Ulm University, 2007

[105] El-Ghaoui L., and Lebret H., *Robust solutions to least-square problems to uncertain data matrices*, SIAM J. Matrix Anal. Appl. **18**, 1035-1064, 1997.

[106] Herrmann H., Kreplak L., and Aebi U., *Isolation, Characterization, and In Vitro Assembly of Intermediate Filaments*, Intermediate Filament Cytoskeletion - Meth. Cell Biol. **78**, 3-24, 2004.

[107] Martin I., personal communication, 2012.

[108] Rogers S.S., Waigh T.A., Zhao X., and Lu J.R., *Precise particle tracking against a complicated background: polynomial fitting with Gaussian weight*, Phys. Biol. **4**, 220-227, 2007.

[109] Köster S., Lin Y.-C., Herrmann H., and Weitz D.A., *Nanomechanics of Vimentin Intermediate Filament Networks*, Soft Matter **6**, 1910-1914, 2010.

[110] van Zanten J.H., and Rufener K.P., *Brownian motion in a single relaxation time Maxwell fluid*, Phys. Rev. E **62**, 5389-5396, 2000.

[111] Sugar Engineers, *Viscosity of Sugar Factory Products*, 2012, `http://www.sugartech.co.za/viscosity/index.php`, 15.10.1012.

[112] Schellart W.P., *Rheology and density of glucose syrup and honey: Determining their suitability for usage in analogue and fluid dynamic models of geological processes*, J. Struct. Geol. **33**(6), 1079-1088, 2011.

[113] Luan Y., Lieleg O., Wagner B., and Bausch A.R., *Micro- and macrorheological properties of isotropically cross-linked actin networks*, Biophys. J. **94**, 688-693, 2008.

[114] Lindl T., Zell- und Gewebekultur, Spektrum Akademischer Verlag **6th edition**, 133-141, 2008.

[115] Windoffer R., Kolsch A., Woell S., and Leube R.E., *Focal adhesions are hotspots for keratin filament precursor formation*, J. Cell Biol. **173**, 341-348, 2006.

[116] Walther P., personal communication, 2011.

[117] Blumenfeld R., *Isostaticity and controlled force transmission in the cytoskeleton: a model awaiting experimental evidence*, Biophys. J. **91**, 970-1983, 2006.

[118] Sivaramakrishnan S., DeGiulio J.V., Lorand L., Goldman R.D., and Ridge K.M., *Micromechanical properties of keratin intermediate filament networks*, Proc. Natl. Acad. Sci. USA **105**, 889-894, 2008.

[119] Yamada S., Wirtz D., and Kuo S.C., *Mechanics of living cells measured by laser tracking microrheology*, Biophys. J. **78**, 1736-1747, 2000.

[120] Wöll S., Windoffer R., Leube R.E., *Dissection of keratin dynamics: different contributions of the actin and microtubule systems*, Eur. J. Cell. Biol. **84**(2-3), 311-328, 2005.

[121] Paschke S., Weidner A.F., Paust T., Marti O., Beil M., and Ben-Chetrit E., *Colchicine modulates the viscoelastic properties of distinct cellular compartments in neutrophils*, in press, 2012.

[122] Maghelli N., *Mechanical properties of biological assemblies*, Dissertation, Ulm University, Institute for Experimental Physics, Dissertation, 2005.

[123] Sailer M., Höhn K., Lück S., Schmidt V., Beil M., and Walther P., *Novel electron tomographic methods to study the morphology of keratin filament networks*, Microsc. Microanal. **16**, 462-471, 2010.

[124] Gonçalves M.R., Makaryan T., Enderle F., Wiedemann S., Plettl A., Marti O., and Ziemann P., *Plasmonic nanostructures fabricated using nanosphere-lithography, soft-lithography and plasma etching*, Beilstein J. Nanotechnol. **2**, 448-458, 2011.

[125] Vollmer S., *Brownsche Bewegung von Nanoteilchen in Zytoskeletten*, Bachelor thesis, Ulm University, Institute for Experimental Physics, 2010.

[126] Steinbach A., Paust T., Pluntke M., Marti O., and Volkmer D., *Selective Adsorption of Functionalized Nanoparticles to Patterned Polymer Brushes and its Probing with an Optical Trap*, in press, 2012.

[127] Drechsler A., Synytska A., Uhlmann P., Elmahdy M.M., Stamm M., and Kremer F., *Interaction Forces between Microsized Silica Particles and Weak Polyelectrolyte Brushes at Varying pH and Salt Concentration*, Langmuir **26**(9), 6400, 2010.

[128] Elmahdy M.M., Drechsler A., Gutsche C., Synytska A., Uhlmann P., Kremer F., and Stamm M., *Forces between Blank Surfaces As Measured by the Colloidal Probe Technique and by Optical Tweezers - A Comparison*, Langmuir **25**, 12894, 2009.

[129] Visscher K., Gross S.P., and Block S.M., *Construction of Multiple-Beam Optical Traps with Nanometer-Resolution Position Sensing*, IEEE J. Sel. Top. Quantum Electron. **2**, 1066, 1996.

[130] Eriksen R.L., et al., *Fully dynamic multiple-beam optical tweezers*, Opt. Express **10**, 597, 2002.

[131] Lee W.M., Yuan X.-C., and Tano D.Y., *Optical tweezers with multiple optical forces using double-hologram interference*, Opt. Express **11**, 199, 2003.

[132] Curtis J.E., et al., *Dynamic holographic optical tweezers*, Opt. Commun. **207**, 169, 2002.

[133] Dholakia K., and Reece P., *Optical manipulation takes hold*, Nano Today **1**, 18-27, 2006.

[134] Guilford W.H., Tournas J.A., Dascalu D., and Watson D.S., *Creating multiple time-shared laser traps with simultaneous displacement detection using digital signal processing hardware*, Anal. Biochem. **326**(2), 153-166, 2004.

[135] Bührdel S., *Properties of keratin 8/18*, Master thesis, Ulm University, Institute

for Experimental Physics, 2012.

# List of Figures

1.1 Sketch of an epithelial cell with important proteins and molecules . . 2
1.2 Sketch of the pancreas . . . . . 4
1.3 Sketch of an actin filament . . . . . 6
1.4 A microtubule in theory . . . . . 7
1.5 Schematic drawing of an intermediate filament . . . . . 8
1.6 Dimer structure of intermediate filaments . . . . . 10
1.7 Assembly process of vimentin . . . . . 11

2.1 Pathway of the outermost rays of the laser beam in the geometrical optics regime . . . . . 17
2.2 A Gaussian beam gets focused . . . . . 18
2.3 Simulations for varying scattering and gradient forces . . . . . 21
2.4 Interference pattern on the quadrant photo diode . . . . . 23
2.5 Simulations to show the dependency of the potential on the binning of the displacement . . . . . 30

3.1 Simulation of MSD, G' and G" corresponding to the compliance of the publication . . . . . 40
3.2 MSD, G' and G" corresponding to the compliance of the publication with added noise . . . . . 41
3.3 MSD,G' and G" at the viscous fluid case . . . . . 42
3.4 MSD, G' and G" at the elastic solid scenario . . . . . 42

4.1 Principal setup of the light microscope . . . . . 48
4.2 Sketch of the sample holder . . . . . 50
4.3 Setup of the optical tweezers . . . . . 52
4.4 Setup of the TIRF microscope . . . . . 54

5.1 Master curve of the MSD in a viscoelastic medium . . . . . 56
5.2 Simulation of the motion of a particle in a purely viscous fluid . . . . 62

5.3 Brownian motion of a particle with spatial confinements of varying size 63
5.4 MSD of the particle motion with varying confinement size . . . . . 63
5.5 Dependency of the fitting parameters on the confinement size . . . . . 64
5.6 MSD in a confinement is different spatial limits . . . . . 65
5.7 Brownian motion and added drift with varying confinement size . . . 66
5.8 Surfaces of equal probability for different media . . . . . 67
5.9 BM-Simulations in an ellipsoidal confinements . . . . . 68
5.10 Fit parameter dependency on the ellipsoidal confinement size . . . . . 68
5.11 Harmonic potential analysis of the Brownian motion of particles . . . 70
5.12 Brownian motion of particles with a repelling force . . . . . 70
5.13 Brownian motion of particles in a cuboid confinement with added repelling force . . . . . 71
5.14 MSD of Evan's compliance function . . . . . 72
5.15 MSD of Evan's compliance function with noise . . . . . 73
5.16 Theortical MSD in a viscous fluid and elastic solid . . . . . 74
5.17 Storage modulus $G'$ and loss modulus $G''$ for the case of a viscous fluid 74
5.18 Shear modulus in an elastic solid scenario . . . . . 75
5.19 Dynamic shear modulus of Brownian motion simulation with varying network force constant . . . . . 76
5.20 Dynamic shear modulus of Brownian motion simulation with varying drift of the network . . . . . 77
5.21 Dynamic shear modulus of Brownian motion simulation with varying viscosity in the network . . . . . 78

6.1 Transfer matrix values with varying ratios of SNR . . . . . 92
6.2 Propagation of amplitude of the excitement dependent on $G$ and the force . . . . . 93
6.3 Displacement dependent on the ratio of forces acting in lateral directions 94

7.1 Double-logarithmic plot of the averaged MSD of BM in bi-distilled water . . . . . 100
7.2 Residuals of the fitting of the MSD in bi-distilled water . . . . . 101
7.3 Double logarithmic plot of the single fitting terms of the MSD . . . . 103
7.4 Storage and loss modulus of the measurements in bi-distilled water . 104
7.5 MSD of the particle motion in saccharose solution . . . . . 105
7.6 Residuals of the fitting with the model-based function . . . . . 106
7.7 Double logarithmic plot of the single fitting terms of the MSD in saccharose solution . . . . . 107

7.8 Resulting storage and loss modulus in saccharose solution . . . . . 108
7.9 SEM images of the *in vitro* assembled K8/18 networks . . . . . 109
7.10 MSD with fit for varying $MgCl_2$ concentrations - 1 . . . . . 110
7.11 MSD with fit for varying $MgCl_2$ concentrations - 2 . . . . . 111
7.12 95% confidences of the MSD . . . . . 112
7.13 Storage modulus of K8/18 dependent on the $MgCl_2$ concentration . . 113
7.14 Loss modulus of K8/18 dependent on the $MgCl_2$ concentration . . . . 114
7.15 Comparison of storage and loss modulus between a K8/18 network and the saccharose solution . . . . . 115
7.16 Comparison of a Brownian motion simulation in an elliptical confinement with the measurement . . . . . 116
7.17 Electron microscope image of an extracted cell of line Panc-1 . . . . . 118
7.18 Electron microscopy image of extracted cells . . . . . 119
7.19 Electron microscope image of an extracted cell showing the radial alignment . . . . . 120
7.20 Histogram of measured particles in the extracted cell . . . . . 121
7.21 MSD in extracted cell networks with varying distances to the rim of the nucleus - 1 . . . . . 122
7.22 MSD in extracted cell keratin 8/18 networks with varying distance to the rim of the nucleus - 2 . . . . . 123
7.23 MSD in extracted cell keratin 8/18 networks with varying distance to the rim of the nucleus - 3 . . . . . 123
7.24 G' in extracted cell keratin 8/18 networks . . . . . 125
7.25 G" in extracted cell keratin 8/18 networks . . . . . 126
7.26 Plateau storage and loss moduli $G_0'$ and $G_0''$ dependent on the distance to the rim of the nucleus . . . . . 127
7.27 MSD and corresponding fit for human granulocytes . . . . . 129
7.28 Residuals plot of colchicine treated and untreated neutrophils . . . . 130
7.29 Storage and loss modulus of treated and untreated cells . . . . . 131
7.30 Response of the reference particle in water . . . . . 133
7.31 Reference particle motion due to the excitation with the laser . . . . 136
7.32 Response particle motion due to the excitation of the reference particle 137
7.33 Histogram of the response of the reference particle to an oscillation of the laser . . . . . 138
7.34 Amplitude propagation in the invitro assembled network (0mM $MgCl_2$) 140
7.35 Amplitude propagation in the invitro assembled network (1 mM $MgCl_2$) 141
7.36 Histogram of the amplitudes of the higher harmonics (0 mM $MgCl_2$) . 142

7.37 Histogram of the amplitudes of the higher harmonics (1 mM $MgCl_2$) . 142
7.38 Semi-logarithmic plot of the averaged network force constant . . . . . 145
7.39 Goodness of the fit for the network force constants . . . . . 146
7.40 Exemplary surfaces of equal probability . . . . . 148
7.41 Surface area of the isosurface dependent on density value . . . . . 149
7.42 Volume of the isosurface dependent on density value . . . . . 149
7.43 Semi-principal axes fitting an ellipsoid to the isosurface . . . . . 151

A.1 Overview scan with pancreatic cancer cells . . . . . 168
A.2 Overviews of scratched Fisher Projection Pattern . . . . . 169
A.3 FPP-Dislocations in the Optical Tweezers and the Electron Microscope 170

B.1 Response of the particles upon approaching a PMAA coated polymer brush substrate . . . . . 172

C.1 Screenshot of trapped particles of 1 µm diameter located in water . . 176

# List of Tables

5.1 Table of used parameters for the fitting of the MSD. . . . . 59

7.1 Preparation methods for the dialysis. . . . . 97
7.2 Results of the fitting of the MSD of bi-distilled water. A $R^2$ value of 0.9991 led to a high goodness of the fit. . . . . 102
7.3 Results of the fitting of the MSD of saccharose solution. . . . . 106
7.4 Results of the fitting of the MSD of *in vitro* assembled keratin 8/18 networks. . . . . 111
7.5 Results of the comparison to the simulated Brownian motion. . . . . 116
7.6 Resulting fitting parameter $a$, $b$, $c$ and $d$ dependent on the distance to the rim of the nucleus. The $R^2$ value shows the goodness of the fit. 124
7.7 Resulting standard errors of the fitting parameter $\Delta a$, $\Delta b$, $\Delta c$ and $\Delta d$ dependent on the distance to the rim of the nucleus. . . . . 125
7.8 Results of the fitting of the MSD at treated and untreated human granulozytes. . . . . 130
7.9 Response parameters of a particle excited in bi-distilled water. . . . . 134

D.1 Overview of custom-made scripts. . . . . 187

# Curriculum Vitae

| Zur Person | Tobias Paust |
|---|---|
| 06.01.1983 | geboren in Günzburg, Bayern |
| | |
| Schulbildung | Gymnasium |
| 09/1993-06/2002 | Dossenberger Gymnasium<br>Günzburg, Bayern |
| | |
| Wehrdienst | Einheit |
| 07/2002-09/2002 | 3. Kompanie Luftwaffenausbildungsregiment,<br>Oberschwaben-Kaserne Mengen/Hohentengen |
| 10/2002-04/2003 | Lufttransportgeschwader 61,<br>Fliegerhorst Landsberg/Lech, Penzing |
| | |
| Studium | Universität Ulm, Ulm |
| 10/2003-10/2008 | Wirtschaftsphysik, Diplom |
| | |
| Diplomarbeit | Thema |
| 04/2008-10/2008 | Experimentelle Physik:<br>*Pulsed-Force Mode Messungen des Optischen Nahfeldes* |
| | |
| Abschluss | Universität Ulm, Ulm |
| 15.10.2008 | Wirtschaftsphysik, Diplom |
| | |
| Promotion | Institut für Experimentelle Physik - Universität Ulm |
| 10/2008-12/2012 | *New Methods for Passive and Active Microrheology*<br>Prof. Dr. sc. nat. ETH Zürich Othmar Marti<br>Prof. Dr. Kay-Eberhard Gottschalk |
| | |
| Förderungen | |
| 06/2010 | Gordon-Konferenz, Tilton, USA, Graduiertenkolleg |

| Praktika | |
|---|---|
| 08/1999 | Praktikum Metalwarenfabrik WANZL GmbH |
| 08/2000 | ” |
| 08/2001 | ” |
| 05/2003-09/2003 | ” |
| 09/2004 | ” |
| 09/2005 | ” |
| 09/2006 | ” |

| Engagement | |
|---|---|
| 10/2006-03/2007 | Seminar, Physik Praktikum für Mediziner |
| 04/2007-08/2007 | Seminar, Physik Praktikum für Zahnmediziner |
| 10/2007-03/2008 | Seminar, Physik Praktikum für Mediziner |
| 10/2008-03/2009 | Seminar, Grundlagen der Physik I |
| 10/2008-10/2012 | Praktikum, Fortgeschrittenen Praktikum für Physiker - Optische Pinzette |
| 04/2009-08/2009 | Seminar, Grundlagen der Physik II |
| 04/2010-08/2010 | Praktikum, Physikalisches Praktikum für Biologen Optische Pinzette |
| 10/2010-03/2011 | Praktikum, Fortgeschrittenen Praktikum für Physiker Holographie |
| 04/2011-03/2012 | Praktikum, Fortgeschrittenen Praktikum für Physiker Regelungstechnik |
| 05/20011-06/2011 | Seminar - Introduction to MATLAB |
| 06/2011-08/2011 | Betreuung von Studenten, DAAD RISE Projekt |
| 07/2011 | jDPG - Physikerfrühstück |
| 04/2012-10/2012 | Praktikum, Fortgeschrittenen Praktikum für Physiker Gammaspektroskopie |
| 07/2012 | jDPG - Physikerfrühstück |
| 10/2008-10/2012 | Betreuung Diplom-, Master-, Bachelorarbeiten, Hilfswissenschaftler |

| Sprachen | |
|---|---|
| English | fließend |
| Französisch | Grundkenntnisse |
| Spanisch | Grundkenntnisse |

| Engagement | in anderen Bereichen |
|---|---|
| | Jugendbetreuung im Fussballverein |

| Programmiersprachen | |
|---|---|
| Mathworks®MATLAB | gut |
| C | gut |
| Oberon | Grundkenntnisse |
| VBA | Grundkenntnisse |

| Hobbies | |
|---|---|
| | Fussball (Verein), Sport allg., Sprachen, Computer, Musik, |

## Publications

- Leitner A., Paust T., Marti O., Walther P., Herrmann H., and Beil M., Properties of Intermediate Filament Networks Assembled from Keratin 8 and 18 in the Presence of Mg2+, Biophys. J., 103-2, 195-201, 2012.

- Steinbach A., Paust T., Pluntke M., Marti O., and Volkmer D., Selective Adsorption of Functionalized Nanoparticles to Patterned Polymer Brushes and its Probing with an Optical Trap, submitted to ACS Appl. Mater. Interfaces, 2012.

- Paschke S., Weidner A.F., Paust T., Marti O., Beil M., and Ben-Chetrit E., Colchicine modulates the viscoelastic properties of distinct cellular compartments in neutrophils, submitted to J. Rheum., 2012.

- Paust T., Leitner A., Beil M., and Marti O., A model-based conversion of microrheological particle displacement data into dynamic shear moduli, submitted to PLoS ONE, 2012.

- Paust T., Beil M., and Marti O., Active multi-point microrheology - a new method, in preparation, based on chapter 6, 2012.

## Talks

- "Regulation of the viscoelastic properties of the keratin cytoskeleton in pancreatic carcinoma cells", Seminar of the Department, Ulm, 02/09.
- "Optical tweezers for measuring IF network mechanics", IF-Consortium Meeting, Ulm, 04/09.
- "Microrheology: Extracted Panc1 cytoskeleton versus assembled keratin network", Seminar of the Department, Ulm, 10/09.
- "Microrheology of K8/18 networks - In search of cells at the EM", IF-Consortium Meeting, Heidelberg, 02/10.
- "Microrheology - Microparticles: The passengers of the cell", Meeting, Heidelberg, 07/10.
- "Progress report - Optical Tweezers / Microrheology", Seminar of the Department, Ulm, 11/10.
- "Methods to determine the mechanical properties of carcinoma cells - Overview & Problems", Seminar Intergrated Graduate School, Ulm, 01/11.
- "Progress Report - Overview & Problems", Seminar of the Department, Ulm, 04/11.
- "*In vitro* assembly keratin 8/18 and panc1 networks - active rheological measurements", IF-Consortium Meeting, Heidelberg, 11/11.
- "Heidelberg Meeting - Discussions", Seminar of the Department, Ulm, 01/12.
- "Progress Report - Prefinal Talk In preparation for results", Seminar of the Department, Ulm, 02/12.
- "News in microrheological research", IF-Consortium Meeting, Göttingen, 02/12.
- "Progress Report - Brownian Motion Simulations", Seminar of the Department, Ulm, 06/12.

- "Final talk - Passive and active Microrheology", Seminar of the Department, Ulm, 01/13.

## Poster

- "Optical Tweezers: A system for tracking several beads incorporated in the keratin cytoskeleton of pancreatic carcinoma cells", T. Paust, A. Schmatulla, U. Nolte, M. Beil, and O. Marti, DPG Frühjahrstagung, Dresden, 03/09.

- "Microrheology: A system for the comparison of pancreatic carcinoma cells in an optical tweezers device and an electron microscope", T. Paust, A. Leitner, U. Nolte, M. Beil, P. Walther, and O. Marti, DPG Frühjahrstagung, Regensburg, 03/10.

- "Comparison of nanomechanical properties of *in vivo* and *in vitro* keratin 8/18 networks", T. Paust, A. Leitner, H.Herrmann, M. Beil, and O. Marti, Gordon research Conference Intermediate Filaments, Tilton NH, 06/10.

- "Microrheology: A system for the comparison of pancreatic carcinoma cells in an optical tweezers device and an electron microscope", T. Paust, T. Fröhlich, S. Vollmer, T. Pusch, M. Beil, P. Walther, and O. Marti, DPG Frühjahrstagung, Dresden, 03/11.

- "Microrheology: A new algorithm for the conversion of mean squared displacement to the dynamic shear modulus", T. Paust, A. Leitner, M. Beil, O. Marti, DPG Frühjahrstagung, Dresden, 03/11.

- "Active Microrheology: A new approach to determine mechanical properties of assembled networks", T.Paust, I.Martin, M.Beil, H.Herrmann, and O.Marti, DPG Frühjahrstagung, Berlin, 03/12.

- "Microrheology: Brownian motion simulations in spatial confined geometry", T. Paust, M. Beil, and O. Marti, Kompetenznetz Funktionelle Nanostrukturen, Bad Herrenalb, 09/12.

**Erklärung** Hiermit erkläre ich, dass ich die vorliegende Arbeit selbständig und nur mit den angegebenen Hilfsmittel angefertigt habe und dass alle Stellen, die im Wortlaut oder im Sinne nach anderen Werken übernommen sind, durch Angabe der Quelle als Entlehnung kenntlich gemacht worden sind.

Ulm, den 12. Dezember 2012

Tobias Paust